



## Tomographic Techniques for Radar Ice Sounding

Nielsen, Ulrik

*Publication date:*  
2015

*Document Version*  
Publisher's PDF, also known as Version of record

[Link back to DTU Orbit](#)

*Citation (APA):*  
Nielsen, U. (2015). *Tomographic Techniques for Radar Ice Sounding*. Danmarks Tekniske Universitet (DTU).

---

### General rights

Copyright and moral rights for the publications made accessible in the public portal are retained by the authors and/or other copyright owners and it is a condition of accessing publications that users recognise and abide by the legal requirements associated with these rights.

- Users may download and print one copy of any publication from the public portal for the purpose of private study or research.
- You may not further distribute the material or use it for any profit-making activity or commercial gain
- You may freely distribute the URL identifying the publication in the public portal

If you believe that this document breaches copyright please contact us providing details, and we will remove access to the work immediately and investigate your claim.

# Tomographic Techniques for Radar Ice Sounding



PhD Thesis

Ulrik Nielsen  
February 2015



DISSERTATION FOR THE DEGREE OF DOCTOR OF PHILOSOPHY

# Tomographic Techniques for Radar Ice Sounding

Ulrik Nielsen



National Space Institute  
Technical University of Denmark  
Copenhagen, Denmark 2015



Ørsted's Plads  
Building 348  
DK-2800 Kongens Lyngby  
Tel. +45 4525 9500  
[www.space.dtu.dk](http://www.space.dtu.dk)

$$I(v, T) =$$

A collage of mathematical symbols and formulas, including Planck's law, the Riemann zeta function, and various mathematical notations like epsilon, theta, infinity, and chi-squared.

Printed by GraphicCo  
Svendborg, Denmark 2015

# Abstract

Low frequency radars, also known as sounders, can be used for subsurface measurements of Earth's massive ice sheets. Radar data are essential to improving ice sheet models for better prediction of the response of these ice sheets to global climate change. While airborne sounders are needed for detailed measurements of fast-flowing outlet glaciers, a space-based sounder is potentially capable of broad coverage with high spatial and uniform sampling over the interior of the ice sheets. For both types of systems, however, surface clutter that obscures the depth signal of interest is a major technical challenge.

This dissertation deals with tomographic techniques based on multi-phase-center radars that represent state-of-the-art technology within the field of ice sounding. The use of advanced tomographic processing for clutter suppression is investigated, which up to this point has been largely unexplored in the literature. The investigation also includes a theoretical study of beamforming and direction-of-arrival (DOA) estimation techniques. In addition to the primary treatment of clutter suppression, additional novel applications of tomography are also explored.

Based on an experimental multi-phase-center dataset acquired with the POLarimetric Airborne Radar Ice Sounder (POLARIS), single-pass tomographic surface clutter suppression capabilities are demonstrated for the system. Using repeat-pass POLARIS data, a method based on data-driven DOA estimation is used to show an along-track variation of the effective scattering center of the surface return, which is caused by a varying penetration depth.

As an alternative to the traditional echogram, a new DOA representation that offers a better visualization of the desired signals and clutter is suggested. Based on this alternative presentation, a novel technique for discrimination of the desired bed return from strong surface clutter is presented. The technique is applied to data from the channel of the challenging Jakobshavn Glacier acquired with the Multi-channel Coherent

Radar Depth Sounder/Imager (MCoRDS/I), where it is shown how the technique can be used to close some of the critical gaps in bed detection along the channel.

Finally, a geometric model is used to show how the across-track slope of the bed is related to the DOA pattern of the bed return. Based on this, a technique for estimation of the backscattering characteristics is presented. Furthermore, waveform analysis is investigated for estimation of the bed roughness.

# Preface

This dissertation is submitted in partial fulfilment of the requirements for obtaining the PhD Degree at the Technical University of Denmark. The work described herein has been conducted at the Department of Microwaves and Remote Sensing, National Space Institute, under the PhD program of Electronics, Communication and Space Science.

The PhD study was supervised by Assoc. Prof. Dr. Jørgen Dall, National Space Institute.

Ulrik Nielsen  
Copenhagen, February 2015



## Acknowledgements

First of all, I would like to thank my supervisor Jørgen Dall for his excellent guidance, engagement and support during the study. Jørgen has been a significant and inspiring mentor for me, taken me under his wing, and believed in and fought for my project. His extensive experience and comprehensive knowledge on signal processing and radar systems, has been an invaluable help, but he has also taught me much more broader competences and helped me with anything and everything, when it was needed during the study.

The friendliness and support from the rest of my colleagues in the Microwaves and Remote Sensing group was also much appreciated. Especially Birte Kronbak Andersen has been a key driver for the social environment in the group, and I am grateful for her providing me with left over food for late evening hours at the office.

I would also like to thank the director of the Center for Remote Sensing of Ice Sheets Professor Prasad Gogineni and his group for hosting my external research stay at the University of Kansas.

I am grateful to the Otto Mønsted foundation, the Idella foundation, and the foundation of Kaj and Hermilla Ostenfeld for contributing to the expenses for conferences and external research stay undertaken during the PhD study.

I would also like to thank my fellow PhD students Niels Christian Jerichau Clausen and Morten Fischer Rasmussen, with whom I have discussed everything from technical to personal matters.

Further, a thank you to Anders Kusk and Niels Christian Jerichau Clausen for valuable comments to the dissertation.

Finally, a special thank to Line for patience and support during the study.



# Contents

<b>Abstract</b>	<b>iii</b>
<b>Preface</b>	<b>v</b>
<b>Acknowledgements</b>	<b>vii</b>
<b>List of Figures</b>	<b>xi</b>
<b>List of Tables</b>	<b>xiii</b>
<b>1 Introduction</b>	<b>1</b>
1.1 Background . . . . .	1
1.2 Ice Sounding . . . . .	2
1.3 Surface Clutter . . . . .	3
1.4 Radar Tomography . . . . .	9
1.5 Scope and Outline of the Dissertation . . . . .	10
<b>2 Sounding Radar Principles</b>	<b>13</b>
2.1 Electromagnetic Waves . . . . .	13
2.2 Fresnel Reflection and Transmission . . . . .	17
2.3 Radar Basics . . . . .	20
2.4 Surface Scattering . . . . .	21
2.5 Synthetic Aperture Radar . . . . .	27
2.6 Antenna Arrays . . . . .	34
<b>3 Array Signal Processing</b>	<b>39</b>
3.1 Signal Model . . . . .	40
3.2 Beamforming . . . . .	45
3.3 Direction of Arrival . . . . .	55
3.4 Compressive Sensing . . . . .	68



3.5	DOA Simulation . . . . .	71
<b>4</b>	<b>Multi-Phase-Center Ice Sounding Data</b>	<b>79</b>
4.1	POLARIS . . . . .	79
4.2	MCoRDS/I . . . . .	89
<b>5</b>	<b>Tomographic Processing</b>	<b>95</b>
5.1	Spatial Aliasing . . . . .	95
5.2	Effective Surface Scattering Center . . . . .	98
5.3	DOA Representation of Radar Echograms . . . . .	105
5.4	Recovery of Ice Bed Detection Gap . . . . .	108
5.5	Clutter Suppression . . . . .	109
5.6	Summary . . . . .	111
<b>6</b>	<b>Basal Surface Scattering Estimation</b>	<b>115</b>
6.1	Tomographic Backscattering Estimation . . . . .	115
6.2	Waveform Analysis . . . . .	124
<b>7</b>	<b>Conclusions</b>	<b>131</b>
7.1	Suggestions for Future Work . . . . .	134
<b>A</b>	<b>Paper</b>	<b>137</b>
<b>B</b>	<b>Paper</b>	<b>143</b>
<b>C</b>	<b>Paper</b>	<b>155</b>
	<b>Nomenclature</b>	<b>169</b>
	<b>Bibliography</b>	<b>175</b>
	<b>Index</b>	<b>187</b>

## List of Figures

1.1	Sounding geometry associated with surface clutter . . . . .	3
1.2	Surface footprints . . . . .	5
1.3	Doppler processed surface footprints . . . . .	5
1.4	Masking surface clutter . . . . .	7
2.1	Linear polarization . . . . .	15
2.2	Electromagnetic spectrum . . . . .	15
2.3	Oblique incidence . . . . .	19
2.4	Basic pulse radar . . . . .	20
2.5	Surface scattering components . . . . .	22
2.6	Sidelobe surface clutter . . . . .	34
2.7	Weighted impulse responses . . . . .	35
2.8	Excited uniform linear array . . . . .	36
3.1	Uniform linear array with impinging plane wave . . . . .	41
3.2	Beamforming . . . . .	51
3.3	Noise scaling . . . . .	53
3.4	Successive iterations of the AM algorithm . . . . .	65
3.5	Spatial spectrum . . . . .	72
3.6	DOA resolvability dependency on SNR . . . . .	73
3.7	DOA resolvability dependency on signal separation . . . . .	74
3.8	DOA algorithm accuracy . . . . .	76
3.9	DOA algorithm accuracy dependency on SNR . . . . .	76
3.10	DOA algorithm accuracy dependency on signal separation . . . . .	77
3.11	DOA algorithm accuracy dependency on snapshots . . . . .	77
4.1	POLARIS 4-element antenna array . . . . .	80
4.2	POLARIS 8-element antenna array . . . . .	81
4.3	Technical drawing of 8-element antenna array . . . . .	81
4.4	Flight tracks at Jutulstraumen Glacier . . . . .	84

4.5	Baselines of repeat-pass dataset . . . . .	86
4.6	Jutulstraumen echogram . . . . .	87
4.7	Navigational data for aircraft roll manoeuvre . . . . .	87
4.8	Estimated transmit antenna pattern . . . . .	88
4.9	Measured transmit antenna pattern . . . . .	89
4.10	POLARIS receive antenna pattern, V-polarization. . . . .	90
4.11	MCoRDS/I Antenna Array . . . . .	91
4.12	Flight tracks at Jakobshavn Glacier . . . . .	92
4.13	Jakobshavn echogram . . . . .	93
4.14	North Greenland flights tracks . . . . .	93
4.15	Echogram with smooth and rough bedrock . . . . .	94
5.1	DOA estimate of surface clutter . . . . .	97
5.2	DOA estimate of lowered effective phase center . . . . .	99
5.3	Geometry related to a lowered effective phase center . . . . .	100
5.4	Penetration depth . . . . .	100
5.5	Parameter signal . . . . .	102
5.6	Parameter signal enlargement . . . . .	102
5.7	Cross-correlation of scaling parameter and radar intensity . . . . .	103
5.8	Waveforms at selected locations . . . . .	105
5.9	DOA image, MUSIC . . . . .	107
5.10	DOA image, ML . . . . .	107
5.11	Jakobshavn echogram enlargement, Z1 . . . . .	108
5.12	DOA-based bed detection . . . . .	109
5.13	Surface clutter suppressed nadir waveform . . . . .	110
5.14	Echogram processed with beamsteering . . . . .	112
5.15	Echogram processed with Capon's method . . . . .	112
6.1	Jakobshavn echogram enlargement, Z2 . . . . .	116
6.2	Sounding geometry of sloped bed . . . . .	117
6.3	One-singal DOA estimate of sloped bed return . . . . .	118
6.4	Two-singal DOA estimate of sloped bed return . . . . .	119
6.5	Echogram detrending . . . . .	120
6.6	Bed return waveform . . . . .	120
6.7	Transmit pattern filling . . . . .	122
6.8	Bed surface backscatter estimation . . . . .	124
6.9	Waveforms . . . . .	126
6.10	Waveform fitting based on the convolution model . . . . .	126
6.11	Backscattering coefficient . . . . .	129

List of Tables

2.1 Radar-frequency bands . . . . . 16

4.1 POLARIS system parameters . . . . . 82

4.2 Jutulstraumen data inventory . . . . . 85

5.1 Scaling parameter correlation . . . . . 103

5.2 Correlation of scaling parameter and radar intensity . . . . . 104



# Introduction

## 1.1 Background

The behavior of planet Earth can be understood in terms of the coupling between the dynamic processes in the atmosphere, the solid Earth, the hydrosphere, the cryosphere, the biosphere, and the anthroposphere. This set of coupled dynamical systems is referred to as the Earth System.

During the last 150 years the Earth System has been subject to radical changes. Both human-induced changes and the variability of the natural system have to be fully understood and quantified to determine whether the consequence could be destabilization of the Earth System. This insight implies understanding of the major subsystems and the coupling between them. For this reason, understanding of the cryosphere is one of the main objectives of European Space Agency's (ESA's) Living Planet Programme [1]. A central part of the cryosphere consist of ice sheets that modulates the global sea level by storing water, deposited as snow, on the surface and discharging water back into the ocean through melting and calving. Approximately 3% of the Earth's surface is covered by ice. The largest contribution by far is the Antarctic ice sheet, which holds 63% of the fresh water on the Earth's surface [2] and is equivalent to about 57 m of sea level [3].

A number of investigations show that both the Greenland and Antarctic ice sheets are rapidly and unexpectedly losing mass [4, 5]. These documented changes have potentially catastrophic consequences such as global sea-level rise. The Intergovernmental Panel on Climate Change (IPCC) estimates that sea level could increase by 26–98 cm by the end of this century, relative to year 2000 [6]. A part of the reason for the large range in projected sea-level rise is due to an incomplete understanding of the mechanisms causing the rapid changes in Greenland and Antarctica. It is therefore essential to understand the processes causing

the mass loss, as well as to improve the ice-sheet models for generating more accurate estimates of the ice sheets' contribution to sea-level rise. To address this deficiency, more thorough information on ice thickness, internal stratigraphy, subglacial topography and basal conditions is critically needed.

To investigate ice sheets, direct methods such as ice core drilling can provide detailed information on the ice sheet internals. However, such approaches are very time consuming and are limited with respect to geographical coverage. In order to obtain large-scale spatial sampling of the global ice sheets, remote sensing techniques are needed. Due to the electromagnetic properties of ice, glaciers and ice sheets are well suited to investigation by radar that offers subsurface exploration capabilities. Furthermore, a radar can be operated from a moving platform that makes high spatial and temporal coverage possible. Actually, radar measurements from a moving platform may be the *only* efficient way to carry out subsurface exploration of large ice sheets.

The study of glaciers and ice sheets using radar is known as radio-glaciology, also referred to as *ice sounding*.

## 1.2 Ice Sounding

The word *sounding* derives from the Old English *sund*, meaning swimming, water, sea. Traditional sounding refers to the act of measuring depth in a body of water in relation to maritime navigation. Originally this was done by hand with sounding poles or a weighted sounding line when measuring greater depths. Today the word sounding is used for all types of depth measurements in all kind of bodies. A special case of this is radio echo sounding of ice, which is often referred to as ice sounding.

Airborne ice sounding radars, or just sounders, have been used since the 1960s to measure ice sheets by profiling their glaciological features from the surface to the bedrock. Sounders operate at low frequencies to avoid excessive attenuation of the transmitted and reflected signals within the ice. In this way, sounders are able to penetrate deep into the ice and map the bedrock underneath. A comprehensive overview of systems developed before 1998 is presented in [7].

While airborne sounders are needed for detailed measurements of fast-flowing outlet glaciers, a space-based sounder might be capable of broad coverage with high spatial and uniform sampling over the interior of the ice sheets, which cannot be realized from an aircraft with a limited range. Therefore, when the International Telecommunication Union in

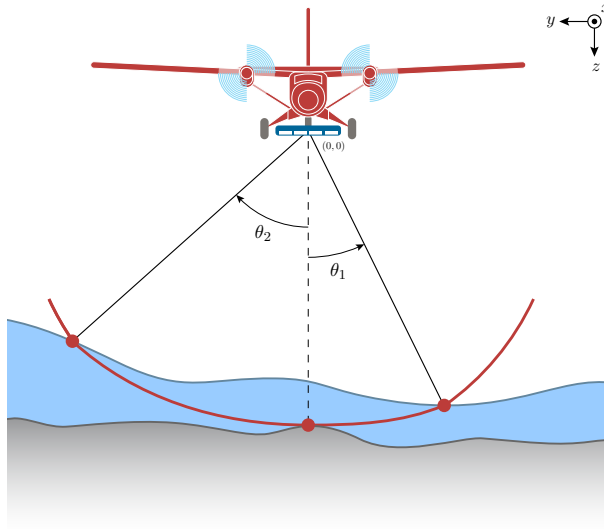


**Figure 1.1:** Vertical cross section of an ice sounding scenario illustrating the across-track surface clutter geometry.

2003 allocated a 6 MHz band at 435 MHz (P-band) for remote sensing, a space-based ice sounding radar was proposed to ESA as a possible Earth Explorer mission. Due to lack of knowledge of ice sounding at frequencies as high as P-band, ESA commissioned the development of the POLarimetric Airborne Radar Ice Sounder (POLARIS) [8] with the objective of assessing the feasibility of ice sounding at P-band from space.

### 1.3 Surface Clutter

The geometry associated with ice sounding is illustrated in Figure 1.1 along with the definition of a right-handed Cartesian coordinate system. The  $z$ -axis is aligned with the direction of the force of gravity and is referred to as the nadir direction, or just nadir. The  $x$ -axis is aligned with the nominal flight track orthogonal to nadir. This along-track direction is often denoted azimuth despite the fact that azimuth conventionally mean angle in a rotating radar, or more generally, in an equatorial plane. Lastly, the  $y$ -axis is defined as the direction orthogonal to azimuth and nadir that makes the system right-handed. This direction is referred to as the across-track direction. Based on this geometry and notation,



signal components referred to as surface clutter is now defined.

Clutter is a term used for unwanted echoes received by a radar. Due to the curved wavefront of a propagating pulse, an echo backscattered from a certain ice depth will be received by the radar simultaneously with an echo backscattered by the surface within the same range resolution cell, as illustrated in Figure 1.1. This surface component is referred to as surface clutter. The weak depth signal of interest may be masked by these off-nadir surface clutter signals located at the same electrical distance as the depth signal from nadir. In general surface clutter may be divided into three types:

1. clutter from the near-nadir surface overlaid through pulse range sidelobes,
2. clutter from the surface in the along-track direction, and
3. clutter from the surface in the across-track direction.

The first type is considered as indirect surface clutter since it is not related to the geometry from Figure 1.1. Instead it is caused by range sidelobes in the impulse response related to the pulse compression technique that typically is employed in modern ice sounders. Sidelobes for strong echo responses may in this way mask weaker echoes at other range locations, which is critical in ice sounding since the surface reflection is much stronger than echoes from the ice volume. Fortunately the sidelobes can be greatly reduced by spectral and temporal weighting, which is treated in more detail in Section 2.5.4. In the following, the focus is instead brought to the geometric clutter corresponding to the last two of the listed types.

Assuming flat topography and a nadir-looking sensor, the clutter footprints corresponding to different ice depths are described by annuli, as shown in Figure 1.2. Clutter scattered in the along-track direction can effectively be suppressed for a synthetic aperture system by Doppler processing [9, 10], as illustrated in Figure 1.3. The figure shows how the blue surface footprints from Figure 1.2 after Doppler processing are reduced in the along-track direction to the much smaller red areas. Since the effectively illuminated surface area is reduced, surface clutter is suppressed accordingly.

In this way, the problem of surface clutter reduces to the across-track direction in the form of surface returns from two angles ( $\pm\theta$ ) symmetric about nadir. In the case of sloped, undulating, or more complex topography, the surface clutter can consist of returns from multiple non-

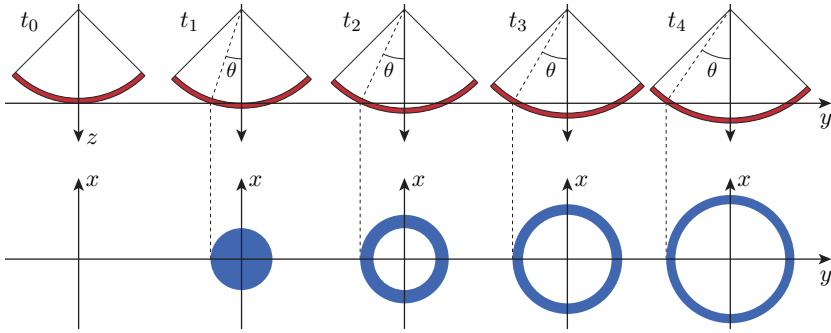


**Figure 1.2:** Surface clutter footprint (blue) and the corresponding position of the propagating pulse (red) at different time instants.

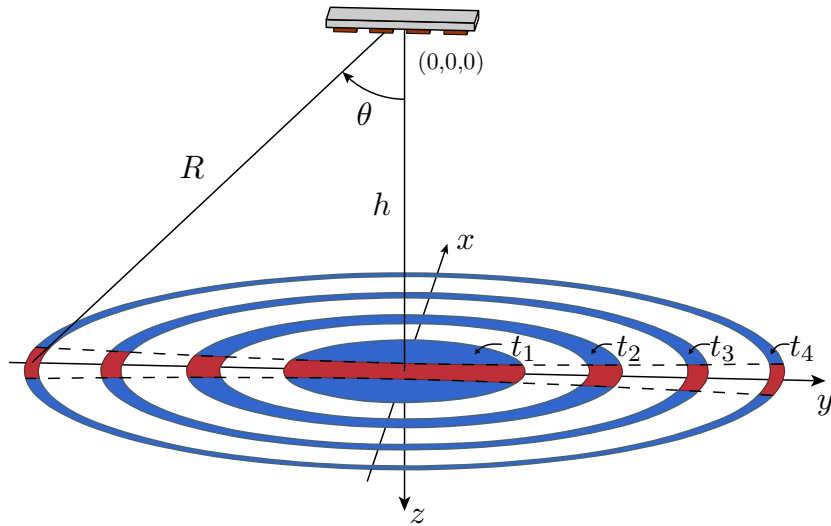


**Figure 1.3:** Doppler processed surface footprints. The footprints are illustrated by the red areas enclosed by the dashed black hyperbola. The blue annuli are the corresponding pulse limited footprints without Doppler processing.

symmetric angles that are a function of both range and along-track position, which can be intuitively deduced from the geometry in Figure 1.1.

By a trigonometric consideration of Figure 1.3, the following expression for the direction-of-arrival (DOA)  $\theta$  of the masking surface clutter can be derived for the flat surface scenario

$$\theta(R) = \arccos\left(\frac{h}{R}\right), \quad (1.1)$$

where  $h$  is the radar height over the ice surface and  $R$  is the range in air. For a more intuitive measure of range when subsurface targets are considered, the so-called equivalent nadir depth is defined

$$z = \frac{R - h}{n_{\text{ice}}}, \quad R \geq h, \quad (1.2)$$

where  $n_{\text{ice}}$  is the refractive index of ice. In terms of equivalent nadir depth, the DOA of masking surface clutter is given by [11]

$$\theta(z) = \arccos\left(\frac{h}{h + zn_{\text{ice}}}\right), \quad z > 0. \quad (1.3)$$

Plots of the clutter DOA for different radar heights are presented in Figure 1.4. It is seen from the figure that the clutter angle for low altitudes increases very rapidly with depth in the near surface region, while it increases more slowly for the larger depths. On the other hand, at the high altitudes used by satellites, the clutter angle increases very slowly with penetration depth, with a nearly constant rate down through the ice sheet. In continuation of this, it has been shown in [12] that surface clutter is the primary scattering mechanism that obscures the subsurface echoes at higher operating altitudes, and surface clutter is therefore a major issue in space-based ice sounding.

### 1.3.1 Suppression Technique

Airborne sounders have traditionally dealt with surface clutter by employing large antennas in the across-track direction, combined with low altitude. The low altitude implies large off-nadir clutter angles (Figure 1.4) at which the across-track clutter is suppressed due to the antenna pattern and the backscattering pattern of the ice surface. For a space-based sounder, a high altitude is implied by the orbit and the antenna dimensions are restricted by the launch vehicle. Therefore, alternative and more sophisticated clutter suppression techniques are

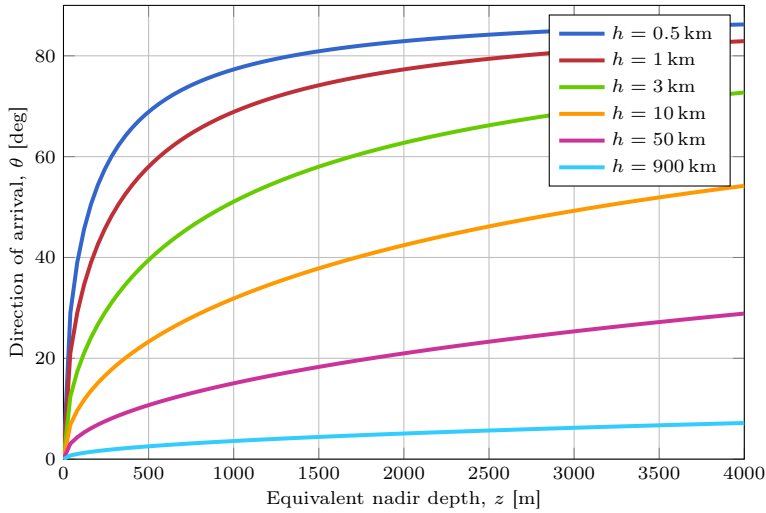


**Figure 1.4:** Direction-of-arrival of masking surface clutter.

needed. Even though the problem of surface clutter is less pronounced for airborne systems, sounding of areas with complex topography and roughness, such as heavily crevassed glaciers, is still a major technical challenge due to surface clutter.

The state-of-the-art technique for surface clutter suppression is based on a multi-phase-center antenna combined with sophisticated coherent post-processing. By using an antenna array aligned in the across-track direction combined with a multi-channel-receiver, beamforming techniques can subsequently be used to synthesize adaptive antenna patterns that suppress the surface clutter from off-nadir angles while a high gain is maintained in the nadir direction.

### 1.3.2 Previous Research on Surface Clutter Suppression

Dedicated techniques for surface clutter suppression have been a topic of research since the beginning of space-based ice sounding in the late 1990s. The Mars Express spacecraft developed by ESA and launched in 2003 was carrying the MARSIS ice sounder [13]. MARSIS was designed with a dual antenna clutter reduction technique [14]. The technique is based on two antennas with two specific antenna patterns: a primary antenna with a pattern maximum in the nadir direction, and a sec-

ondary antenna with a pattern null in the nadir direction. Only the primary antenna is used for transmission, while both antennas are used for reception at two separate channels. The primary antenna mainly receives the nadir subsurface signal, while the secondary antenna mainly receives off-nadir surface clutter. Now, if the secondary channel is appropriately scaled and coherently subtracted from the primary channel, the difference only contains the nadir subsurface signal, assuming ideally symmetrical conditions. In the case of MARSIS, the primary and secondary antenna patterns were implemented as a thin dipole, mounted parallel to the surface and normal to the direction of motion, and a short monopole mounted vertically aligned with the nadir axis, respectively. However, for various technical reasons the secondary antenna was not put into operation.

In 2003–2004, the European Space Research and Technology Center (ESTEC) considered the dual antenna clutter reduction technique with the intention to support the feasibility study of a space-based P-band radar as an ice sounding mission over Antarctica [15–17]. A three-channel extension was considered, in order to deal with surface slope and antenna de-pointing errors. It was also suggested that the specific antenna patterns needed could be synthesised by using an antenna array. The POLARIS demonstrator [18] developed around 2007 was designed to support the two-channel technique by employing a 4-element antenna array and a multi-channel receiver.

The Martian ice sounder SHARAD [19] is flown on NASA’s Mars Reconnaissance Orbiter and was launched in 2005. SHARAD has no dedicated hardware for clutter suppression but stereo processing based on adjacent parallel orbits has been used to obtain some suppression. A suppression technique based on multiple passes was proposed in the frame of the Advanced Concepts for Radar Sounders (ACRAS) study [20]. The method proposed [21, 22] combined the multiple acquisitions to synthesize adaptive antenna patterns in the across-track direction using null-steering.

In [23] a polarimetric technique based on a circularly-polarized transmitted field and a coherent dual-polarized receiver is suggested for clutter suppression. The suppression follows from processing strategies that are designed to distinguish between nadir signal and clutter based on differences in their polarimetric signatures.

The first ice sounding experiments with multi-phase-center antenna systems were reported in [12] using the Multi-Channel Radar Depth Sounder (MCRDS) [24] developed by the Center for Remote Sensing of Ice Sheets (CRaSI) at the University of Kansas (KU). The experiments

were conducted to assess proposed techniques in relation to the Global Ice Sheet Mapping Orbiter (GISMO) concept [25]. In a bistatic configuration beam-steering was used to suppress surface clutter and reveal the bedrock by coherently combining 6 phase centers. The same experiments also considered clutter suppression based on interferometric processing [26].

In 2014, CRISIS conducted the first test flights with a single-channel Unmanned Aircraft System (UAS). The system is designed for clutter suppression using 2D aperture synthesis based on closely and accurately spaced repeat-pass acquisitions [27, 28].

In parallel with this PhD study, multi-phase-center data acquired with MCRDS and its successor MCoRDS/I have been processed with the Capon beamformer for clutter suppression [29, 30]. The related Optimum beamformer has been studied by ESA based on POLARIS data [31–33]. Recently, a comparison of different beamforming algorithms based on simulations and multi-phase-center POLARIS data are presented in [34, 35].

## 1.4 Radar Tomography

The word *tomography* derives from the Greek word *tomos* meaning slice or section and *graphie* meaning drawing. In line with this, tomography refers to imaging by sections. The term originated during the development of computer-aided imaging and is today a well known technique in several scientific fields.

Since the beginning of the 2000s, airborne radar tomography has been used to produce 3D images of surface volume scatterers, as presented in [36] and [37] to name a few. In radar tomography the synthetic aperture principle of SAR is extended into the across-track direction. Spatial samples in this direction are acquired using a physical array or a synthetic array based on repeat-pass acquisitions. By using beamforming and DOA estimation techniques, different scatters in the resolution cell can be resolved. In combination with the along-track SAR processing, a 3D volume can in this way be imaged.

Recently, tomographic techniques have also been used for ice sounding [38]. A sledge mounted sounder with an across-track antenna array is used for ice sheet bed 3D tomography producing bed topography. The same technique is also used for airborne ice sounding based on MCoRDS/I data, where topographic measurements of both the ice sheet surface and bed are produced [39, 40]. The radar system in the experiment is

operated in ping-pong mode to provide 12 effective receive phase centers. Estimation of the DOA angles of the surface and bed returns are used to compute relative elevations in slant-range geometry, followed by a mapping to ground range to obtain the topographic map in Cartesian coordinates.

Even though tomographic techniques based on data-driven DOA estimation are demonstrated in relation to ice sounding, none of the previous methods implemented had clutter suppression as the primary objective.

## 1.5 Scope and Outline of the Dissertation

Multi-phase-center radar ice sounding is a very recent technology that represents state-of-the-art within the field of radioglaciology. This PhD study deals with tomographic techniques based on this technology. The primary objectives are to:

1. Investigate the use of advanced tomographic processing for surface clutter suppression which is previously unexplored in the literature; and
2. Explore additional novel applications of tomography based on multi-phase-center sounding systems.

A secondary objective is to assess the tomographic capabilities of the POLARIS system based on the experimental multi-phase-center dataset acquired in Antarctica. The main outcome of the study has been documented in three papers [41–43]. The dissertation includes the main contributions presented in the above-mentioned papers, as well as results and discussions not previously published.

The dissertation is organized as follows. In Chapter 2, the fundamental theory and basic principles related to multi-phase-center ice sounding radars are presented.

Array signal processing is the topic of Chapter 3, where an array signal model is formulated as a foundation for radar tomography. Tomographic techniques are investigated in terms of beamforming and DOA estimation methods. The techniques are assessed based on theory, presented through various simulations, and discussed in relation to ice sounding and surface clutter suppression.

In Chapter 4, the multi-phase-center ice sounding data used in the study are presented. The corresponding radar systems are described and information on the radar scenes is provided.

Tomographic techniques are applied to the data in Chapter 5. Novel processing techniques and glaciological findings based on tomographic methods are also presented and discussed; this includes a demonstration of tomographic surface clutter suppression based on data-driven DOA estimation.

In Chapter 6, novel tomography-based estimation of the basal scattering characteristics is addressed along with experimental waveform analysis of the basal return. Conclusion and suggestions for future work are given in Chapter 7.

In addition to these chapters, a series of appendices are included, which contain publications that have been prepared during the study. The appendices are followed by an overview of the nomenclature used throughout the dissertation. This includes lists of functions, operators, symbols, abbreviations, and acronyms.





## Sounding Radar Principles

A radar is an electromagnetic system for detection and localization of objects. The term *radar* was originally an acronym for RADio Detection And Ranging, but has now entered the language as a common noun, losing all capitalization. The key feature of the classical radar is ability to measure distance, or range, to a target. The range is determined by transmitting an electromagnetic pulse and measuring the time taken for the signal to travel to the target and back. A modern radar, however, can extract much more information from the received target signal than just the range.

An ice sounder is a dedicated radar system for probing ice sheets and glaciers. The design of modern ice sounders involves a number of techniques on both the hardware and software side. In the following the main sounding principles are described starting with a brief review of the fundamental electromagnetic theory and basic radar principles.

### 2.1 Electromagnetic Waves

A radar uses electromagnetic radiation to interact with a target. The foundation of classical electromagnetic analysis is based on Maxwell's equations [44]:

$$\nabla \cdot \mathbf{D} = \rho \quad (2.1a)$$

$$\nabla \cdot \mathbf{B} = 0 \quad (2.1b)$$

$$\nabla \times \mathbf{E} = -\frac{\partial \mathbf{B}}{\partial t} \quad (2.1c)$$

$$\nabla \times \mathbf{H} = \frac{\partial \mathbf{D}}{\partial t} + \mathbf{J} \quad (2.1d)$$

where  $\mathbf{E}$  and  $\mathbf{H}$  are the electric and magnetic field,  $\mathbf{D}$  and  $\mathbf{B}$  are the electric and magnetic flux densities,  $\mathbf{J}$  is the current density, and  $\rho$  is

the electric charge density. For a linear and isotropic medium, the flux densities are related to the corresponding fields by

$$\mathbf{D} = \epsilon \mathbf{E}, \quad (2.2)$$

$$\mathbf{B} = \mu \mathbf{H}, \quad (2.3)$$

where  $\epsilon$  and  $\mu$  is the permittivity and permeability of the medium.

From Maxwell's equations the wave equations can be derived that for simple (linear, isotropic, and homogeneous) lossless source-free media are given by [44]

$$\nabla^2 \mathbf{E} - \frac{1}{u^2} \frac{\partial^2 \mathbf{E}}{\partial t^2} = 0 \quad (2.4a)$$

$$\nabla^2 \mathbf{H} - \frac{1}{u^2} \frac{\partial^2 \mathbf{H}}{\partial t^2} = 0 \quad (2.4b)$$

where  $t$  is time and  $u$  is the velocity of wave propagation given by

$$u = \frac{1}{\sqrt{\epsilon\mu}}. \quad (2.5)$$

The propagation velocity is seen to be dependent on the medium and is for free space given by

$$c = \frac{1}{\sqrt{\epsilon_0\mu_0}}, \quad (2.6)$$

where  $\epsilon_0$  and  $\mu_0$  denotes the permittivity and permeability of free space. For an arbitrary medium, the relative permittivity and permeability are defined with respect to these free space quantities, i.e.  $\epsilon_r = \epsilon/\epsilon_0$  and  $\mu_r = \mu/\mu_0$ . Similar, the reciprocal of the relative velocity referred to as the index of refraction is defined as

$$n = \frac{c}{u} = \sqrt{\epsilon_r\mu_r}. \quad (2.7)$$

Eqs. (2.4) are the homogeneous wave equations for which the solutions represents waves, as indicated by the name. A particular solution is the time-harmonic uniform plane wave. Based on these, electromagnetic radiation can be defined as a composition of waves in terms of synchronized oscillations of the electric and magnetic fields that propagate at the speed of light.

The oscillations of the two fields are perpendicular to each other and perpendicular to the direction of energy and wave propagation, forming

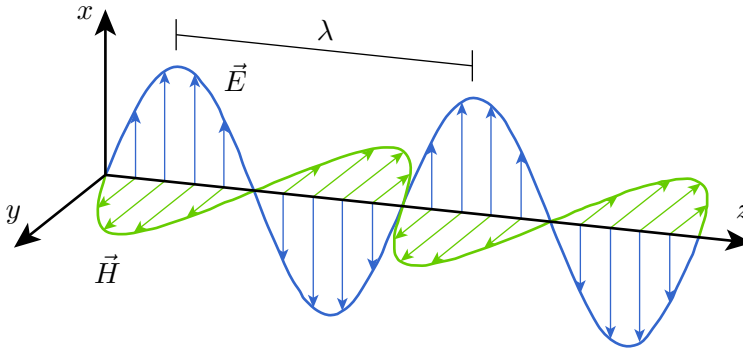


Figure 2.1: Linear polarized electromagnetic wave.

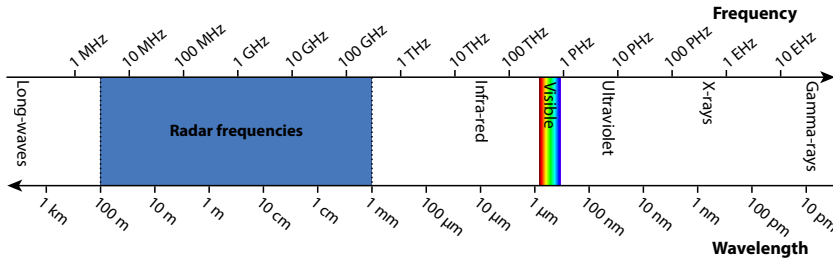


Figure 2.2: The electromagnetic spectrum.

a transverse wave as depicted in Figure 2.1. Electromagnetic waves can be characterized by either the frequency,  $f$ , or wavelength,  $\lambda$ , of their oscillations to form the electromagnetic spectrum as illustrated in Figure 2.2. Wavelengths from 1 mm to 100 m are defined as radar frequencies by IEEE [45]. This range is divided into a number of bands each assigned a letter designation as listed in Table 2.1.

### 2.1.1 Polarization

Polarization is a property of waves that can oscillate with more than one orientation. For electromagnetic waves, polarization refers to the direction of oscillation of the electric field. The oscillation may be in a single direction defined as linear polarization, or the field may rotate corresponding to circular or elliptical polarization. The wave in Figure 2.1 is linearly polarized.

**Table 2.1:** Radar-frequency bands according to IEEE standard [45].

Band designation	Frequency	Wavelength
HF	3–30 MHz	10–100 m
VHF	30–300 MHz	1–10 m
P <sup>1</sup>	250–500 MHz	60–120 cm
UHF	300–1000 MHz	30–100 cm
L	1–2 GHz	15–30 cm
S	2–4 GHz	7.5–15 cm
C	4–8 GHz	3.75–7.5 cm
X	8–12 GHz	25–37.5 mm
Ku	12–18 GHz	16.7–25 mm
K	18–27 GHz	11.1–16.7 mm
Ka	27–40 GHz	7.5–11.1 mm
V	40–75 GHz	4–7.5 mm
W	75–110 GHz	2.7–4 mm
mm <sup>2</sup>	110–300 GHz	1–2.7 mm

<sup>1</sup> P-band is an obsolete designation and is not a part of the current IEEE standard.

<sup>2</sup> The designation mm is derived from *millimeter* wave radar, and is also used to refer to V- and W-bands, and part of Ka-band, when general information relating to the region above 30 GHz is to be conveyed.

Most sources of light are classified as incoherent and unpolarized since they consist of a random composition of waves having different spatial characteristics, frequencies, phases, and polarization states. However, in a radar system the waves are systematically generated with a fixed phase center and with a well-defined polarization determined by the antenna in combination with the signal waveform. The choice of polarization is important for how the waves interact with a given type of target and thereby how the target or scene is sensed by the radar. Therefore, radar systems supporting multiple polarizations can be designed to obtain further information on a scene for the price of increased system complexity.

Linear polarization with the electric field oscillating in either the horizontal (H) or vertical (V) direction is typically used in imaging radar systems. The two configurations are in general referred to as perpendicular and parallel polarization when observed relative to the plane of incidence, which is defined as the plane including the direction of the

wave propagation and the normal to the interface (imaged surface). A different polarization configuration can be chosen for reception than the one used for transmission, which can provide additional information on the scattering mechanism of a given target [46]. Based on the H and V configurations, four combinations can be formed that are denoted HH, HV, VV, and VH, where the first letter refers to the transmit polarization and the second letter to the receive polarization. A radar system that is capable of measuring all four combinations is called *fully polarimetric*. By representing the four measurements in the so-called scattering matrix, a change of basis can be performed during offline data processing to synthesize any polarization configuration and thereby the corresponding polarimetric response of a given target. This technique is referred to as polarization synthesis [47].

In relation to ice sounding, polarimetric techniques can be used to measure the anisotropic electromagnetic propagation and reflection properties related to the crystal orientation fabric. This can provide valuable information on the stress and strain of the polar ice sheets [48]. It should be noted that for a nadir-looking sounding geometry, the H-V convention is in principle ambiguous since both directions are contained in the horizontal plane. However, the notation is adopted from SAR in order to be consistent with the well-established polarimetric theory. In this way, in the case of a nadir geometry, the H-V convention is interpreted as the natural limit of a side-looking radar configuration where the look-angle approaches zero.

## 2.2 Fresnel Reflection and Transmission

Reflections of electromagnetic waves are caused by changes in the complex dielectric properties in terms of the permittivity that in general, for a lossy medium, is a complex quantity. The permittivity can be decomposed into its real part  $\epsilon'$  (the dielectric constant) and its negative imaginary part  $\epsilon''$ , i.e.  $\epsilon = \epsilon' - i\epsilon''$ , where  $\epsilon''$  is proportional to the conductivity  $\sigma$ .

In the case of ice sounding, a number of phenomena cause changes in permittivity as an electromagnetic wave is propagating through the scene. At the boundaries between air-ice and ice-bedrock, a large change in the dielectric constant occurs. For the internal stratigraphy, or layers, the following three main phenomena cause change in the permittivity [49]:

1. changes of snow/ice density affecting the dielectric constant,

2. changes of crystal orientation fabrics affecting the dielectric constant, and
3. changes in concentration of chemical impurities (acids and sea salts) causing changes of the conductivity.

Ice has relatively low conductivity at MHz frequencies and can be assumed to be non-magnetic. For calculations of reflection and transmission coefficients, the ice is typically assumed lossless [50]. However, when modelling the propagation within the ice, the conductivity should be included in order to account for absorption. A mean relative real permittivity of  $\epsilon_{\text{ice}} = 3.15$  can be assumed for ice [50]. In relation to reflections from a ice–rock interface at the bedrock, a value for rock (Basalt) of  $\epsilon_{\text{rock}} = 7.1$  can be assumed [50]. The conductivity depends on the temperature in the way that attenuation increases with increasing temperature. For one-way propagation in cold ice, values for the attenuation constant  $\alpha$  is typically of about 1–2 dB/100 m [39]. For warm ice the attenuation can be twice as large [51]. A comprehensive summary of the complex dielectric permittivity of ice at MHz frequencies is given in [52]. A description of the Antarctic ice in relation to ice sounding at P-band can be found in [53].

### 2.2.1 The Fresnel Equations

In this section, the theory related to reflections of electromagnetic waves at dielectric interfaces will be described.

When a uniform plane electromagnetic wave is moving between media of different dielectric properties, both reflection and transmission may occur, as illustrated in Figure 2.3. For lossless media ( $\sigma = 0$ ), the fraction of the wave which is reflected and transmitted is described by the Fresnel equations [44]

$$R_{\perp} = \frac{\eta_2 \cos \theta_i - \eta_1 \cos \theta_t}{\eta_2 \cos \theta_i + \eta_1 \cos \theta_t} \quad (2.8a)$$

$$R_{\parallel} = \frac{\eta_1 \cos \theta_i - \eta_2 \cos \theta_t}{\eta_1 \cos \theta_i + \eta_2 \cos \theta_t} \quad (2.8b)$$

$$T_{\perp} = \frac{2\eta_2 \cos \theta_i}{\eta_2 \cos \theta_i + \eta_1 \cos \theta_t} \quad (2.8c)$$

$$T_{\parallel} = \frac{2\eta_2 \cos \theta_i}{\eta_1 \cos \theta_i + \eta_2 \cos \theta_t} \quad (2.8d)$$

where  $R$  and  $T$  are the Fresnel reflection and transmission coefficient, the subscripts  $\perp$  and  $\parallel$  denote perpendicular and parallel polarization,

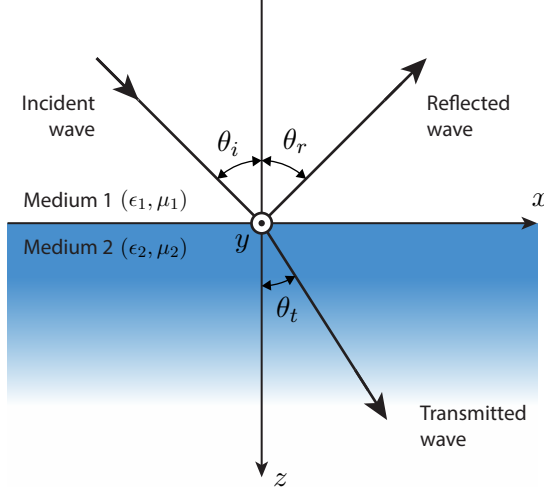


**Figure 2.3:** Uniform plane wave incident obliquely on a plane dielectric boundary.

$\eta = \sqrt{\mu/\epsilon}$  is the intrinsic impedance. The angles  $\theta_i$ ,  $\theta_r$ , and  $\theta_t$  are the angles of incidence, reflection, and transmission. The latter is also referred to as the angle of refraction.

The fraction of the incident power that is reflected from the interface is given by the reflectance or reflectivity  $\Gamma$  and the fraction that is transmitted through the interface is given by the transmittance or transmissivity  $\Upsilon$ . These quantities are related to the Fresnel coefficients of (2.8) in the following way [54]

$$\Gamma_{\perp} = |R_{\perp}|^2 \quad (2.9a)$$

$$\Gamma_{\parallel} = |R_{\parallel}|^2 \quad (2.9b)$$

$$\Upsilon_{\perp} = \frac{\operatorname{Re}\{(\cos \theta_t)/\eta_2\}}{\operatorname{Re}\{(\cos \theta_i)/\eta_1\}} |T_{\perp}|^2 \quad (2.9c)$$

$$\Upsilon_{\parallel} = \frac{\operatorname{Re}\{(\cos \theta_t)/\eta_2\}}{\operatorname{Re}\{(\cos \theta_i)/\eta_1\}} |T_{\parallel}|^2. \quad (2.9d)$$

It is noted that the power coefficients satisfy

$$\Gamma_{\perp} + \Upsilon_{\perp} = \Gamma_{\parallel} + \Upsilon_{\parallel} = 1, \quad (2.10)$$

which is in accordance with the law of conservation of energy.



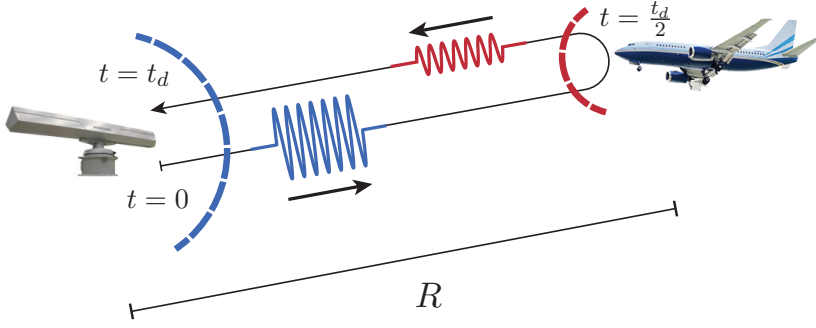


**Figure 2.4:** Principle of a basic pulse radar.

### 2.2.2 Snell's Law

The relationship between the angles of incidence, reflection, and refraction is described by Snell's laws [55]

$$\theta_i = \theta_r \quad (2.11a)$$

$$k_1 \sin \theta_i = k_2 \sin \theta_t \quad (2.11b)$$

where  $k = \omega \sqrt{\mu \epsilon}$  is the wavenumber and  $\omega = 2\pi f$  is the angular frequency. Eq. (2.11b) is referred to as Snell's law of refraction. For non-magnetic media, which includes ice,  $\mu_r = 1$ , thus the refractive index equals  $n = \sqrt{\epsilon_r}$ . In this case, Snell's law and the Fresnel equations is often rewritten and expressed in terms of the refractive index or the relative dielectric constant.

### 2.3 Radar Basics

The principle of range measurement with a basic pulse radar is illustrated in Figure 2.4. By assuming a propagation velocity of the transmitted pulse, e.g. the speed of light in free space,  $c$ , the range is given by

$$R = \frac{c t_d}{2}, \quad (2.12)$$

where  $t_d$  is the two-way propagation time of the pulse. The theoretical range resolution of the basic pulse radar is given by

$$\rho = \frac{c \tau}{2}, \quad (2.13)$$

where  $\tau$  is the width of the transmitted pulse.

The power of the received signal can be described by the radar equation that relates the range of the radar to the characteristics of the transmitter, receiver, antenna, target, and environment. The fundamental form of the radar equation can be expressed as [56, 57]:

$$P_r = \frac{P_t G_t G_r \lambda^2 \sigma}{(4\pi)^3 R^4}, \quad (2.14)$$

where  $P_r$  and  $P_t$  are the received and transmitted power,  $G_t$  is the transmit antenna gain,  $G_r$  is the receive antenna gain,  $\lambda$  is the wavelength in the medium in which the receive antenna is located,  $\sigma$  is the radar cross section, and  $R$  is the range to the target. The radar cross section is the parameter that contains the reflection characteristics of a given target [58]

$$\sigma = \lim_{R \rightarrow \infty} 4\pi R^2 \frac{|E_s|^2}{|E_i|^2}, \quad (2.15)$$

where  $E_i$  is the electric-field strength of the incident wave impinging on the target and  $E_s$  is the electric-field strength of the reflected wave at the radar. In the case of a distributed target such as a surface, the radar cross-section per unit area, or scattering coefficient, is defined as

$$\sigma^\circ = \frac{1}{A} \lim_{R \rightarrow \infty} 4\pi R^2 \frac{|E_s|^2}{|E_i|^2} = \frac{\sigma}{A}, \quad (2.16)$$

where  $A$  is the illuminated area.

The following section deals with modeling of the radar cross section for natural surfaces.

## 2.4 Surface Scattering

Natural surfaces are often rough in contrast to the smooth interfaces treated in Section 2.2. When such natural objects, or targets, are illuminated by an electromagnetic wave, the incident energy is dispersed in all directions. This spatial distribution of energy is called scattering and the target is referred to as a scatterer.

An electromagnetic wave incident upon a rough surface is partly reflected in the specular direction and partly scattered in all directions. A monostatic radar would receive no return power from a perfect smooth or specular surface except at normal incidence. On the other hand, when

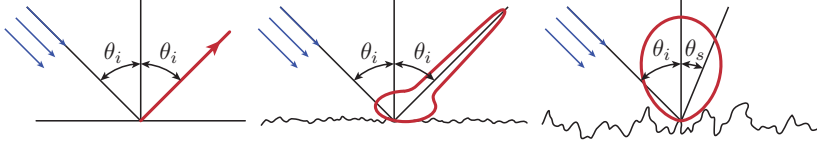


**Figure 2.5:** Scattering patterns (red) for different roughnesses, from left: specular, slightly rough, and rough surface.

illuminating a rough surface, a monostatic radar receives the backscattered component of the scattered energy. The reflected and scattered components are often referred to as the coherent and incoherent scattering components. Surfaces where the associated scattering consists of only coherent or incoherent scattering can be considered as the extremes as illustrated in Figure 2.5.

For pure coherent scattering from a perfectly flat surface, the angular radiation pattern of the reflected wave is a delta function with a magnitude determined by the Fresnel reflection coefficient centered about the specular direction, cf. (2.11a). Based on this, for the perfectly flat infinite surface illuminated by a point source the cross-polarized scattering coefficient is zero while the like-polarized coefficient is given by [59]

$$\sigma^\circ(\theta_i, \theta_s) = \frac{4\pi}{A} \frac{R_i^2 R_s^2}{R_i^2 + R_s^2} \Gamma(\theta_i) \delta(\theta_i - \theta_s) \quad (2.17)$$

where  $\theta_i$  is the angle of incidence,  $\theta_s$  is the scattered direction towards the receiver,  $R_i$  is the range from the transmitter to the illuminated surface area,  $R_s$  is the range from the illuminated surface area to the receiver, and  $\delta(\cdot)$  is the Dirac delta function. The expression corresponds to the image solution of a point source above an infinite plane.

The other extreme is the perfectly rough surface, known as the Lambertian surface after Lambert's law that defines the bistatic scattering coefficient as

$$\sigma^\circ(\theta_i, \theta_s) = \sigma_0^\circ \cos \theta_i \cos \theta_s, \quad (2.18)$$

where  $\sigma_0^\circ$  is a constant related to the dielectric properties of the scattering surface.

In relation to a monostatic radar, it is the power scattered back towards the radar that is of interest. This often used special case of the scattering coefficient is defined as the backscattering coefficient given by

$$\sigma^\circ(\theta) = \sigma^\circ(\theta_i) = \sigma^\circ(\theta_i, -\theta_i). \quad (2.19)$$

A random surface is typically characterized in terms of statistical parameters. Two commonly used parameters are the standard deviation of the surface height variation relative to a reference surface,  $\sigma_h$ , and the surface correlation length,  $L$ . The correlation length is defined as the displacement for which the surface height autocorrelation function is equal to  $e^{-1}$ .

The degree of roughness, or simply the roughness, of a random surface depends of the exploring frequency. Therefore, for characterization of roughness, the statistical surface parameters are measured in units of the wavelength, which is often done in terms of the wavenumber, i.e.  $k\sigma_h$  and  $kL$ . In general, a surface may be considered smooth if  $k\sigma_h < 0.2$  and very rough if  $k\sigma_h > 1.0$ , [54]. However,  $kL$  should also be considered. A measure of the roughness that includes both parameters is the root mean square (RMS) surface slope that for a Gaussian correlation function is defined as the ratio of the standard deviation to the correlation length [50].

$$m_s = \frac{\sqrt{2}\sigma_h}{L}. \quad (2.20)$$

The larger the RMS slope the rougher the surface.

While reflection and transmission at a plane interface between two homogeneous media can be described by simple analytical expressions as presented in Section 2.2, no exact closed-form solution exists for irregular surfaces. However, approximate analytic solutions are possible but only when the roughness is much smaller or much greater than the wavelength of the incident wave. In the following, models representing these two scenarios will be described.

### 2.4.1 The Kirchhoff Model

For large-scale horizontal roughness corresponding to a surface with gentle undulations, the Kirchhoff method or Physical Optics formulation is one of the most widely used. The basic assumption is that plane-interface reflection occurs at every point on the surface, which is equivalent to considering the surface locally as an inclined plane. This assumption is valid when the horizontal-scale roughness in terms of the correlation length is large compared to the wavelength and the vertical-scale roughness in terms of the standard deviation is sufficiently small, such that the average curvature is large compared to the wavelength.

Mathematically, when the surface height variation is Gaussian distributed, the restrictions are [60]

$$kL > 6, \quad (2.21a)$$

$$kL > 2\sqrt{k\sigma_h\sqrt{6\pi}} \approx 4.17\sqrt{k\sigma_h}. \quad (2.21b)$$

Furthermore, application of Geometric Optics (Stationary-Phase Approximation) requires that [56]

$$(2k\sigma_h \cos \theta)^2 > 10. \quad (2.21c)$$

When the conditions in (2.21) are fulfilled, the incoherent Kirchhoff Model (IKM) in terms of the like-polarized backscattering coefficient, is given by [50, 56]

$$\sigma_{\text{IKM}}^{\circ}(\theta) = \frac{\Gamma(0)}{2m_s^2 \cos^4 \theta} \exp\left(-\frac{\tan^2 \theta}{2m_s^2}\right), \quad (2.22)$$

while the cross-polarized coefficient is zero. As seen from the expression, the IKM only depends on the RMS slope and is therefore invariant with respect to a common scaling of  $L$  and  $\sigma_h$  as long as the validity conditions are fulfilled.

When (2.21c) is not fulfilled but the surface RMS slope is small,

$$m_s < 0.25, \quad (2.23)$$

the Scalar Approximation is valid. In this case a coherent component is introduced and the scattering coefficient can be modeled as [56]

$$\sigma_{\text{KM}}^{\circ} = \sigma_c^{\circ} + \sigma_n^{\circ} + \sigma_s^{\circ}, \quad (2.24)$$

where  $\sigma_c^{\circ}$  is a coherent component while  $\sigma_n^{\circ}$  and  $\sigma_s^{\circ}$  are both incoherent with the latter related to surface slopes. The coherent component is given by

$$\sigma_c^{\circ} = \pi k^2 |a_{0,pq}|^2 e^{-4k^2 \sigma_h^2} \delta(\theta), \quad (2.25)$$

where  $p$  and  $q$  represent transmit and receive polarization, and

$$a_{0,\text{HH}} = 2R_{\perp} \cos \theta, \quad (2.26)$$

$$a_{0,\text{VV}} = -2R_{\parallel} \cos \theta, \quad (2.27)$$

$$a_{0,\text{HV}} = a_{0,\text{VH}} = 0. \quad (2.28)$$

### 2.4.2 The Small Perturbation Model

A standard approach for modeling scattering from a slightly rough surface where both the standard deviation and the correlation length are smaller than the wavelength, is the small-perturbation method, which is also referred to as the Bragg model. Expressed mathematically the validity conditions are [56]

$$k\sigma_h < 0.3, \quad (2.29a)$$

$$kL > \frac{\sqrt{2}}{0.3} k\sigma_h \quad (2.29b)$$

In the case of non-magnetic media, the backscattering coefficient described by the Small Perturbation Model (SPM) is given by [56]

$$\sigma_{pq}^o = 8k^4 \sigma_h^2 \cos^4 \theta |\alpha_{pq}|^2 W^{(1)}(k_e) \quad (2.30)$$

where

$$\alpha_{HH} = R_{\perp}, \quad (2.31)$$

$$\alpha_{VV} = - \left( R_{\parallel} + T_{\parallel}^2 \frac{(\epsilon_2/\epsilon_1 - 1) \tan^2 \theta}{2\epsilon_2/\epsilon_1} \right), \quad (2.32)$$

$$\alpha_{HV} = \alpha_{VH} = 0, \quad (2.33)$$

and  $W^{(n)}(k_e)$  is the surface roughness spectrum corresponding to the Fourier transform of the surface autocorrelation function raised to its  $n$ th power. For a Gaussian shaped correlation function the spectrum is given by

$$W^{(n)}(k_e) = \frac{1}{2n} L^2 \exp \left( -\frac{(k_e L)^2}{4n} \right), \quad (2.34)$$

where  $k_e$  is the effective wavenumber

$$k_e = 2k \sin \theta. \quad (2.35)$$

### 2.4.3 The Integral Equation Model

In the Integral Equation Model (IEM), the surface integral equation is used to derive an approximate form of the surface current, which is then integrated to get the scattered field. In this way, the IEM is able to model scattering from interfaces with large values of roughness

that cannot be modeled with the SPM. For non-magnetic media, the backscattering coefficient of the simplified IEM is given by [61, 62]

$$\sigma_{pq}^o = \frac{k^2}{4\pi} \exp(-2k^2 \sigma_h^2 \cos^2 \theta) \sum_{n=1}^{\infty} |I_{pq}^n|^2 \frac{W^{(n)}(k_e)}{n!}, \quad (2.36)$$

where

$$I_{pq}^n = (2k\sigma_h \cos \theta)^n f_{pq} \exp(-k^2 \sigma_h^2 \cos^2 \theta) + (k\sigma_h \cos \theta)^n F_{pq}, \quad (2.37)$$

$$f_{vv} = \frac{2R_{\parallel}}{\cos \theta}, \quad f_{hh} = \frac{-2R_{\perp}}{\cos \theta}, \quad f_{hv} = f_{vh} = 0, \quad (2.38)$$

$$F_{vv} = \left(E - \frac{C}{\epsilon_r}\right) A_{\parallel}^2 - H A_{\parallel} B_{\parallel} + \left(E + \epsilon_r \frac{D}{C}\right) B_{\parallel}^2, \quad (2.39)$$

$$F_{hh} = - \left[ \left(E - \frac{C}{1}\right) A_{\perp}^2 - H A_{\perp} B_{\perp} + \left(E + \frac{D}{C}\right) B_{\perp}^2 \right], \quad (2.40)$$

$$A_p = 1 + R_p, \quad B_p = 1 - R_p, \quad (2.41)$$

$$C = \sqrt{\epsilon_r - \sin^2 \theta}, \quad D = 1 + \sin^2 \theta, \quad (2.42)$$

$$E = \frac{\sin^2 \theta}{\cos \theta}, \quad H = 2 \sin^2 \theta \left( \frac{1}{\cos \theta} + \frac{1}{C} \right). \quad (2.43)$$

#### 2.4.4 Multiscale Roughness

A multiscale surface is defined as one with superposition of roughness scales. At a given frequency and look angle, surface scattering is dominated by roughness scales over which the scattered signal remains correlated [61]. For a surface containing only one scale of roughness, the scattered signal will remain correlated over the correlation length of the surface. In this way, the given roughness is effective in generating scattering regardless of it being large or small compared to the exploring wavelength. For a multiscale surface, however, an exploring wave may sense only roughness scales smaller or comparable to the wavelength at mid- or large-incident angles. The larger scales are not detected because the coherence of the scattered signal at these scales is not retained due to the presence of the smaller scales. The smaller scales are destroying the signal coherency over the larger scales since the scattered signal

cannot remain correlated over the correlation length of the large-scale roughness. This can be seen as the large-scale roughness is acting locally as a reference plane of scattering for the small-scale roughness.

To determine the dominating roughness scale for a multiscale surface, the effective wavelength is the relevant parameter to assess [61]

$$\lambda_e = \frac{2\pi}{k_e} = \frac{\lambda}{2 \sin \theta}. \quad (2.44)$$

In general, only scales comparable to the effective wavelength are effective in generating scattering. From (2.44) it is seen that, as the incident angle increases, the effective wavelength decreases. Thus, the large-scale roughness dominates the return at small angles of incidence where the effective wavelength is large, while smaller scales of roughness become more important at large angles of incidence.

Naturally occurring surfaces may include both small and large scale roughness in various proportions or even as a continuous distribution. Analytically there is no simple method to treat surfaces with a continuous distribution of roughnesses. However, for two-scale roughness surfaces which can be modeled as having only two average sizes of roughness with one small and one large, simple approximate treatments are possible. A two-scale scattering model may successfully explain multiscale scattering even in the case of a continuous spectrum of roughness scales. Even though that the total backscattering is not the incoherent sum of the scattering due to individual scales, two models such as the IKM and SPM are sometimes combined as a simple approach for modelling the problem. In this case, the surface standard deviation in the models are only based on frequency components of the surface responsible for scattering at the different given effective wavelengths. If all frequencies of a surface contributed, substantially different values of the statistical parameters may occur.

## 2.5 Synthetic Aperture Radar

A Synthetic Aperture Radar (SAR) is a high resolution radar operated from a moving platform, typically an aircraft or a satellite. Movement is required in order to obtain the high resolution, and provides at the same time the possibility to cover large terrain area. A SAR is a coherent system that is based on the ability to accurately measure phase differences between the transmitted pulse and the received echoes. The high resolution is obtained in both the range and along-track direction,



by using the pulse compression and Doppler processing techniques, respectively. These techniques are briefly described in the following. For further information on SAR, a comprehensive introduction can be found in [63].

### 2.5.1 Pulse Compression

Pulse compression is a way to transmit long pulses while maintaining a good range resolution. A longer pulse allows more energy to be emitted, and hence received, which is necessary in order to detect targets at long distances. For ordinary pulse radars this implies a poor range resolution, but with pulse compression the transmit pulse length is decoupled from the effective pulse length, and hence a good resolution can be maintained. This is achieved by modulating the transmitted pulse and then correlating the received signal with a replica of the transmitted waveform. Typically, a linear frequency modulation is used, where the frequency is swept linearly over a certain bandwidth, centered around the center frequency. The transmission time, and thereby the emitted energy, is controlled by the rate the frequency is swept through the bandwidth.

The correlation of the received signal corresponds to a matched filtering process which produces a resulting signal with a much smaller width compared to the actual transmitted waveform, hence the name pulse compression. The effective pulse width is only determined by the bandwidth used for the frequency sweep. In this way, the following theoretical range resolution can be obtained [56]

$$\rho_r = \frac{c}{2B}, \quad (2.45)$$

where  $B$  is the bandwidth. Strictly speaking, pulse compression is not a part of SAR. A SAR that uses an ordinary short pulse to obtain a high range resolution would work just as well. However, the major part of SAR systems use pulse compression to achieve an acceptable signal-to-noise ratio (SNR), and pulse compression is in this way an integrated part of SAR in practise. A potential disadvantage of pulse compression in relation to ice sounding is that the technique requires a minimum flight altitude which is undesirable due to increased surface clutter according to Figure 1.4. Since transmission with a monostatic system for practical reasons has to be completed before reception is initiated, a minimum altitude is therefore determined by the transmitted pulse length and the range to the closest target of interest.

### Power Gain

Using pulse compression, the peak power of the pulse is increased by the pulse compression ratio that is given by [57]

$$R_c = T/\tau \approx BT, \quad (2.46)$$

where  $T$  is the width of the transmitted pulse and  $\tau$  is the width of the compressed pulse. Since the noise is a random signal, it is uncorrelated with the transmitted pulse and noise power is therefore unaffected by the filtering. In this way, by using pulse compression the SNR  $S$  is improved by the compression ratio. The resulting SNR after compression is given by

$$S_c = BTS. \quad (2.47)$$

The above consideration is only valid for a point target. For a distributed target, no pulse compression gain is achieved.

### 2.5.2 Synthetic Aperture Processing

To obtain a good resolution in the along-track direction, we know from antenna theory that a large aperture length is required. The length of a real aperture is in practice limited, especially in the case of airborne or space-based systems. Instead, by using a moving platform, a large aperture length can be obtained by forming a synthetic aperture. This is done by acquiring signals with a small real aperture at different azimuth positions at different time instants. By proper signal processing, all acquisitions containing information of a given target can be combined as if the target was illuminated by a correspondingly large real aperture at a single time instant.

A SAR can in theory provide an azimuth resolution equal to half the azimuth length of the physical aperture, independent of range, i.e. [56]

$$\rho_s = \frac{L_s}{2}, \quad (2.48)$$

where  $L_s$  is the length of the physical aperture in azimuth. This is one of the key characteristics of a SAR, which is in contrast to a real aperture radar where the azimuth resolution is range dependent.

The formation of a synthetic aperture and the corresponding acquired signals is a completely geometric process, i.e. a function of spatial position. However, it is convenient to analyse the SAR system as

a function of time which is related to the spatial position through the velocity of the moving platform.

In the temporal domain, a relative radar-to-target velocity can be expressed for a given target, which is found to be varying over time. When the target is far in front of the radar, the relative velocity is large negative and increases to zero, when the target is perpendicular to the track. The velocity ends up large positive when the target is far behind the radar. This varying velocity gives rise to a correspondingly varying Doppler shift in the echoes returning from the target. This implies a phase variation along the synthetic aperture.

If the antenna looks perpendicular to the trajectory and has reasonably narrow beam in azimuth, the Doppler frequency variation for a given target will be linear within the beam. This implies that the signal along the synthetic aperture will have a linear frequency modulation with a bandwidth determined by the total Doppler variation along the aperture, i.e. the Doppler bandwidth. With processing similar to that of pulse compression, a high resolution signal can now be obtained. Although processing of a linear frequency modulated signal is convenient, a nonlinear modulation can also be exploited, in order to obtain a higher resolution, e.g. in the case of a forward looking radar.

Even though the fundamental synthetic aperture processing can be described as a matched filtering process and with a signal modulation similar to one that can be used in pulse compression, it is in general much more complicated. More factors complicate the synthetic aperture processing such as motion deviations of the moving platform, possible refraction in the case of sounding, and a point target response that is range dependent and two-dimensional.

The synthetic aperture processing is also referred to as azimuth compression or Doppler processing.

### Power Gain

When forming a synthetic aperture, a coherent integration takes place corresponding to the number of pulse in the aperture,  $N_s$ . Since the signals add coherently, the voltage is increased by  $N_s$  and hence the power by  $N_s^2$ . The noise, however, do not add up this way. Since noise is a stochastic process, its variance is increased by  $N_s$ . Thus, the SNR of the corresponding real aperture radar  $S_r$  is improved by  $N_s^2/N_s$  resulting in the following nominal SNR for the SAR [56]

$$S_s = N_s S_r. \quad (2.49)$$

The number of pulse  $N_s$  can be expressed as the ratio of the length of the synthetic aperture to the distance traveled between two successive pulses, that is

$$N_s = \frac{L_s}{uT_p} + 1, \quad (2.50)$$

where  $u$  is the velocity of the moving platform and  $T_p$  is the pulse repetition period.

The above consideration is valid for point targets. When it comes to a distributed target, no SNR improvement is achieved by SAR focusing.

### 2.5.3 Unfocused SAR

Synthetic aperture processing is used in ice sounding in order to improve the SNR and azimuth resolution, and to suppress clutter in the along-track direction. When considering the different targets of interest in an ice sounding scenario, the internal layers stand out as a special case. The signal from the subsurface layers is dominated by a strong specular component which is affected by a coherent phenomenon known as Fresnel zoning. Fresnel zones are regions on the surface for which the propagated distance of the reflected waves differ by less than a half wavelength [64]. A boundary between such two zones is found each time the two-way propagation distance is increased by a half wavelength, corresponding to an increase in range by a quarter of a wave length. For a flat surface, these boundaries of constant range are circular corresponding to annular shaped zones except for the innermost (first) zone which is a disk. By counting the zones starting with the innermost, the outer radius  $r_n$  of the  $n$ th zone can be derived using Pythagoras's theorem

$$r_n^2 + h^2 = \left(h + n\frac{\lambda}{4}\right)^2 \quad (2.51)$$

$\Updownarrow$

$$r_n = \sqrt{n\lambda \left(\frac{n\lambda}{4^2} + \frac{h}{2}\right)} \quad (2.52)$$

$$\approx \sqrt{\frac{n\lambda h}{2}}, \quad \text{for } n\lambda \ll h. \quad (2.53)$$

Due to mutual cancellations of the signals from the different zones, the resulting signal can be considered as if the first Fresnel zone, or just *the* Fresnel zone, is the only contributor. The effective footprint, and

thereby the effective aperture length, for the specular return is in this way limited correspondingly.

The derivation of the Fresnel zone is closely related to what is known as an unfocused SAR. For an unfocused SAR the length of the synthetic aperture is shortened to the point where no phase correction is needed for the range variation across the aperture. The corresponding criterion is defined as a maximum phase variation of  $\pi/4$  across the aperture. This corresponds to an aperture length of

$$L_u = \sqrt{\frac{R_0 \lambda}{2}}, \quad (2.54)$$

where  $R_0$  is the minimum range to the target along the aperture. The expression is seen to be completely analog to (2.53) with  $n = 1$ . This shorting results in great simplifications of the processing, but for the price of a degraded nominal resolution that depends on range. The best possible unfocused resolution is given by [54]

$$\rho_u = \frac{\lambda R_0}{2L_u} = \sqrt{\frac{R_0 \lambda}{2}} = L_u. \quad (2.55)$$

However, for the case of internal layers, the aperture length and resolution of an unfocused SAR corresponds exactly to the best achievable performance due to the analogy with the Fresnel zone. Actually, the longer aperture of a fully focused SAR leads to degraded performance since the surface clutter energy scales with  $L_s$  while the specular energy is constant for  $L_s > L_u$ . In theory, an simple unfocused SAR would therefore be sufficient to obtain optimal performance. In practice, however, this may not be the case. The signal from the subsurface specular reflection is by its nature perpendicular to the surface, i.e. nadir for a flat surface. In the case of surface slopes, the incidence angle deviates from nadir, according to the slope. In this way, a specular return may be completely undetectable in the case of larger surface slopes. In order to ensure detection of internal sloped layers, a focused SAR is therefore used to process a higher Doppler bandwidth, corresponding to a wider processed beam that is able to capture an off-nadir specular return.

In relation to the bedrock, no SNR improvement is in general achieved using synthetic aperture processing due the distributed target characteristics of a flat horizontal bed. However, a large synthetic aperture is still desired. Beside along-track clutter suppression, synthetic aperture processing improves the resolution of the bedrock. Furthermore, synthetic aperture processing includes range cell migration correction

which is convenient in further data analysis. In principle, the longer an aperture the better. However, in practise the aperture length is limited compared to traditional SAR due to uncertainties related to the propagation velocity within the ice, and to the refraction at the air-ice interface.

For the sake of completeness, the simplified 1D focusing approach that lies in-between a unfocused SAR and a fully focussed SAR, should be mentioned. A 1D-focused aperture corresponds to a maximum range migration of half a range cell. With this shorting of the aperture, the processing can be done without range migration correction and the matched filters become one-dimensional. Based on this categorization, fully focused SAR, or processing using range migration correction, is referred to as 2D processing.

#### 2.5.4 Weighting

The impulse response of a compressed pulse has sidelobes which introduce an indirect type of surface clutter that in the following is referred to as sidelobe surface clutter. This type of clutter is only a problem for sounders employing pulse compression, which most of the modern sounders do, though. The clutter originates from the surface in the near-nadir region. Due to pulse compression, the strong surface return from nadir has sidelobes, which then can mask the internal ice layers. The problem is illustrated in Figure 2.6. A sounding profile for a given azimuth position can be considered as the superposition of the responses for each range cell. It is seen in the figure how a internal layer coincide with a sidelobe of the surface response, and hence this surface sidelobe is added to the mainlobe of the internal layer, at the corresponding depth. Since the return of the internal layer is weak compared to the that of the surface, the mainlobe peak of the layer can be smaller than the sidelobe of the surface response, even if it is a distant sidelobe. It is therefore important to suppress such sidelobes. Sidelobe suppression is typically obtained by time-domain and spectral weighting [8, 65].

The effect of weighting on the impulse response is illustrated in Figure 2.7. It is seen how the close-in sidelobes are suppressed by the spectral Blackman window, and the distant sidelobes by the time-domain Tukey weight.

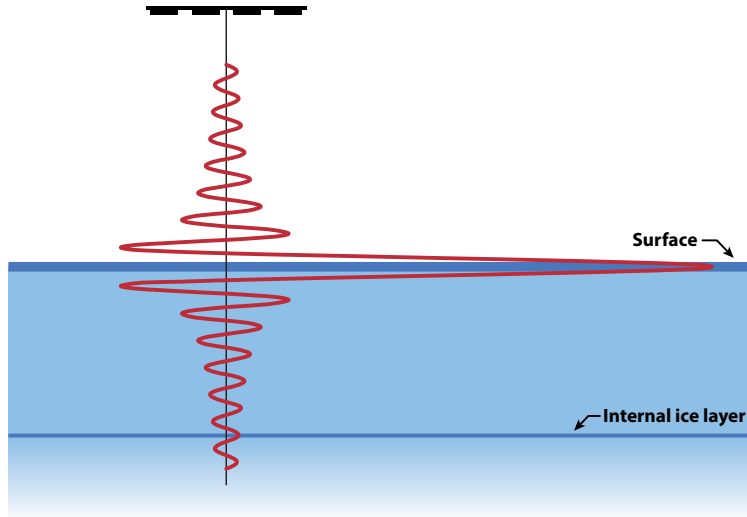


**Figure 2.6:** Sidelobe surface clutter at an internal ice layer introduced by the pulse compressed surface response (red curve).

## 2.6 Antenna Arrays

From the principles and the characteristics of the SAR, we now move on to theory related to the physical antenna. Different types of antennas can be used to form the synthetic aperture in the along-track direction. In the context of tomography and surface clutter suppression, it is more interesting to focus the attention on the antenna design in the across-track direction.

In several applications, it is necessary to design antennas with very directive characteristics. This includes ice sounding where a narrow beam in the across-track direction is desired in order to suppress surface clutter. The only way to obtain such characteristics is to increase the electrical size of the antenna. This can be done by enlarging the physical dimensions of single antenna which is feasible at high frequencies where the wavelength is short. However, when lower frequencies are of interest, a constellation of multiple antenna elements can often synthesize a much larger spatial aperture than that practical with a single physical antenna. Such a constellation of multiple antenna elements in an electrical and geometrical configuration is referred to as an antenna array.

In most cases, the elements of an array are identical. This is not

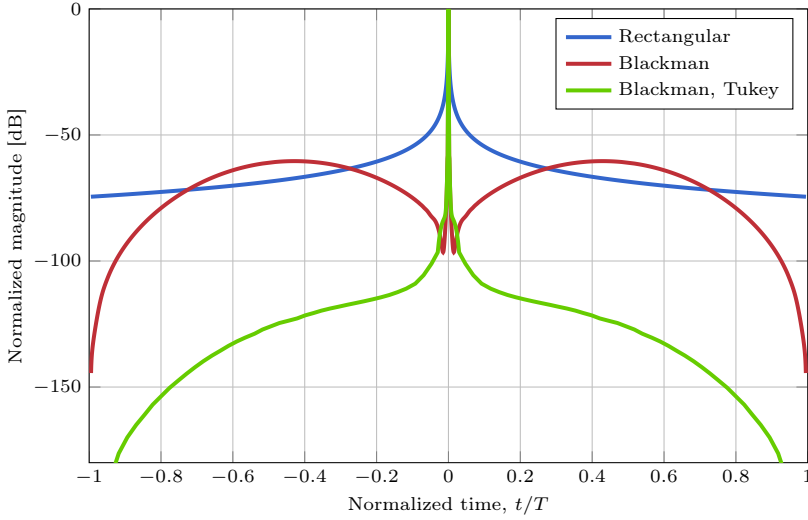


**Figure 2.7:** Sidelobe envelopes of impulse responses for a linear chirp with different weighting functions. A  $20\text{ }\mu\text{s}$  pulse with 85 MHz bandwidth is assumed. All impulse responses have been normalized.

necessary, but it is often convenient, simpler, and more practical. The individual elements of an array may be of any form, e.g. wires, microstrips, apertures, etc. The directive characteristics of the array are obtained as a consequence of the coherent addition of the individual element fields that interfere constructively in some desired directions and destructively in the remaining space. Assuming no coupling between the elements, the total radiated field at a given position in space equal the sum of the fields of the individual elements, i.e.

$$\mathbf{E} = \sum_{n=1}^N \mathbf{E}_n, \quad (2.56)$$

where  $\mathbf{E}_n$  is the field at the  $n$ th element. For an array of identical elements observed in the far field, the total field can be described as the product of the field of a single element  $\mathbf{E}_0$  and the array factor AF of that array. That is,

$$\mathbf{E} = \mathbf{E}_0 \text{AF}. \quad (2.57)$$



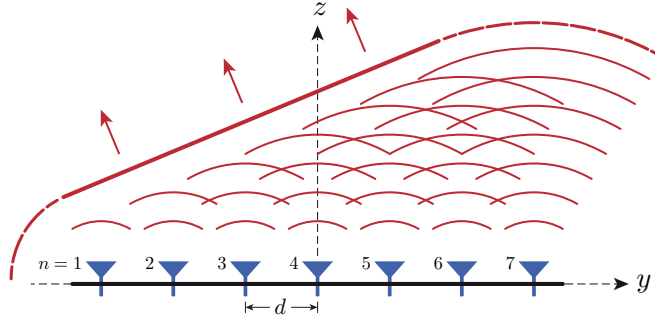


**Figure 2.8:** Uniform linear array excited with a progressive phase across the elements. The red thick line illustrates the wavefront of constructively interference in the direction determined by the progressive phase.

The array factor is a function of number of elements, their geometrical arrangement, relative magnitudes, phases, and their spacings. The array factor does not depend on the characteristics of the individual element and can in this way be interpreted as a description of the array configuration. A particular array configuration of interest is the uniform linear array (ULA) that consists of identical elements uniformly distributed on a straight line, as illustrated in Figure 2.8. For a ULA with identical magnitude element excitation and a progressive excitation phase, the array factor is given by

$$AF = \sum_{n=0}^{N-1} e^{jn\Omega}, \quad (2.58)$$

where  $\Omega = kd \sin \theta + \beta$ ,  $k$  is the wavenumber,  $d$  is the element spacing,  $\theta$  is the direction, and  $\beta$  is a possible phase excitation difference between consecutive elements. When the physical center of the array is chosen as the origin, the geometric series in (2.58) can be expressed as the following compact form [66]

$$AF = \frac{\sin\left(\frac{N}{2}\Omega\right)}{\sin\left(\frac{1}{2}\Omega\right)}. \quad (2.59)$$

The angular pattern of the array factor may comprise several local maxima, or lobes, which are separated by nulls. Non-global maxima are called sidelobes. From (2.58) it is seen that a global maximum is found

when  $\Omega = 0$ , which is referred to as the mainlobe. This maximum value can be considered as the array gain and is given by

$$G_{AF} = \lim_{\Omega \rightarrow 0} AF = N. \quad (2.60)$$

Other global maxima may exist and are referred to as grating lobes. A global maximum is found at the singularity points of (2.59), i.e.

$$\sin\left(\frac{1}{2}\Omega\right) = 0 \quad (2.61)$$

$$\Updownarrow \quad \frac{1}{2}(kd \sin \theta + \beta)|_{\theta=\theta_m} = \pm m\pi, \quad m \in \mathbb{N}_0 \quad (2.62)$$

$$\Updownarrow \quad \theta_m = \arcsin\left(\frac{\lambda}{2\pi d}(-\beta \pm m2\pi)\right). \quad (2.63)$$

The number of grating lobes ( $m > 0$ ) depends on  $\lambda$  and  $d$ . In order to avoid grating lobes, the argument of arcsin in (2.63) must be numerically larger than one for all  $m > 0$ . In the case of a broadside array ( $\beta = 0$ ), that is

$$\frac{m\lambda}{d} > 1, \quad \forall m > 0 \quad (2.64)$$

which corresponds to

$$d < \lambda. \quad (2.65)$$

In this way, to avoid any grating lobes, the element spacing should be less than the wavelength.

Nulls of the array are located where (2.59) is non-singular and the numerator is zero, which corresponds to

$$\theta_n = \arcsin\left(\frac{\lambda}{2\pi d}(-\beta \pm \frac{m2\pi}{N})\right), \quad m, l \in \mathbb{N} \mid m \neq lN \quad (2.66)$$



## Array Signal Processing

In Section 2.6 it was shown how the array factor could describe the characteristics of an array as a single unit. In such a configuration, the elements are typically connected through a hardwired feeding network to a single transceiver channel. Any complex weighting of the elements are in this way determined by the feeding network which produces the same fixed beam for both transmission and reception.

An alternative approach is to access each element separately at reception by using multiple channels. This preserves the total information available at the array, in contrast to the hardwired network that reduces the dimensionality from  $N$  to 1. The multi-channel approach adds great flexibility without degradation in the signal-to-noise ratio (SCR), for the price of increased system complexity and data volume.

With a multi-phase-center system, beamforming techniques can be utilized to synthesize adaptive-antenna patterns that for the ice sounding case can suppress the surface clutter from specific off-nadir angles while a high gain is maintained in the nadir direction. In addition to beamforming, the multi-phase-center systems also provide the opportunity to perform direction-of-arrival (DOA) estimation of the different signal components within the received returns, which is interesting in relation to ice sounding and surface clutter suppression.

Processing based on a multi-phase-center system such as beamforming and DOA estimation is referred to as array signal processing, which is the subject of this chapter. First a model for the output signal of a receiving sensor array is developed. The model formulation is based on [67], [68], and [69].

### 3.1 Signal Model

A  $N$ -element one-dimensional array is considered in receive configuration while impinged by the waveform from a single source. The array elements, or sensors, are assumed to be well modelled as linear time-invariant (LTI) systems, and, furthermore, no coupling between the sensors is assumed. With these assumptions, the multiple source case can be handled by making use of the superposition principle.

The single source considered is assumed to be situated in the far field of the array, i.e. that the plane wave approximation is valid. Mathematically expressed, that is

$$\theta_n \simeq \theta \quad (3.1a)$$

$$R_n \simeq R + y_n \sin \theta \quad \text{for phase variations} \quad (3.1b)$$

$$R_n \simeq R \quad \text{for amplitude variations} \quad (3.1c)$$

where  $\theta$  is the DOA,  $R$  is the range to a given reference point on the array, and  $y$  is the relative sensor position. The subscript  $n$  refers to quantity of the  $n$ th sensor. The far-field region is commonly defined as

$$r > \frac{2D^2}{\lambda}, \quad (3.2)$$

where  $D$  is the maximum overall antenna (array) dimension. The scenario of a plane wave impinging on a ULA is illustrated in Figure 3.1. Let  $\tau_n$  denote the time needed for the impinging wave to travel from a reference point to sensor  $n$ , where  $n = 1, \dots, N$ . The output of sensor  $n$  can now be expressed as

$$\bar{x}_n(t) = h_n(t) \star \bar{s}(t - \tau_n) + \bar{e}_n(t), \quad (3.3)$$

where  $h_n(t)$  is the sensor impulse response,  $\bar{s}(t)$  is the value of the signal waveform measured at the reference point,  $\star$  denotes the convolution operator and  $\bar{e}_n(t)$  is an additive noise component independent of  $\bar{s}(t)$ . The signal  $\bar{s}(t)$  is modelled as a modulated carrier signal with angular frequency  $\omega_c$ , i.e.

$$\bar{s}(t) = A(t) \cos(\omega_c t + \Phi(t)), \quad (3.4)$$

where  $A(t)$  and  $\Phi(t)$  are the amplitude and phase modulation, respectively. Furthermore, the signal  $\bar{s}(t)$  is assumed to be narrowband, which

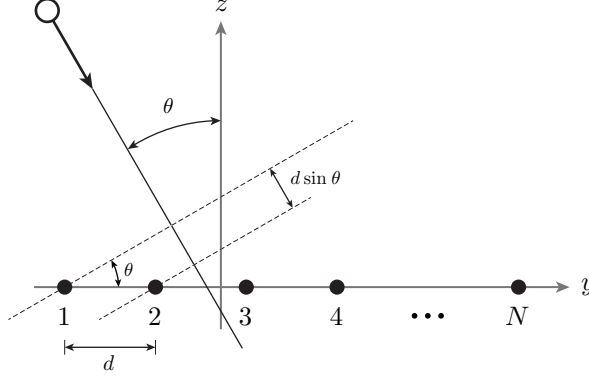


**Figure 3.1:** Uniform linear array with impinging plane wave.

means that the variations in amplitude and phase are assumed to be slow, relative to the propagation time across the array, i.e.

$$A(t - \tau_n) \simeq A(t) \quad \text{and} \quad \Phi(t - \tau_n) \simeq \Phi(t), \quad \forall n. \quad (3.5)$$

By using (3.4) and (3.5) we can write

$$\bar{s}(t - \tau_n) = A(t - \tau_n) \cos \left( \omega_c(t - \tau_n) + \Phi(t - \tau_n) \right) \quad (3.6)$$

$$\simeq A(t) \cos \left( \omega_c(t - \tau_n) + \Phi(t) \right), \quad (3.7)$$

and by inserting into (3.3)

$$\bar{x}_n(t) \simeq h_n(t) \star A(t) \cos \left( \omega_c(t - \tau_n) + \Phi(t) \right) + \bar{e}_n(t) \quad (3.8)$$

$$= |H_n(j\omega_c)| A(t) \cos \left( \omega_c(t - \tau_n) + \Phi(t) \right. \\ \left. + \arg \left( H_n(j\omega_c) \right) \right) + \bar{e}_n(t), \quad (3.9)$$

where  $H_n(j\omega_c)$  is the transfer function for the  $n$ th sensor,  $|\cdot|$  denotes the modulus, and  $\arg(\cdot)$  denotes the argument.

It is seen that the propagation time for the signal across the array reduces to a phase shift of the carrier signal, which makes a complex notation convenient. A complex representation of  $\bar{s}(t)$  can be obtained by expressing  $\bar{s}(t)$  as the real part of the complex signal  $\tilde{s}(t)$ , i.e.

$$\bar{s}(t) = \frac{1}{2} \left( \tilde{s}(t) + \tilde{s}^*(t) \right), \quad (3.10)$$

where  $(\cdot)^*$  denotes the complex conjugate and  $\tilde{s}(t) = A(t)e^{j\Phi(t)}e^{j\omega_c t}$ . The parts  $e^{j\omega_c t}$  and  $s(t) = A(t)e^{j\Phi(t)}$  are called the carrier and the complex envelope, respectively. The real and imaginary parts of  $s(t)$  are known as the in-phase and quadrature components of  $\tilde{s}(t)$ , respectively. In practice, the components are often obtained directly from  $\tilde{s}(t)$  by means of a quadrature demodulator, where  $\tilde{s}(t)$  typically is preprocessed by a superheterodyne receiver.

By assuming the sensors to be identical and omnidirectional over the  $\theta$ -range of interest, the sensor reference signal  $s(t)$  can be redefined to include the sensor transfer function  $H(j\omega_c)$ , i.e.  $H(j\omega_c)s(t)$  is redefined as  $s(t)$ .

Now, the complex envelope of the output for the  $n$ th sensor can be expressed as

$$x_n(t) = s(t)e^{-j\omega_c \tau_n} + e_n(t). \quad (3.11)$$

Furthermore, the so-called steering vector is defined as

$$\mathbf{a}(\theta) = [e^{-j\omega_c \tau_1} \ \dots \ e^{-j\omega_c \tau_N}]^T. \quad (3.12)$$

By this definition, (3.11) can be written vectorial as

$$\mathbf{x}(t) = \mathbf{a}(\theta)s(t) + \mathbf{e}(t), \quad (3.13)$$

where  $\mathbf{x}(t) = [x_1(t) \ \dots \ x_N(t)]^T$  and  $\mathbf{e}(t) = [e_1(t) \ \dots \ e_N(t)]^T$ .

Now, for the case of multiple sources, the superposition principle is applied. If  $Q$  signals impinge on the array from distinct DOAs  $\theta_1, \dots, \theta_Q$ , the output vector takes the form

$$\mathbf{x}(t) = \sum_{q=1}^Q \mathbf{a}(\theta_q)s_q(t) + \mathbf{e}(t) \quad (3.14)$$

$$= [\mathbf{a}(\theta_1) \ \dots \ \mathbf{a}(\theta_Q)] \begin{bmatrix} s_1(t) \\ \vdots \\ s_Q(t) \end{bmatrix} + \mathbf{e}(t) \quad (3.15)$$

$$\triangleq \mathbf{A}(\boldsymbol{\Theta})\mathbf{s}(t) + \mathbf{e}(t), \quad (3.16)$$

where  $\theta_q$  is the direction of arrival and  $s_q(t)$  is the signal corresponding to the  $q$ th source. The  $N \times Q$  steering matrix  $\mathbf{A}$  is a function of  $\boldsymbol{\Theta}$ , which is a vector containing the  $Q$  DOA angles.

Equation (3.16) constitutes our array data model. The model can be expanded a bit further, in order to include multiple array samples in a compact matrix notation.

The  $N \times 1$  vector  $\mathbf{x}(t_m)$  from the data model constitutes a sample of the array at time instant  $t_m$ . Such an array sample is denoted a *snapshot*. Let  $t_1 \dots t_M$  denote the time instants at which  $M$  snapshots are taken. The total amount of sampled data can be expressed as

$$\mathbf{X} = \mathbf{A}(\Theta)\mathbf{S} + \mathbf{E}, \quad (3.17)$$

where  $\mathbf{X}$  and  $\mathbf{E}$  are the  $N \times M$  matrices

$$\mathbf{X} = [\mathbf{x}(t_1) \dots \mathbf{x}(t_M)], \quad (3.18)$$

$$\mathbf{E} = [\mathbf{e}(t_1) \dots \mathbf{e}(t_M)], \quad (3.19)$$

and  $\mathbf{S}$  is the  $Q \times M$  matrix

$$\mathbf{S} = [\mathbf{s}(t_1) \dots \mathbf{s}(t_M)]. \quad (3.20)$$

In this way, each column in  $\mathbf{X}$ ,  $\mathbf{S}$ , and  $\mathbf{E}$  corresponds to a specific snapshot.

### 3.1.1 Spatial Uniform Sampling

Now we derive the steering vector and define convenient notation for a particular array of interest, namely the ULA.

Consider the case of a ULA, as depicted in Figure 3.1, with the sensor  $n = 1$  chosen as the reference point. In this case,  $\tau_n$  can be expressed as

$$\tau_n = (n - 1) \frac{d \sin \theta}{c} \quad \text{for } \theta \in [-90^\circ, 90^\circ] \quad (3.21)$$

The restriction on  $\theta$  is required in order to avoid geometric symmetric ambiguities, which are related to planar arrays.

By inserting (3.21) into (3.12) we get the following expression for the steering vector

$$\mathbf{a}(\theta) = \left[ 1 \ e^{-j\omega_c d \sin \theta / c} \ \dots \ e^{-j(N-1)\omega_c d \sin \theta / c} \right]^T \quad (3.22)$$

Now let

$$\omega_s = \omega \frac{d \sin \theta}{c} = 2\pi \frac{d \sin \theta}{\lambda} = kd \sin \theta, \quad (3.23)$$

where  $\lambda$  is the wavelength, and  $k$  is the wavenumber. With this definition, the steering vector can be written as

$$\mathbf{a}(\theta) = \left[ 1 \ e^{-j\omega_s} \ \dots \ e^{-j(N-1)\omega_s} \right]^T, \quad (3.24)$$



which is completely analogous to a uniform sample vector of the sinusoidal signal  $\{e^{-j\omega_s t}\}$ . Motivated by this analogy,  $\omega_s$  is called the spatial angular frequency. Following this terminology, the ULA can be thought of as a uniform spatial wavefield sampling device.

In the following section the established model is extended in order to feature spatial aliasing.

### 3.1.2 Spatial Aliasing

In order to ensure that  $\mathbf{a}(\theta)$  is uniquely defined (i.e. to avoid spatial aliasing), it is seen from (3.24) that the following condition must be satisfied:

$$\begin{aligned} & |\omega_s| < \pi \\ \Updownarrow & \end{aligned} \quad (3.25)$$

$$d < \frac{\lambda}{2|\sin \theta|} \quad \forall \theta. \quad (3.26)$$

In this way, for  $\theta \in [-90^\circ, 90^\circ]$  we get the well-known constraint [70]

$$d < \lambda/2, \quad (3.27)$$

which says that the spatial sampling period  $d$  should be less than half of the wavelength in order to avoid aliasing. From the analogy with temporal sampling, (3.26) can be interpreted as a spatial Nyquist–Shannon sampling theorem. For a given sensor spacing that does not satisfy (3.27), the spatial Nyquist frequency in  $\theta$ -space can be derived from (3.26)

$$\theta_{\text{NQ}} = \arcsin \frac{\lambda}{2d}, \quad \text{for } d \geq \lambda/2. \quad (3.28)$$

Again, analog to a temporal sinusoid we have that,

$$e^{-j(\omega_s + 2\pi m)n} = e^{-j\omega_s n}, \quad \forall m, n \in \mathbb{Z} \quad (3.29)$$

which shows that a spatial discrete-time sinusoid of any frequency is identical to some sinusoid of frequency  $\omega_f$  in the fundamental spatial frequency range  $[-\pi, \pi]$ , i.e.,

$$\omega_s = \omega_f + 2\pi m, \quad |\omega_f| \leq \pi \wedge m \in \mathbb{Z}. \quad (3.30)$$

By combining (3.23) and (3.30), a spatial angular frequency in the fundamental range can be related to the corresponding set of under-sampled DOA angles

$$\theta = \arcsin \frac{\omega_f + 2\pi m}{kd}. \quad (3.31)$$

### 3.2 Beamforming

In line with the definition of a spatial spectrum and analog to temporal FIR filtering, a spatial filter is defined as a complex linear combination of the spatial samples in terms of the sensor outputs

$$y(t) = \mathbf{h}^H \mathbf{x}(t), \quad (3.32)$$

where  $\mathbf{h}$  is the filter weight vector. Using (3.16), the noise free spatial filtered output can be expressed as

$$y(t) = [\mathbf{h}^H \mathbf{a}(\theta)] s(t). \quad (3.33)$$

Even though that spatial filtering intuitively might be associated with reception, it is applicable to either radiation or reception of energy in accordance with the reciprocity theorem. Spatial filtering is known as beamforming, which derives from the early spatial filters that were designed to form pencil beams in order to receive a signal from a specific direction and attenuate signals from other directions [71]. However, modern beamforming methods are used to form various complex-shaped antenna patterns. This is what can be utilized for surface clutter suppression in relation to ice sounding where gain towards the nadir signal of interest is maximized while the surface returns are attenuated as much as possible by synthesising antenna patterns that varies as a function of range and geographical position.

Returning to the array model in (3.16), the sensor output vector  $\mathbf{x}(t)$  can be viewed as a multivariable random process, whose characteristics can be well understood from its first and second order statistics determined by the underlying signals and noise. Since the signal parameters of interest are spatial in nature, the cross-covariance information among the sensors are needed, which are contained in the spatial covariance matrix

$$\mathbf{R} = E\{\mathbf{x}(t)\mathbf{x}^H(t)\} \quad (3.34a)$$

$$= \mathbf{A}E\{s(t)s^H(t)\}\mathbf{A}^H + E\{e(t)e^H(t)\} \quad (3.34b)$$

$$\triangleq \mathbf{A}\mathbf{P}\mathbf{A}^H + \sigma_n^2 \mathbf{I} \quad (3.34c)$$

where  $E\{\cdot\}$  denotes statistical expectation,  $\mathbf{P}$  is the source covariance matrix,  $\sigma_n^2 \mathbf{I}$  is the noise covariance matrix, and  $\sigma_n^2$  is the noise variance. The argument of  $\mathbf{A}$  has been omitted to simplify notation. It should be noted that the definition of the covariance matrix implies the Hermitian property. The theoretical covariance matrix  $\mathbf{R}$  cannot be exactly

determined from a finite set of array samples. Instead an estimate is used in terms of the sample covariance matrix  $\hat{\mathbf{R}}$  that is calculated as the average over  $M$  snapshots

$$\hat{\mathbf{R}} = \frac{1}{M} \sum_{m=1}^M \mathbf{x}(t_m) \mathbf{x}^H(t_m) \quad (3.35a)$$

$$= \frac{1}{M} \mathbf{X} \mathbf{X}^H. \quad (3.35b)$$

The power of the spatially filtered signal in (3.32) is given by

$$P = E\{|y(t)|^2\} \quad (3.36a)$$

$$= \mathbf{h}^H E\{\mathbf{x}(t) \mathbf{x}^H(t)\} \mathbf{h} \quad (3.36b)$$

$$= \mathbf{h}^H \mathbf{R} \mathbf{h} \quad (3.36c)$$

Different beamforming approaches correspond to different choices of the weighting vector  $\mathbf{h}$  and thereby different performance when used for surface clutter suppression. A design criteria common for all approaches is that a filter  $\mathbf{h}$  should fulfill the distortionless constraint

$$\mathbf{h}^H \mathbf{a}(\theta_s) = 1, \quad (3.37)$$

i.e. that signals impinging from the direction  $\theta_s$  of interest passes undistorted, cf. (3.33). In the following we will examine different beamforming algorithms and discuss their applicabilities with respect to ice sounding.

### 3.2.1 Beam-steering

Beam-steering (BS) is a spatial filter directly related to the filter bank interpretation of the classical spectral Fourier theory. Beam-steering is also known as delay-and-sum, classical, conventional, or standard beamforming.

For an arbitrary array geometry and under the assumption of a spatially white input, beam-steering minimizes the output power under the constraint given in (3.37). A spatially white signal corresponds to a signal impinging on the array with equal power from all directions, i.e. at all spatial frequencies. Assuming uncorrelated sources, this corresponds to a diagonal covariance structure, i.e.  $\mathbf{R} \propto \mathbf{I}$ . Using (3.36), the corresponding power of the filtered signal equals

$$E\{|y(t)|^2\} = \mathbf{h}^H \mathbf{h}, \quad (3.38)$$

leading to the following design problem

$$\min_{\mathbf{h}} \mathbf{h}^H \mathbf{h} \quad \text{subject to} \quad \mathbf{h}^H \mathbf{a}(\theta_s) = 1. \quad (3.39)$$

By using the technique of Lagrange multipliers [72], it can be shown that the filter vector that satisfy this constrained optimisation problem equals

$$\mathbf{h}_{\text{BS}} = \frac{\mathbf{a}(\theta_s)}{\mathbf{a}^H(\theta_s) \mathbf{a}(\theta_s)}, \quad (3.40)$$

where  $\mathbf{a}^H(\theta_s) \mathbf{a}(\theta_s) = N$  in the case of normalized steering vectors as for the ULA model in (3.22). By inserting into (3.36), the corresponding power spectrum estimate is obtained

$$P_{\text{BS}}(\theta) = \frac{\mathbf{a}^H(\theta) \mathbf{R} \mathbf{a}(\theta)}{N^2}. \quad (3.41)$$

With the design criterion from (3.39), beam-steering is optimal with respect to SNR improvement since the signal components are added coherently whereas the thermal noise of the individual receive channels are out of phase, similar to the SNR improvement for a synthetic aperture as described in Section 2.5. However, similar to a bandpass filter from a conventional Fourier filter bank, BS suffers from high spectral leakage and a wide mainlobe. In the spatial domain, spectral leakage determines the rejection of interfering signals while the width of mainlobe corresponds to the angular resolution.

### 3.2.2 Null-steering

With null-steering (NS) [73], the antenna pattern is designed to have nulls towards the directions of interfering signals, i.e. the surface clutter signals. The design problem can be formulated mathematically as a system of linear equations

$$\mathbf{h}^H \mathbf{A}(\boldsymbol{\Theta}) = \mathbf{g}^T, \quad (3.42)$$

where  $\mathbf{g}$  is a real  $Q \times 1$  vector specifying the desired gain for each of the  $Q$  directions contained in  $\boldsymbol{\Theta}$ . By specifying unity gain for the direction of interest and zero gain for the remaining, the desired signal passes undistorted while nulls are placed in the direction of the disturbing signals. The solution to (3.42) can be found by inverting  $\mathbf{A}(\boldsymbol{\Theta})$ . The inverse exists when  $\mathbf{A}(\boldsymbol{\Theta})$  is regular which requires that the number of

constraints equals  $N$ . In the case where the number of constraints are less than  $N$ , the system is underdetermined and has an infinite number of solutions. The solution that fulfils the least squares criterion for the signal estimation problem is given by

$$\mathbf{h}_{\text{NS}} = \mathbf{A}[\mathbf{A}^H \mathbf{A}]^{-1} \mathbf{g}, \quad (3.43)$$

where the argument of  $\mathbf{A}$  has been left out for simplicity. The solution requires that the columns of  $\mathbf{A}$  are linearly independent such that  $\mathbf{A}^H \mathbf{A}$  will not be singular and inversion is possible. In cases where the columns are highly correlated and  $\mathbf{A}^H \mathbf{A}$  thereby is poorly conditioned, a singular value decomposition can be applied to  $\mathbf{A}$  in order to form a matrix based on the dominating singular values only. For the presented array and noise model, the least squares solution corresponds to the maximum likelihood estimator for the signal of interest, as shown later in Section 3.3.5.

The number of constraints are limited by the degrees of freedom corresponding to the number of sensors. In this way, by assigning one degree of freedom for the distortionless constraint, up to  $N - 1$  nulls can be specified and hence the same number of interfering signals cancelled. If the number of interferers is less than this number then additional degrees of freedom ( $N - Q$ ) can be used to place additional nulls near an interferer in order to obtain a wider effective null. If no such additional nulls are explicitly specified, the additional degrees of freedom will lead to nulls positioned in the end-fire direction corresponding to the Nyquist frequency from (3.28), which maximizes the gain in the direction of interest.

The nulls specified using (3.42) are referred to as zero-order nulls. An  $n$ th-order null refers to the constraint where the  $n$ th derivative of the filtered output is set to zero. Additional degrees of freedom can also be used to enforce such constraints in order to broaden a null.

Assuming narrowband signals and a calibrated array, null-steering can in theory provide perfect clutter cancellation. However, this requires knowledge of the DOA of the clutter signals. Furthermore, null-steering does not take noise into consideration, which can lead to noise amplification, or noise scaling, and thereby significant degradation of the SNR. Noise scaling is discussed in more detail in Section 3.2.5.

### 3.2.3 Capon Beamforming

A spatial filter designed using the Capon method (CM) [74, 75] minimizes the output power similar to beam-steering. However, where beam-

steering assumed spatial white noise, CM exploits the covariance matrix to minimize the power based on the actual spatial structure of the received signal. The Capon method, or Capon's beamformer, is also known as the Minimum Variance Distortionless Response (MVDR) filter in the acoustics literature. Based on (3.36) and similar to (3.39), the design problem can be expressed as

$$\min_{\mathbf{h}} \mathbf{h}^H \mathbf{R} \mathbf{h} \quad \text{subject to} \quad \mathbf{h}^H \mathbf{a}(\theta_s) = 1. \quad (3.44)$$

The solution is given by

$$\mathbf{h}_{\text{CM}} = \frac{\mathbf{R}^{-1} \mathbf{a}(\theta_s)}{\mathbf{a}^H(\theta_s) \mathbf{R}^{-1} \mathbf{a}(\theta_s)}, \quad (3.45)$$

which corresponds to the following power spectrum estimate

$$P_{\text{CM}}(\theta) = \frac{1}{\mathbf{a}^H(\theta) \mathbf{R}^{-1} \mathbf{a}(\theta)}. \quad (3.46)$$

It is assumed that  $\mathbf{R}^{-1}$  exists, which can be ensured with probability 1 under the weak condition that  $M \geq N$  and the noise has a positive definite spatial covariance matrix, which is true for Gaussian noise [67].

One can consider the beam-steering beamformer as paying uniform attention to all other directions different from  $\theta_s$ , even when there might not arrive any signals from most of these directions. The CM filter, on the other hand, tries only to attenuate directions from which signals actually impinge on the array. While beam-steering does not depend on data, CM can be characterized as data-dependent approach. The data-dependent property of the CM filter allows it to use its degrees of freedom to vary the nulls of the stopband, in order to cancel the impinging signals different from  $\theta_s$  in an optimal manner. The CM optimization can be interpreted as some noise suppression are sacrificed in favour of a focused nulling. The nulling reduces the spectral leakage from closely separated sources, which improves the resolution capabilities significantly compared to beam-steering. However, the resolution capabilities of CM still depends on the array length but also the SNR. Furthermore, CM fails when the signal of interest is correlated with the interfering signals.

The data-dependent minimization can lead to critical distortion of the estimated signal for some scenarios. If the desired signal is received from a direction slightly different from what is assumed, the CM attempts to suppress it as any other interfering signal. This phenomenon is referred to as self-nulling [76].

### 3.2.4 Optimum Beamforming

The Optimum Beamformer (OB) [77] is closely related to CM. However, instead of the sample covariance matrix estimated from the data, OB is using a modeled covariance matrix representing noise and interfering signals only. In relation to OB, the interfering signals are sometimes referred to as colored noise due to bandlimited characteristics in the spatial spectral domain. The covariance matrix of the white noise is modeled as a scaled identity matrix as in (3.34c), while the interfering signals are assumed to be monochromatic, i.e. represented by a single spatial frequency component or equivalently, DOA angle. This leads to the following covariance matrix model of the disturbing components

$$\mathbf{R}_d = \sigma_n^2 \mathbf{I} + \sum_{q=1}^{Q_c} \sigma_q^2 \mathbf{a}(\theta_q) \mathbf{a}^H(\theta_q), \quad (3.47)$$

where  $Q_c$  are the number of interfering signals,  $\sigma_q^2$  are the power of the  $q$ th interfering signal, and  $\theta_q$  are the corresponding DOA. The filter design problem is identical to that of CM and hence the solution of OB is given by (3.44) where  $\mathbf{R} = \mathbf{R}_d$ .

OB can be seen as a combination of BS and NS, where both the white noise and the interfering signals are taken into account in order to find the optimal filter weights. This can be interpreted as OB attenuating the interfering signals only down to the noise level, and in this way undesired noise scaling can be avoided.

For practical applications of OB, the challenge is to obtain accurate estimates of the noise and clutter power. This information can be expressed in terms of the clutter-to-noise ratio (CNR) given by

$$\text{CNR} = \frac{\sigma_i^2}{\sigma_n^2}, \quad (3.48)$$

where the power of the different clutter signals are assumed to be identical and equal to  $\sigma_i$ . In the case of ice sounding, the CNR depends on range, system parameters, antenna patterns, sounding geometry, surface scattering mechanism, and the assumed clutter model.

OB can be directly related to BS and NS in the extreme noise scenarios in terms of purely white and colored noise, respectively. In the absence of colored noise, i.e. when  $\sigma_q^2 = \sigma_i^2 = 0$  (CNR = 0) in (3.47), the filter design problem (3.44) is seen to be identical to that of beam-steering, (3.39). Similar, in the absence of white noise,  $\sigma_n^2 = 0$  (CNR =  $\infty$ ), OB

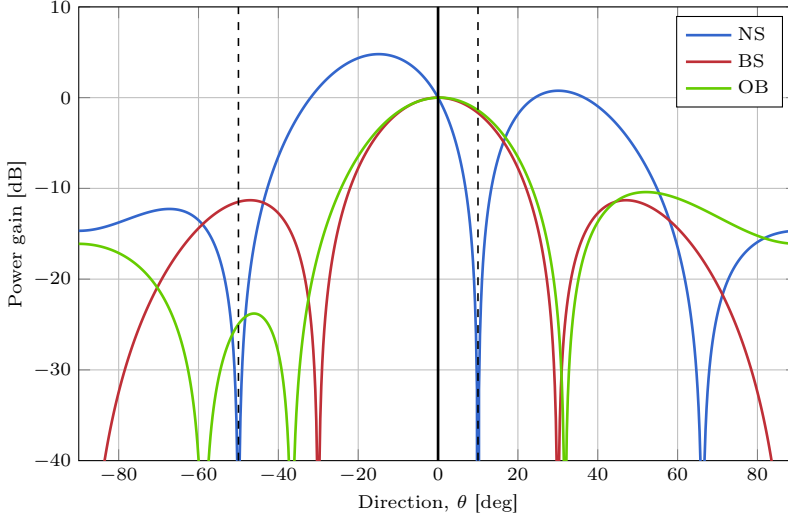


**Figure 3.2:** Synthesized antenna patterns for a 4-element ULA with sensor spacing  $d = \lambda/2$ . A signal of interest (solid black) impinging from  $\theta_s = 0^\circ$  along with two interfering signals (dashed black). The CNR is 0 dB.

corresponds to NS which, however, is not as easily seen directly from the equations.

The weights of OB and CM can be shown to be equivalent in theory under the assumption of the presented signal model [78]. In practice, however, where CM is based on the sample covariance statistics, the resulting weights can be very different.

In Figure 3.2 antenna patterns have been synthesized using NS, BS, and OB for a 4-element ULA with sensor spacing  $d = \lambda/2$ . A desired signal is impinging from  $\theta_s = 0^\circ$  along with two interfering signals from  $-50^\circ$  and  $10^\circ$ . In relation to OB the CNR = 0 dB. From the synthesized patterns in the figure, the different characteristics of the algorithms are evident. All patterns have unity gain towards the signal of interest as enforced by the distortionless constraint. The pattern obtained with BS is symmetric with maximum at the direction of interest and is unaffected by the interfering signals. For NS, on the other hand, nulls are located right at the interfering signals while OB is seen to provide the expected trade-off between BS and NS according to the CNR.



### 3.2.5 Noise scaling

The noise scaling is defined as the ratio between the white noise response, where  $\mathbf{R}_n = \mathbf{I}$ , and the signal response, where  $\mathbf{R}_s = \mathbf{a}(\theta_s)\mathbf{a}^H(\theta_s)$ , that is

$$\kappa = \mathbf{a}^H(\theta_s)\mathbf{a}(\theta_s) \frac{\mathbf{h}^h \mathbf{R}_n \mathbf{h}}{\mathbf{h}^h \mathbf{R}_s \mathbf{h}} \quad (3.49)$$

$$= |\mathbf{a}(\theta_s)|^2 \frac{\mathbf{h}^h \mathbf{h}}{|\mathbf{h}^h \mathbf{a}(\theta_s)|^2} \quad (3.50)$$

$$= N \mathbf{h}^h \mathbf{h}, \quad (3.51)$$

where (3.37) has been used along with the assumption of normalized steering vectors to obtain the last equality. The prefixed factor is a normalization constant. The noise scaling can be considered as a measure that is inversely proportional to the SNR.

In Figure 3.3 simulated noise scaling is shown for NS, BS, and OB. The simulation is based on a 4-element ULA with sensor spacing  $d = 1.5\lambda$ , which results in grating lobes at  $\theta = \pm 41.8^\circ$  according to (2.63). The filters are designed for a signal of interest impinging from  $\theta_s = 0^\circ$  and a single clutter signal from  $\theta_i$ . BS is seen to provide the optimal SNR corresponding to 0 dB noise scaling independent of clutter DOA in contrast to NS where the noise scaling approaches infinity at the grating lobe. OB is simulated with three different values of the CNR, which illustrates the trade-off between noise and clutter suppression. It is seen how OB approaches BS when the CNR is low and approaches NS when the CNR is high.

### 3.2.6 Discussion

Four beamforming algorithms have been presented in terms of BS, NS, CM, and OB. Based on the presented theory, the algorithm properties are now related to the signal structure associated with ice sounding, in order to assess the applicability of clutter suppression.

BS provides the optimal SNR while no attention is paid to colored noise that represents surface clutter. However, for regular scenes combined with a low operating altitude, surface clutter can be neglected and the subsurface detectability is limited by the SNR. In this case BS is the algorithm of choice for synthesizing the receive beam. Optionally weighting can be applied to reduce sidelobes for the prize of an increased mainlobe. DOA algorithms can be used for determining slopes of inter-

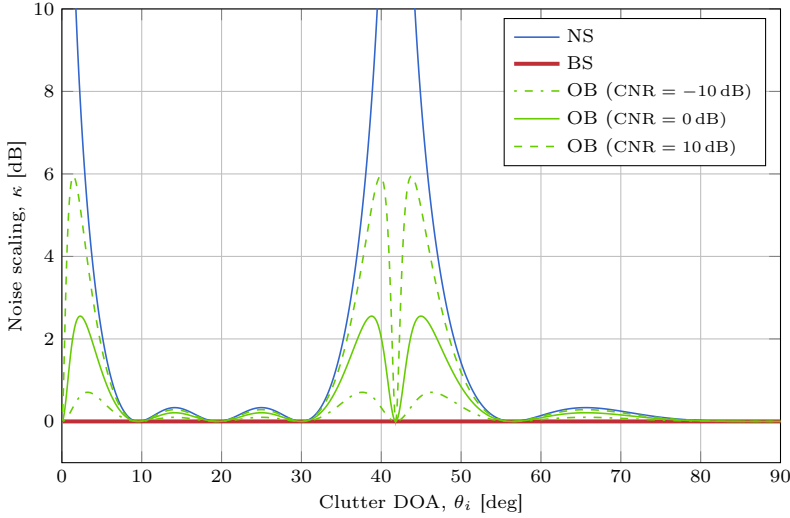


**Figure 3.3:** Noise scaling as a function of clutter DOA for a 4-element ULA with sensor spacing  $d = 1.5\lambda$  and a signal of interest impinging from  $0^\circ$ .

nal layers or the bed in order to adaptively steer the beam in the optimal direction with respect to the targets of interest.

For more irregular scenes not necessarily strictly dominated by white noise, BS may still be considered for data analysis since the formed beam pattern is robust and provides a synthesis that is easy to interpret. Furthermore, BS is very computational efficient.

NS provides the optimal suppression of monochromatic interfering signals. However, due to the finite width of the radar pulse, the illuminated surface area extents in the across-track direction as illustrated in Figure 1.3. In this way, the corresponding clutter signal originates from a range of incidence angles and thereby an interval of spatial frequencies. For this reason, NS may not fully suppress a given clutter signal in practice. In the case of broadband clutter signals, the suppression performance can be improved by synthesizing multiple or higher order nulls.

NS requires prior knowledge of the clutter DOA in order to correctly steer the nulls. Such information can be obtained using a model-based approach by calculating the clutter DOA from the geometry, e.g. by using (1.1). Alternatively, the DOA can be calculated using an existing

digital elevation model or it can be obtained from the radar data itself using data-driven DOA estimation. For sounding scenarios where the interference is dominated by a few distinctive clutter signals, NS can provide a robust and effective suppression. However, depending on the geometry the surface clutter might only dominate at some parts of the depth range. For instance, if the clutter is suppressed at large off-nadir angles due to a low operating altitude combined with a smooth surface, NS is suboptimal at the corresponding large depths due to noise scaling. In this case, OB can be used to obtain the optimal trade-off between clutter suppression and noise scaling. However, OB requires knowledge of the CNR which may be difficult to obtain since the clutter power varies with off-nadir angle and local surface characteristics. One approach could be based on surface scattering models if appropriate roughness parameters are known. As an alternative, procedures for CNR estimation based on radar data are considered in [34]. Even if no information on the CNR is available, OB can be an advantage compared to pure NS. For instance, OB can be used to regularize the weight of NS near a grating lobe in order to avoid extensive noise scaling as demonstrated in [33].

In contrast to NS and OB, CM is very convenient from an implementation point of view since no external information is required by the algorithm. The optimal filter weights are designed exclusively based on the sample covariance matrix. This may especially be an advantage in complex scenarios where the dominating disturbing mechanism is changing rapidly as a function of both range and azimuth. The same might be true if the surface clutter does not consist of a few dominating narrowbanded components but instead a continuum in the spatial spectrum. However, the data-adaptive nature of CM may also be a disadvantage since the resulting filter may be difficult to interpret, but also in the shape of the phenomenon of self-nulling. Since CM assumes a monochromatic signal of interest, depth signals that extend in spatial frequency may be affected using this algorithm. Maybe even worse, if the signal of interest is strong and narrowbanded but is arriving from another direction than expected, such as a specular return from a sloped internal layer, CM may to a larger extent suppress this desired component. One approach to prevent this could be to estimate the DOA of the sloped layer and use this information for specification of the direction of interest when synthesizing the CM beam. This, however, complicates the algorithm and implementation which contradicts with the advantage of simplicity highlighted earlier. A less adaptive but more simple solution is based on so-called robust variants of CM that attempt to

protect a range of DOAs around the direction of interest with respect to suppression [30].

### Performance Degradation

Practical issues may degrade the suppression performance compared to the theory even if the assumptions of the signal model hold true [79].

Firstly, imperfect array calibration in terms of an incorrect model of the array manifold prevents the optimal performance to be reached.

Secondly, mechanical vibrations and deformation may cause the extrema of the radiation pattern to shift and at the same time limit the depths of the synthesized nulls. Such effects are most pronounced for airborne systems operating at low altitudes and with the antenna elements mounted directly under the wings of the aircraft. Turbulence related to the dense air at low altitudes causes wing flexure and vibrations in the case of airborne operation while a very stable flight can be obtained in free space with space-based system.

Thirdly, mutual coupling in terms of interchange of energy between the array elements have similar effects on the synthesized patterns. The algorithms produce inaccurate or suboptimal results unless this effect is taken into account. The detrimental effect of mutual coupling intensifies as the sensor spacing is reduced [80, 81].

## 3.3 Direction of Arrival

The problem of determining the directions of impinging signals, i.e. the angles contained in  $\Theta$ , is known as the source location problem within spatial spectral estimation theory. Due to the relation between DOA and spatial frequency in (3.23), DOA estimation is equivalent to a spectral estimation problem. Several algorithms exist for spectral estimation and in the following a subset of suitable techniques in relation to multi-phase-center radar ice sounding will be assessed.

DOA estimation techniques can be classified into two main categories: parametric and non-parametric methods. Non-parametric methods do not make any assumption on the signal structure or the statistical properties of the data while parametric methods rely on such model-based information.

### 3.3.1 Beamforming Techniques

Beamforming can be used for DOA estimation by steering the beam in all possible directions. In this way, the power received by the array is estimated as a function of DOA, which corresponds to the an estimate of the spatial spectrum. The DOA is then determined as the local maxima of this computed spatial spectrum. In general, an estimation technique that is based on peak analysis of a (pseudo) spectral spectrum is referred to as a spectral method. Spectral methods based on beamforming is considered as the conventional methods for DOA estimation.

Based on this spatial approach, the beamformers described in Section 3.2 in terms of BS and CM can be used for DOA estimation directly. Due to the nature of the beamforming approach, the DOA estimators based on BS and CM are non-parametric. The estimators possess the same characteristics as the corresponding beamformers described earlier. The major disadvantage of BS with respect to DOA estimation is its poor resolution. The BS DOA estimator can be considered as spatial extension of the periodogram. More precisely, it is analog to the Bartlett periodogram [82] where the total dataset is subdivided into a number of non-overlapping segments, which can be considered equivalent with snapshots in the spatial case. In this way, BS inherits the resolution properties from the periodogram, which in terms of angular frequency corresponds to [67]

$$\Delta\omega_s = \frac{2\pi}{N}. \quad (3.52)$$

By differentiating (3.23) with respect to  $\theta$  we get

$$\frac{d\omega_s}{d\theta} = kd \cos \theta \quad (3.53)$$

and by letting  $\Delta\omega_s/\Delta\theta \approx d\omega_s/d\theta$ , we can express the resolution limit of BS as

$$\Delta\theta \approx \frac{\Delta\omega_s}{kd \cos \theta} = \frac{\lambda}{Nd \cos \theta}. \quad (3.54)$$

The resolution is seen to be inversely proportional to the physical length of the array measured in wavelengths, i.e.  $Nd/\lambda$ .

An estimate is said to be consistent if it converges to the true value when the number of samples tends to infinity. The temporal Bartlett periodogram is consistent since the number of non-overlapping segments

can be increased without bound, as the number of samples tends to infinity. In the case of BS, on the other hand, the number of array elements is limited by physical considerations and hence prevents the estimate from being consistent in the general case of multiple sources. The bias of the estimates may be significant if the sources are strongly correlated or closely separated. However, when the DOA separation is sufficiently large compared to the array length, the signals are uncorrelated, and the noise is spatially white, beam-steering may provide reasonably accurate estimates [67].

Due to the data-adaptive properties of CM, the resolution is significantly improved compared to BS. However, when the impinging signals are correlated, CM fails. DOA estimation based on CM corresponds to the Capon transformation known from temporal power spectral density estimation.

### 3.3.2 Parametric Methods

The advantage of the non-parametric methods are that they do not assume anything about the statistics of the data, and can therefore be used in cases where no such information is available. On the other hand, when prior information is available, higher performance can be obtained by a model-based approach. The two parametric methods presented in the following sections both assume the signal model in (3.16) including the structure of the covariance matrix given in (3.34c), which is repeated here for convenience

$$\mathbf{R} = \mathbf{A}\mathbf{P}\mathbf{A}^H + \sigma_n^2\mathbf{I}. \quad (3.34c)$$

The signal covariance matrix  $\mathbf{P}$  is diagonal when the signals are uncorrelated, that is  $\mathbf{P} = \text{diag}(P_1, \dots, P_Q)$  where  $P_q$  is the power of the  $q$ th impinging signal.

The parametric methods exploit the structure of the received data, resulting in a significant improvement in resolution, but at the cost of increased computational load. In order to ensure a unique solution, the methods assume that the number of signals is smaller than the number of sensors, i.e.  $Q < N$ , and that every set of  $N$  steering vectors is linearly independent. Furthermore, the number of signals is assumed to be known.

In the following sections, three well-established and high performing parametric methods are presented.

### 3.3.3 MUSIC

The Multiple Signal Classification (MUSIC) algorithm [67, 83, 84] is a widely used subspace-based method originally presented in [85] as a DOA estimator. Subspace methods exploits the eigen-decomposition of the covariance matrix and assume this to be well-conditioned. An eigen-decomposition of  $\mathbf{R}$  is considered

$$\mathbf{R} = \mathbf{U}\mathbf{\Lambda}\mathbf{U}^H, \quad (3.55)$$

where  $\mathbf{\Lambda}$  is the diagonal matrix  $\text{diag}(\lambda_1, \dots, \lambda_N)$ , where  $\lambda_n$  is the  $n$ th eigenvalue arranged in a nonincreasing order such that  $\lambda_1 \geq \lambda_2 \geq \dots \geq \lambda_N$ . The matrix  $\mathbf{U}$  is an orthonormal basis consisting of the corresponding eigenvectors.  $\mathbf{U}$  can be chosen orthogonal since  $\mathbf{R}$  is Hermitian. The eigenvalues are real and positive since, again,  $\mathbf{R}$  is Hermitian and thereby positive definite. The same is true for  $\mathbf{A}\mathbf{P}\mathbf{A}^H$ , but due to the rank of  $Q$ , only  $Q$  eigenvalues are strictly positive, while the  $(N - Q)$  remaining are equal to zero.

For the structure of  $\mathbf{R}$  given in (3.34c), the eigenvalues can be written as

$$\lambda_k = \tilde{\lambda}_k + \sigma_n^2, \quad (3.56)$$

where  $\tilde{\lambda}_k$  is the  $k$ th eigenvalue of  $\mathbf{A}\mathbf{P}\mathbf{A}^H$ , arranged in nonincreasing order. It now follows that

$$\begin{cases} \lambda_k > \sigma_n^2 & \text{for } k = 1, \dots, Q \\ \lambda_k = \sigma_n^2 & \text{for } k = Q + 1, \dots, N \end{cases} \quad (3.57)$$

This shows that the  $Q$  largest eigenvalues of  $\mathbf{R}$  are related to the signal, and the  $N - Q$  smallest, all equal to  $\sigma_n^2$ , are related to the noise.

The eigen-decomposition of  $\mathbf{R}$  is now expressed in the following way

$$\mathbf{R} = \mathbf{U}\mathbf{\Lambda}\mathbf{U}^H = \mathbf{U}_s\mathbf{\Lambda}_s\mathbf{U}_s^H + \mathbf{U}_n\mathbf{\Lambda}_n\mathbf{U}_n^H, \quad (3.58)$$

where

$$\mathbf{\Lambda}_s = \text{diag}(\lambda_1, \dots, \lambda_Q), \quad (3.59)$$

$$\mathbf{\Lambda}_n = \text{diag}(\lambda_{Q+1}, \dots, \lambda_N) = \sigma_n^2 \mathbf{I}, \quad (3.60)$$

and  $\mathbf{U}_s$ ,  $\mathbf{U}_n$  are the corresponding eigenvectors, respectively. The subspaces spanned by  $\mathbf{U}_s$  and  $\mathbf{U}_n$  are called the signal subspace and the noise subspace, respectively.

From the definition of an eigenvector and by combining (3.34c) and (3.57) we get that

$$\mathbf{R}\mathbf{U}_n = \mathbf{U}_n\boldsymbol{\lambda}_n = \sigma_n^2\mathbf{U}_n = \mathbf{A}\mathbf{P}\mathbf{A}^H\mathbf{U}_n + \sigma_n^2\mathbf{U}_n, \quad (3.61)$$

where it follows that

$$\mathbf{A}^H\mathbf{U}_n = \mathbf{0}. \quad (3.62)$$

This shows that the steering vectors are orthogonal to the noise subspace and hence the true DOAs  $\{\theta_q\}_{q=1}^Q$  are the only solutions to the equation

$$\mathbf{U}_n^H\mathbf{a}(\theta) = \mathbf{0}. \quad (3.63)$$

In practice, when the sample covariance matrix is used,  $\mathbf{U}_n$  will deviate from the true value, and no steering vector is exactly orthogonal to the estimated noise subspace. Instead, the following expression can be used as a measure of orthogonality

$$P_{\text{MU}}(\theta) = \frac{1}{\|\mathbf{U}_n^H\mathbf{a}(\theta)\|^2} = \frac{1}{\mathbf{a}^H(\theta)\mathbf{U}_n\mathbf{U}_n^H\mathbf{a}(\theta)}. \quad (3.64)$$

This is what is known as the MUSIC estimator, where the  $Q$  largest peaks of the so-called MUSIC-spectrum are taken as the DOA estimate. The spectrum is called a pseudo-spectrum since it is not a true PSD, but indicates the presence of sinusoidal components in the signal. In this way, MUSIC is considered as a spectral-method. Since various extensions and modifications the algorithm exist, the estimator presented is referred to as conventional or Spectral MUSIC (MU).

The Spectral MUSIC algorithm can be summarised by the following steps

1. Compute the sample covariance matrix of the signal.
2. Perform an eigendecomposition of the matrix and form the basis  $\mathbf{U}_n$ , spanning the noise subspace, of the eigenvectors corresponding to the  $N - Q$  smallest eigenvalues.
3. Determine the DOA estimates as the locations of the  $Q$  highest peaks of (3.64).

With MUSIC it is possible to obtain arbitrary accuracy on the DOA estimate if the data volume is sufficiently large, or the SNR is sufficiently high. So, in contrast to the beamforming methods, MUSIC is a consistent estimator [83]. The MUSIC algorithm breaks down in the case of coherent signals, but the algorithm can be modified in order to handle coherency when a ULA is used.



### 3.3.4 Root MUSIC

We will now consider an variant of MUSIC which is based on polynomial rooting. The DOA is estimated by MUSIC as the peaks of (3.64), which, in absence of noise, approaches infinity. The DOA is in this case therefore found where the expression is infinite, i.e. where the denominator equals zero. In the case of a ULA, the steering vector equals the Fourier vector as shown in (3.24), when the DOA is expressed in spatial frequency through (3.23). In this case, the generalization of the Fourier transform to the Z-transform can be exploited. The steering vector can be expressed in the Z-domain by replacing  $e^{j\omega_s}$  by  $z$ , i.e.

$$\mathbf{a}(z) = \begin{bmatrix} 1 & z^{-1} & \dots & z^{-(N-1)} \end{bmatrix}^T \quad (3.65)$$

The denominator is now expressed in the Z-domain by

$$\mathbf{a}^H(z) \mathbf{U}_n \mathbf{U}_n^H \mathbf{a}(z). \quad (3.66)$$

In the Z-domain, the spatial frequencies corresponding to the DOAs are found as the angular positions of the zeros located on the unit circle. In presence of noise, the zeros are not located exactly on the unit circle, and hence the  $Q$  zeros closest to the unit circle are chosen.

The expression is not a polynomial in  $z$ , due to the presence of  $z^*$  powers through the Hermitian transpose, which complicates the search for zeros. Since the values of  $z$  on the unit circle are of interest,  $\mathbf{a}^H(z)$  can be replaced by  $\mathbf{a}^T(z^{-1})$  which makes the expression a polynomial in  $z$ , i.e.

$$\mathbf{a}^T(z^{-1}) \mathbf{U}_n \mathbf{U}_n^H \mathbf{a}(z). \quad (3.67)$$

This is known as the Root MUSIC (RM) polynomial, which is of degree  $2(Q-1)$ , whose roots occur in mirrored pairs with respect to the unit circle. The DOAs are now estimated from the  $Q$  roots that are nearest and inside the unit circle,

$$\theta_q = \arcsin \left( \frac{1}{kd} \arg\{z_q\} \right), \quad q = 1, 2, \dots, Q. \quad (3.68)$$

MUSIC and Root MUSIC have identical asymptotic properties, but Root MUSIC has empirically been found to perform significantly better with small samples. At the same time, Root MUSIC is computationally more efficient, but is only applicable to ULAs as seen from the derivation.

### 3.3.5 Maximum Likelihood

Within the field of estimation theory, a widely used estimation approach is to choose the model parameters as the values for which the probability of the observed data set is maximized. This technique is referred to as maximum likelihood (ML) estimation where a so-called likelihood function is representing the probability of the observed data set. In this section, the ML estimator [86] for DOA estimation in sensor arrays will be presented.

The noise  $\{e(t)\}$  is assumed to be a stationary and ergodic complex valued Gaussian process with zero mean. Furthermore, the noise samples  $\{e(t)\}$  are assumed to be statistically independent. The assumptions represent the conventional noise model in sensor arrays and is a realistic model of the background and receiver noise and makes the ML estimator applicable from a theoretical point of view.

The impinging signals are regarded as unknown deterministic sequences. In this regard and under the assumed Gaussian noise model, it follows from (3.16) that the probability density function of a snapshot at time instant  $t$  can be expressed by the multivariate Gaussian distribution, which is given by [87]:

$$\mathcal{N}(\mathbf{x}(t)) = \frac{1}{(2\pi)^{N/2} (\det[\sigma_n^2 \mathbf{I}])^{1/2}} \cdot \exp\left(-\frac{1}{2} \mathbf{e}^H(t) (\sigma_n^2 \mathbf{I})^{-1} \mathbf{e}(t)\right) \quad (3.69)$$

$$= \frac{1}{(2\pi\sigma_n^2)^{N/2}} \cdot \exp\left(-\frac{1}{2\sigma_n^2} \|\mathbf{x}(t) - \mathbf{A}(\boldsymbol{\Theta})\mathbf{s}(t)\|^2\right), \quad (3.70)$$

where  $\det[\cdot]$  denotes the determinant of the bracketed matrix.

The joint density function of the sampled data is given by

$$f(\mathbf{X}) = \prod_{m=1}^M \mathcal{N}(\mathbf{x}(t_m)) \quad (3.71)$$

$$= \prod_{m=1}^M \frac{1}{(2\pi\sigma_n^2)^{N/2}} \cdot \exp\left(-\frac{1}{2\sigma_n^2} \|\mathbf{x}(t_m) - \mathbf{A}(\boldsymbol{\Theta})\mathbf{s}(t_m)\|^2\right) \quad (3.72)$$

The corresponding log-likelihood, ignoring constant terms and common constant factors, is given by

$$\mathcal{L} = -MN \ln(\sigma_n^2) - \frac{1}{\sigma_n^2} \sum_{m=1}^M \|\mathbf{x}(t_m) - \mathbf{A}(\boldsymbol{\Theta})\mathbf{s}(t_m)\|^2 \quad (3.73)$$

In order to derive the ML estimator we have to maximise the log-likelihood with respect to the unknown parameters. First the likelihood is maximized with respect to  $\sigma_n^2$  while fixing  $\Theta$  and  $\mathbf{S}$ . By this maximisation we get

$$\hat{\sigma}_n^2 = \frac{1}{MN} \sum_{m=1}^M \|\mathbf{x}(t_m) - \mathbf{A}(\Theta)\mathbf{s}(t_m)\|^2. \quad (3.74)$$

This result is substituted back into the log-likelihood, and the ML estimator is then obtained by solving the following maximisation, where constant terms are ignored:

$$\max_{\Theta, \mathbf{S}} \left\{ -MN \ln \left( \frac{1}{MN} \sum_{m=1}^M \|\mathbf{x}(t_m) - \mathbf{A}(\Theta)\mathbf{s}(t_m)\|^2 \right) \right\}. \quad (3.75)$$

This maximisation problem is equivalent to the following minimisation problem, where it is exploited that the natural logarithm is a monotonic function:

$$\min_{\Theta, \mathbf{S}} \left\{ \sum_{m=1}^M \|\mathbf{x}(t_m) - \mathbf{A}(\Theta)\mathbf{s}(t_m)\|^2 \right\}. \quad (3.76)$$

This is recognised as the least squares criterion for the estimation problem. By fixing  $\Theta$  and minimising with respect to  $\mathbf{S}$ , the following solution is obtained

$$\hat{\mathbf{s}}(t_m) = \left( \mathbf{A}^H(\Theta)\mathbf{A}(\Theta) \right)^{-1} \mathbf{A}^H(\Theta)\mathbf{x}(t_m) \quad (3.77)$$

$$= \mathbf{A}^+(\Theta)\mathbf{x}(t_m), \quad (3.78)$$

where  $(\cdot)^H$  denotes the Hermitian transpose and  $(\cdot)^+$  denotes the Moore-Penrose pseudoinverse. This result is the ML estimate of the parameter  $\mathbf{S}$ , which corresponds to the null-steering beamformer described in Section 3.2.2.

By substituting (3.78) back into (3.76) we end up with the following minimisation problem

$$\min_{\Theta} \left\{ \sum_{m=1}^M \|\mathbf{x}(t_m) - \mathbf{A}(\Theta)\mathbf{A}^+(\Theta)\mathbf{x}(t_m)\|^2 \right\}, \quad (3.79)$$

which can be written as

$$\min_{\Theta} \left\{ \sum_{m=1}^M \|\mathbf{x}(t_m) - \mathcal{P}_{\mathbf{A}(\Theta)}\mathbf{x}(t_m)\|^2 \right\}, \quad (3.80)$$

where  $\mathcal{P}_{\mathbf{A}(\boldsymbol{\Theta})}$  denotes the projection operator [88] onto the space spanned by the columns of  $\mathbf{A}(\boldsymbol{\Theta})$ ,

$$\mathcal{P}_{\mathbf{A}(\boldsymbol{\Theta})} = \mathbf{A}(\boldsymbol{\Theta})\mathbf{A}^+(\boldsymbol{\Theta}). \quad (3.81)$$

Due to the properties of the projection operator, the following likelihood function can be expressed, based on the minimisation problem in (3.80)

$$\mathcal{L}_{\boldsymbol{\Theta}} = \sum_{m=1}^M \|\mathcal{P}_{\mathbf{A}(\boldsymbol{\Theta})}\mathbf{x}(t_m)\|^2. \quad (3.82)$$

The ML estimate of the parameter  $\boldsymbol{\Theta}$  is obtained by maximising this likelihood function. By using that the projection matrix is idempotent and Hermitian, and  $\text{tr}[\mathbf{A}\mathbf{B}] = \text{tr}[\mathbf{B}\mathbf{A}]$  for the square matrices  $\mathbf{A}$  and  $\mathbf{B}$ , the function can be rewritten in the following form that is convenient for implementation purposes

$$\mathcal{L}_{\boldsymbol{\Theta}} = \text{tr}[\mathcal{P}_{\mathbf{A}(\boldsymbol{\Theta})}\hat{\mathbf{R}}], \quad (3.83)$$

where  $\text{tr}[\cdot]$  is the trace of the bracketed matrix. In this way, the ML DOA estimate for the presented signal model is given by the maximization of (3.83) in terms of a  $Q$ -dimensional search, i.e.

$$\hat{\boldsymbol{\Theta}} = \arg \max_{\boldsymbol{\Theta}} \text{tr}[\mathcal{P}_{\mathbf{A}(\boldsymbol{\Theta})}\hat{\mathbf{R}}]. \quad (3.84)$$

### Alternating Projection

In the following, an efficient algorithm for computing the ML estimator, which is referred to as the Alternating Projection algorithm [86], is described. The algorithm is based on Alternating Maximisation (AM) which is a maximisation technique that transforms a multidimensional search into a sequence of much simpler one-dimensional searches. Furthermore, the algorithm exploits the projection-matrix update formula, which provides a computationally efficient scheme for the problem at hand.

### Alternating Maximisation

AM [86] is a simple iterative technique for multidimensional maximisation. A one-dimensional maximisation is performed at each iteration for a single parameter, while the others are held fixed. The target parameter is alternated for each iteration.

Recall the notation from the array model and the ML derivation, where  $\mathcal{P}_{\mathbf{B}}$  denotes the projection operator onto the space, spanned by the columns of the arbitrary matrix  $\mathbf{B}$ ,  $\mathbf{R}$  denotes the sample covariance matrix and  $\mathbf{A}(\boldsymbol{\Theta})$  denotes the steering matrix of the DOAs, collected in the  $Q$ -dimensional vector  $\boldsymbol{\Theta}$ . The estimated value for the  $q$ th parameter at the  $(k + 1)$ th iteration is obtained by solving the following one-dimensional maximisation problem, which is derived from the DOA log-likelihood function  $\mathcal{L}_{\boldsymbol{\Theta}}$  in (3.83)

$$\theta_q^{(k+1)} = \arg \max_{\theta_q} \text{tr} \left[ \mathcal{P}_{\left[ \mathbf{A}(\boldsymbol{\Theta}_q^{(k)}), \mathbf{a}(\theta_q) \right]} \mathbf{R} \right], \quad (3.85)$$

where  $\boldsymbol{\Theta}_q^{(k)}$  denotes the  $(Q - 1) \times 1$  vector of the parameters computed in the  $k$ th iteration given by

$$\boldsymbol{\Theta}_q^{(k)} = \left[ \theta_1^{(k)}, \dots, \theta_{q-1}^{(k)}, \theta_{q+1}^{(k)}, \dots, \theta_Q^{(k)} \right]^T. \quad (3.86)$$

Described with words,  $\boldsymbol{\Theta}_q^{(k)}$  contains values of all parameters calculated in iteration  $k$ , except for the parameter  $\theta_q$ . A combined steering matrix is obtained by augmenting the steering matrix of  $\boldsymbol{\Theta}_q^{(k)}$  with the steering vector of  $\theta_q$ , as seen in (3.85). Although maximisation is performed for only one parameter at each iteration, the other parameters are also referred to as being *computed* at that iteration, by adopting their values from the previous iteration.

The algorithm, in terms of iterations, ends when all parameters are converged, according to a suitable threshold value, which should be adjusted corresponding to the chosen grid size.

The algorithm can be considered as it is, walking along a staircase towards the peak of  $\mathcal{L}_{\boldsymbol{\Theta}}$ , which is illustrated for a two-dimensional function in Figure 3.4. Since a maximisation is performed at each iteration, the value of  $\mathcal{L}_{\boldsymbol{\Theta}}$  cannot decrease. This implies that the algorithm will always converge to a local maximum, but not necessary the global one. Whether or not the algorithm converges to the global maximum is highly dependent on the initial values of the parameters, which are referred to as iteration  $k = 0$ . The following initialisation procedure has empirically been found to provide excellent results [86]. The procedure starts by solving the problem in (3.85) for a single source

$$\theta_1^{(0)} = \arg \max_{\theta_1} \text{tr} \left[ \mathcal{P}_{\mathbf{a}(\theta_1)} \mathbf{R} \right]. \quad (3.87)$$

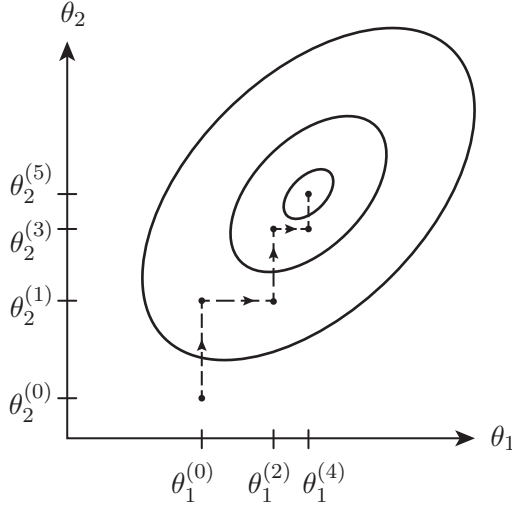


**Figure 3.4:** Successive iterations of the alternating maximisation algorithm, in the maximisation of a 2-dimensional function. Figure adopted from [86].

Next, the problem is solved for the second source, with the first fixed at the previously computed initial value  $\theta_1^{(0)}$ , i.e.

$$\theta_2^{(0)} = \arg \max_{\theta_2} \text{tr} \left[ \mathcal{P} \left[ \mathbf{A}(\boldsymbol{\theta}_1^{(0)}), \mathbf{a}(\theta_2) \right] \mathbf{R} \right], \quad (3.88)$$

Continuing this way, at the  $q$ th init-iteration, the parameter  $\theta_q^{(0)}$  is initialised, while the former computed parameters  $\theta_1^{(0)}, \dots, \theta_{q-1}^{(0)}$  are held fixed in the maximisation. The procedure continues until all the  $Q$  initial values  $\theta_1^{(0)}, \dots, \theta_Q^{(0)}$  are computed.

### Projecting-matrix Decomposition

The AM algorithm reduces the number of evaluations of  $L_{\boldsymbol{\theta}}$ , with respect to a full multidimensional search. Nevertheless, the computational load is still high, due to the matrix inversions and multiplications that arise from the matrix projection  $\mathcal{P}_{\mathbf{A}(\boldsymbol{\theta})}$ . These operations can be reduced by exploiting the projection-matrix update formula, which is to be described now.

Let  $\mathbf{B}$  and  $\mathbf{C}$  denote two arbitrary matrices with the same number of rows. The projecting-matrix update formula now says that

$$\mathcal{P}_{[\mathbf{B}, \mathbf{C}]} = \mathcal{P}_{\mathbf{B}} + \mathcal{P}_{\mathbf{C}_B}, \quad (3.89)$$

where  $\mathbf{C}_B$  denotes the residual of the columns of  $\mathbf{C}$  when projected on  $\mathbf{B}$ ,

$$\mathbf{C}_B = (\mathbf{I} - \mathcal{P}_{\mathbf{B}})\mathbf{C}. \quad (3.90)$$

By applying the projecting-matrix update formula to the projection matrix from (3.85), we get that

$$\mathcal{P}[\mathbf{A}(\boldsymbol{\Theta}_q^{(k)}), \mathbf{a}(\theta_q)] = \mathcal{P}_{\mathbf{A}(\boldsymbol{\Theta}_q^{(k)})} + \mathcal{P}_{\mathbf{a}(\theta_q)_{\mathbf{A}(\boldsymbol{\Theta}_q^{(k)})}}. \quad (3.91)$$

The first term does not depend on  $\theta_q$ , hence it can be considered as being constant with respect to the maximisation. Since we are only interested in the argument corresponding to the maximum peak, and not the peak value itself, the first constant term can be ignored. The problem is now reduced to

$$\theta_q^{(k+1)} = \arg \max_{\theta_q} \text{tr} \left[ \mathcal{P}_{\mathbf{a}(\theta_q)_{\mathbf{A}(\boldsymbol{\Theta}_q^{(k)})}} \mathbf{R} \right], \quad (3.92)$$

which can be rewritten to

$$= \arg \max_{\theta_q} \text{tr} \left[ \mathbf{b}^H \left( \theta_q, \boldsymbol{\Theta}_q^{(k)} \right) \mathbf{R} \mathbf{b} \left( \theta_q, \boldsymbol{\Theta}_q^{(k)} \right) \right], \quad (3.93)$$

where  $\mathbf{b}^H \left( \theta_q, \boldsymbol{\Theta}_q^{(k)} \right)$  is the unit vector given by

$$\mathbf{b}^H \left( \theta_q, \boldsymbol{\Theta}_q^{(k)} \right) = \frac{\mathbf{a}(\theta_q)_{\mathbf{A}(\boldsymbol{\Theta}_q^{(k)})}}{\left\| \mathbf{a}(\theta_q)_{\mathbf{A}(\boldsymbol{\Theta}_q^{(k)})} \right\|}. \quad (3.94)$$

Now,  $\mathcal{P}_{\mathbf{A}(\boldsymbol{\Theta}_q^{(k)})}$  is the only computational-heavy projection matrix that needs to be computed. The matrix appears in equation through  $\mathbf{a}(\theta_q)_{\mathbf{A}(\boldsymbol{\Theta}_q^{(k)})}$ , which corresponds to  $\mathcal{P}_{\mathbf{B}}$  in (3.90). The matrix is independent of  $\theta_q$ , i.e. constant over each one-dimensional search, and is therefore only needed to be computed once per iteration.

Without the projecting-matrix update formula, the needed projection matrix  $\mathcal{P}[\mathbf{A}(\boldsymbol{\Theta}_1^{(0)}), \mathbf{a}(\theta_2)]$  depends on  $\theta_q$ , and it will therefore be necessary to compute the matrix for each  $\theta_q$ -step in the one-dimensional search. This implies many computations per iteration, dependent on the resolution of the search grid.

### 3.3.6 Cramér-Rao bound

The Cramér-Rao bound (CRB) expresses a lower bound on the variance of estimators of a deterministic parameter. An unbiased estimator that attains this lower bound is said to be efficient. An efficient estimator attains the lowest possible mean square error (MSE) of all unbiased estimators. The CRB is in this way useful for performance evaluation of estimators.

For a given DOA vector  $\Theta$  and noise variance  $\sigma_n^2$ , the CRB on DOA estimation is given by [89]

$$\mathbf{CRB}(\Theta) = \frac{\sigma_n^2}{2} \left( \sum_{m=1}^M \text{Re} \left[ \mathbf{X}^H(t_m) \mathbf{D}^H \mathcal{P}_{\mathbf{A}(\Theta)}^\perp \mathbf{D} \mathbf{X}(t_m) \right] \right)^{-1}, \quad (3.95)$$

where

$$\mathbf{X}(t) = \text{diag}(s_1(t), \dots, s_Q(t)), \quad (3.96)$$

$$\mathbf{D} = [\mathbf{d}(\theta_1), \dots, \mathbf{d}(\theta_Q)], \quad (3.97)$$

$$\mathbf{d}(\theta) = \frac{\partial \mathbf{a}(\theta)}{\partial \theta}, \quad (3.98)$$

$$\mathcal{P}_{\mathbf{A}(\Theta)}^\perp = \mathbf{I} - \mathcal{P}_{\mathbf{A}(\Theta)}. \quad (3.99)$$

The CRB expression is a  $Q \times Q$  matrix with the diagonal elements representing a lower variance bound on  $\theta$  estimates, ordered corresponding to  $\Theta$ .

An expression for the asymptotic behaviour of the CRB can be derived. For sufficiently large  $M$ , the CRB is given by [89, 75]

$$\mathbf{CRB}(\Theta) = \frac{\sigma_n^2}{2M} \left( \text{Re} \left[ \left( \mathbf{D}^H \mathcal{P}_{\mathbf{A}(\Theta)}^\perp \mathbf{D} \right) \odot \mathbf{P}^T \right] \right)^{-1}, \quad (3.100)$$

where  $\odot$  denotes the Hadamard product, i.e. elementwise multiplication. This formula is easier to evaluate than the exact finite-case formula, and it provides good approximations to the exact CRB for reasonably large values of  $M$ .

With the assumed complex Gaussian noise and uncorrelated signals, it can be shown that the ML method provides a solution, which is theoretically very close to the optimum, evaluated on the Cramér-Rao bound [89, 90]. At the same time, ML can be very computationally intensive, due to the multidimensional search in connection to the log-likelihood maximisation in (3.83).



Since the impinging signals are assumed to be unknown deterministic signals, the derived ML estimator is known as the deterministic ML-method (DML). Another approach is to model the impinging signal waveforms as stationary, stochastic processes with some specified probability function. This approach leads to the stochastic ML-method (SML). Both methods provide consistent DOA estimates, but only the stochastic method is efficient. SML have shown to have better large sample accuracy than the corresponding DML estimates, but only in situations with low SNR, small number of sensors, and highly correlated signals.

### 3.4 Compressive Sensing

The methods described so far are in principle all based on the Nyquist-Shannon sampling theorem. In the following, we are going to describe a new sampling paradigm that goes against the well known Nyquist-Shannon theory, namely compressive sampling or sensing (CS). CS is a technique that is able to recover signals from data that is normally considered as undersampled, under the assumption that the data is sparse or compressible. A signal is sparse when it in some domain or space can be expressed by a few components, i.e. that it essentially only depends on a number of degrees of freedom, which is smaller than its length in the space where it is observed.

We will now describe CS from a mathematical point of view. The presentation is based on [91, 92, 37, 69].

A signal of interest  $\mathbf{x}$  with a length  $L$  is said to be  $K$ -sparse in an orthogonal basis  $\Psi$  if the projection coefficient vector  $\mathbf{s} = \Psi\mathbf{x}$  only has  $K$  nonzero or significant elements. The signal of interest  $\mathbf{x}$  can be represented as

$$\mathbf{x} = \Psi^H \mathbf{s}, \quad (3.101)$$

where  $\Psi$  is known as the sparsity matrix. A measurement vector  $\mathbf{y}$  with  $N$  measurements can be obtained by projecting the signal onto  $N$  random basis functions collected in the  $N \times L$  sensing matrix  $\Phi$ ,

$$\mathbf{y} = \Phi \mathbf{x}, \quad (3.102)$$

where  $N \ll L$  is the undersampled case of interest. By combining the sensing matrix and the sparsity matrix, the measurement vector can be expressed as

$$\mathbf{y} = \Phi \Psi^H \mathbf{s} = \Theta \mathbf{s}, \quad (3.103)$$

where  $\Theta = \Phi\Psi^H$  is called the mapping matrix. This corresponds to an underdetermined linear system, since the number of unknowns  $L$  is larger than the number of equations  $N$ , and hence no unique solution exists in the general case. However, when the signal is known to be sparse and when  $\Phi$  and  $\Psi$  satisfy a certain incoherency constraint, the CS theory ensures that it is possible to recover the signal uniquely from the samples.

The vector  $\mathbf{s}$  can be reconstructed from the measurements by finding the solution of (3.103), employing the least number of coefficients.

By using the notation  $\|\cdot\|_p$  to denote the usual  $L_p$ -norm, we can let  $\|\cdot\|_0$  denote the  $L_0$ -norm that merely counts the number of nonzero entries in the vector. By using this norm, the solution of (3.103) employing the least number of coefficients can be found as

$$\min_{\mathbf{s}} \|\mathbf{s}\|_0 \quad \text{subject to} \quad \mathbf{y} = \Theta\mathbf{s}, \quad (3.104)$$

which is equivalently maximising the number of zero coefficients in the  $\Psi$  basis, i.e. finding the solution that is "most" sparse.

For  $N = \mathcal{O}(K \log(L/K))$ , it can be shown that  $L_1$ -norm minimisation leads to the same result as  $L_0$ -norm minimisation [92],

$$\min_{\mathbf{s}} \|\mathbf{s}\|_1 \quad \text{subject to} \quad \mathbf{y} = \Theta\mathbf{s}. \quad (3.105)$$

This is convenient, since the  $L_1$ -norm is much more attractive when it comes to implementation.

In the case of noisy measurements, we got

$$\mathbf{y} = \Theta\mathbf{s} + \mathbf{e}, \quad (3.106)$$

where  $\mathbf{e}$  is a complex Gaussian vector with zero mean and uncorrelated elements. Instead of (3.105), the solution now comes from a threshold constraint of the measurement error

$$\min_{\mathbf{s}} \|\mathbf{s}\|_1 \quad \text{subject to} \quad \|\Theta\mathbf{s} - \mathbf{y}\|_2 \leq \varepsilon, \quad (3.107)$$

where  $\varepsilon$  is a small positive number, adjusted according to the noise level.

In order to find the unique sparse solution, the sensing matrix and sparsity matrix must be mutually incoherent. The incoherence ensures that the highly localized sparse signal will be spread out in the entire sampling space and thus makes the signals insensitive to undersampling. The coherence between the matrices is defined as [92]

$$\mu(\Phi, \Psi) = \max_{k,i} \frac{|\langle \varphi_k, \psi_i \rangle|}{\|\varphi_k\|_2 \|\psi_i\|_2}, \quad (3.108)$$

where  $\varphi_k$  is the  $k$ th row from  $\Phi$ ,  $\psi_i$  is the  $i$ th column from  $\Psi$ , and  $\langle \cdot, \cdot \rangle$  denotes the inner product. The coherence is bounded by

$$\frac{1}{\sqrt{L}} \leq \mu(\Phi, \Psi) \leq 1. \quad (3.109)$$

When  $\mu$  is close to the minimum value  $1/\sqrt{L}$ , the two bases are completely different, i.e. high incoherence occurs. The greater incoherence of the basis pair, the smaller number of measurements is needed, which can be expressed by [92]

$$N \geq \mathcal{O}(\mu^2(\Phi, \Psi)KL(\log L)^4). \quad (3.110)$$

For the case of ice sounding where volume scattering can be neglected, the signal of interest is sparse in the object domain with up to four pointlike contributions corresponding to two reflection from the bedrock and two from the surface. This signal is therefore sparse in the identity orthogonal basis, i.e.  $\Psi = \mathbf{I}$ . The measurements are obtained by sampling the array. As seen earlier in terms of the steering vector, the sensing matrix  $\Phi$  is therefore the Fourier sampling matrix that can be shown to have the best incoherence property with the identity orthogonal basis  $\mathbf{I}$ .

In the undersampled case, we do not have a full Fourier matrix but a thinned Fourier matrix, corresponding to a subset of the Fourier samples. In order to guarantee sufficiently sparse reconstruction with a given thinned matrix, the mapping matrix  $\Theta$  need to follow the restricted isometry property (RIP) defined by

$$1 - \epsilon \leq \frac{\|\Theta \mathbf{s}\|_2}{\|\mathbf{s}\|_2} \leq 1 + \epsilon, \quad (3.111)$$

where  $\epsilon$  is the smallest positive number that makes the inequality true for all  $K$ -sparse vectors  $\mathbf{s}$ . The mapping matrix is said to obey the RIP of order  $K$  if  $\epsilon$  is not too close to one. When the RIP holds, the mapping matrix preserves the Euclidean length of  $K$ -sparse signals. This implies that  $K$ -sparse vectors is not mapped onto the null space of  $\Theta$ , which would make any recovery impossible.

The RIP can be utilised to evaluate the resolution properties of the CS estimate when it is used for the spectral analysis problem at hand. In order to resolve two sparse signals  $\mathbf{s}_1$  and  $\mathbf{s}_2$ , the RIP must be fulfilled for the pairwise distances, i.e.

$$1 - \epsilon \leq \frac{\|\Theta \mathbf{s}_1 - \Theta \mathbf{s}_2\|_2}{\|\mathbf{s}_1 - \mathbf{s}_2\|_2} \leq 1 + \epsilon. \quad (3.112)$$

By evaluating the inequality for a mapping matrix corresponding to an array of interest, over a given DOA range, the value  $\epsilon$  can be used as a measure for resolution [92].

It turns out that if the subset of Fourier samples from the full Fourier matrix are chosen at random, the resulting mapping possesses good incoherence properties and tends to fulfil the RIP to a large extent, relative to different systematic mapping matrix (array aperture) formations. This makes CS especially interesting for single-channel repeat-pass measurements, which are often used to form the array in the case of space-based systems. Here the measurements can be considered to be sampled uniformly at random along the baseline, due to variation in positions between each acquisition. This non-uniform sampling normally complicates the signal processing, but with CS this randomness leads to a more effective sensing mechanism. The ability of CS to reconstruct signals from undersampled data can be used to reduce the number of measurements, or to use the same number of measurements to form a larger effective array.

In [37], CS is used for tomographic reconstruction of the elevation dimension in an urban area with data from a spaceborne SAR, which is similar to the problem of tomographic SCS. The array aperture is formed by single-channel repeat-pass measurements and the signal for each volume cell can be described by a few pointlike scatters and can be considered as sparse. The performance of the CS method is compared with the ML estimator, where CS with respect to accuracy is close to ML while CS is found to be more robust against phase noise.

Since CS algorithms use  $L_1$ -norm minimization and regularization they are more computationally efficient compared to fully parametric  $L_2$ -norm methods as ML. CS does not need model selection including prior knowledge of the number of scatterers. Furthermore, CS does not suffer from self-cancellation artifacts as can be seen with CM.

### 3.5 DOA Simulation

The presented algorithms for DOA estimation is now compared through simulations and based on this, their applicability with respect to tomographic SCS is discussed.

The simulations are based on the Monte Carlo method for the scenario of two equal power signals impinging on a ULA with sensor spacing  $d = \lambda/2$ . The signals are simulated as uncorrelated by applying uniform random phase noise. Independent zero mean complex Gaussian white

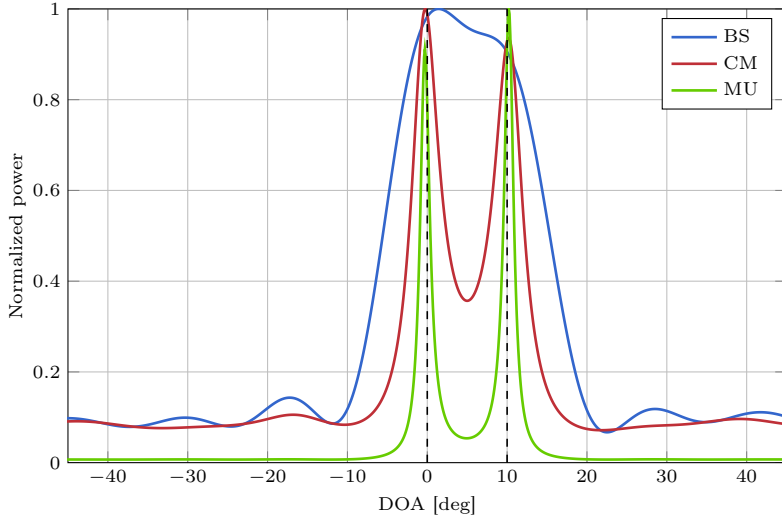


**Figure 3.5:** Spatial spectrum for a 10-element ULA and two impinging signals of equal power (dashed black). The SNR equals 0 dB and the number of snapshots is 100.

noise is added to each array sensor with a variance defined by the SNR. All simulations are based on  $10^5$  Monte Carlo iterations.

### 3.5.1 Resolvability

First resolvability of the spectral methods are considered. Figure 3.5 shows a single realization of a spatial spectrum estimated using the DOA algorithms BS, CM, and MU. The spectrum corresponds to a 10-element ULA, 0 dB SNR, and 100 numbers of snapshots. As seen from the figure, the signals are resolved by CM and MU in terms of two distinctive peaks. For BS, however, the peaks are merged into one and cannot be resolved. In this way, the two signals are in the following defined as resolved if the two largest peaks in the spatial spectrum corresponds to the true signal DOAs. For a realization where the error of one of the estimated DOAs is above ten times the CRB, it is classified as unresolved. Furthermore, if the estimated spectrum contains less than two peaks it is also classified as unresolved.

The probability of resolvability is in this study defined as the ratio between the resolved estimates and the number of Monte Carlo itera-

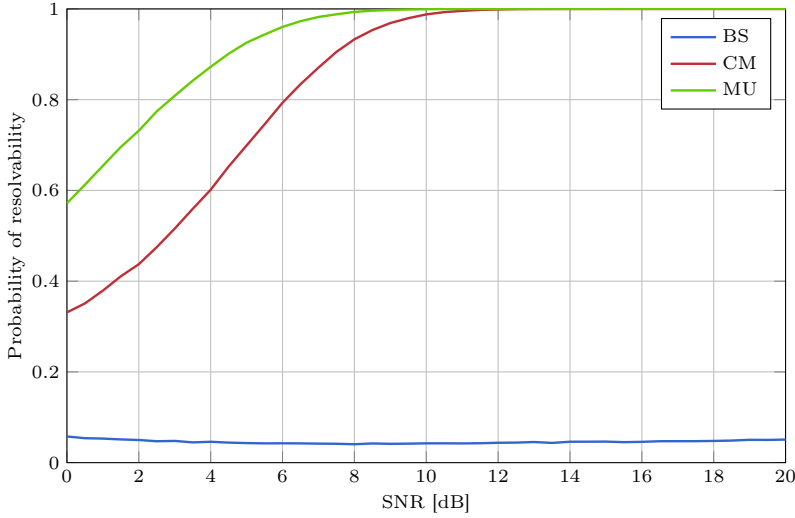


**Figure 3.6:** Resolvability for a 4-element ULA, 10 snapshots, and two signals impinging from  $0^\circ$  and  $20^\circ$ .

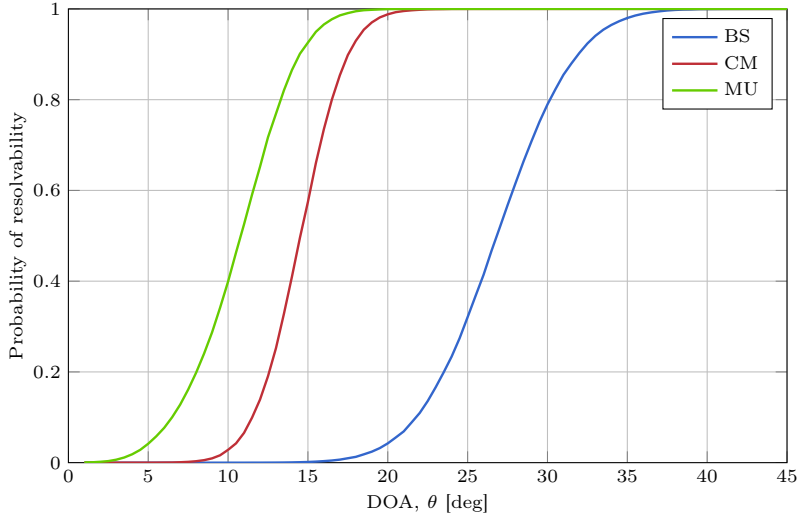
tions. Figure 3.6 illustrates the resolvability dependency on SNR for a 4-element ULA, 10 snapshots and two signals of equal power impinging from  $0^\circ$  and  $20^\circ$ . As expected the probability of resolvability increased with SNR for the super-resolution methods CM and MU, while it for BS is independent of SNR. The simulation shows that MU performs better than CM at low SNR.

Figure 3.7 illustrates the dependency on signal separation for the same configuration but with the SNR fixed at 10 dB. It is seen that MU is capable of resolving closer separated signals than CM. It is also seen how BS is able to resolve the signals when the separation becomes sufficiently large relative to the array length.

### 3.5.2 Accuracy

The accuracy of the algorithms is now investigated. The evaluation of accuracy is based on the root-mean-square error (RMSE) defined as

$$\text{RMSE} = \sqrt{\frac{1}{K} \sum_{i=1}^K |\hat{\theta}_i - \theta|^2}, \quad (3.113)$$



**Figure 3.7:** Resolvability for a 4-element ULA, 10 snapshots, 10 dB SNR, and two signals impinging from  $0^\circ$  and  $\theta$ .

where  $K$  is the number of Monte Carlo iterations,  $\hat{\theta}_i$  is the estimated DOA at the  $i$ th iteration, and  $\theta$  is the true DOA. The RMSE corresponds in this way to the sample standard deviation of the estimator. All simulations are based on two signals where one of these are impinging from  $0^\circ$ . The RMSEs simulated and presented in the following corresponds to this signal.

First the accuracy of the DOA algorithms are assessed in gentle conditions where the probability of resolvability is 1. Such a scenario is simulated in Figure 3.8 in terms of a 10-element ULA, 20 snapshots, and two signals impinging from  $0^\circ$  and  $20^\circ$ . The RMSE is plotted as a function of SNR along with the CRB. It is seen that RM and MU are indistinguishable and very close to the CRB. ML is very similar but performs slightly better at the lower SNR values. A more pronounced underperformance is observed for CM at low SNR while it at higher SNR approaches ML, MUSIC and the CRB. The worst performance is obtained with BS that for increasing SNR approaches a high constant RMSE value and not the CRB as the super-resolution algorithms.

In the difficult conditions with low SNR, few snapshots, small signal separations, and a small array, the accuracy analysis can be mislead-

ing for the spectral methods due to the low probability of resolvability. Therefore, for this part of the parameter space the analysis is carried out only for the non-spectral methods in terms of RM and ML that do rely on peak analysis. The accuracy is evaluated with respect to SNR, snapshots, and signal separations. The results are presented in Figure 3.9, Figure 3.11, and Figure 3.10. In all three simulations MUSIC performs significantly worse than ML at the difficult (low) end of the parameter ranges while the performances become indistinguishable for more gentle conditions. ML, on the hand, stays reasonable close to the CRB in the difficult conditions.

### 3.5.3 Discussion

As already discussed in relation to signal estimation in Section 3.2.6, BS is a simple and efficient algorithm but suffers from poor resolution. Although the resolution is greatly improved with CM, it is still limited by the size of the antenna array. With parametric methods it is possible to more fully exploit the structure of data, if such information is known. It can be shown that ML provides a solution that theoretically is very close to the optimum [89], but for the prize of a high computational load, even when the alternating projection scheme is applied.

In large sample cases, MUSIC approaches ML and in some cases performs slightly better [90]. However, ML is in general superior to the subspace methods regarding performance, especially in cases with low SNR or when the number of snapshots is small as seen in the Monte Carlo simulations. In cases where the number of snapshots is smaller than the number of sensors or where the impinging signals are fully correlated, the subspace methods and CM fail completely, while ML handles this without any difficulty [86].

The relation between the ML estimator and the subspace methods can be seen by rewriting the eigen-decomposition of  $\mathbf{R}$  from (3.55)

$$\mathbf{R} = \sum_{n=1}^N \lambda_n \mathbf{u}_n \mathbf{u}_n^H, \quad (3.114)$$

where  $\mathbf{u}_n$  is the  $n$ th eigenvector, i.e. the  $n$ th column of  $\mathbf{U}$ . The DOA likelihood function from (3.83) can be rewritten using this eigen-decomposition [86]

$$\mathcal{L}_{\Theta} = \sum_{n=1}^N \lambda_n |\mathcal{P}_{\mathbf{A}(\Theta)} \mathbf{u}_n|^2. \quad (3.115)$$



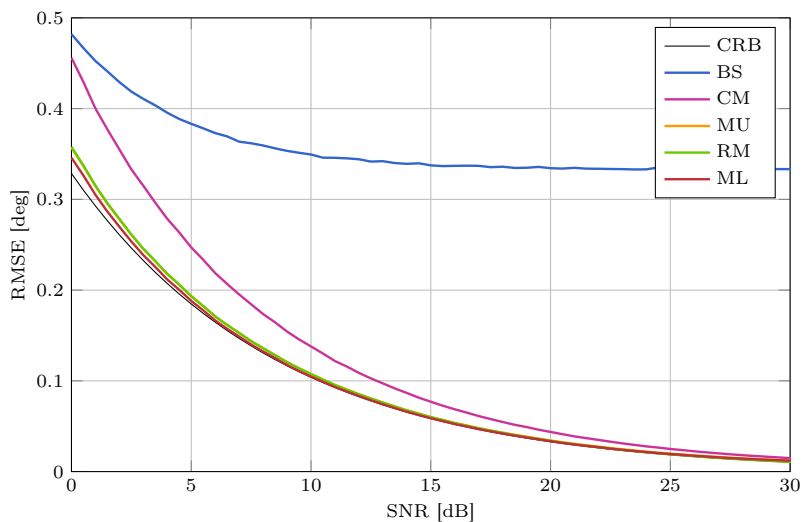


**Figure 3.8:** DOA algorithm accuracy for a 10-element ULA, 20 snapshots, and two signals impinging from  $0^\circ$  and  $20^\circ$ .

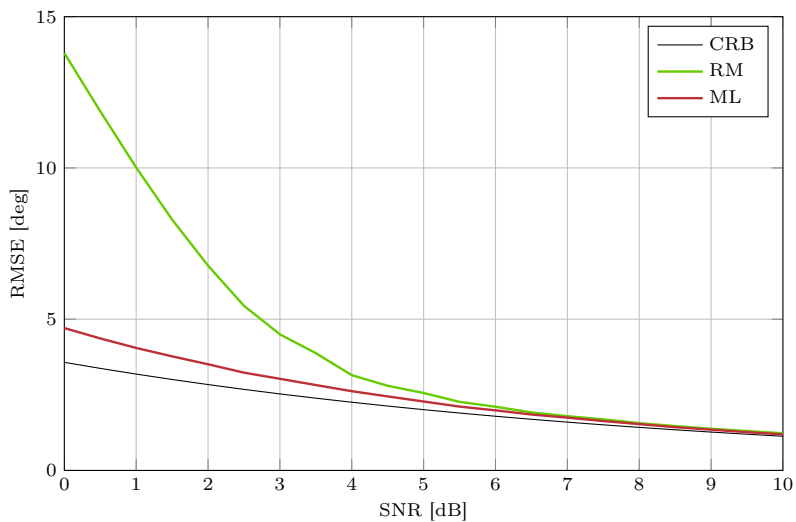


**Figure 3.9:** DOA algorithm accuracy for the same configuration as in Figure 3.8 but with a 4-element ULA and 10 snapshots.

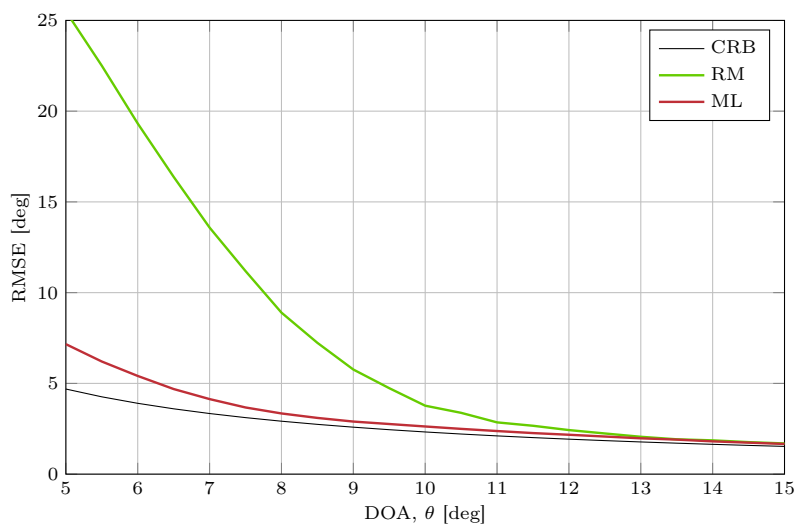


**Figure 3.10:** DOA algorithm accuracy for a 4-element ULA, 10 snapshots, 10 dB SNR, and two signals impinging from  $0^\circ$  and  $\theta$ .

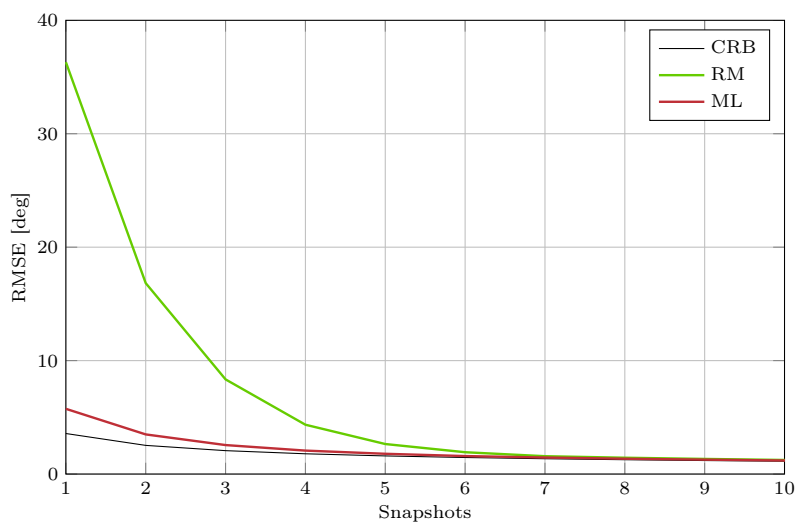


**Figure 3.11:** DOA algorithm accuracy for a 4-element ULA, 20 dB SNR, and two signals impinging from  $0^\circ$  and  $20^\circ$ .

This expression shows that ML, in contrast to the subspace methods, involves all eigenvalues and eigenvectors from the eigen-decomposition of  $\mathbf{R}$ . This is conducted in a way such that eigenvectors with a high eigenvalue are the most important. Intuitively, when ML utilises all available eigen-information, it makes sense that ML in general performs better than the subspace methods, which only use a part of the available eigen-information.

Computationally, the subspace methods including MUSIC are simpler and more efficient than ML. Therefore, in simple scenarios with large signal separation and high SNR, or when the signal statistics are varying slowly in azimuth such that a large number of snapshots can be used for the estimation of the covariance matrix, MUSIC is the appropriate algorithm choice. This is particularly the case when a ULA is used where the root variant of MUSIC can be applied. This algorithm is even more efficient and is also attractive with respect to implementation since peak analysis of the spatial spectrum can be avoided and the risk of outliers due to the lack of resolvability is eliminated. On the other hand, in the case of a non-uniform array, ML still has the advantage of this direct parametric estimation.

Common for both ML and the subspace methods is that they all need prior information on the number of spectral components in the signal, i.e. the number of impinging signals. However, in unknown or complex sounding scenarios accurate information on the signal structure may be difficult to obtain. Incorrect assumptions of the covariance structure can result in erroneous estimates using parametric methods. In such cases, non-parametric methods may be preferred, in spite of the suboptimal performance. In these instances, the non-parametric method of choice would be CM due to its superior performance compared to BS.

When it comes to multi-path sounding, CS is very interesting. For scenarios where the signal after along-track SAR processing can be assumed sparse, the CS framework is theoretical applicable. This could be in the case of strong surface clutter, but also at low-altitude acquisition for swath imaging of the bed topography. The variation and randomness in the multi-path baselines contribute to increased probability of recovery. CS possess a number of desirable properties where the ability to perform tomographic reconstruction for  $d > \lambda/2$  without knowing of the number of impinging signals is of particular interest.

## Multi-Phase-Center Ice Sounding Data

The sources of multi-phase-center ice sounding data is very limited. CReSIS has for some years acquired multi-phase-center data with MCoRDS/I while POLARIS is presently the only source of data in Europe. In this study data from both systems have been used for the investigation of tomographic surface clutter suppression. In the following the systems are described along with data sets used in the study.

### 4.1 POLARIS

POLARIS [8] is a nadir-looking, fully polarimetric sounding radar featuring aperture synthesis. The system is operating at P-band (435 MHz) and is developed by the Technical University of Denmark (DTU) for ESA. POLARIS is equipped with a multi-phase-center antenna and multi-channel receiver, which in its multi-aperture configuration supports single-polarization coherent surface clutter suppression through offline processing techniques.

In March 2008 the system was certified and functionally tested in Greenland with an installation on a de Havilland Canada DHC-6 Twin Otter aircraft with a 4-element antenna [93], as seen in Figure 4.1. In mid May 2008, a proof-of-concept campaign was carried out in Greenland with the aim of testing the newly integrated POLARIS system in terms of system functionality and technical performance [94, 48]. An additional campaign took place in 2009 which included data acquisition at the NEEM and NGRIP ice core drill-sites in the directions parallel and orthogonal to the ice flow for studying birefringence effects. The results of the campaigns demonstrated capabilities of profiling the bedrock



**Figure 4.1:** POLARIS 4-element antenna array: during assembly (top) and mounted under the fuselage of the DHC-6 Twin Otter aircraft (bottom).

at 3000 m depth. All data collected in the campaigns were acquired in polarimetric single-channel mode.

In 2010 POLARIS was upgraded with an 8-element (E0–E7) ULA of quadratic patches [95] aligned in the across-track direction, as pictured in Figure 4.2. The array elements are divided into four sub-apertures (A0–A3) each consisting of two neighbouring elements as shown in Figure 4.3. All elements are used for transmission with uniform weighting. POLARIS is equipped with a 4-channel receiver, where each receive channel is connected to one of the four sub-apertures of the upgraded antenna. The element spacing is 480 mm, but from an array signal processing point of view, the relevant parameter is the spacing of the effective phase centers corresponding to that of the sub-apertures, i.e.,  $d = 2 \cdot 480$  mm. This parameter corresponds to the sensor spacing in the signal model in Section 3.1.1. At the given operating frequency, this spacing corresponds to

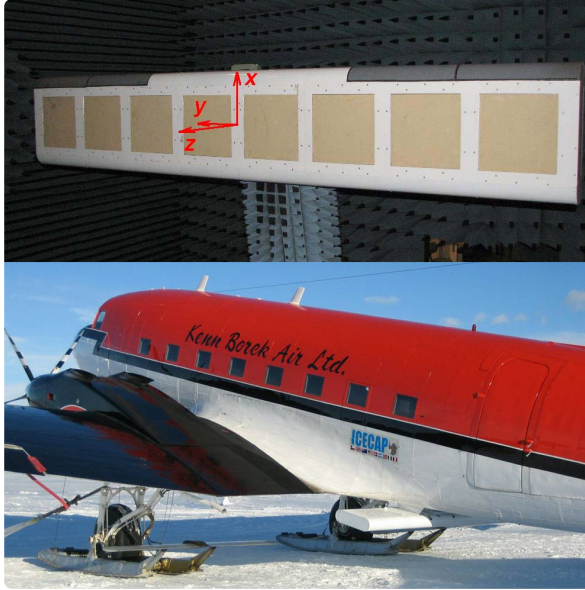


**Figure 4.2:** POLARIS 8-element antenna array: under measurement in the DTU-ESA Spherical Near-Field Antenna Test Facility at DTU (top) and mounted under the fuselage behind the wings of the Basler DC-3 aircraft (bottom).

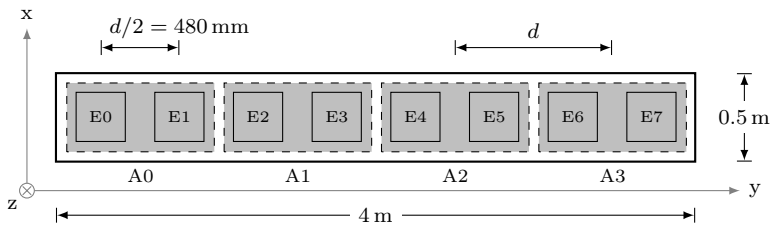


**Figure 4.3:** POLARIS 8-element antenna array showing how the elements (E0–E7) are combined into four sub-apertures (A0–A3).

**Table 4.1:** POLARIS parameters.

Center frequency	435 MHz
Max. bandwidth	85 MHz
Sampling freq.	250 MHz
Max. pulse length	50 $\mu$ s
Max. transmit PRF	20 kHz
No. of receive channels	4
No. of array elements	4/8
Polarisation <sup>1</sup>	quad, dual, or single
Element spacing	480 mm
Peak power	100 W

<sup>1</sup> In multi-aperture configuration, only single-polarisation is supported.

1.4 times the wavelength, which implies a grating lobe at  $\pm 45.9^\circ$  according to (2.63). Furthermore, a Nyquist DOA exists and equals  $\pm 21.1^\circ$  according to (3.26). In this way, any signal received from numerically larger angles is aliased.

POLARIS employs pulse compression using linear frequency modulation pulse chirping with a bandwidth of up to 85 MHz. The transmitted chirp is weighted with a Tukey time-domain window in order to suppress distant sidelobes of the compressed pulse [8]. The key parameters of the upgraded POLARIS system are presented in Table 4.1.

#### 4.1.1 Data Pre-processing

A time-domain back-projection algorithm [96] is used for the SAR focusing and geocoding. As opposed to frequency-domain based processing, this algorithm allows an accurate accommodation of surface slopes, sensor flight track variations, and refraction at the air–ice interface. The algorithm is shown to improve the quality of the focused data compared to conventional frequency-domain sounder processing, but at the cost of increased computational load.

Radar data are stored in a binary matrix in range line order, in complex IEEE single precision (32-bit) floating point, little-endian format. Complex samples are stored as two consecutive floats, real part followed by imaginary part.

The POLARIS system utilizes an Embedded GPS/Inertial Navigation (EGI) system for collecting navigation data. The GPS in the EGI

does not provide differential/kinematic GPS solutions, so absolute precision accuracy is that of standard non-differential GPS, i.e. several meters. However, during offline processing, accurate kinematic GPS data are used to refine the navigation data. Navigation data are also stored in a binary file for each phase center with a record of position, velocity, and attitude for every line of radar data.

There are no headers in either the radar or navigation data—all auxiliary information is stored in a separate configuration file. Further details on the pre-processing and data formats can be found in [97].

#### 4.1.2 Geocoding

The focused data are processed directly to a spatial regular geocoded grid along the actual flight track, accounting for ice refraction using a constant index of refraction. In this study, POLARIS data are often processed, analysed and presented in a  $(s, c, h)$ -coordinate system [98] aligned with the flight track.  $(s, c, h)$ -coordinates are curvilinear coordinates defined on a sphere that locally approximates the reference ellipsoid, where  $s$  is the along-track coordinate,  $c$  is the across-track coordinate, and  $h$  is the altitude above the reference sphere. The origin of the coordinate system is set at the midpoint of the nominal flight track. The radius of the approximating sphere is chosen as the radius of curvature of the WGS84 reference ellipsoid in the along-track direction, evaluated at the origin.

#### 4.1.3 Data Campaign

In February 2011 POLARIS was deployed in Antarctica [99] as part of the IceGrav campaign, where it was flown on a Basler DC-3 aircraft of Kenn Borek Air Ltd. Data were acquired in Queen Maud Land and over Adelaide Island at the Antarctic Peninsula with the objective to provide a dataset suitable for an assessment of space-based sounding in terms of:

1. the attenuation of P-band signals in various ice types,
2. the ability to detect deep internal ice layers,
3. the potential of radar polarimetry for the observation of ice anisotropy, and
4. the suppression of surface clutter by means of novel multi-phase-center techniques.



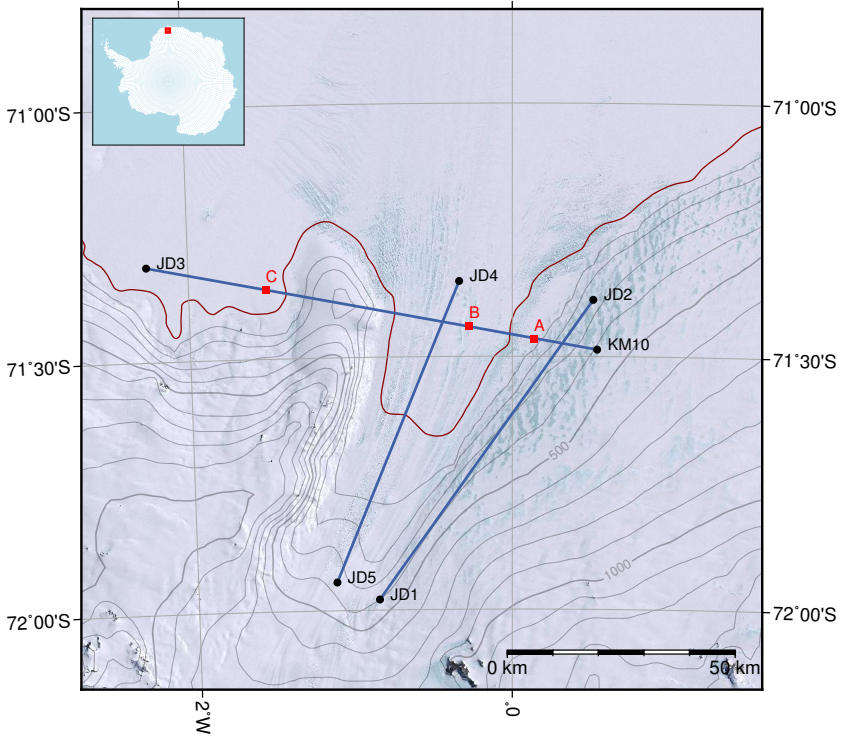


**Figure 4.4:** Overview map with flights track for the acquired POLARIS data over the Jutulstraumen Glacier. Imagery is from the Landsat Image Mosaic of Antarctica (LIMA) [100]. Grounding line (dark red) is from the ASAILD project based on Landsat-7 imagery and ICESat/GLAS laser altimetry [101]. Contours are generated from 2-Minute Gridded Global Relief Data (ETOPO2).

To comply with the last item, multi-phase-center data were acquired over the Jutulstraumen Glacier. Three nominal flight tracks were defined as illustrated in Figure 4.4. Two of the tracks are parallel to the glacier flow while the last track is perpendicular. For the perpendicular track, data from four passes were acquired—two from each direction as presented in Table 4.2 where designations of the tracks are also defined.

NS1 is acquired along the edge of the rising grounded ice sheet which implies a surface slope in the across-track direction. This results in an asymmetric clutter geometry that is useful for algorithm development

**Table 4.2:** Jutulstraumen data inventory.

ID	Waypoints	Passes	Remark
NS1	JD2 $\rightarrow$ JD1	1	across-track slopes with grounded ice
NS2	JD4 $\rightarrow$ JD5	1	upstream profile along the glacier tongue
EW	KM10 $\rightarrow$ JD3	2	ice shelf, grounded ice, and glacier tongue
WE	JD3 $\rightarrow$ KM10	2	

and validation.

NS2 is acquired above the glacier starting at the floating tongue and provides an upstream profile ending inland, above the grounding line. A relative rough surface with minor crevasses are expected, which might imply increased surface clutter.

The results presented in the dissertation are mainly based on the WE/EW track. The four passes of the track are denoted EW1, EW2, WE1, and WE2. As seen in Figure 4.4, three locations are defined along the track: location A, B, and C. At the west end of the track, the scene consist of flat ice shelf. East of location C, the track passes over a peninsula with grounded ice followed by the perpendicular flowing glacier tongue. At the east end of the track the terrain starts rising in the form of the grounded ice sheet. For the ice shelf and the glacier tongue, the topographic variations are small corresponding to a symmetric clutter geometry. The track intersects both NS1 and NS2 which can be used for cross-track analysis and verification. The multiple passes constitute a dataset suitable for investigation of repeat-pass tomography. However, as seen in Figure 4.5, large varying baselines occur for some parts of the track, which may limit repeat-pass analyses to a few smaller segments of the track.

All multi-phase-center data are acquired in VV-polarization and shallow/deep sounding mode (SDS). In SDS mode, the radar alternately transmits short, high-bandwidth pulses and long, low-bandwidth pulses. The short pulses are designed to sound the surface and the upper part of the ice sheet, whereas the long pulses are designed to sound the bedrock and lower part of the ice. Different receiver gains and range windows are employed for the shallow and deep channels, where the range windows are usually designed to overlap. For the Jutulstraumen dataset, a pulse length of 2  $\mu$ s was used in combination with the maximum bandwidth of 85 MHz for the shallow mode, while 15  $\mu$ s pulse of 30 MHz bandwidth

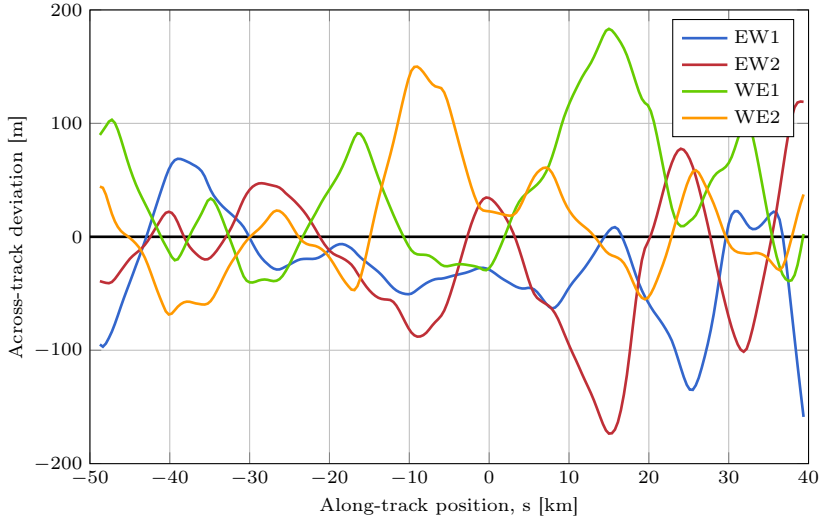


**Figure 4.5:** Horizontal baselines for the WE/EW track in terms of across-track deviation from the mean.

was used for the deep mode.

The data are range compressed using a Blackman-weighted matched filter. The pixel spacing in range is 1 m for the shallow data and 3 m for the deep data. The pixel spacing in the along-track direction is 1.5 m for both modes.

An echogram for the WE1 pass is shown in Figure 4.6 which includes annotation of the three defined locations.

#### 4.1.4 Transmit Antenna Pattern

During a re-configuration of POLARIS from polarimetric mode to multichannel mode, a  $180^\circ$  phase shift was erroneously introduced to the right-hand side of the array (A2–A3). This introduced a nadir null in the transmit pattern, i.e. corresponding to a notch pattern. The error was first discovered during the preliminary data analysis. The actual antenna pattern has been estimated from unfocused radar data acquired during roll manoeuvres. In Figure 4.7 the navigational roll data during such a manoeuvres are shown. The corresponding radar data are interpolated in the range direction, and the ice surface is estimated based on the intensity waveform in a suitable range window. The surface in-

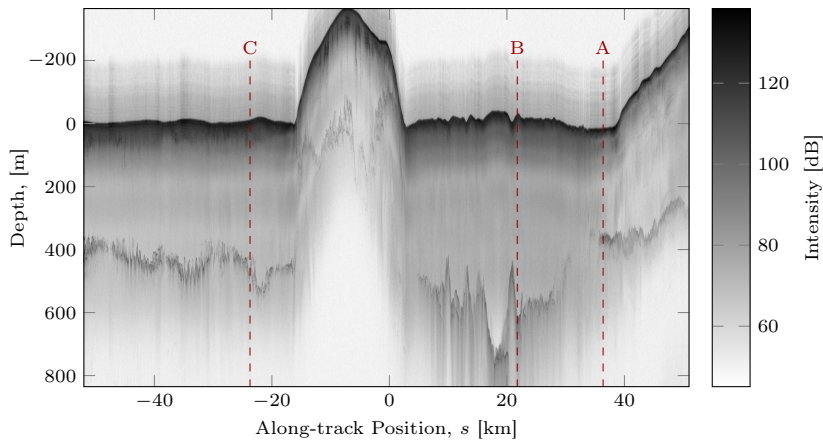


**Figure 4.6:** SAR focused echogram of the WE1 pass. The receive pattern is nadir looking, synthesized using beamsteering. The depth axis is relative to the mean surface elevation of the ice shelf.

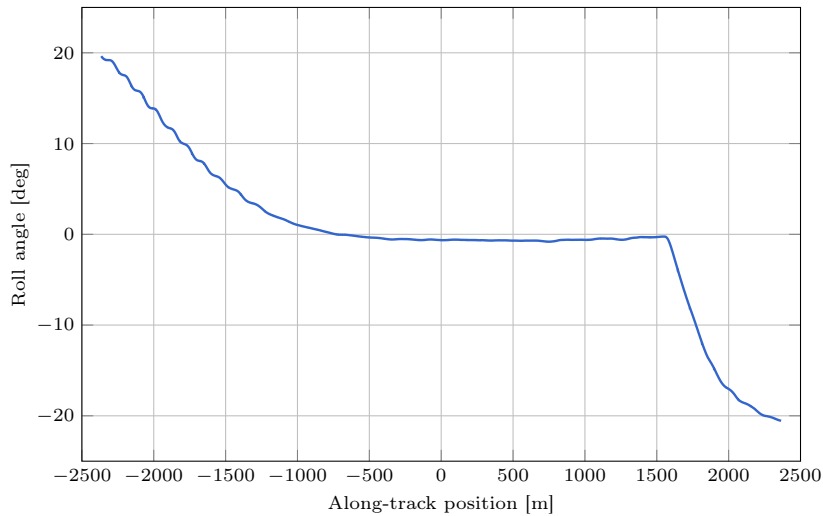


**Figure 4.7:** Navigational data for aircraft roll manoeuvre.

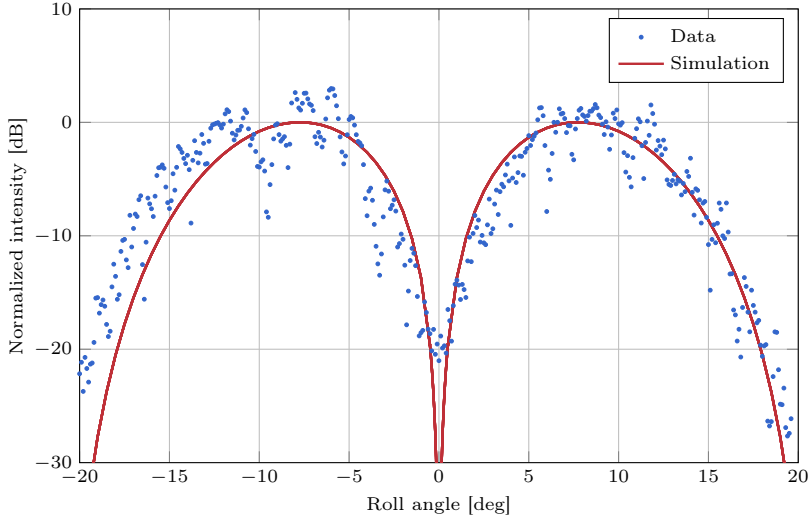


**Figure 4.8:** POLARIS transmit antenna pattern estimated from data.

tensity at a constant range gate relative to the surface is extracted in the along-track direction. The receive channels are combined using uniform weighting and without any phase correction, which corresponds to the two-way erroneous gain of the transmit pattern. The square root is taken to obtain the erroneous one-way gain. A scatterplot between the extracted surface intensity and roll angle is presented in Figure 4.8, which clearly shows the nadir null in the transmit pattern. Furthermore, a simulated pattern based on the assumed erroneous configuration is included in the plot, which is in good agreement with the data. The erroneous transmit pattern has been synthesized from measurements of the individual subapertures conducted in the DTU-ESA Spherical Near-Field Antenna Test Facility [102]. The pattern is synthesized by shifting the measured phase of the A2 and A3 apertures (Figure 4.3) by  $180^\circ$  and combining the steering vectors using unity weighting. The resulting pattern is shown in Figure 4.9 along with the desired nadir-looking pattern. As seen from the figure, the null of the actual pattern is narrow and with finite depth, so the nadir return is detectable but with reduced sensitivity.

The erroneous configuration also affects the reception. However, since the sub-apertures in multi-phase-center sounding mode are sam-

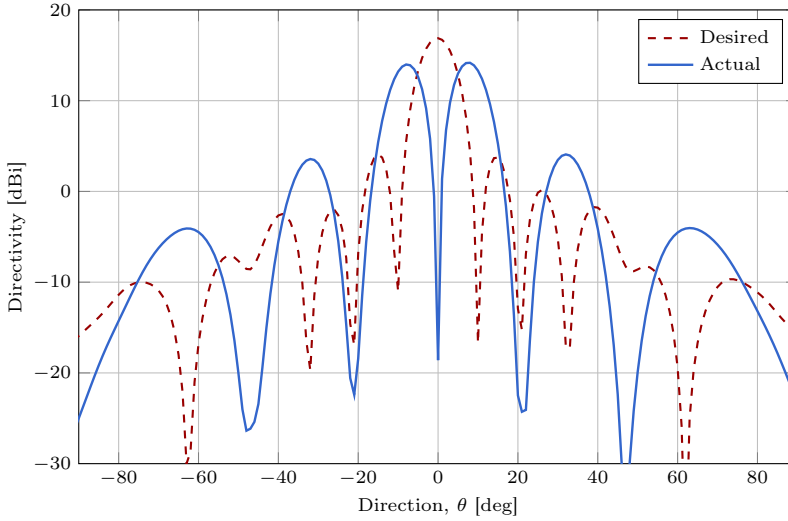


**Figure 4.9:** The actual (erroneous) and desired antenna patterns synthesized from measurements of the individual sub-apertures.

pled using multiple separate channels, the data can without any loss in performance be phase corrected during the offline post-processing.

#### 4.1.5 Receive Antenna Pattern

The antenna patterns for each of the phase-centers corresponding to those of the sub-apertures are 2-element ULAs, cf. Figure 4.3. The measured patterns of the sub-apertures are shown in Figure 4.10, including a simulation based on the array factor and an element pattern modeled as  $\cos \theta$ .

The simulated pattern has a null corresponding to the grating lobe of the full array. However, the nulls of the true receive patterns are displaced depending on the position of the sub-aperture in the array.

## 4.2 MCoRDS/I

The Multi-channel Coherent Radar Depth Sounder/Imager (MCoRDS/I) [103] is a high-sensitivity radar system developed for the collection of ice-sheet data by the Center for Remote Sensing of Ice Sheets (CRE-SIS) at the University of Kansas (KU).

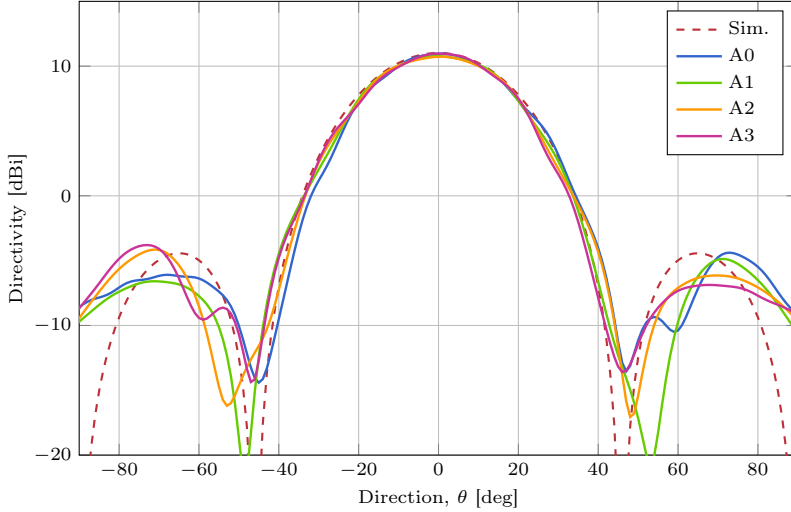


**Figure 4.10:** POLARIS receive antenna pattern, V-polarization.

### Jakobshavn Glacier

During the 2006 Greenland field mission, MCoRDS/I was installed on a DHC-6 Twin-Otter aircraft from de Havilland Canada Ltd. At this time, the system was referred to as the Multi-Channel Radar Depth Sounder (MCRDS) [24] and was operated at 150 MHz with a bandwidth of 20 MHz. The system was effectively configured with a 10-element antenna array of folded dipoles mounted in the across-track direction. The array was divided into two 5-element sub-arrays installed under each wing, as shown in Figure 4.11. The left wing sub-array was used for transmission and the right for reception. All elements in the transmit array were excited with uniform weights during transmission. The pulse length was 10  $\mu$ s with a total transmit power of 800 W. A multi-channel receiver was used to sample signals from each receive-antenna element individually. The spacing of the effective phase centers was approximate  $0.3\lambda$ .

Data acquired with the MCoRDS/I system in 2006 at the Jakobshavn Glacier are used for DOA analysis. The data were acquired according to the flight tracks shown in Figure 4.12. Results for a segment perpendicular to the ice flow are presented in this dissertation. The segment was flown northward and is highlighted in red in the figure. The altitude is



**Figure 4.11:** A photography showing the 5-element sub-array of folded dipole elements mounted under the right wing of the Twin-Otter aircraft.

approximately 750 m above the ice surface.

A linear frequency-modulated chirp is used for transmitted pulses to employ pulse compression. The received data are compressed using a matched filter with frequency-domain Hanning window to suppress range sidelobes. The frequency-wavenumber (F-K) focusing algorithm that exploits the Fast Fourier Transform (FFT) for computational efficiency is used for the SAR processing. By using pulse compression and SAR processing, a nominal resolution in range and azimuth of 25 ns (7.5 m in air) and 5 m, respectively, is obtained.

An echogram corresponding to the flight track based on nadir-looking BS is shown in Figure 4.13. For the given combination of altitude and pulse length, the radar is still transmitting when the first surface echo arrives at the radar. Since reception is first initiated after transmission is complete, only a part of the signal bandwidth for the surface and near-surface volume is received. Instead the received data are zero padded in order to obtain a partly compression. Since the convolution procedure does not represent a matched filtering for this region the compression is suboptimal and with reduced resolution due to the limited bandwidth. The distinctive transition in range at  $2\ \mu\text{s}$  is related to the zero padding while the defocused surface of high intensity is seen slightly below at  $2.5\ \mu\text{s}$ . The surface-parallel feature at  $7.5\ \mu\text{s}$  is a multiple surface return.



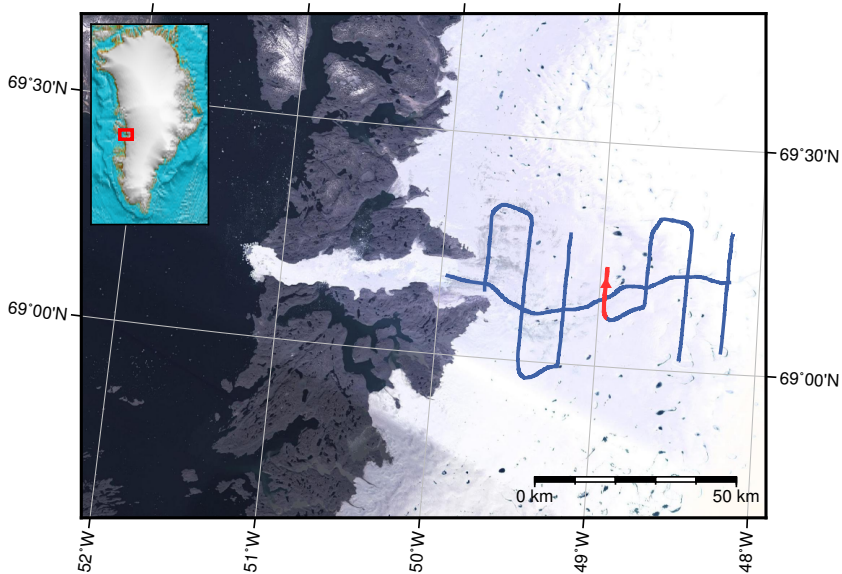


**Figure 4.12:** Flight tracks over the Jakobshavn Glacier at the west coast of Greenland in the 2006 field season.

Two regions of interest is marked in the echogram in terms of the glacier channel (Z1) and a part of the bedrock (Z2).

The bedrock appears strong at each side of the channel. Strong surface clutter is evident in Z1 and in particular below the bedrock at 1–2 km along-track. The bedrock in the channel becomes indistinguishable from the clutter and is to a great extent undetectable.

### North Greenland

In 2012, data over the northern part of Greenland were acquired with MCoRDS/I according to the flight tracks shown in Figure 4.14. The system was installed in the NASA P-3B aircraft and operated at 195 MHz with a bandwidth of 30 MHz. With similar processing as for the 2006 dataset, a nominal resolution in range and azimuth of 16.7 ns (5 m in air) and 5 m is achieved. Data were acquired in SDS mode with pulse lengths of 1  $\mu$ s and 10  $\mu$ s. A 7-element array mounted under the fuselage was used for transmission with a peak power of 1500 W. The individual elements of the same array were sampled using a multi-channel receiver during reception.

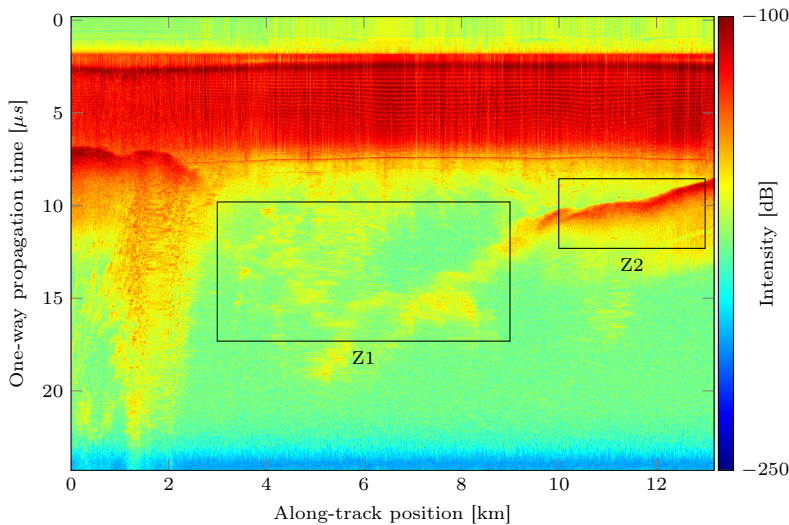


**Figure 4.13:** Echogram based on coherently averaging of the receive channels. The black rectangles show regions of interest: glacier channel (Z1) and bedrock (Z2).

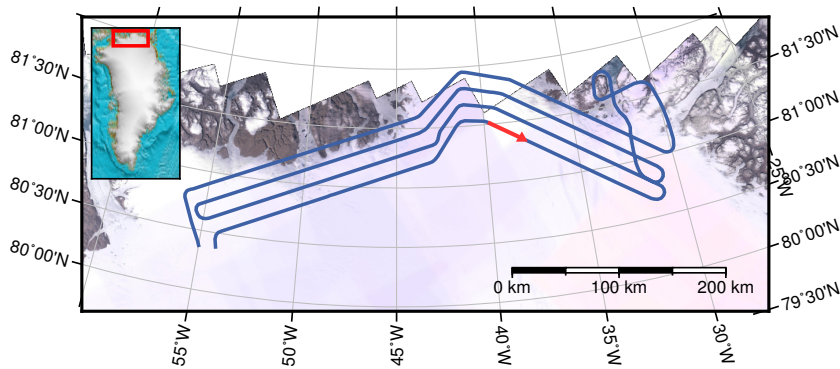


**Figure 4.14:** Flight track at the northern part of Greenland.

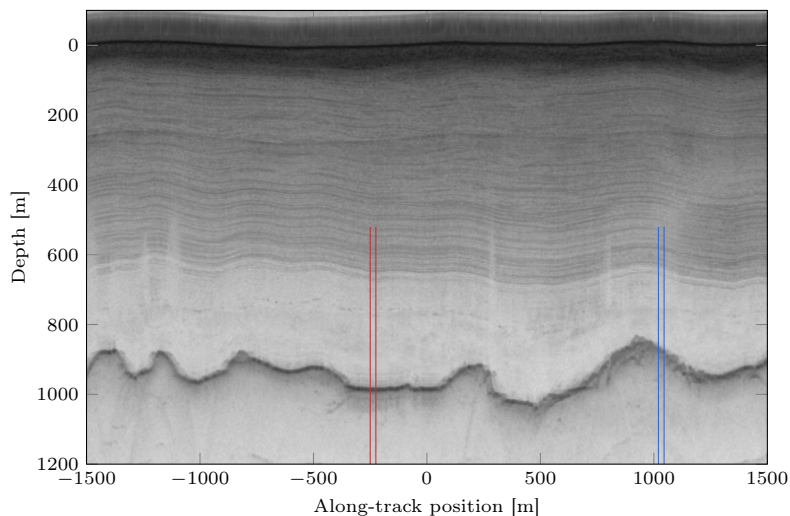


**Figure 4.15:** Echogram with smooth (red) and rough (blue) bedrock.

Figure 4.15 shows an echogram at ( $81^{\circ}26'N$ ,  $38^{\circ}52'W$ ) from the red segment in Figure 4.14. The echogram is a composite of the shallow and deep channel, and is formed by coherently averaging the channels corresponding to a nadir-looking receive pattern. The mean altitude corresponding to the echogram is 470 m.

## Tomographic Processing

In this chapter, tomographic techniques in terms of DOA estimation and beamforming are applied to ice sounding data. Tomographic data analyses are conducted along with the presentation of several novel tomography-based techniques.

First the proposed theory related to spatial aliasing is validated based on POLARIS data and the applicability of the theory for unwrapping of spatial aliased signals is assessed.

### 5.1 Spatial Aliasing

In order to reduce the system complexity and development costs of a sounder, the number of receive channels are in general kept at a minimum. At the same time, a large antenna length in the across-track dimension with a large number of elements is desired for obtaining high gain and angular resolution. Therefore, multiple elements might be connected to each of the receive channels, and the resulting spacing of the effective phase centers can be up to several wavelengths. This implies ambiguities in terms of grating lobes or, when seen from a signal processing point of view, spatial aliasing, which complicates both DOA estimation and beamforming.

Based on the mathematical foundation of spatial aliasing formulated in Section 3.1.2, it is shown how the theory can be used to unwrap the DOA estimate of spatial under-sampled sounding data. The analysis is based on the spatial under-sampled POLARIS data at location A in the WE1 pass, as defined in Table 4.2 and Figure 4.4.

### 5.1.1 Unwrapping

A 2-signal ML DOA estimation, corresponding to the left and right clutter signals, is applied to each range bin in every line of the scene. A moving average of 21 snapshots in the along-track direction is used to estimate the covariance matrix. Following this procedure, the snapshots correspond to azimuth looks in SAR terminology. The ML estimator is chosen due to its superior theoretical performance. The regular sounding scenario is expected to be in good agreement with the signal model assumed, which makes ML estimator applicable from a theoretical point of view. The number of snapshots is found to be a good compromise between noise reduction and azimuth resolution such that quasi-stationary statistics can be assumed.

Recall the clutter DOA model and the definition of equivalent nadir depth from Section 1.3. The estimated DOA as a function of equivalent nadir depth at location A is shown in Figure 5.1. The estimate is an incoherent average over 350 lines (525 m in along-track), where each line has been roll corrected. Before averaging, the data are filtered as described in detail at the end of the subsection. Gaps in the curve indicate range gates with no valid data points. The figure also includes a simulation based on the flat surface model (1.1) corresponding to the geometry in Figure 1.2. The model is in the figure and in the following designated by  $\theta$ . The sensor height is estimated from the radar data as the range of the first surface return. A constant relative permittivity equal to 3.15 is assumed.

From (3.28) we get that the spatial Nyquist frequency corresponds to  $21^\circ$ . By inverting (1.1), this corresponds to an equivalent nadir depth of 134 m. Therefore, spatial frequencies corresponding to larger angles are aliased. According to this, an aliased version of the model is also included in the figure. Based on the data points from the 350 lines, the RMSE are calculated with respect to the aliased model. Before the calculation, extreme outliers defined as data points with opposite sign compared to the model, are removed.

Down to a depth of 75 m the estimate fits the model very well. As we get closer to the equivalent Nyquist depth, the estimate becomes noisy and starts deviating from the model. Below 200 m the noise again decreases and a deterministic signal is clearly estimated. Since the signal at these depths is undersampled, the estimate is corrected by shifting the positive and negative branch by an amount corresponding to  $\mp 2\pi$  in spatial angular frequency, respectively, according to (3.31). As seen from the figure, the corrected estimate is clearly in agreement with the model.

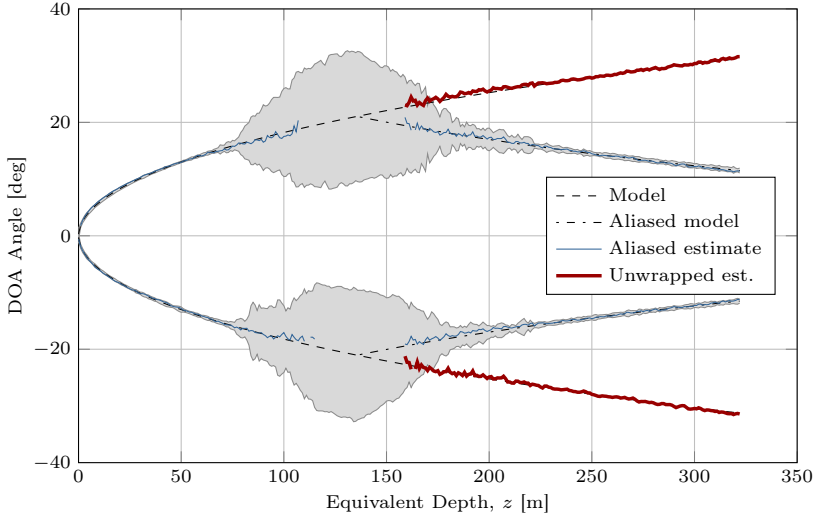


**Figure 5.1:** 2-signal ML DOA estimate from pass WE1 at location A with spatial aliasing (blue). The aliased part of the estimate is unwrapped and plotted separately (red). A simulation based on a flat surface model is shown with (black, dash-dotted) and without (black, dashed) aliasing. The estimate is an incoherent average over 350 lines (525 m) where plus-minus one RMSE w.r.t. the aliased model is represented by the gray shaded area. The sensor height above surface is 3350 m.

In this way, an aliased estimate of a regular scene can be unwrapped by using (3.31) and some rough prior knowledge of the topography.

The deviation around the Nyquist depth are caused by more factors. First of all, the first off-nadir null in the transmit antenna pattern coincides with the Nyquist angle. Therefore the surface return is highly attenuated around the Nyquist depth, which gives rise to increased noise. Furthermore, as the attenuation of the surface return is increasing, the near-surface volume scattering becomes more dominant. This will lower the effective scattering center, which results in smaller estimated DOA angles and thereby a deviation from the model. Thirdly, the signal model with the assumption of two signal components might in practice not be valid near the Nyquist depth due to noise combined with a limited angular resolution. In this way, only one effective signal component might be present, which can lead to the second signal estimated being artificial.

For these reasons, the data are filtered before the incoherent aver-

aging by removing any points that deviates more than 10% from the model. The threshold is chosen large enough such that the filtering does not affect the estimate outside the depth range from 75–200 m.

The data are also processed with root MUSIC which is found to provide a very similar performance compared to ML. However, at very small depths corresponding to closely separated signals, ML is seen to provide a slightly better estimate. This observation is in agreement with the theory and the simulations from Chapter 3.

## 5.2 Effective Surface Scattering Center

The same DOA estimation based on ML is repeated at location B, but now only considering the near-nadir part of the estimate that is non-aliased and undistorted. The estimate is seen as the blue curve in Figure 5.2. A clear systematic deviation from the model is evident at location B. It turns out that the deviation can be modeled by a scaling of the spatial model frequency. Motivated by this, a scaled spatial angular model frequency  $\tilde{\omega}_s$  is defined as  $\hat{\omega}_s$  from (3.23) divided by a given parameter  $a$ , i.e.,

$$\tilde{\omega}_s = a^{-1} \hat{\omega}_s, \quad a \in \mathbb{R}^+. \quad (5.1)$$

The scaled DOA model with a scaling parameter equal to  $a = 1.16$  is shown as the dashed curve in the figure, which is seen to fit the estimate very well. Based on this, the scaling parameter is considered as a measure of the deviation between the estimated DOA and the reference in terms of the flat surface model simulation.

The following analysis suggests that the deviation is related to a penetration depth of the clutter signal which is varying as a function of both along-track position and off-nadir angle. A scaling parameter  $a > 1$  means that the estimated spatial frequency, and thereby the DOA, is numerically lower than that of the model assuming pure surface scattering (Figure 1.2). For a given range cell, a smaller DOA corresponds to increased penetration in terms of a deeper located effective scattering center, as illustrated in Figure 5.3. The off-nadir penetration length is defined as

$$r_i = \frac{R - r_a}{\sqrt{\epsilon_{\text{ice}}}}, \quad R \geq r_a \quad (5.2)$$

where

$$r_a = \frac{h}{\cos \theta} \quad (5.3)$$

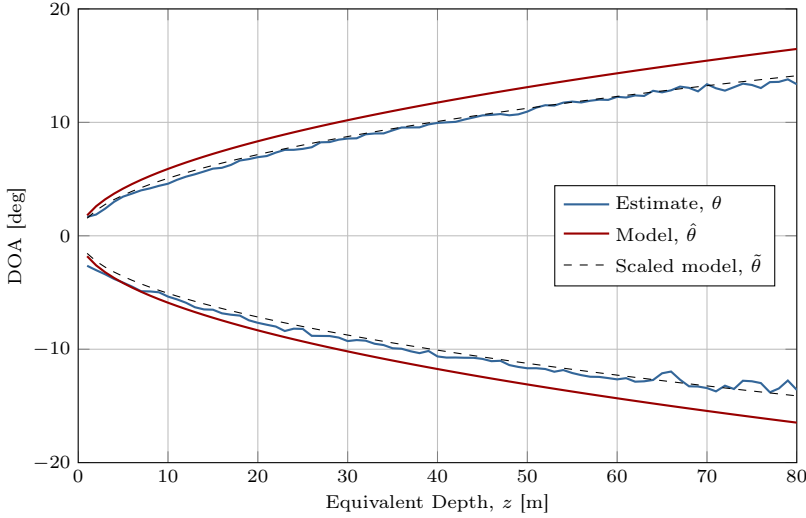


**Figure 5.2:** 2-signal ML DOA estimate from pass WE1 at location B (blue). A simulation based on a flat surface model is included (red) along with a corresponding spatial frequency scaled version that fits the estimate (black, dashed). The estimate is an incoherent average over 350 lines (525 m). The sensor height above surface is 3300 m.

is the range from the radar to the point of refraction at the ice surface. The penetration depth is then defined as the vertical projection of the penetration length

$$z_p = r_i \cos \theta_r \quad (5.4)$$

where  $\theta_r$  is the angle of refraction. In this way, the deviation in Figure 5.2 corresponds to the penetration depth shown in Figure 5.4. As seen from the figure, the DOA deviation at 80 m equivalent nadir depth corresponds to a 27 m vertical penetration of the surface signals.

Simulations are performed in order to access the impact of such penetration on surface clutter suppression based on DOA models. The simulations are based on NS with a SCR of  $-10$  dB, a sensor height above surface equal to 3300 m, two uncorrelated clutter signals from  $\pm 11^\circ$ , and are otherwise matching the parameters of the POLARIS system. The simulations show a 10 dB increase in the estimated intensity of the nadir signal for a 27 m uncompensated penetration of the clutter signals.



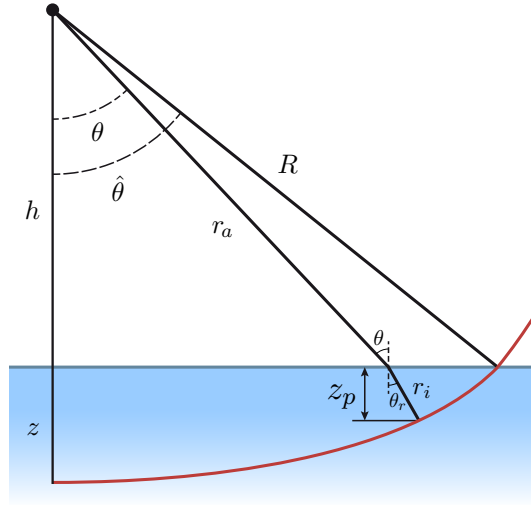


**Figure 5.3:** Geometry of the modeled and estimated DOA illustrating the corresponding penetration depth.

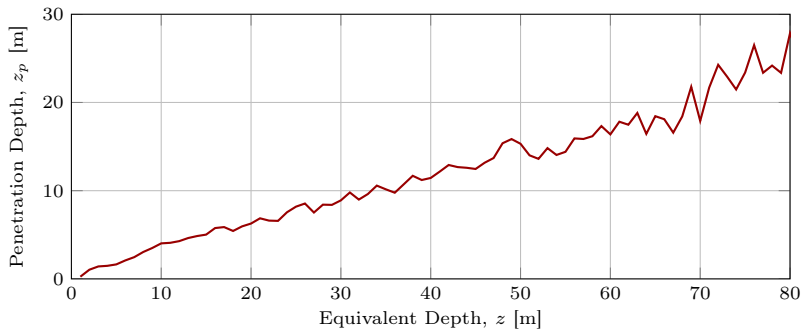


**Figure 5.4:** Penetration depth corresponding to the observed deviation of the DOA estimate at location B.

In order to test the hypothesis of an along-track varying penetration depth, the deviation along the entire track for all four passes is investigated. In order to do this, an automated fitting procedure is designed for the scaling parameter. The procedure is described in the following.

The first surface return in each line is detected and used to flatten the data with respect to nadir surface elevation changes. The DOA is estimated using the ML estimator with a 2-signal search based on 9 snapshots in the along-track direction. The DOA estimate is divided in the along-track direction into segments of 200 lines. For each segment, samples with an equivalent clutter depth between 10 m and 40 m are used to calculate the RMSE of the DOA estimate with respect to the scaled model, i.e.,

$$RMSE(a, \theta_{\text{offs}}) = \sqrt{\frac{1}{N} \sum_{n=1}^N (\theta_n - \tilde{\theta}_n(a) + \theta_{\text{offs}})^2} \quad (5.5)$$

where  $N$  is the number of samples,  $\theta$  is the DOA estimate,  $\tilde{\theta}(a)$  is the DOA predicted by the scaled model, and  $\theta_{\text{offs}}$  is an angular offset to handle any minor across-track slopes or uncompensated aircraft roll residuals. Both of the two surface signal DOA estimates are included in the RMSE calculation. The RMSE is then minimized with respect to the scaling and the offset parameter as a two-dimensional optimization problem. The scaling parameter minimizing the function is stored for the along-track position corresponding to the center of the segment, while the offset parameter is disregarded in the further analysis.

To be able to directly compare all four passes, the scaling parameter for each pass is resampled to a common grid. An  $(s, c, h)$ -coordinate system aligned with the flight track is defined with positive  $s$ -direction from JD3 towards KM10, i.e. eastward. An equidistant grid is now defined in the  $s$ -dimension of this system to which the data are resampled.

Since the flat surface model is inappropriate at the peninsula, the fitted scaling parameter is unreliable for this region. The corresponding data are therefore masked out in all plots and disregarded in the further analysis.

When the scaling parameter is considered as a function of along-track position, it is referred to as the *parameter signal*. The resampled parameter signal for WE1 is shown in Figure 5.5. The signal is seen to vary along the track in terms of a slow negative linear trend overlaid by some faster smaller variations including a number of distinctive spikes. To test the null hypothesis stating that the variations could be an artefact e.g.

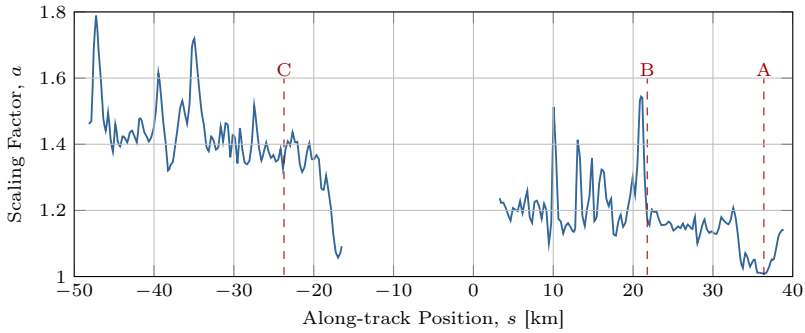


**Figure 5.5:** Scaling parameter for WE1 with the peninsula masked out.

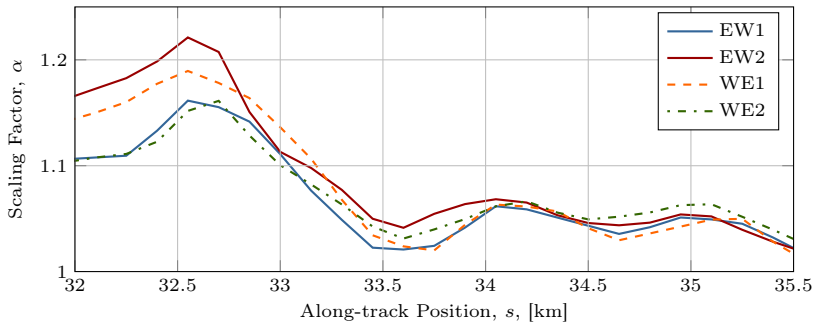


**Figure 5.6:** Zoom of the parameter signal for all four passes.

introduced by the system or related to the acquisition, the data from the different passes are mutually correlated. The moving average based on 100 datapoints (30 km) is subtracted from each parameter signal before correlating. The correlation coefficients of the mutual correlations are shown in Table 5.1. The coefficients vary from 0.62 to 0.90 between the different combinations suggesting that the parameter variation is not an artefact and therefore is related to the ice. A zoom of the parameter signal for all four passes is shown in Figure 5.6, which illustrates the correlation between the signals.

In addition to the mutual correlations of the different passes, the parameter signal is also correlated with the intensity of the radar reflection for each pass separately. The intensity signal is extracted in the along-track direction at a fixed range gate. Correlations are in this

**Table 5.1:** Correlation of scaling parameter between passes.

	EW1	EW2	WE1	WE2
EW1	1.00			
EW2	0.90	1.00		
WE1	0.62	0.63	1.00	
WE2	0.85	0.84	0.67	1.00

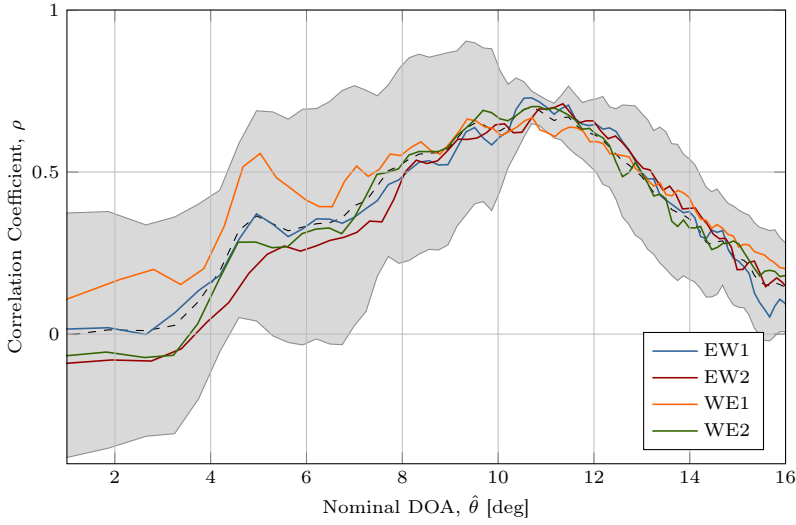


**Figure 5.7:** Along-track correlation coefficient of the scaling parameter and the radar reflection intensity for each pass. The independent variable (nominal DOA) represents the simulated off-nadir angle at which the intensity signal is extracted. The dashed black line is the average of the four passes. The gray shaded area represents the distance of plus-minus one standard deviation from the mean.

way performed for a number of range gates. The results are shown in Figure 5.7 where the range is expressed as the nominal DOA according to the flat surface model in (1.1). Before each correlation, the moving average is subtracted from both of the two signals.

To assess any along-track variation of the correlation coefficient, the signals are divided into non-overlapping segments of 100 datapoints

**Table 5.2:** Correlation of scaling parameter and radar intensity.

EW1	EW2	WE1	WE2
0.75	0.71	0.72	0.73

(30 km). Corresponding segments of the scaling parameter and the intensity are correlated and statistics based on all segments from all passes are calculated and presented in the figure. A large variation is observed for the near-nadir returns, while a relatively low variation is seen at larger off-nadir angles with a minimum around  $11^\circ$ . Beside the minimum variation, the correlation coefficients themselves attain a maximum at this same DOA. The correlation coefficients at this extremum are presented in Table 5.2. The relatively high correlation coefficients are strengthen the hypothesis of a relation between the ice characteristics and the scaling parameter.

The hypothesis of varying penetration as the underlying mechanism is supported by the three following observations.

Firstly, from Figure 5.5 it is seen that the scaling parameter is larger than one for all along-track positions, which is consistent with the occurrence of a lowered effective scattering center.

Secondly, the intensity waveforms at location A, B, and C (Figure 4.6) indicate different dominating scattering mechanisms, which can explain the variation in depth of the effective scattering center. The A-scopes for the three locations are shown in Figure 5.8. At location A, the shape of the two-way antenna pattern is clearly seen in the intensity. This indicates that the signal is dominated by scattering related to the air-ice interface, and therefore also is in agreement with the model ( $a \approx 1$ ). When looking at location B and C the scaling increases and the shape of the antenna pattern becomes less distinct. This indicates that the scattering is less dominated by an interface but rather volume scattering, which means larger penetration. The antenna pattern is smeared out in the case of volume scattering since the wave is reflected from a large DOA range, which makes the effective backscattering coefficient insensitive to a narrow null. The stronger peak with faster rise and fall times at location A is also characteristic for surface scattering. A larger specular component due to the smooth ice surface increases the received power at very small incidence angles, while increased forward-scattering decreases the backscatter power at larger angles.

Thirdly, the extremum at  $11^\circ$  in Figure 5.7 coincides with the first

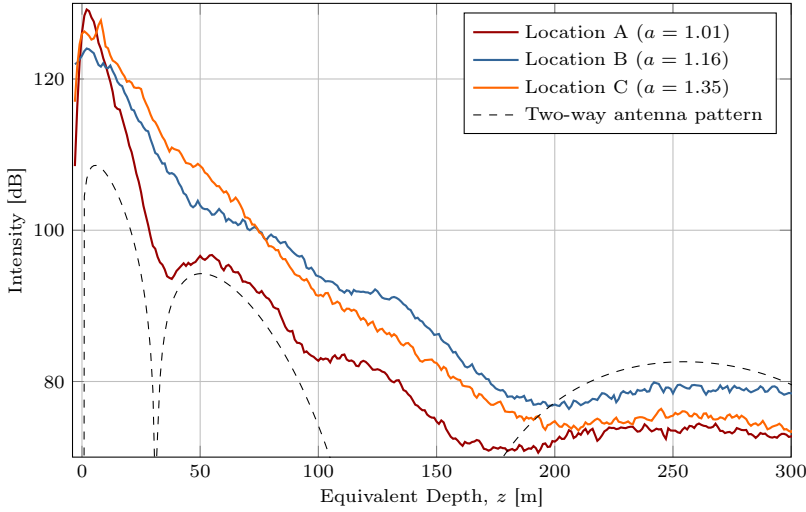


**Figure 5.8:** A-scopes at location A, B, and C in pass WE1. The receive pattern is nadir-looking, synthesized using beamsteering. Simulated normalized two-way antenna power pattern included for comparison.

null in the nadir-looking receive pattern, which corresponds to the dashed curve in Figure 4.9. This means that the extremum occurs where the gain towards the surface is low, which could indicate that the correlation is related to volume scattering. Since the correlation coefficients are positive, high intensity corresponds to a large DOA deviation and thereby a large penetration depth. This is consistent in the way that stronger volume scattering would be expected for a lowered effective scattering center.

The analysis suggests a relation between penetration depth and intensity. The interpretation of this is a glaciological aspect that will not be treated further in this dissertation.

### 5.3 DOA Representation of Radar Echograms

In the following, the DOA algorithms are utilized to obtain a novel alternative representation of the radar data. Consider the MCoRDS/I intensity echogram from Jakobshavn Glacier in Figure 4.13, which was generated by coherently averaging data from all receive channels corresponding to nadir-looking BS. The DOA is estimated for each pixel in

the echogram. The number of signal components to be estimated can be difficult to determine for the individual pixels. For this reason, and to simplify the processing and interpretation, the number of signal components are assumed to be one for all pixels, i.e.  $Q = 1$ , even though this is incorrect for some regions of the image. When this assumption does not hold, the DOA of the dominating signal component tends to be the one estimated, and in this way the estimate is still meaningful.

By presenting the DOA estimates as an image with the pixel color representing the DOA angle, the procedure can be considered as a DOA representation of the echogram. The DOA representation of the echogram from Figure 4.13 can be seen in Figure 5.9 and Figure 5.10 using MUSIC and ML respectively. The covariance matrix is estimated based on 5 snapshots, and the DOA images are filtered using a  $5 \times 5$  median filter to reduce noise and outliers. The low number of snapshots is chosen in order to ensure quasi-stationary statistics in the complex and rapidly changing clutter scenario. The array manifold, i.e. the set of steering vectors for the DOA interval of interest, is simulated [104] using the electromagnetic FEM simulation software package HFSS by ANSYS Inc., based on a combined model of the antenna elements and the aircraft.

The outputs of the two algorithms are similar with respect to the large-scale content. The DOA of the near-range pixels are estimated with small (numerical) values, while the DOA of the far-range pixels is large. Dark blue and dark red represent far off-nadir signals while green represents near-nadir returns. Parts of the ice-bed interface can be detected as an abrupt transition from large to small estimated DOA angles, where the dominating signal component changes from off-nadir surface clutter or noise, to the first (near-nadir) return from the bedrock. With respect to the small scale content, the MUSIC images are much noisier compared to the ML image. Furthermore, the ML image reveals large areas of off-nadir surface clutter that appears due to a change of sign in DOA angle compared to the background. The transition from ice surface/volume to bed is much more significant in the ML image. In both images, a distinctive color sweep-pattern in the estimated DOA angle is seen right after the first bed return. Again, the phenomenon is more pronounced in the ML image. Based on this visual comparison of the MUSIC image and the ML image, we conclude that the ML algorithm for this specific scene and clutter scenario is preferable for the further analysis.

The next two sections address observations in the DOA representation in terms of the detectability of the ice-bed interface, and the

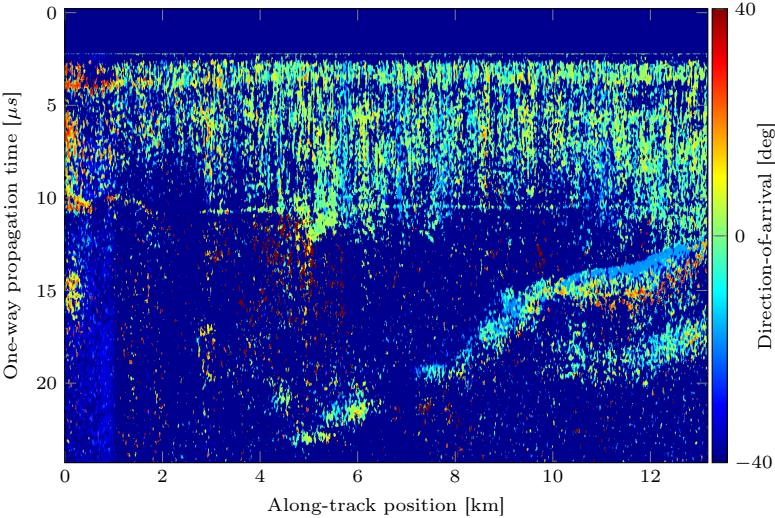


Figure 5.9: DOA image based on MUSIC.

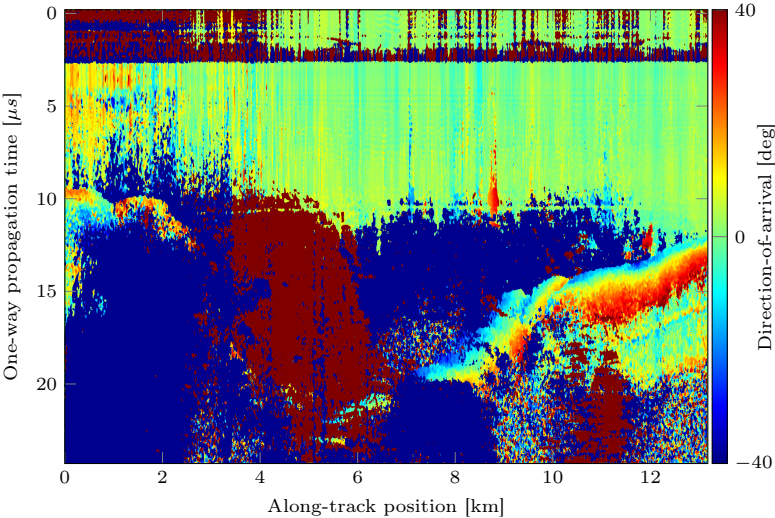
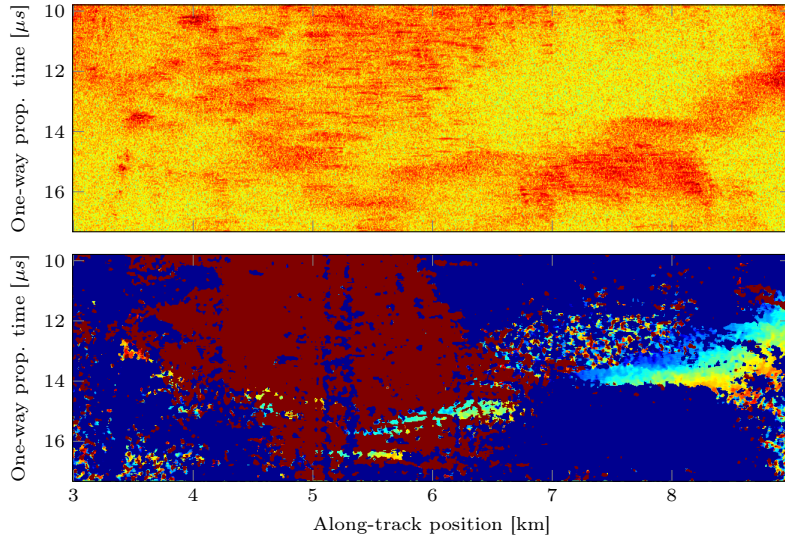


Figure 5.10: DOA image based on ML.





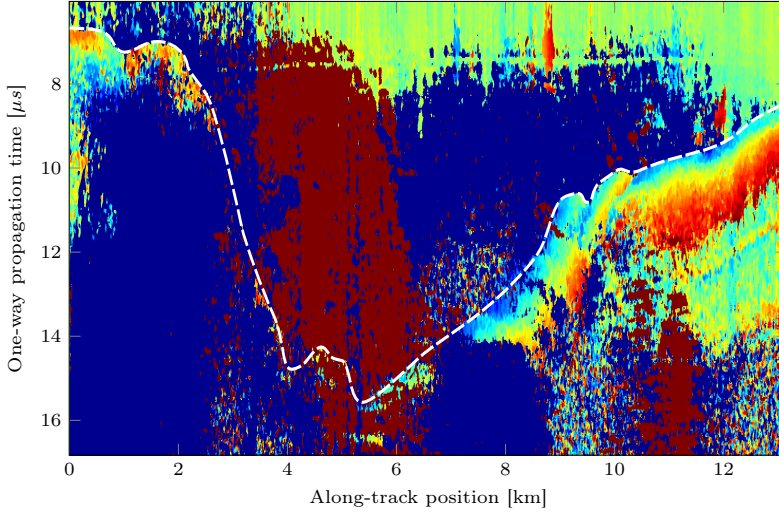
**Figure 5.11:** Enlargement (Z1) of glacier channel, echogram (upper) and ML DOA image (lower).

sweep-pattern in the estimated DOA angle at the bed.

#### 5.4 Recovery of Ice Bed Detection Gap

By examining the echogram in Figure 4.13, we can see that the subsurface returns are highly contaminated by surface clutter. The bedrock is detectable at the beginning and end of the frame (left/right of the glacier channel), but at the middle section (glacier channel), the weak bed-return cannot be discriminated from the clutter. Therefore, detection of the bed is not possible, which nevertheless constitutes an important data product in glaciological modelling.

Instead we consider the ML DOA representation for bed detection. In Figure 5.11 enlargements of the glacier channel in the echogram and DOA image are stacked for easy comparison. The colormap of the enlarged echogram is scaled to enhance the local features. It is seen that the bed signal can be discriminated from the clutter in the DOA image, which is not possible in the radar-intensity echogram. Even though the bed signal is flickering in the strong clutter region, the coverage is sufficient to perform a reasonable trace of the interface as illustrated in



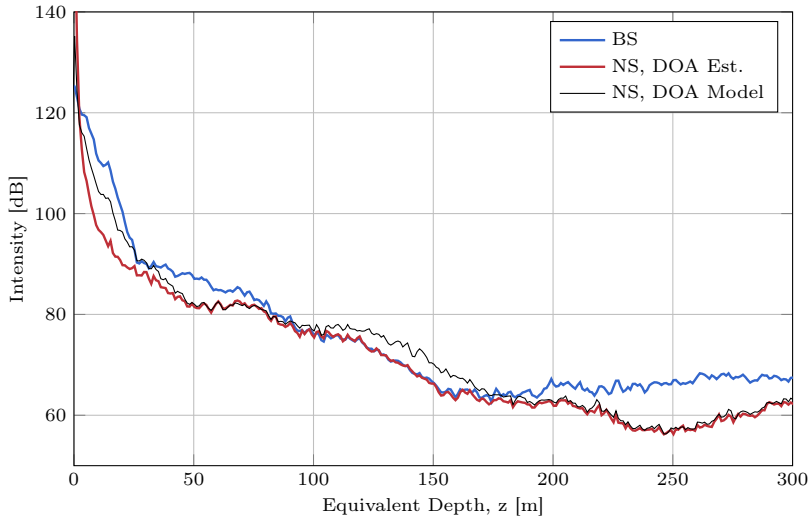
**Figure 5.12:** Bed detection (white, dashed) based on the ML DOA image.

Figure 5.12. The tracing is done by scanning each line through range until a significant discontinuity from off-nadir to near-nadir is detected. In the strong clutter region, the detection might be based only on a few pixels in range. The trace is interpolated at lines where no bed signal is present at all.

In this way the DOA image can be a powerful representation for discrimination and visualization of different types of targets, which can be used to interpret the echogram or for direct applications such as bed detection.

## 5.5 Clutter Suppression

Tomographic SCS will now be applied to radar data. First, an approach based on data-driven DOA estimation will be validated and assessed using POLARIS data at location A in the WE1 pass. The data have been processed with three suppression approaches, namely BS and two variants of NS. The NS algorithm has been chosen due to the regular and well-defined clutter scenario. In the case of BS, the beam has been steered towards nadir by coherently summing the channels corresponding to traditional single-channel sounding. NS has been used with both ML DOA estimated topography data, and flat-surface simulated topography data,



**Figure 5.13:** Surface clutter suppressed nadir waveform.

corresponding to the dashed curves in Figure 5.1. The resulting nadir power signals are shown as functions of depth in Figure 5.13.

It is seen how NS, applied with ML DOA data, suppresses a significant amount of clutter compared to BS, down to 85 m and between 200 m and 300 m. This is consistent with the surface clutter expected from the transmit pattern. In the interval between 85 m and 200 m the two curves coincide, which can be explained primarily by lack of surface clutter near the first null of the transmission pattern. The gain limits associated with this null is 0 dB and  $-3$  dB, respectively. It should be noted that DOA estimation from Figure 5.1 is also used for this interval, as for the "valid" segments, even though the estimate does not describe the true surface. This makes sense, since the DOA estimation describes the dominating off-nadir clutter.

The ML SCS algorithm applied with simulated DOA data is seen to provide suppression similar to that of the ML DOA variant, except for the region around the first null where the performance of the simulation based variant is inferior, presumably due to volume clutter. The performance is also inferior near nadir where the SCS algorithm is highly sensitive to DOA angle deviations.

Tomographic SCS based on data-DOA estimation has been applied to

data acquired with POLARIS over Antarctica. The DOA estimation for a flat surface has been verified by comparison with simulations. Both simulated and estimated topography data have been used for SCS by means of the ML algorithm. The SCS results seem to be consistent with the expected SCR pattern. Both approaches are successful but a superior result is obtained by estimating the topography using the data-driven approach.

### 5.5.1 Echogram Processing

Now the tomographic SCS technique is demonstrated on a full data frame for a complex clutter scenario in terms of the Jakobshavn dataset. The data are processed both with BS and CM. BS is nadir-looking and represents the echogram obtained with a traditional single-channel system. CM is chosen due to the complex surface topography and thereby complex clutter scenario. In the CM processing, nadir is specified as the direction of interest. The echogram based on BS and CM are seen in Figure 5.14 and 5.15, where 11 snapshots in azimuth are used for estimation of the covariance the covariance matrix. By visually comparing the echogram it is seen how CM successfully has suppressed the clutter to a great extend resulting in a more clean echogram. However, when considering the bedrock at the end of the track (Z2 in Figure 4.13), the intensity is lower with CM corresponding to a factor of  $-10$  dB. This observation is presumably due to self-nulling since the signal is spatially broadbanded and impinges from an off-nadir direction according to the DOA analysis in Figure 5.10.

## 5.6 Summary

Experimental multi-phase-center data acquired with the POLARIS system over Jutulstraumen Glacier have been analyzed and validated. Based on the dataset, the capability of supporting advanced array signal processing in terms of DOA estimation has been demonstrated for the system. Spatially under-sampled sections of the dataset are used for validation of the spatial sampling theory, which is used to successfully unwrap aliased surface returns. The problem of spatial aliasing is relevant in relation to future ice sounding systems. It may be necessary to used a large spacing between the effective array phase centers, despite the possibility of spatial under-sampling, to reduce system complexity while maintaining a large antenna length.

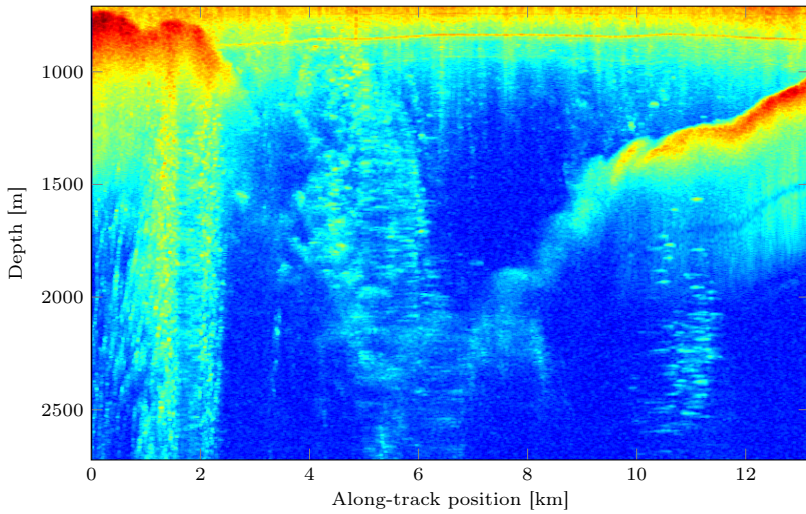


**Figure 5.14:** Echogram based on beamsteering processing.

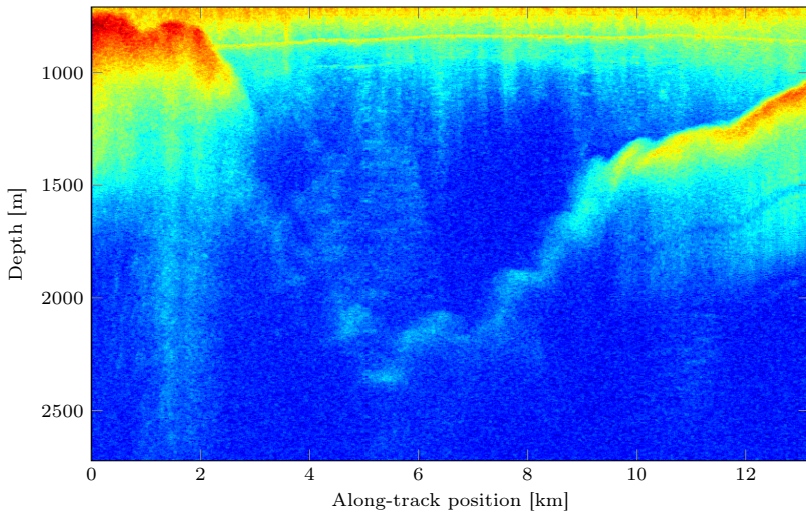


**Figure 5.15:** Echogram based on Capon processing.

DOA estimates of the surface return for repeat-pass POLARIS data are analyzed, and based on this analysis, a deviation in the DOA estimate compared to a flat surface model is observed. The deviation varies as a function of geographic location, and the analysis suggests a varying depth of the effective phase center as the underlying mechanism. This finding is highly relevant in relation to the development of DOA-based surface clutter suppression algorithms, where simulations show that the reported DOA deviations can significantly degrade the suppression performance. This applies to algorithms based on not only simple surface models, but high accuracy digital elevation models as well. Such models represent the physical air-ice interface and not the surface defined by the effective phase center as seen by a low-frequency sounding radar. Using a correlation-based method, the DOA deviation as a function of the along-track position is compared to the radar intensity of the surface return for a range of off-nadir angles. It is found that the correlation coefficient attains a positive maximum at an off-nadir angle corresponding to minimum antenna gain towards the surface. This suggests that the depth variation of the effective phase center is related to the intensity of the volume scattering. Besides the finding itself and its relevance to clutter suppression, the presented method is a novel application of DOA estimation that can be used to characterize the ice surface and directly provide glaciological information.

Further novel applications of DOA estimation is presented based on MCoRDS/I data. The MUSIC and ML estimators are used to convert the radar data into a DOA representation, where the latter is seen to provide superior performance. The DOA representation offers a better visualization of the desired signals and clutter. Based on these findings, it has been possible to discriminate the desired bed return from strong surface clutter in the channel of the challenging Jakobshavn Glacier. This dissertation demonstrates how this can be used to close some of the critical gaps in bed detection along the channel.

Finally, tomographic SCS based on POLARIS data is demonstrated using BS and NS. An approach based on data-driven DOA estimation is shown to provide improved performance compared to the more traditional model-based tomography. CM is applied to a strong and complex clutter scenario based on data acquired with the MCoRDS/I system. A full echogram is processed where CM are able to suppress the clutter to a large extend resulting in a much cleaner echogram.



## Basal Surface Scattering Estimation

As outlined in the introduction of the dissertation, more thorough information on the basal conditions is critically needed in climate change research. This includes information on the roughness that is related to the scattering characteristics of the bed surface. However, such information is also relevant for the further development and optimization of sounding hardware and processing algorithms. A study of the scattering from extended glaciological targets can provide a general characterization of the depth sounder sensitivity. This applies to the interior of the ice sheet, to the transition zones, and to the outlet glaciers and margins. This characterization can be used for simulations of the performance of array processing algorithms in realistic signal environments, which are needed in order to improve and optimize the techniques.

Motivated by this, estimation of the basal conditions is addressed in this chapter, where tomographic techniques are used to study the backscattering characteristics of the base. First a DOA-based approach is presented and demonstrated for the Jakobshavn dataset and thereafter an approach based on return waveforms.

### 6.1 Tomographic Backscattering Estimation

The DOA sweep-pattern observed near the bed of Jakobshavn Glacier are now analysed. An enlargement containing a part of the bed is shown in Figure 6.1. A sub-image for further analysis is marked in the figure. The following analysis suggests that the DOA pattern represents an off-nadir return from a rough sloped bed.

The sounding geometry with notation associated with a sloped (across-track) bed is illustrated in Figure 6.2. Since the data are Doppler processed in the along-track direction, the along-track extent of the resolution cell is small. In this way, the extent of the resolution cell is (pulse)



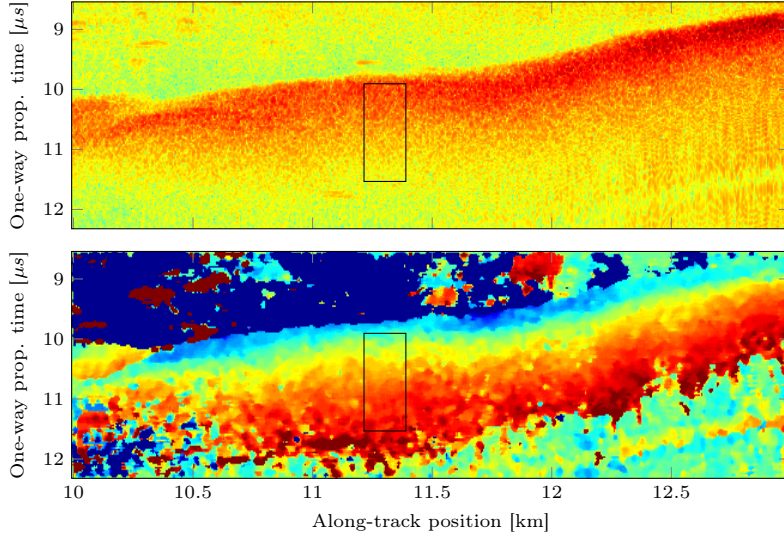


**Figure 6.1:** Enlargement (Z2) of the bed, echogram (top) and ML DOA image (bottom).

limited to the across-track direction at zero Doppler. At  $t_0$  the first bed return is reflected corresponding to the shortest electrical distance from the radar to the bed. By taking the refraction at the air–ice interface into account, the DOA of this return corresponds to the across-track slope of the bed. Later time, i.e. at  $t_1, t_2, \dots$ , two signals are reflected corresponding to the left-hand side (LHS) and right-hand side (RHS) intersections of the wavefront with the ice–bed interface, as illustrated in the figure. It should be noted that when referring to one of these two components, a specific point on the bed can be described by either range, DOA, or (propagation) time. Therefore, the representations should be read as being ambiguous or interchangeable if either the LHS or RHS intersection is considered. A rough ice–bed interface is assumed such that energy is scattered back towards the radar.

The across-track slope,  $\theta_t(t_0)$ , and depth,  $s_i(t_0)$ , of the bed is estimated using radar and DOA data for the boxed region in Figure 6.1. Based on these parameters, a DOA simulation for a flat sloped bed is conducted. Furthermore, the DOA estimate of the boxed region is averaged in the along-track direction to a single line and plotted with the simulation as a function of time in Figure 6.3.

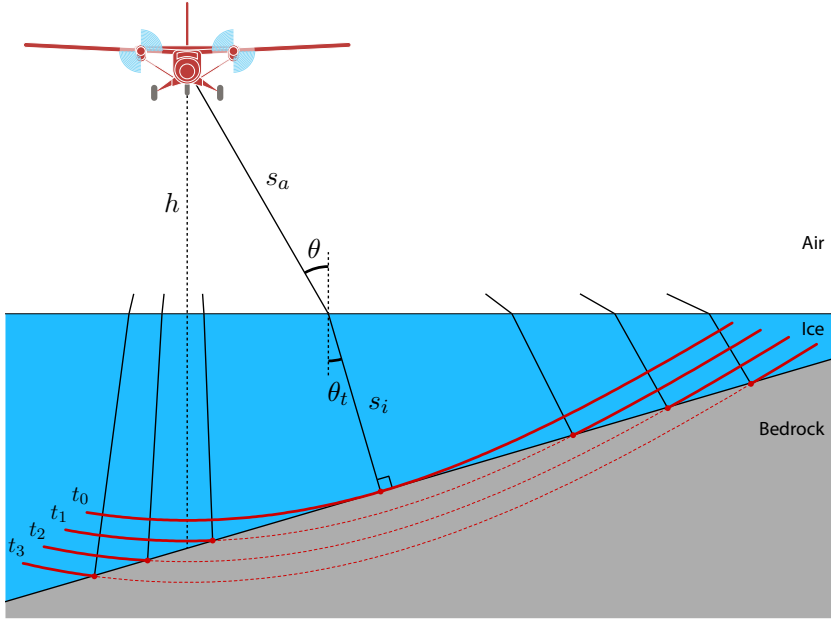


**Figure 6.2:** Geometry and notation associated with illumination of sloped (across-track) bed at different range gates.

The simulation consists of an approximately symmetric two-legged curve, where each leg corresponds to the LHS and RHS bed signal, respectively. It is seen that the estimate and simulation fits very well, but clearly only one of the two components is estimated by the DOA algorithm. The reason for this is that a one-signal ( $Q = 1$ ) ML estimation was performed. In this case, the most positive DOA component is estimated because of the transmit antenna pattern. Since the pattern is directed towards nadir, the given signal component is the one dominating the combined signal, hence the one estimated by the DOA algorithm. At a less sloped part of the bed, it was possible with a two-signal estimation to recover both of the signal components from the bed, as seen in Figure 6.4. In the case of a small slope, the geometry is symmetric which results in bed signals of equal amplitude. The retrieval of both bed signals in the low slope scenario strengthens the hypothesis of the bed reflections being the mechanism behind the sweep-pattern.

The case of a single dominating bed signal combined with the DOA

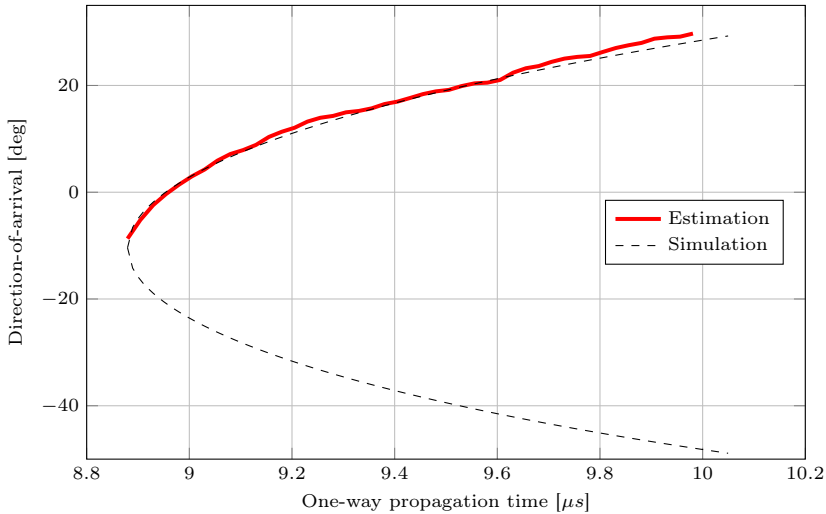


**Figure 6.3:** DOA estimation of the bed return along with a simulation based on the geometric model from Figure 6.2.

information makes it possible to estimate the backscattering characteristics of the bed for a range of incidence angles. This is done by combining the intensity waveform with the corresponding DOA estimate. However, the backscattering information contained in the waveform is affected by several factors such as a varying propagation distance, antenna patterns, refraction at the air–ice interface etc. These factors need to be taken into account to get an accurate estimate of the bed characteristics. In the following section, we will describe a procedure for estimating the backscattering pattern of the bed, which includes corrections of the intensity waveform.

### 6.1.1 Detrending

We are still considering the data region marked in Figure 6.1. To get an accurate estimate of the DOA trace and the waveform of the bed return, both the DOA data and the intensity radar data are averaged in the along-track direction. However, the bed has an along-track slope, which distorts the shape of the DOA trace and the waveform when the data are averaged. Therefore, the data are detrended with respect to the along-track slope before averaging. This is done by tracing the leading

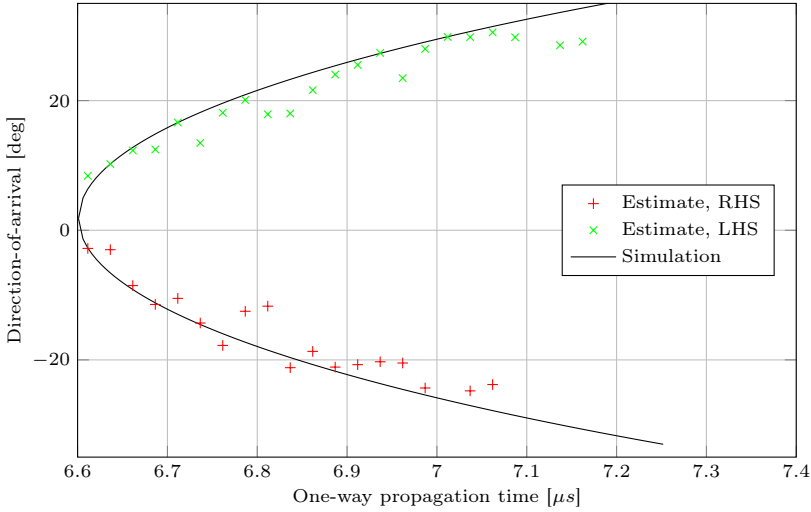


**Figure 6.4:** Two-signal ML DOA estimation and simulation of bed return.

edge of the waveform and shifting each line in range accordingly. The procedure is equivalent to averaging in the surface parallel direction and is illustrated in Figure 6.5. The resulting DOA trace and waveform after averaging are plotted as a function of time in Figure 6.6.

### 6.1.2 Fitting of Bed Model

To correct for attenuation and refraction at the air–ice interface etc., the geometric model in Figure 6.2 is adopted. The model is fitted to the data shown in Figure 6.6. As illustrated in the figure with the vertical dashed lines, the data are clipped in the range direction to capture the trailing edge of the waveform and the valid part of the DOA trace. The bed model is now fitted to the data by adjusting the slope parameter and the propagation time corresponding to the closest approach. The error, which is minimized, is evaluated in the DOA representation corresponding to the difference between the data and the model in Figure 6.3. The across-track slope of the bed is estimated by the fitted parameter to  $\theta_t = 9^\circ$ , which for the specific flight segment corresponds to the slope of the glacier channel.

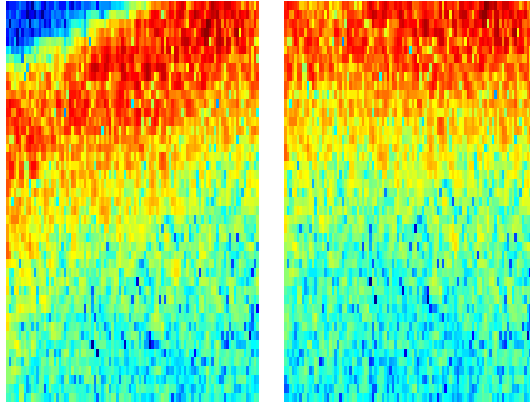


**Figure 6.5:** Illustration of the detrending procedure. Original echogram (left) and the corresponding detrended output (right).

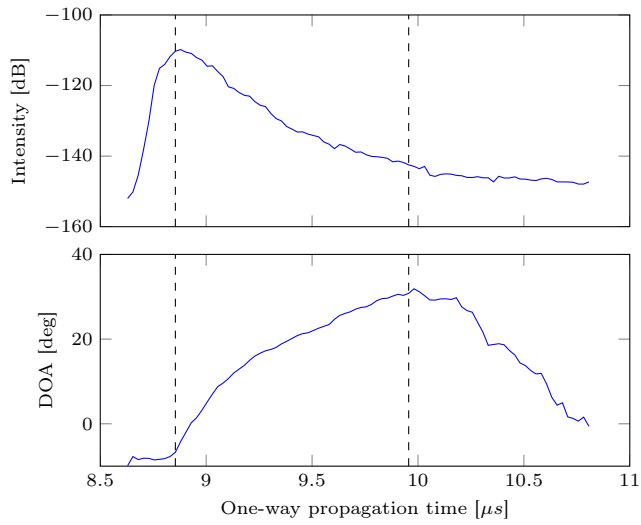


**Figure 6.6:** Along-track averaged waveform of the bed return (top) and the correspondingly averaged DOA estimate (bottom).

### 6.1.3 Waveform Correction

The data are now corrected for four mechanisms:

1. Receive gain
2. Transmit gain
3. Attenuation loss
4. Geometric spreading

#### Receive Gain

To improve the SCR, suppress clutter and the secondary bed return, beamforming is used to steer the receive-beam towards the direction of the dominating bed return. The normalization of the BS beamformer in terms of the distortionless constraint ensures unity gain in the  $\theta$ -direction, and the correction for the receive gain is in this way incorporated in the filtering process.

DOA data are simulated based on the fitted model and are used as the steering angle in (3.40). A range varying beam is in this way synthesized for, and applied to, each azimuth line. The filtered data are then detected, detrended, and averaged according to the procedure described earlier.

#### Transmit Gain

All transmit elements are used for transmission without any tapering. The resulting transmit pattern is shown in Figure 6.7. By using the estimated DOA data in combination with the pattern, the waveform can be corrected for the antenna transmit gain. The antenna pattern is based on simulations [104] and does not take dynamic factors such as wing flexure and vibration into account. This affects the true pattern particularly regarding the depth of the nulls. Furthermore, energy from the secondary bed return and from surface and volume clutter contributes to the received signal, which smoothens the waveform when the transmit gain towards the bed is low. Therefore, if the waveform is corrected with the unmodified simulated pattern with deep nulls, high amplification of the clutter will occur at angles corresponding to the nulls. To avoid this clutter amplification, the nulls of the pattern are filled before the correction is applied. The modified transmit pattern is shown in blue in Figure 6.7.

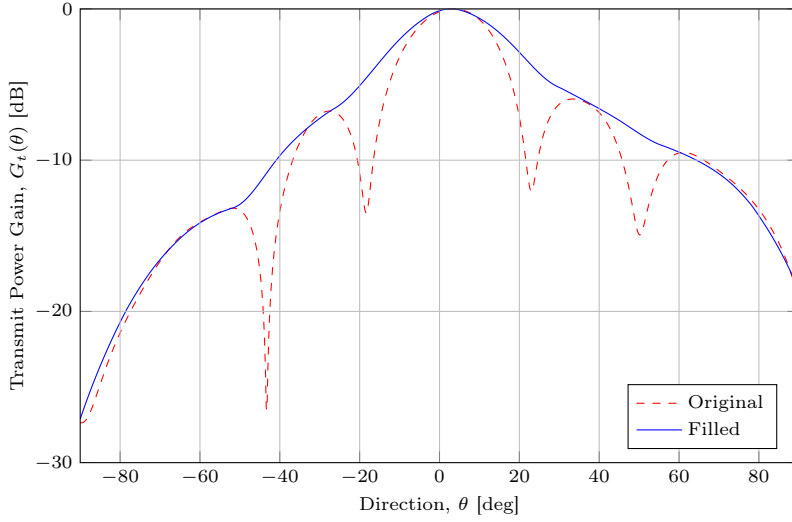


**Figure 6.7:** Filled MCoRDS/I transmit pattern based on a HFSS-simulated array manifold.

### Attenuation Loss

The electromagnetic propagation within the ice involves attenuation losses due to absorption and internal scattering. It is seen from the geometry in Figure 6.2 that the propagation distance in ice ( $s_i$ ) for the bed return varies with DOA. When the attenuation coefficient is assumed constant, the attenuation loss is exponentially proportional to the propagated distance in ice, i.e.

$$L_A \propto 10^{s_i}. \quad (6.1)$$

The attenuation loss varies with DOA and it can be taken into account. Using the model, the distance is calculated as a function of range and the waveform is corrected accordingly.

### Geometric Spreading

The inverse-square law and the two-way propagation of the pulse result in the geometric spreading loss factor that is related to range in the following way

$$L_{GS} \propto R^4. \quad (6.2)$$

When  $s_a$  is the propagated distance in air, the range is defined as  $R = s_a + s_i$  which takes the refraction at the air–ice interface into account. As for the attenuation loss, the geometric model is used to calculate the range for each sample, and the data are corrected accordingly.

#### 6.1.4 Backscattering Pattern

The corrected waveform that represents backscatter from the bed surface can be expressed as

$$\sigma(\theta) = K \frac{P_{BS}(\theta) 10^{s_i} R^4}{G_t(\theta)} \quad (6.3)$$

where  $P_{BS}(\theta)$  is the received power using beamsteering, and  $K$  is a product of factors independent of DOA such as the system gain and the attenuation coefficient of the ice. The normalized backscatter is computed by dividing with the backscatter at zero incidence, i.e.

$$\hat{\sigma}(\theta) = \frac{\sigma(\theta)}{\sigma(\theta_0)} \quad (6.4)$$

where  $\theta_0$  is the DOA angle corresponding to zero incidence at the bed, i.e.  $t = t_0$  in Figure 6.2. Based on the model, the angle of incidence at the bed is calculated from the refracted angle  $\theta_t$  and the estimated bed slope. The normalized backscatter as a function of incidence angle is plotted in Figure 6.8.

With the assumption of a random surface with a Gaussian height distribution, the IKM described in Section 2.4.1 is used to model the backscattering coefficient. The IKM only depends on the RMS slope and is therefore invariant with respect to a common scaling of  $\lambda_h$  and  $\sigma_h$  as long as the validity conditions are fulfilled.

The backscatter is obtained by multiplying the coefficient with the time-varying illuminated area, which is calculated based on the fitted geometric model. Since the illuminated area is rapidly changing for small incidence angles, backscatter is only modeled for larger angles, where the estimate of the area is more accurate and robust. The IKM is fitted to the estimated data and is included in Figure 6.8. A relative permittivity for ice and bedrock equal to 3.2 and 6, respectively, is assumed. Based on the fit of the IKM, the RMS slope is estimated to 0.22 or 12°, which represents a measure of the bed roughness. For comparison, a recent study [105] estimates bed RMS slopes of Thwaites Glacier in West Antarctica based on radar ice sounding, but with a different surface model.



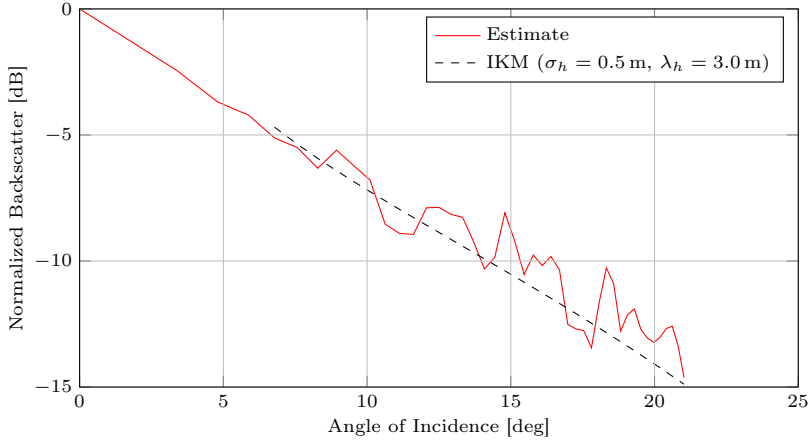


**Figure 6.8:** Estimated and simulated backscattering pattern of the bed surface.

The slopes are estimated to be between  $6^\circ$  and  $8^\circ$ , which are comparable with the findings for Jakobshavn Glacier in this analysis.

## 6.2 Waveform Analysis

In the presented method, the normalized backscattering pattern is retrieved since the absolute attenuation cannot be decoupled from the backscatter coefficient based on the radar intensity measurements alone. As an attempt retrieve absolute scattering information and thereby the bed roughness, waveform analysis is investigated as an extension to the technique.

In [106] it is shown that pulse return waveforms at lower frequencies are sensitive to the normalized radar cross section as a function of angle. In this way it is possible to retrieve surface statistical information from pulse return measurements. In relation to this, the convolution model for predicting the incoherent impulse response is presented and validated for the purpose.

The convolution model, commonly referred to as the Brown Model [107], models the pulse return as a convolution product of the flat surface impulse response (FSIR), the radar point target response (PTR), and the surface height probability density function (PDF), that is

$$P_b(t) = P_{\text{PTR}}(t) \star P_{\text{FSIR}}(t) \star P_{\text{PDF}}(t). \quad (6.5)$$

When the convolution of the FSIR and PTR are known, the total convolution product can be calculated for different values of  $\sigma_h$  by assuming an appropriate PDF, e.g. a Gaussian distribution. The estimated pulse returns can then be compared to real radar data where the value of  $\sigma_h$  corresponding to the best match is used as an estimate of the parameter.

This approach is investigated using the MCoRDS/I data from the northern part of Greenland. As an estimate of the convolution of the FSIR and PTR, a specular bed return is used. Such returns are often found at outlet glaciers where the bed in some channels can be covered with a thick film of water that implies a strong specular return. Such a strong specular return is found in the data from northern part of Greenland.

In the echogram in Figure 4.15 it is seen how the bed marked by the vertical red lines is relatively smooth and with a strong peak return. The bed marked by the blue lines is where the roughness parameters are to be estimated. The corresponding A-scopes are shown in Figure 6.9, where the waveforms represent the average in azimuth over the intervals defined by the pairs of vertical lines in the echogram. The peaks of the two returns are aligned in range and plotted as a function of depth relative to the peak position in Figure 6.9. It is seen how the specular return has a very distinctive peak while the rough return is more broadened.

In Figure 6.10, the results of the fitting is shown. The black dashed curve is a fit of a Gaussian function to the peak of the smooth return that is used to model the convolution product  $\text{PTR} \star \text{FSIR}$ . Since the mainlobe of the PTR is well-described by a Gaussian function and by modeling the FSIR for the specular return as a Dirac delta function, the Gaussian fit for the convolution product is appropriate. The assumption of a specular return and the corresponding modeling with a delta function is substantiated by comparing the width of the Gaussian fit the range resolution of the radar which are found to be very similar.

The fitted convolution product is then convolved with a Gaussian PDF to match the leading edge of the rough return according to the Brown Model. The resulting fit is represented by the pink curve in the figure. The parameter fit that provides the optimal match of the leading edge corresponds to  $\sigma_h = 3.5$  m. However, the PDF convolution based on this value only contributes to a peak reduction of 2.6 dB and a large additional offset of  $-21.8$  dB is needed in order to vertical align the peaks as presented in the figure. Based on the fitted value of  $\sigma_h$  and the assumption of correlation lengths in the order of meters, the RMS surface slope is estimated several times larger than the results in [105] and what was found for Jakobshavn Glacier using the tomographic technique in

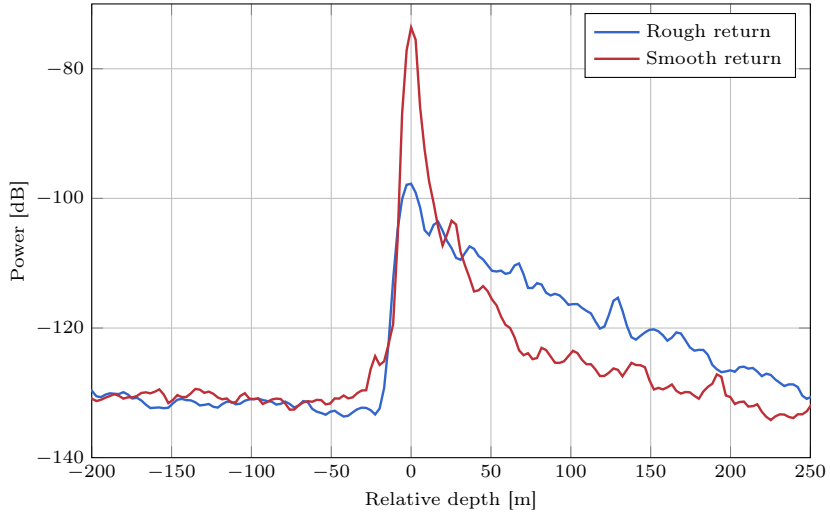


**Figure 6.9:** Waveforms corresponding to the smooth and rough bed in Figure 4.15.

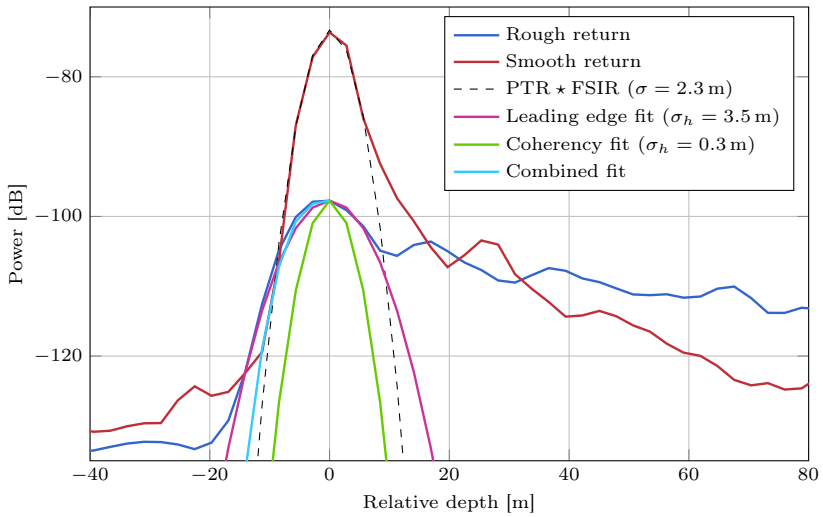


**Figure 6.10:** Convolution model fit to leading edge and the peak.

Section 6.1. Based on this, the fit of  $\sigma_h = 3.5$  m is considered as being unrealistic.

From (2.24), it is seen that a coherent component of a rough return is scaled due to roughness by the factor  $e^{-4k^2\sigma_h^2}$ . If the rough return is assumed to be dominated by the coherent component at the peak, this factor should be taken into account as an additional factor multiplied on the convolution product, since the Brown Model only accounts for the incoherent component. The value of  $\sigma_h$  can then be estimated by optimizing with respect to the peak values. In this way, the peak is reduced partly by the convolution of the PDF and partly by the additional exponential factor. The result of this fitting procedure is shown as the green curve in the figure. With this approach, the parameter is estimated to 29 cm which is more realistic compared to the 3.5 m based on the previous argumentation. However, as seen from the figure, this approach are not able to match and explain the leading edge. On the other hand, the incoherent component may not be neglectable, which could be the reason for the unexplained broadening of the rough return. In this case the FSIR is not appropriate modeled by a delta function. Instead, as a first order approximation for analysis of the leading edge only, the FSIR is modeled as a Heaviside step function. This approach is in the figure referred to as the combined fit represented by the light blue curve, which is seen to explain the broadening to a larger extend.

The falloff of the trailing edge of the rough return is determined by backscatter from increasing incident angles, which is influenced by the surface height correlation length,  $L$ . An approach to retrieve this parameter from the trailing edge is to use a surface scattering model as the IEM for forward modeling. By using and fixing the estimated value of  $\sigma_h$ , the correlation length can be varied in the IEM to match the model output to data.

The matching is done for the backscattering coefficient over a range of incidence angles, where the backscattering coefficient  $\sigma^\circ$  is related to the received power  $P_r$  through the radar equation from (2.14). In order to estimate  $\sigma^\circ$ , a radar calibration is needed and the loss due to ice attenuation has to be known. Since the smooth peak return  $P_{\text{ref}}$  can be well modeled by a specular reflection based on the previous argumentation, this return can be used for calibration and to cancel out the effect of the lossy ice. The received power for the rough return is expressed using the radar equation, i.e.

$$P_r = \frac{P_t G \lambda^2 \sigma^0 A}{(4\pi)^3 R^4 L_S L_A}, \quad (6.6)$$

where  $G$  is the total system gain,  $L_S$  accounts for system losses, and  $L_A$  is the attenuation loss due to the propagation within the ice. For the smooth return, the received power is modeled using the specular scattering coefficient from (2.17), that is

$$P_{\text{ref}} = \frac{P_t G \lambda^2 \Gamma}{(4\pi)^2 (2R)^2 L_S L_A} \quad (6.7)$$

Now, by taking the ratio of the two returns, the unknown loss factors can be eliminated and the backscattering coefficient for the rough return can be isolated, i.e.

$$\frac{P_r}{R_{\text{ref}}} = \frac{\sigma^0 A}{\pi R^2 \Gamma} \quad (6.8)$$

$$\Downarrow$$

$$\sigma^0(\theta_i) = \frac{P_r(\theta_i)}{P_{\text{ref}}} \frac{\pi R^2 \Gamma}{A(\theta_i)}. \quad (6.9)$$

This requires that  $P_{\text{ref}}$  and  $P_r$  are acquired in the same area such that the properties of the ice sheet can be assumed constant, and that the bed returns are located at approximately the same depth. By calculating an estimate for the reflection coefficient  $\Gamma$  corresponding to the change in permittivity across the basal interface, and by calculating the time varying illuminated area  $A$  from the geometry, the backscattering coefficient as a function of angle can be estimated from the data.

For estimation of the geometrical parameters, the leading and trailing edges of the pulse are simulated using ray tracing based on Snell's law, the geometry, and by constraining equal propagation time for all points on each of the edges. The illuminated bed area as a function of incidence angle is calculated corresponding to the Doppler processed footprint. The across-track width at a given incidence angle is determined by the intersections of the simulated pulse edges with a plane bed model corresponding to Figure 6.2. The along-track width is determined by the Doppler bandwidth. The varying additional return loss due to a larger propagation distances within the ice for backscattering at increasing incidence angles is corrected similar to the procedure in Section 6.1.3. Also any minor range mismatch between the specular and rough return is corrected.

Following this procedure, the backscattering coefficient as a function of incidence angle is estimated as seen in Figure 6.11. The output of the IEM is fitted to the data corresponding to an estimate of correlation length equal to approximately 3.2 m. In order to match the curves,

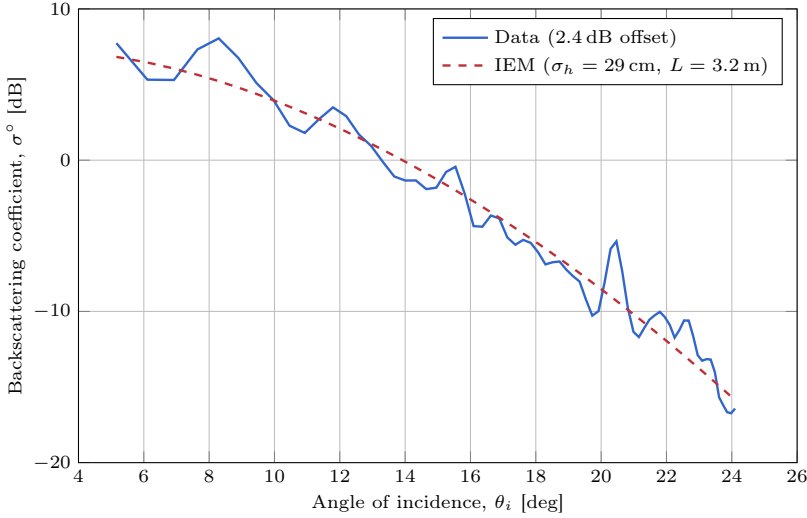


**Figure 6.11:** Backscattering coefficient

a minor offset of 2.4 dB is applied to the data estimate. A Gaussian shaped surface height correlation function in the IEM was found to provide a good match for the curvature. For calculation of the reflection coefficient of the smooth return, the permittivity for ice and rock given in Section 2.2 are used. The ranges to the bed at the two locations corresponding to the analysed waveforms differ by 120 m of which 97 m is within the ice. Based on this, minor corrections are applied as previously described.

Since a high SNR is present, only a single channel is used for the analysis instead of the full 7-element array. This simplifies the complexity of the antenna pattern and makes the correction procedure less sensitive to errors in the pattern model.

Based on the method presented in this section, a good match between the IEM and the radar data is found and an estimate of the bed roughness in terms of  $\sigma_h$  and  $L$  is obtained. However, the method rely on a number of assumptions that may affect the estimate. Returning to Figure 6.10, the first order approximation of the FSIR was shown to explain the broadening of the pulse to some extent. The remaining error can probably be explained by different bed conditions at the locations for the smooth specular and the rough return. The underlying assump-

tion is that the Fresnel reflectivity for the coherent component of the two returns is the same. This is not the case if the strong specular return is reflected from an ice–water interface while the interface for the rough return is frozen ice–rock. If the basal conditions differ in this way, an erroneous calibration is obtained from the calculated specular reflectivity which introduces an incorrect scaling. However, such a scaling couples with the width and shape of the modeled waveform through the fitting procedure and can in this way explain the observed error. The scenario of varying bed conditions can be considered as an underdetermined retrieval problem where the variation cannot be uniquely decoupled in the roughness estimation.

The proposed method has the potential for providing information on the bed roughness over large and various areas. However, further development and solid validation is needed. One validation approach could be to acquire data from a deglaciated bedrock in connection with a retreating glacier. The data from the exposed bed could serve as ground truth by assuming the statistics to be stationary for sounding measurements further upstream. Furthermore, by conducting dedicated multi-frequency experiments, the inversion problem could be further constrained and the different varying mechanisms could be decoupled.

## Conclusions

In this PhD study, tomographic techniques based on multi-phase-center sounding systems are investigated. First, the fundamental techniques and theory related to radar ice sounding are presented. The review provides a solid background for the discussion of the investigated techniques as well as for interpretation of the subsequent data analysis.

An in-depth theoretical treatment of algorithms for radar tomography is conducted, beginning with the formulation of an array signal model. In relation to this, the problem of direction-of-arrival (DOA) ambiguities for a uniform linear array is formulated as spatial aliasing and a mathematical foundation that is analog to what is known from the classical temporal sampling theory is provided.

Based on the array signal model, different beamforming methods and DOA estimators are investigated and assessed for the application of radar tomography and surface clutter suppression. The theoretical properties of the individual algorithms are discussed and related to ice sounding applications. The performance of the algorithms are further assessed and compared through various simulations. Based on this, different algorithm strategies are suggested depending on the sounding scenario and array configuration. For scenarios where the radar sensitivity is limited by the signal-to-noise ratio, beam-steering is an adequate choice of beamforming method. For a complex clutter scenario in terms of an unstructured covariance matrix with non-stationary statistics, the Capon method is considered to be the best choice, even though self-nulling in the form of an erroneous direction of interest can degrade the performance. For both strategies, optional DOA estimation is suggested for optimization of the specified direction of interest. In the case of scenarios characterized by strong directional surface clutter, or signal structure in general, null-steering or Optimal beamforming are able to



provide good performance in which the synthesized beams are robust and easy to interpret.

With respect to DOA estimation, it is concluded based on theory and simulations that the Maximum Likelihood estimator is superior, especially under difficult conditions. In more relaxed conditions, MUSIC is found to perform just as well while also being much more computational efficient. Particularly when a uniform linear array is used, the root variant of MUSIC is desirable due to its direct parametric estimation, which is convenient with respect to implementation and provides increased efficiency. However, in complex scenarios with unknown and varying signal structure, the Capon method may be considered due to its non-parametric properties that do not rely on assumptions about the covariance matrix. Based on existing experiments with Compressive Sensing applied to SAR and through a theoretical review, Compressive Sensing is found to be very interesting in the case of repeat-pass ice sounding.

Experimental multi-phase-center data acquired with the POLARIS system over Jutulstraumen Glacier have been analyzed and validated. Based on the dataset, the capability of supporting advanced array signal processing in terms of DOA estimation has been demonstrated for the system. Sections of the dataset that are spatially under-sampled are used for validation of the spatial sampling theory. The proposed theory related to spatial aliasing is used to successfully unwrap aliased surface returns.

Since the problem of spatial aliasing is caused by the wide spacing of the array element relative to the wavelength, it can, in principle, be avoided during the system design process. However, the treatment of under-sampled data is relevant since such sub-optimum antenna designs might be the compromise in future sounding systems in order to reduce system complexity.

Using repeat-pass POLARIS data, a method based on DOA estimation is used to show a deviation in the DOA estimate compared to a flat surface model. The deviation varies as a function of geographic location, and the analysis suggests a varying depth of the effective phase center as the underlying mechanism. This finding is highly relevant in relation to the development of DOA-based surface clutter suppression algorithms, where simulations show that the reported DOA deviations compared to a flat surface model can significantly degrade the suppression performance. This applies to algorithms based both on simple surface models, as well as high accuracy digital elevation models. Such models represent the physical air-ice interface and not the surface defined by the effective

phase center as seen by a low-frequency sounding radar.

By using a correlation-based method, the DOA deviation as a function of along-track position is compared to the radar intensity of the surface return for a range of off-nadir angles. It is found that the correlation coefficient attains a positive maximum at an off-nadir angle corresponding to the minimum antenna gain towards the surface. This suggests that the variation in depth of the effective phase center is related to the intensity of the volume scattering. Besides the finding itself and its relevance to clutter suppression, the presented method is a novel application of DOA estimation that can be used to characterize the ice surface and in this way directly provide glaciological information.

Tomographic surface clutter suppression is also demonstrated based on POLARIS data using beam-steering and null-steering. An approach based on data-driven DOA estimation is shown to provide improved performance compared to the more traditional model-based tomography. The Capon method is applied to a strong and complex clutter scenario based on data acquired with the MCoRDS/I system. A full echogram is processed using the Capon method to suppress clutter to a large extent which resulted in a much cleaner echogram.

The MUSIC and Maximum Likelihood DOA estimators are applied to the same dataset. The algorithms are used to convert the radar data into a novel DOA representation that offers a better visualization of the desired signals and clutter. For this particular application and dataset, Maximum Likelihood is found to provide superior performance compared to MUSIC. Based on the Maximum Likelihood representation, it is possible to discriminate the desired bed return from strong surface clutter in the channel of the challenging Jakobshavn Glacier. It is shown how this can be used to close some of the critical gaps in bed detection along the channel.

Furthermore, a geometric model is used to show how the across-track slope of the bed is related to the DOA pattern of the bed return for the same dataset. In a low slope scenario where the associated geometry gives rise to comparable amplitudes of the two bed signals, the DOA for both components is retrieved and validated with the model. For larger slopes, it is shown that the bed component received closest to nadir is dominant due to amplification caused by the combination of the transmit pattern and asymmetric geometry. This is exploited to retrieve bed characteristics by combining DOA data and waveforms of the radar data. By fitting the geometric model to the data, the across-track slope is estimated. Based on the model, a number of corrections are applied to the waveform to retrieve the received backscatter of the bed surface

as a function of the local incidence angle. Information on the roughness contained in the pattern is quantified by fitting the incoherent Kirchhoff Model to the data.

Finally, a novel technique based on waveform analysis is investigated for retrieval of the effective statistical roughness parameters of the bed surface. Using a specular return for calibration, the parameters are obtained by fitting the Brown model and the Integral Equation Model to the data. A good match is obtained for the experimental dataset and the proposed method has the potential to provide information on the bed roughness for large areas. However, further development and solid validation of the method is needed.

Information on the basal conditions, such as the estimated quantities, is critically needed in climate change research and is crucial to the improvement and optimization of advanced surface clutter suppression algorithms through realistic simulations.

## 7.1 Suggestions for Future Work

There are several topics related to the work presented in this dissertation that are interesting for future studies.

Additional multi-phase-center datasets acquired for the purpose of dedicated tomographic experiments would be beneficial for several reasons. First of all, additional campaigns would provide more suitable data compared to the existing POLARIS data, which are negatively affected by an erroneous radar configuration. Furthermore, by operating a lidar along with the sounder, a high-accuracy and co-registered DEM of the scene could be obtained. This could be very useful for the development and validation of tomographic techniques.

Using high altitude acquisition with the same antenna configuration as was used to collect the Jutulstraumen dataset would make it possible to avoid spatial aliasing and disturbance related to grating lobes. The need for surface clutter suppression increases with high altitude, since the associated geometry implies that strong surface clutter with near-nadir DOA are received at the same time as the bed return. A high-altitude dataset is therefore also useful for thorough validation of suppression algorithms, especially in order to evaluate the performance for space geometries, which is crucial to assessing the feasibility of space-based ice sounding. To further assess the feasibility of space-based ice sounding, a natural study for future work would be to conduct comprehensive performance simulations of the tomographic techniques for the

space-based scenario.

Another interesting experiment would be to configure POLARIS with its small four-element antenna to avoid spatial aliasing and combine it with a low flight altitude to obtain a dataset with minimum surface clutter. This could offer possibilities for swath mapping of the bed topography, despite the fact that the small number of phase centers may significantly limit the performance. Since the number of phase centers available for this PhD study were limited, it would be interesting to upgrade POLARIS with four additional receive channels combined with its large eight-element antenna. This could provide new opportunities for clutter suppression and topography swath mapping. Beside these new possibilities, spatial aliasing, grating lobes, and the nulls in the element receive patterns would be avoided when the full array is sampled. Data based on such an upgraded POLARIS system are further relevant in order to explore the potential and possibilities of the large volume of data from systems with a high phase-center count that will be available in the future.

An additional interesting subject with large potential is repeat-pass acquisition combined with processing techniques based on Compressive Sensing. The subject can be initially investigated using the existing repeat-pass dataset acquired at Jutulstraumen Glacier. The baselines of the acquisition are large for the greater part of the track, but a preliminary study could be conducted on a few applicable sections of the track. A more exhaustive study would benefit from an additional dedicated acquisition with more stable baselines using the small antenna to avoid the aforementioned disadvantages related to the Jutulstraumen configuration. In the context of space-based ice sounding, the orbits typically provides temporal baselines in the order of days. Airborne repeat-pass experiments with temporal baselines are therefore important in order to evaluate how decorrelation affects the tomographic techniques and thereby evaluate their applicability to space-based sounding.

Dedicated repeat-pass data could also support experiments on tomographic 3D imaging of the ice volume, which could be used for mapping the internal structure of the ice or locating buried objects.

Finally, further validation of the suggested techniques for bedrock scattering and roughness estimation are needed. For this purpose, data acquired from a deglaciated bedrock in connection with a retreating glacier could be useful. The data from the exposed bed could serve as ground truth by assuming the statistics to be stationary for sounding measurements further upstream. Furthermore, multi-frequency experiments would be useful for validation and improvement of the techniques.



## **Coherent Surface Clutter Suppression Techniques with Topography Estimation for Multi-Phase-Center Radar Ice Sounding**

Ulrik Nielsen, Jørgen Dall, Steen Savstrup Kristensen, and Anders Kusk

Published in Proceedings of European Conference on Synthetic Aperture Radar, Nuremberg, Germany, Apr. 2012, pp. 247–250.



# Coherent Surface Clutter Suppression Techniques with Topography Estimation for Multi-Phase-Center Radar Ice Sounding

Ulrik Nielsen, Jørgen Dall, Steen Savstrup Kristensen and Anders Kusk

Technical University of Denmark (DTU) – Ørstedss Plads, Building 348, DK-2800 Kgs. Lyngby, Denmark  
E-mail: ulrik@space.dtu.dk – Phone (+45) 45253834 – Fax (+45) 45931634

## Abstract

Radar ice sounding enables measurement of the thickness and internal structures of the large ice sheets on Earth. Surface clutter masking the signal of interest is a major obstacle in ice sounding. Algorithms for surface clutter suppression based on multi-phase-center radars are presented. These algorithms incorporate estimation of the required topographical information, thereby making the processing independent of such external data. The algorithms are applied to data collected by ESA's POLarimetric Airborne Radar Ice Sounder (POLARIS) over Antarctica in February 2011.

## 1 Introduction

Understanding of the dynamics of the large ice sheets on Earth is important in order to model the climate evolution and to predict future changes induced by human activity. The ice sheet structure, layering, and flow-patterns contain information on past Earth climate and atmospheric events at a 100,000 year time scale, which is valuable information for the ongoing climate research.

A satellite-based sounding radar can provide complete and homogeneous coverage of the large ice sheets on Earth with sufficient spatial and temporal sampling. When the International Telecommunication Union (ITU) in 2003 allocated a 6 MHz band at 435 MHz (P-band) for remote sensing, a space-based ice sounding radar was proposed to ESA as a possible Earth Explorer mission. Previous ice sounders were typically operating in the lower MHz frequency region in order to obtain satisfactory characteristics with respect to the maximum penetration depth, the strength of disturbing surface clutter and practical antenna dimensions for accommodation on an aircraft. Due to lack of knowledge on ice sounding at frequencies as high as P-band, ESA commissioned the development of POLarimetric Airborne Radar Ice Sounder (POLARIS) [1] with the objective to assess the feasibility of ice sounding at P-band from space.

### 1.1 Surface Clutter

Due to the spherical wavefront of a propagating pulse, an echo backscattered by a resolution cell located at a certain ice depth will be received by the radar simultaneously with an echo backscattered by the surface. The weak depth signal of interest may in this way be masked by the off-nadir surface clutter signals at the same electrical distance as the depth signal from nadir.

It is shown [2] that surface clutter is the primary scattering

mechanism that obscure the subsurface echoes at higher altitudes, and surface clutter is therefore a major issue in space based ice sounding.

Clutter footprints corresponding to different ice depths are described by annuli, as illustrated in **Figure 1**. Clutter scattered in the along-track direction can effectively be suppressed with Doppler processing, and the problem reduces to the across-track surface clutter as illustrated in the figure.

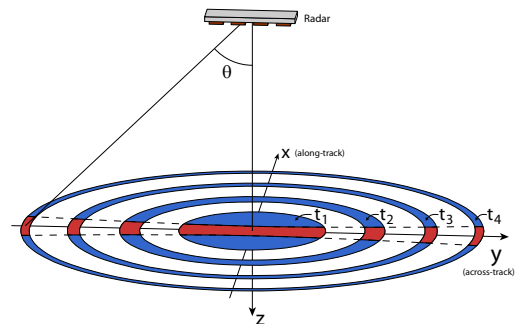


**Figure 1:** Doppler processed surface footprints at different time instants. The footprints are illustrated by the red areas enclosed by the dashed black hyperbola. The blue annuli are the corresponding pulse limited footprints without Doppler processing. The figure is not to scale.

The across-track clutter is suppressed for large off-nadir angles, due to the antenna pattern and the backscattering pattern of the ice surface. However, the clutter can still mask the subsurface signal for a considerable angle range, since the subsurface signal at the same time is attenuated, due to propagation through the lossy ice. The direction of arrival (DOA) for the clutter, at a given range cell, is determined by the sounding geometry and the local topography. The problem related to surface clutter increases with alti-



tude, due to smaller and slower increasing clutter DOAs. This makes across-track surface clutter suppression (SCS) essential for satellite geometries, but also for modern airborne sounders where high pulse compression prevents operation at low altitudes.

A narrow antenna beam in the across-track could suppress surface echoes from off-nadir angles, but this would require antenna dimensions which are impractical for accommodation on moving platforms. An alternative approach is to suppress the surface clutter through coherent processing of echo signals received by a multi-phase-center antenna.

## 1.2 The POLARIS instrument

POLARIS is a nadir-looking, fully polarimetric sounding radar featuring aperture synthesis. POLARIS is equipped with a multi-phase-center antenna and multi-channel receiver which supports single-polarisation coherent surface clutter suppression through offline processing techniques. The antenna aperture is a uniform linear array (ULA) of quadratic patches aligned in the across-track direction. POLARIS is developed and operated by DTU and was tested with a 4-element antenna over Greenland in 2008 and again in 2009. In February 2011 POLARIS acquired multi-phase-center data over Antarctica with an 8-element antenna. POLARIS is equipped with a 4-channel receiver, where groups of two neighbouring elements are connected to each channel. The element spacing is 480 mm.

## 2 DOA Estimation

In order to suppress surface clutter through processing techniques the clutter DOA must be known. By a geometric consideration, one can for a given range cell calculate the clutter DOA from the local topography, the radar altitude, and the roll angle. If the surface is flat, only altitude and roll are needed, which will typically be available as housekeeping data. In the case of a sloped and/or uneven surface, one solution is to rely on an external digital elevation model (DEM) in order to obtain the topographical information needed, as seen in [3].

Another solution is to estimate the topography from the radar data and in this way make the sounding and clutter suppression independent of any external data.

Using the plane wave approximation, the same echo signal is received by each of the elements but with a progressive time delay across the array corresponding to a phase shift. In this way, the signal received at the  $n^{\text{th}}$  element at time  $t$  can be expressed as

$$x_n(t) = s(t)e^{-j\omega_c\tau_n} + e_n(t), \quad (1)$$

where  $s(t)$  is the complex echo signal at a reference element,  $\omega_c$  is center angular frequency,  $\tau_n$  is the time delay at the  $n^{\text{th}}$  element relative to the reference and  $e_n(t)$  is an additive Gaussian noise component.

The so-called steering vector describes the phase shifts of the elements

$$\mathbf{a}(\theta) = [e^{-j\omega_c\tau_1} \dots e^{-j\omega_c\tau_N}]^T, \quad (2)$$

where  $(\cdot)^T$  is the transpose operator and  $N$  is the number of elements. For a ULA, the steering vector can be expressed as

$$\mathbf{a}(\theta) = [1 e^{-j\omega_s} \dots e^{-j(N-1)\omega_s}]^T, \quad (3)$$

where  $\omega_s$  is called the spatial angular frequency, defined as

$$\omega_s = kd \sin \theta, \quad (4)$$

with  $k$  denoting the wavenumber and  $d$  the element spacing.

From (3) it is seen that the problem of estimating the DOA,  $\theta$ , for a given echo, now reduces to a spectral estimation problem. A wide range of techniques for spectral estimation exist, but for the problem at hand, super-resolution techniques like the maximum likelihood (ML) estimator and subspace-based methods like the MUSIC-algorithm [4] are found to provide good results. In [5] ML is used to map the surface and bedrock topography from airborne ice sounding data. Under certain statistical conditions, ML is shown to approach the theoretical optimal solution, and are in general superior to the sub-optimal subspace-based techniques. ML is computational heavy due to multi-dimensional searches, whereas MUSIC is faster since a closed-form solution exists.

### 2.1 Data Model

In the case of  $Q$  simultaneously received echo signals with different DOAs, the following array model is obtained by writing (1) on vectorial form and making use of the superposition principle

$$\mathbf{x}(t) = \mathbf{A}(\Theta)\mathbf{s}(t) + \mathbf{e}(t), \quad (5)$$

where  $\mathbf{A}$  is the steering matrix formed by column-wise concatenation of the steering vectors corresponding to each of the  $Q$  signals, and  $\mathbf{s}(t)$  is a vector collecting the  $Q$  signals at time  $t$ , i.e.

$$\mathbf{s}(t) = [s_1(t) \dots s_Q(t)]^T. \quad (6)$$

The  $N \times 1$  vector  $\mathbf{x}(t_m)$  constitutes a sample of the array at time instant  $t_m$ . Such an array sample is denoted an azimuth-“look”. When  $t_1 \dots t_M$  denotes the time instants at which  $M$  looks are taken, at the same scene and range gate, a complete data model can be expressed in the following matrix form

$$\mathbf{X} = \mathbf{A}(\Theta)\mathbf{S} + \mathbf{E}, \quad (7)$$

where  $\mathbf{X}$  and  $\mathbf{E}$  are  $N \times M$  matrices,  $\mathbf{A}$  is  $N \times Q$ , and  $\mathbf{S}$  is  $Q \times M$ . Each column in  $\mathbf{X}$ ,  $\mathbf{S}$ , and  $\mathbf{E}$  corresponds to a look. For further details see [5].

## 2.2 Maximum Likelihood

The ML solution of the DOA vector can be expressed as [5]

$$\hat{\Theta} = \min_{\Theta} \text{tr} [A(\Theta)A^\dagger(\Theta)R], \quad (8)$$

where  $A^\dagger$  is the Moore-Penrose pseudoinverse of  $A$  and  $R$  is the  $N \times N$  data covariance matrix.

## 3 Surface Clutter Suppression Techniques

Different approaches for clutter suppression with multi-phase-center antennas can be chosen. Beamforming is used in [3], where beam-steering is a simple special case. In [6] a generalized approach is adapted from a previously suggested repeat-pass method. An ML solution from [5], where each of the  $Q$  impinging echo signals are estimated from the known DOAs, is found to coincide with the generalized approach, as a special case. The ML solution is given by

$$\hat{S} = A^\dagger(\Theta)X. \quad (9)$$

The surface clutter suppressed signal for each look is found as the elements in the  $q^{\text{th}}$  row of  $\hat{S}$  corresponding to the provided nadir signal DOA  $\theta_q$ , which determines the  $q^{\text{th}}$  column of  $A$ .

The complex weights obtained with the ML estimator can be thought of as a synthesised antenna pattern. Furthermore, the pattern is, loosely speaking, characterized by nulls located in direction of the impinging clutter signals, while the gain in the direction of interest is maximised at the same time.

## 4 Application to POLARIS Data

### 4.1 Data description

The described processing techniques have been applied to the Antarctica data acquired by POLARIS. The processing is based on a west-east track that is crossing the Jutulstraumen glacier, as shown in **Figure 2**.

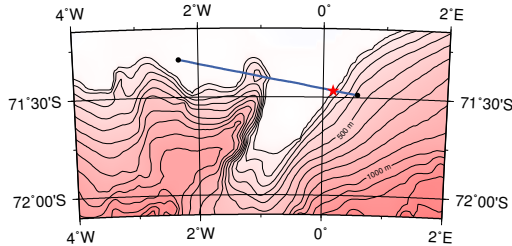


**Figure 2:** Flight track and surface contours. Contour levels are with respect to mean sea level.

The first part of the track consists of ice shelf which is flat and relative smooth. Further on, the track crosses grounded ice followed by floating tongue of the glacier. At the very end of the track, terrain with grounded ice sheet starts rising. The exact location of the acquired data that underlies the following results is just before this rising terrain, as marked in the figure. At this position, the surface and the basal interface are both flat and have strong echoes. The altitude flight is approximately 3350 m with respect to the surface. The azimuth-look spacing is 1.5 m and the bandwidth equals 85 MHz.

### 4.2 Topographical estimation results

The ML estimator is used for topographical estimation in terms of surface clutter DOA. The estimation of the covariance matrix is based on 25 looks. The flat scene under study results in two surface clutter components – a left-hand return, and a right-hand return. The two components will be symmetrical around nadir for a perfect flat surface. The results are shown in **Figure 3**.

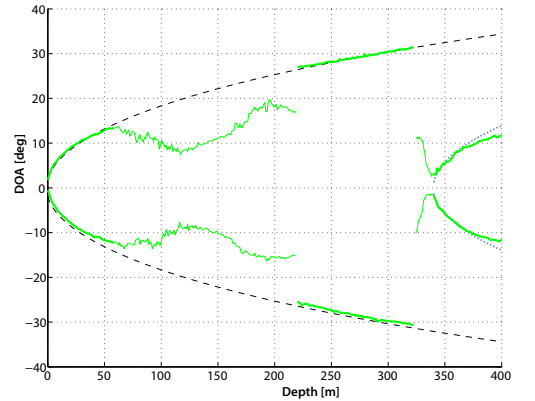


**Figure 3:** Unwrapped ML DOA estimate. The black dashed curve is a flat-surface model. The blue dotted curve is a flat-base model.

The algorithm was configured for a two-signal estimation, since the two off-nadir surface echoes are the dominating signal components. Due to the antenna element spacing, spatial undersampling of the surface echoes occurs at the larger equivalent depths. The spatial Nyquist frequency corresponds to  $\pm 21^\circ$ . The undersampling implies aliasing of the estimated DOA. The curves presented in Figure 3 are unwrapped. The basal return appearing at 340 m accounts for the dominating components over a limited depth interval. The basal return is not aliased since the corresponding DOA is close to nadir.

Parts of the curves are plotted with a thin solid linestyle in order to indicate invalid surface DOA estimation. The deviation of the curve segment at the depth interval from 60 m to 220 m is primary due to the first null in the trans-

mission pattern, which corresponds to the depth of 135 m. The limits of the antenna gain corresponding to this curve segment is 8 dB and 0 dB, respectively. Besides the antenna null, the surface DOA estimation is affected by the signal-to-clutter ratio (SCR) which are range dependent due to nadir signal attenuation and the clutter backscattering pattern. It is seen from the figure that the valid segments are consistent with the simulations.

### 4.3 Clutter Suppression results

The data have been processed with three surface clutter suppression techniques, namely beam-steering and two variants of ML. In the case of beam-steering, the beam has been steered towards nadir by coherently summing the channels corresponding to the full aperture. The ML technique has been used with both the ML DOA estimated topography data, and flat-surface simulated topography data, corresponding to the dashed curves in Figure 3. The resulting nadir power signals are shown as functions of depth in Figure 4.

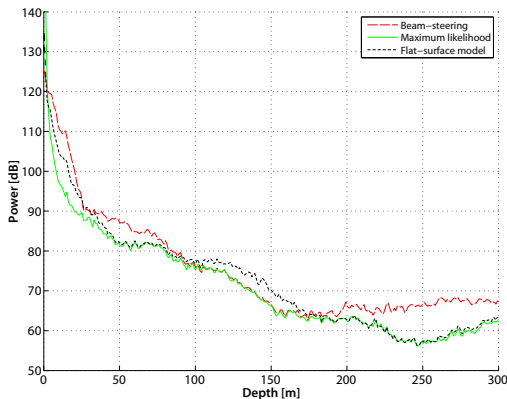


**Figure 4:** Surface clutter suppressed nadir intensity profile.

It is seen how the ML SCS algorithm, applied with ML DOA data, suppresses a significant amount of clutter compared to beam-steering, down to 85 m and between 200 m and 300 m. This is consistent with the surface clutter expected from the transmit pattern. In the interval between 85 m and 200 m the two curves coincide, which again can be explained primarily by lack of surface clutter near the first null of the transmission pattern. The gain limits associated with this null is 0 dB and -3 dB, respectively. It should be noted that DOA estimation from Figure 3 is also used for this interval, as for the "valid" segments, even though the estimate does not describe the true surface. This makes sense, since the DOA estimation describes the dominating off-nadir clutter.

The ML SCS algorithm applied with simulated DOA data is seen to provide suppression similar to that of the ML DOA variant, except for the region around the first null where the performance of the simulation based variant is

mance is also inferior near nadir where the SCS algorithm is highly sensitive to DOA angle derivations.

## 5 Conclusion

Different algorithms for DOA estimation and SCS have been described and applied to data acquired with POLARIS over Antarctica. The DOA estimation for a flat surface has been verified by comparison with simulations. Both simulated and estimated topography data have been used for SCS by means of the ML algorithm. The SCS results seem to be consistent with the expected SCR pattern. Both approaches are successful but a superior result is obtained by estimating the topography.

## 6 Acknowledgement

This research was carried out at the Technical University of Denmark (DTU), supported by ICEGRAV data. ICEGRAV is a DTU airborne geophysics project in co-operation with University of Texas (UT), the Norwegian Polar Institute, University of Bergen, Instituto Antartico in Argentina, and the British Antarctic Survey. Funding was provided by the US National Geospatial-Intelligence Agency, DTU, ESA and NASA.

## References

- [1] J. Dall, S. S. Kristensen, V. Krozer, C. C. Hernández, J. Vidkjær, A. Kusk, J. Balling, N. Skou, S. S. Søjbjerg, and E. L. Christensen, "ESA'S POLARimetric Airborne Radar Ice Sounder (POLARIS): design and first results," *IET Radar, Sonar & Navigation*, vol. 4, no. 3, pp. 488–496, 2010.
- [2] K. C. Jezek, S. Gogineni, X. Wu, E. Rodriguez, F. Rodriguez-Morales, A. Hoch, A. Freeman, and J. G. Sonntag, "Two-Frequency Radar Experiments for Sounding Glacier Ice and Mapping the Topography of the Glacier Bed," *IEEE Transactions on Geoscience and Remote Sensing*, vol. 49, no. 3, pp. 920–929, 2011.
- [3] D. Bekaert, N. Gebert, C.-C. Lin, F. Hélière, J. Dall, A. Kusk, and S. S. Kristensen, "Surface Clutter Suppression Techniques for P-band Multi-channel Synthetic Aperture Radar Ice Sounding," in *EUSAR 2012*, Nuremberg, Germany, April 2012.
- [4] R. O. Schmidt, "Multiple emitter location and signal parameter estimation," *IEEE Trans. Antennas Propag.*, vol. 34, no. 3, pp. 276–280, 1986.
- [5] X. Wu, K. Jezek, E. Rodriguez, P. Gogineni, F. Rodriguez, and A. Freeman, "Ice Sheet Bed Mapping with Airborne SAR Tomography," *IEEE Trans. Geosci. Remote Sens.*, to be published.
- [6] R. Scheiber, P. Prats, and F. Hélière, "Surface Clutter Suppression Techniques for Ice Sounding Radars: Analysis of Airborne Data," in *Proc. of EUSAR 2008*, Friedrichshafen, Germany, June 2008.

## **Direction-of-Arrival Estimation for Radar Ice Sounding Surface Clutter Suppression**

Ulrik Nielsen and Jørgen Dall

Published in IEEE Transactions on Geoscience and Remote Sensing,  
vol. 53, no. 9, pp. 5170–5179, Sep. 2015.



# Direction-of-Arrival Estimation for Radar Ice Sounding Surface Clutter Suppression

Ulrik Nielsen, *Student Member, IEEE*, and Jørgen Dall, *Member, IEEE*

**Abstract**—Ice sounding radars are able to measure ice sheets by profiling their glaciological features from the surface to the bedrock. The current airborne and, in particular, future space-based systems are suffering from off-nadir surface clutter, which can mask the depth signal of interest. The most recent surface clutter suppression techniques are based on multi-phase-center systems combined with sophisticated coherent postprocessing. The performance of the techniques can be improved by accurate direction-of-arrival (DOA) estimates of the surface clutter. This paper deals with data-driven DOA estimation for surface clutter signals, which includes a formulation of the mathematical foundation of spatial aliasing. DOA estimation is applied to data acquired with the P-band POLarimetric Airborne Radar Ice Sounder at the Jutulstraumen Glacier, Antarctica. The effects of spatial aliasing related to a large phase center spacing are analyzed, and an unwrapping procedure is presented and applied to the data. Finally, DOA estimation of full-scene data is analyzed and used to show an along-track and incidence (off-nadir) angle dependent variation of the effective scattering center of the surface return, which is caused by a varying penetration depth.

**Index Terms**—Array signal processing, direction-of-arrival (DOA) estimation, ice sounding, radar remote sensing, spatial-spectral aliasing, surface clutter suppression.

## I. INTRODUCTION

**D**URING the last 150 years, the Earth system has been subject to radical changes. Both human-induced changes and the variability of the natural system have to be fully understood and quantified to determine whether the consequence could be destabilization of the Earth system. This insight implies understanding of the major subsystems and the coupling between them. For this reason, understanding of the cryosphere is one of the main objectives of the European Space Agency (ESA)'s Living Planet Programme [1].

### A. Radar Ice Sounding

Airborne ice sounding radars, or just sounders, have been used since the 1960s to measure ice sheets by profiling their glaciological features from the surface to the bedrock. Sounders

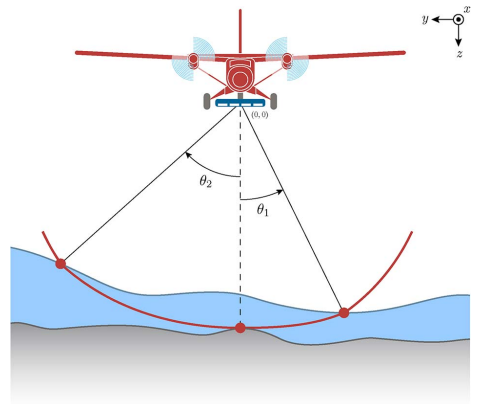


Fig. 1. Vertical cross section of an ice sounding scenario illustrating the across-track surface clutter geometry.

operate at low frequencies to avoid excessive attenuation of the transmitted and reflected signals within the ice. This way, sounders are able to penetrate deep into the ice and map the bedrock underneath. A comprehensive overview of systems developed before 1998 is presented in [2].

While airborne sounders are needed for detailed measurements of fast-flowing outlet glaciers, a space-based sounder might be capable of broad coverage with high spatial and uniform sampling over the interior of the ice sheets, which cannot be realized from an aircraft with a limited range. Therefore, when the International Telecommunication Union in 2003 allocated a 6-MHz band at 435 MHz (P-band) for remote sensing, a space-based ice sounding radar was proposed to ESA as a possible Earth Explorer mission. Due to lack of knowledge of ice sounding at frequencies as high as P-band, ESA commissioned the development of the POLarimetric Airborne Radar Ice Sounder (POLARIS) [3], with the objective of assessing the feasibility of ice sounding at P-band from space.

### B. Surface Clutter Suppression

Due to the curved wavefront of a propagating pulse, an echo backscattered from a certain ice depth will be received by the radar simultaneously with an echo backscattered by the surface within the same range resolution cell, as illustrated in Fig. 1. This surface component is referred to as surface clutter. The weak depth signal of interest may be masked by these off-nadir

Manuscript received August 6, 2014; revised December 20, 2014; accepted February 21, 2015. This work was supported by the U.S. National Geospatial-Intelligence Agency, by the Technical University of Denmark (DTU), by the European Space Agency, and by the National Aeronautics and Space Administration.

The authors are with the Department of Microwaves and Remote Sensing, National Space Institute, Technical University of Denmark, 2800 Kongens Lyngby, Denmark (e-mail: ulrik@space.dtu.dk; jd@space.dtu.dk).

Color versions of one or more of the figures in this paper are available online at <http://ieeexplore.ieee.org>.

Digital Object Identifier 10.1109/TGRS.2015.2418221

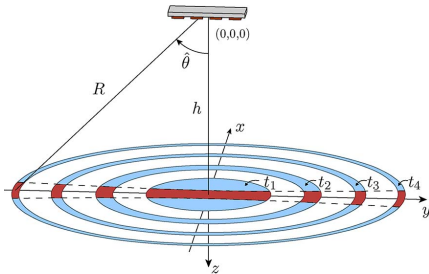


Fig. 2. Doppler-processed surface resolution cells at different time instants. The resolution cells are illustrated by the red areas enclosed by the dashed black hyperbola. The blue annuli are the corresponding pulse limited resolution cells without Doppler processing.

surface clutter signals located at the same electrical distance as the depth signal from nadir.

Assuming flat topography and a nadir-looking sensor, the clutter footprints corresponding to different ice depths are described by annuli, as illustrated in Fig. 2. Clutter scattered in the along-track direction can effectively be suppressed for a synthetic aperture system by Doppler processing. This way, the problem reduces to the across-track direction in the form of surface returns from two angles ( $\pm\theta$ ) symmetric about nadir. In the case of sloped, undulating, or more complex topography, the surface clutter can consist of returns from multiple nonsymmetric angles that are a function of both range and along-track position, which can be intuitively deduced from the geometry in Fig. 1.

It is shown [4] that surface clutter is the primary scattering mechanism that obscures the subsurface echoes at higher operating altitudes, and surface clutter is therefore a major issue in space-based ice sounding.

Airborne sounders have traditionally dealt with surface clutter by employing large antennas in the across-track direction, combined with low altitude. This way, across-track clutter is suppressed for large off-nadir angles, due to the antenna pattern and the backscattering pattern of the ice surface. For a space-based sounder, a high altitude is implied by the orbit, and the antenna dimensions are restricted by the launch vehicle. Therefore, alternative and more sophisticated clutter suppression techniques are needed. Although the problem of surface clutter is less pronounced for airborne systems, sounding of areas with complex topography and roughness, such as heavily crevassed glaciers, is still a major technical challenge due to surface clutter.

The current research focus, which is related to surface clutter suppression, is based on a multi-phase-center antenna combined with sophisticated coherent postprocessing. By using an antenna array aligned in the across-track direction combined with a multichannel receiver, beamforming techniques can be used to synthesize adaptive antenna patterns that suppress the surface clutter from off-nadir angles while a high gain is maintained in the nadir direction.

Early studies based on this technique are presented in [5]. The first experiments used beamsteering to coherently combine the channels [4]. Recent studies have used the opti-

mum beamformer [6], null steering [5], [7], and the minimum variance distortionless response (MVDR) beamformer [8] for clutter suppression. The latter is also referred to as the Capon beamformer. A comparison of the algorithms based on simulations and POLARIS data can be found in [9].

MVDR exploits the covariance matrix of the received signal to minimize the output power by constraining unity gain in the nadir direction while trying to suppress signals coming from all other directions. The MVDR is, in this sense, adaptive and optimal, but the drawback is its lack of robustness for some scenarios. If the desired subsurface signal is received from a direction slightly different from what is expected (nadir), the MVDR beamformer suppresses it, which is a phenomenon known as self-nulling [10].

On the other hand, null steering and the optimum beamformer require knowledge of the direction of arrival (DOA) of the clutter signals. This implies a more cumbersome implementation and a potentially degraded performance compared with MVDR, depending on the clutter scenario. The advantage is more control of the synthesized patterns, which thereby offers robustness. Most studies have relied on assumptions or models of the topography to estimate the surface clutter DOA. However, even for fairly simple scenes, this approach might lead to inaccurate DOA estimates that degrade the suppression performance. Even if high-accuracy surface models are available, due to penetration, this might not describe the surface defined by the effective scattering center at P-band, which is the one needed for the DOA-based clutter suppression.

In [7], the authors of this paper showed that a data-driven DOA estimation leads to a better clutter suppression than a model-based one. The DOA estimation is based on the maximum-likelihood (ML) estimator that has been used by Wu *et al.* [11] for bed topography mapping.

### C. Spatial Aliasing

In order to reduce the system complexity and development costs, the number of receive channels is, in general, kept at a minimum. At the same time, a large antenna length in the across-track dimension with a large number of elements is desired for obtaining high gain and angular resolution. Therefore, multiple elements might be connected to each of the receive channels, and the resulting spacing of the effective phase centers can be up to several wavelengths. This implies ambiguities known as grating lobes or, when seen from a signal processing point of view, spatial aliasing, which complicates both DOA estimation and beamforming.

In this paper, we deal with DOA estimation for surface clutter suppression in the presence of spatial aliasing. We present results based on data acquired with the POLARIS system in East Antarctica in 2011. With a data-driven DOA estimation approach, we present how the effective scattering center elevation of the air-ice interface and near-surface volume changes along the flight track and with incidence angle. This finding is highly relevant in relation to the development of efficient suppression algorithms [7]. Furthermore, the variations can be used to characterize the ice surface and in this way directly provide glaciological information.

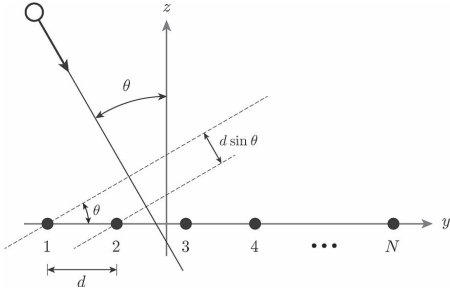


Fig. 3. ULA with incoming plane wave.

#### D. Paper Outline

This paper is organized as follows. In Section II, the problem of DOA estimation is summarized along with a formulation of the mathematical foundation of spatial aliasing. Details on the POLARIS system are provided in Section III. In Section IV, we apply DOA estimation and the spatial sampling theory (see Section II) to spatially undersampled ice sounding data. Finally, in Section V, we summarize and conclude this paper.

## II. DOA

Since the antenna dimensions are small relative to the ranges of the surface and volume resolution cells, the plane wave approximation is valid for the corresponding returns. This way, a return received from a specific direction by each of the antenna phase centers, or sensors, can be modeled as a constant signal, but with a progressive time delay across the array. Assuming narrow-banded signals, such a time delay corresponds to a phase shift, as illustrated for a uniform linear array (ULA) in Fig. 3. The problem of determining the directions of received returns is identical to what is known as the *source location problem* [12] within spatial-spectral estimation theory. The general signal model inherited from this field will now be described and extended in order to feature spatial aliasing.

Based on Fig. 3, the signal received by the  $N$  sensors can be expressed in vectorial form as

$$\mathbf{x}(t) = \mathbf{a}(\theta)s(t) + \mathbf{e}(t) \quad (1)$$

where  $\mathbf{x}(t)$  is an  $N \times 1$  vector,  $s(t)$  is the complex echo signal at a reference sensor,  $\mathbf{e}(t)$  is an additive Gaussian noise component, and  $\mathbf{a}(\theta)$  is the so-called steering vector. The steering vector describes the phase shifts at each of the sensors, i.e.,

$$\mathbf{a}(\theta) = [e^{-j\omega_c \tau_1} \quad \dots \quad e^{-j\omega_c \tau_N}]^T \quad (2)$$

where  $(\cdot)^T$  is the transpose operator,  $\omega_c$  is the center angular frequency, and  $\tau_n$  is the time delay at the  $n$ th sensor relative to the reference. For a ULA, the steering vector can be expressed as

$$\mathbf{a}(\theta) = [1 \quad e^{-j\omega_s} \quad \dots \quad e^{-j(N-1)\omega_s}]^T \quad (3)$$

where

$$\omega_s = kd \sin \theta, \quad \text{for } \theta \in [-90^\circ, 90^\circ] \quad (4)$$

with  $k = 2\pi/\lambda$  denoting the wavenumber and  $d$  the sensor spacing. The restriction on  $\theta$  is required in order to avoid the geometric symmetric ambiguities, which are related to planar arrays. It is shown that (3) is completely analog with a vector of uniform samples of the complex sinusoid  $e^{-j\omega_s t}$ . Motivated by this analogy,  $\omega_s$  is called the spatial angular frequency.

#### A. Spatial Aliasing

In order to ensure that  $\mathbf{a}(\theta)$  is uniquely defined (i.e., to avoid spatial aliasing), we see from (3) that the following condition must be satisfied:

$$\begin{aligned} |\omega_s| &< \pi \\ \Leftrightarrow d &< \frac{\lambda}{2|\sin \theta|} \quad \forall \theta. \end{aligned} \quad (5)$$

This way, for  $\theta \in [-90^\circ, 90^\circ]$ , we get the well-known [13] constraint, i.e.,  $d < \lambda/2$ , in order to avoid aliasing. From the analogy with temporal sampling, (6) can be interpreted as a spatial Nyquist–Shannon sampling theorem. For a given sensor spacing, the spatial Nyquist frequency in  $\theta$ -space can be derived from (6), i.e.,

$$\theta_{\text{NQ}} = \arcsin \frac{\lambda}{2d}, \quad \text{for } d \geq \lambda/2. \quad (7)$$

Again, analog to a temporal sinusoid, we have that

$$e^{-j(\omega_s + 2\pi m)n} = e^{-j\omega_s n} \quad \forall m, n \in \mathbb{Z} \quad (8)$$

which shows that a spatial discrete-time sinusoid of any frequency is identical to some sinusoid of frequency  $\omega_f$  in the fundamental spatial frequency range  $[-\pi, \pi]$ , i.e.,

$$\omega_s = \omega_f + 2\pi m, \quad |\omega_f| \leq \pi \wedge m \in \mathbb{Z}. \quad (9)$$

By combining (4) and (9), we can relate a spatial angular frequency in the fundamental range to the corresponding set of undersampled DOA angles

$$\theta = \arcsin \frac{\omega_f + 2\pi m}{kd}. \quad (10)$$

#### B. Estimation Algorithms

The case of  $Q$  simultaneously received echo signals with different DOAs can be modeled as an extension of (1) by making use of the superposition principle

$$\mathbf{x}(t) = \mathbf{A}(\Theta)s(t) + \mathbf{e}(t) \quad (11)$$

where  $\mathbf{A}$  is the  $N \times Q$  steering matrix formed by columnwise concatenation of the steering vectors corresponding to each of the  $Q$  signals, and  $\mathbf{s}(t)$  is a vector collecting the  $Q$  signals at time  $t$ , i.e.,

$$\mathbf{s}(t) = [s_1(t) \quad \dots \quad s_Q(t)]^T. \quad (12)$$

The steering matrix  $\mathbf{A}$  is a function of  $\Theta$ , which is a vector containing the  $Q$  DOA angles.

The  $N \times 1$  vector  $\mathbf{x}(t_m)$  constitutes a sample of the array at time instant  $t_m$ . Such an array sample is denoted a *snapshot*.



When  $t_1, \dots, t_M$  denotes the time instants at which  $M$  snapshots of a specific target are acquired, a complete data model can be expressed as

$$\mathbf{X} = \mathbf{A}(\Theta)\mathbf{S} + \mathbf{E} \quad (13)$$

where  $\mathbf{X}$  and  $\mathbf{E}$  are  $N \times M$  matrices,  $\mathbf{A}$  is  $N \times Q$ , and  $\mathbf{S}$  is  $Q \times M$ . Each column in  $\mathbf{X}$ ,  $\mathbf{S}$ , and  $\mathbf{E}$  corresponds to a specific snapshot. For further details, see [11].

Many algorithms have been proposed for estimation of the DOA angles contained in  $\Theta$ . Conventional methods such as beamsteering are suffering from low resolution, which, on the other hand, is significantly improved with MVDR. The common advantage of these two nonparametric methods is that they do not assume anything about the statistical properties of the data. However, in cases where such information is available, algorithms such as the subspace-based Multiple Signal Classification (MUSIC) [14] and the parametric ML [15] algorithm can more fully exploit the signal structure to provide superresolution at the cost of increased computational load. The primary underlying assumptions for these two algorithms are that the impinging signals can be considered as narrow-banded plane waves and that the number of these is known and less than the number of sensors.

Computationally, MUSIC is a simpler estimator than ML, which, on the other hand, in general, is able to offer better performance, particularly at low SNR or for highly correlated signals [15], [16]. MUSIC and ML provide the similar performance, which is close to the Cramér–Rao bound for reasonably high SNR [17].

The ML solution [15] of the DOA vector can be expressed as

$$\hat{\Theta}_{\text{ML}} = \min_{\Theta} \text{tr} \left[ \mathbf{A}(\Theta) \left( \mathbf{A}^H(\Theta) \mathbf{A}(\Theta) \right)^{-1} \mathbf{A}^H(\Theta) \mathbf{R} \right] \quad (14)$$

where  $\text{tr}[\cdot]$  is the trace of the bracketed matrix,  $(\cdot)^H$  is the Hermitian transpose, and  $\mathbf{R}$  is the  $N \times N$  data covariance matrix estimated as

$$\mathbf{R} = \frac{1}{M} \sum_{m=1}^M \mathbf{x}(t_m) \mathbf{x}^H(t_m). \quad (15)$$

DOA estimation with ML under the assumption of  $Q$  signal components involves a computational intensive  $Q$ -dimensional search. However, using the alternating projection algorithm [15] based on alternating maximization, the optimization problem is transformed into a sequence of much faster 1-D searches. Furthermore, the algorithm exploits the projection-matrix update formula [15], which provides a computationally efficient scheme for the problem at hand.

### III. SYSTEM DESCRIPTION

POLARIS [3] is a nadir-looking fully polarimetric sounding radar featuring aperture synthesis. The system is operating at P-band (435 MHz) and is developed by the Technical University of Denmark (DTU) for ESA. POLARIS is equipped with a multi-phase-center antenna and a multichannel receiver, which, in its multiaperture configuration, supports single-polarization

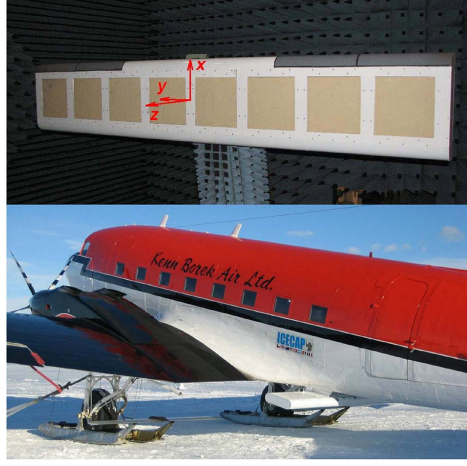


Fig. 4. POLARIS eight-element antenna array: (top) under measurement in the DTU-ESA Spherical Near-Field Antenna Test Facility at DTU and (bottom) mounted under the fuselage behind the wings of the Basler DC-3 aircraft.

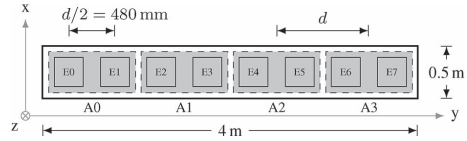


Fig. 5. POLARIS eight-element antenna array showing how the elements (E0–E7) are combined into four subapertures (A0–A3).

coherent surface clutter suppression through offline processing techniques. POLARIS was tested with a four-element antenna [18] over Greenland in 2008 and again in 2009, where the capabilities of profiling the bedrock at 3000-m depth were demonstrated. In 2010, POLARIS was upgraded with an eight-element (E0–E7) ULA of quadratic patches [19] aligned in the across-track direction, as shown in Fig. 4. The array elements are divided into four subapertures (A0–A3), each consisting of two neighboring elements, as sketched in Fig. 5. All elements are used for transmission with uniform weighting. POLARIS is equipped with a four-channel receiver, where each receive channel is connected to one of the four subapertures. The element spacing is 480 mm, but from an array signal processing point of view, the relevant parameter is the spacing of the effective phase centers corresponding to that of the subapertures, i.e.,  $d = 2 \cdot 480$  mm. This parameter corresponds to the sensor spacing in the signal model in Section II. At the given operating frequency, this spacing corresponds to 1.4 times the wavelength, which makes spatial aliasing possible according to (6).

POLARIS employs pulse compression using linear frequency modulation pulse chirping with a bandwidth of up to 85 MHz. The transmitted chirp is weighted with a 5% Tukey time-domain window in order to suppress distance sidelobes of the compressed pulse [3].

For the Antarctica campaign, POLARIS was installed in the Basler DC-3 aircraft of Kenn Borek Air Ltd.

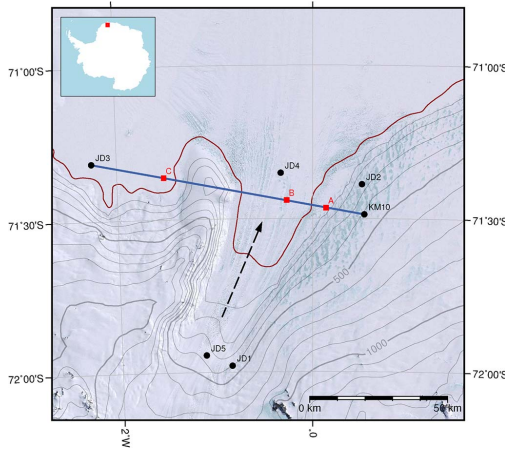


Fig. 6. Overview map with flight track for the acquired POLARIS data over the Jutulstraumen Glacier. The black dashed arrow indicates the direction of the glacier flow. Imagery is from the Landsat Image Mosaic of Antarctica [20]. Grounding line (dark red) is from the ASAlD project based on Landsat-7 imagery and ICESat/GLAS laser altimetry [21]. Contours are generated from 2-Minute Gridded Global Relief Data (ETOPO2).

#### IV. APPLICATION TO MEASURED DATA

In February 2011, POLARIS acquired multi-phase-center data over the Jutulstraumen Glacier, Antarctica, as part of the IceGrav campaign. A nominal flight track approximately perpendicular to the glacier flow was defined by the two waypoints JD3 and KM10, as illustrated in Fig. 6. Data from four separate passes were acquired—two westbound and two eastbound, namely, EW1, EW2, WE1, and WE2. In the figure, three locations are defined along the track: locations A, B, and C. East of location C, the track passes over a peninsula with grounded ice. At the east end of the track where the terrain starts rising, the ice is also grounded. Otherwise, the track consists of ice shelf with low across-track topographic variations.

During a reconfiguration of POLARIS from polarimetric mode to multichannel mode, a  $180^\circ$  phase shift was erroneously introduced to the right-hand side of the array (A2–A3). This introduced a nadir null in the transmit pattern. The erroneous transmit pattern has been synthesized from test facility measurements of the individual subapertures, as shown in Fig. 7. The null is narrow and with finite depth; thus, the nadir return is detectable, but with reduced sensitivity.

A pulse length of  $2 \mu\text{s}$  was used in combination with the maximum bandwidth of 85 MHz.

##### A. SAR Processing

The data are range compressed using a Blackman-weighted matched filter. A time-domain back-projection algorithm [22] is used for the SAR focusing and geocoding. As opposed to frequency-domain-based processing, this algorithm allows an

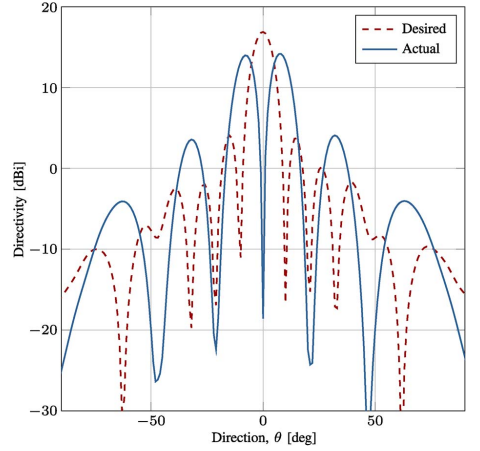


Fig. 7. Transmit antenna pattern estimate. The actual (erroneous) pattern has been synthesized from measured patterns of the individual subapertures.

accurate accommodation of surface slopes, sensor flight track variations, and refraction at the air–ice interface. The algorithm is shown to improve the quality of the focused data compared with conventional frequency-domain sounder processing, but at the cost of increased computational load.

The data are focused to a regular grid with a pixel spacing of 1 m in range and 1.5 m in the along-track direction.

An echogram for the WE1 pass is shown in Fig. 8, which includes annotation of the three defined locations.

##### B. Spectral Aliasing and Unwrapping

A two-signal ML DOA estimation, corresponding to the left and right clutter signals, is applied to each range bin in every line of the scene. A moving average of 21 snapshots in the along-track direction is used to estimate the covariance matrix. Following this procedure, the snapshots correspond to azimuth looks in SAR terminology. The estimated DOA as a function of equivalent nadir depth at location A is shown in Fig. 9. Equivalent nadir depth is defined as

$$z = \frac{R - h}{\sqrt{\epsilon_{\text{ice}}}}, \quad R \geq h \quad (16)$$

where  $h$  is the sensor height above the ice surface at nadir, and  $\epsilon_{\text{ice}}$  is the relative permittivity of ice.  $R$  is the range in air given by

$$R = \frac{ct_d}{2} \quad (17)$$

where  $t_d$  is the two-way propagation delay time, and  $c$  is the speed of light in air. The estimate in Fig. 9 is an incoherent average over 350 lines (525 m in along-track), where each line has been roll corrected. Before averaging, the data are filtered, as described in detail at the end of the subsection. Gaps in the curve indicate range gates with no valid data points. The figure

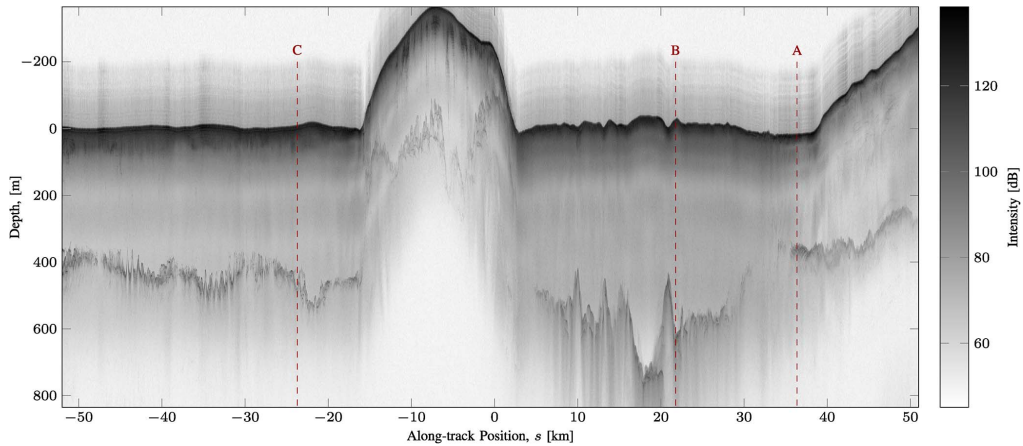


Fig. 8. SAR focused echogram of the WE1 pass. The receive pattern is nadir looking, synthesized using beamsteering. The depth axis is relative to the mean surface elevation of the ice shelf.

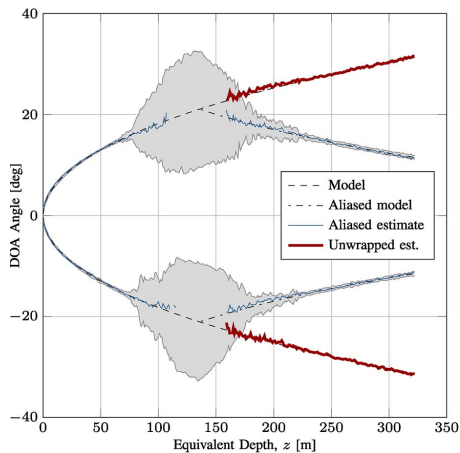


Fig. 9. Two-signal ML DOA estimate from pass WE1 at location A with spatial aliasing (blue). The aliased part of the estimate is unwrapped and plotted separately (red). A simulation based on a flat surface model is shown (black dash-dotted curve) with and (black dashed curve) without aliasing. The estimate is an incoherent average over 350 lines (525 m), where  $\pm 1$  RMSE with respect to the aliased model is represented by the gray shaded area. The sensor height above surface is 3350 m.

also includes a simulation based on a flat surface model corresponding to the geometry in Fig. 2, where the simulated DOA is given by

$$\hat{\theta} = \arccos\left(\frac{h}{R}\right). \quad (18)$$

The sensor height is estimated from the radar data as the range of the first surface return. A constant relative permittivity equal to 3.15 is assumed for the ice.

From (7), we get that the spatial Nyquist frequency corresponds to  $21^\circ$ . By inverting (18) and combining with (16), this corresponds to an equivalent nadir depth of 134 m. Therefore, spatial frequencies corresponding to larger angles are aliased. According to this, an aliased version of the model is also included in the figure. Based on the data points from the 350 lines, the root-mean-square error (RMSE) is calculated with respect to the aliased model. Before the calculation, extreme outliers defined as data points with opposite sign compared with the model are removed.

Down to a depth of 75 m, the estimate fits the model very well. As we get closer to the equivalent Nyquist depth, the estimate becomes noisy and starts deviating from the model. Below 200 m, the noise again decreases, and a deterministic signal is clearly estimated. Since the signal at these depths is undersampled, the estimate is corrected by shifting the positive and negative branches by an amount corresponding to  $\mp 2\pi$  in spatial angular frequency, respectively, according to (10). As shown in the figure, the corrected estimate is clearly in agreement with the model. This way, an aliased estimate of a regular scene can be unwrapped by using (10) and some rough prior knowledge of the topography.

The deviations around the Nyquist depth are caused by more factors. First of all, the first off-nadir null in the transmit antenna pattern coincides with the Nyquist angle. Therefore, the surface return is highly attenuated around the Nyquist depth, which gives rise to increased noise. Furthermore, as the attenuation of the surface return is increasing, the near-surface volume scattering becomes more dominant. This will lower the effective scattering center, which results in smaller estimated DOA angles and thereby a deviation from the model. Third, the signal model with the assumption of two signal components might in practice not be valid near the Nyquist depth due to noise combined with a limited angular resolution. This way, only one effective signal component might be present, which can lead to the second signal estimated being artificial.

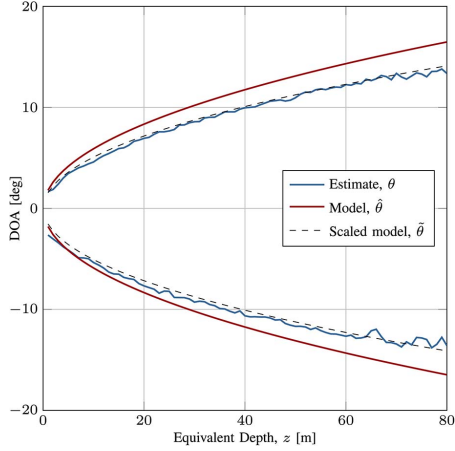


Fig. 10. Two-signal ML DOA estimate from pass WE1 at location B (blue). A simulation based on a flat surface model is included (red) along with a corresponding spatial frequency scaled version that fits the estimate (black dashed curve). The estimate is an incoherent average over 350 lines (525 m). The sensor height above surface is 3300 m.

For these reasons, the data are filtered before the incoherent averaging by removing any points that deviate more than 10% from the model. The threshold is chosen large enough such that the filtering does not affect the estimate outside the depth range from 75 to 200 m.

### C. Effective Surface Scattering Center

The same DOA estimation is repeated at location B, but now only considering the near-nadir part of the estimate that is nonaliased and undistorted. The estimate is seen as the blue curve in Fig. 10. A clear systematic deviation from the model is evident at location B. It turns out that the deviation can be modeled by a scaling of the spatial model frequency. Motivated by this, a scaled spatial angular model frequency  $\tilde{\omega}_s$  is defined as  $\tilde{\omega}_s$  from (4) divided by a given parameter  $a$ , i.e.,

$$\tilde{\omega}_s = a^{-1} \omega_s, \quad a \in \mathbb{R}^+. \quad (19)$$

The scaled DOA model with a scaling parameter equal to  $a = 1.16$  is shown as the dashed curve in the figure, which is seen to fit the estimate very well. Based on this, the scaling parameter is considered as a measure of the deviation between the estimated DOA and the reference in terms of the flat surface model simulation.

The following analysis suggests that the deviation is related to a penetration depth of the clutter signal, which is varying as a function of both the along-track position and the off-nadir angle. A scaling parameter  $a > 1$  means that the estimated spatial frequency, and thereby the DOA, is numerically lower than that of the model assuming pure surface scattering (see Fig. 2). For a given range cell, a smaller DOA corresponds to increased penetration in terms of a deeper located effective scattering

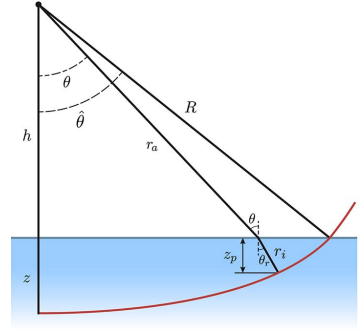


Fig. 11. Geometry of the modeled and estimated DOA illustrating the corresponding penetration depth.

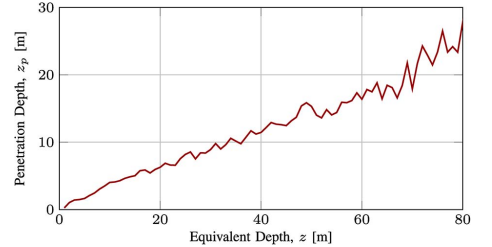


Fig. 12. Penetration depth corresponding to the observed deviation of the DOA estimate at location B.

center, as illustrated in Fig. 11. The off-nadir penetration length is defined as

$$r_i = \frac{R - r_a}{\sqrt{\epsilon_{ice}}}, \quad R \geq r_a \quad (20)$$

where

$$r_a = \frac{h}{\cos \theta} \quad (21)$$

is the range from the radar to the point of refraction at the ice surface. The penetration depth is then defined as the vertical projection of the penetration length

$$z_p = r_i \cos \theta_r \quad (22)$$

where  $\theta_r$  is the angle of refraction. This way, the deviation in Fig. 10 corresponds to the penetration depth shown in Fig. 12. As shown in the figure, the DOA deviation at 80-m equivalent nadir depth corresponds to a 27-m vertical penetration of the surface signals.

Simulations are performed in order to access the impact of such penetration on surface clutter suppression based on DOA models. The simulations are based on null steering with a signal-to-clutter ratio of  $-10$  dB, a sensor height above surface equal to 3300 m, two uncorrelated clutter signals from  $\pm 11^\circ$ , and are, otherwise, matching the parameters of the POLARIS system. The simulations show a 10-dB increase in the estimated

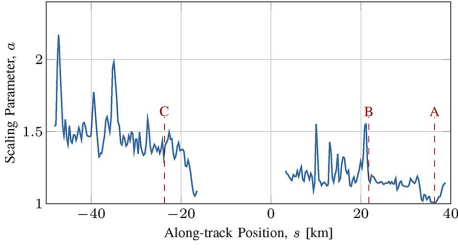


Fig. 13. Scaling parameter for WE1 with the peninsula masked out.

intensity of the nadir signal for a 27-m uncompensated penetration of the clutter signals.

In order to test the hypothesis of an along-track varying penetration depth, we investigate the deviation along the entire track for all four passes. In order to do this, we have designed an automated fitting procedure for the scaling parameter. The procedure is described in the following.

The first surface return in each line is detected and used to flatten the data with respect to nadir surface elevation changes. The DOA is estimated using the ML estimator with a two-signal search based on nine snapshots in the along-track direction. The DOA estimate is divided in the along-track direction into segments of 200 lines. For each segment, samples with an equivalent clutter depth between 10 and 40 m are used to calculate the RMSE of the DOA estimate with respect to the scaled model, i.e.,

$$\text{RMSE}(a, \theta_{\text{offs}}) = \sqrt{\frac{1}{N} \sum_{n=1}^N (\theta_n - \tilde{\theta}_n(a) + \theta_{\text{offs}})^2} \quad (23)$$

where  $N$  is the number of samples,  $\theta$  is the DOA estimate,  $\tilde{\theta}(a)$  is the DOA predicted by the scaled model, and  $\theta_{\text{offs}}$  is an angular offset to handle any minor across-track slopes or uncompensated aircraft roll residuals. Both of the two surface signal DOA estimates are included in the RMSE calculation. The RMSE is then minimized with respect to the scaling and the offset parameter as a 2-D optimization problem. The scaling parameter minimizing the function is stored for the along-track position corresponding to the center of the segment, whereas the offset parameter is disregarded in the further analysis.

To be able to directly compare all four passes, the scaling parameter for each pass is resampled to a common grid. An  $(s, c, h)$  coordinate system [23] aligned with the flight track is defined.  $(s, c, h)$  coordinates are curvilinear coordinates defined on a sphere that locally approximates the reference ellipsoid, where  $s$  is the along-track coordinate,  $c$  is the across-track coordinate, and  $h$  is the altitude above the reference sphere. The origin of the coordinate system is set at the midpoint of the nominal flight track. The radius of the approximating sphere is chosen as the radius of curvature of the WGS84 reference ellipsoid in the along-track direction, evaluated at the origin. The positive  $s$ -direction is from JD3 toward KM10, i.e., eastward. An equidistant grid is now defined in the  $s$ -dimension of this system to which the data are resampled.

TABLE I  
CORRELATION OF THE SCALING PARAMETER BETWEEN PASSES

	EW1	EW2	WE1	WE2
EW1	1.00			
EW2	0.90	1.00		
WE1	0.62	0.63	1.00	
WE2	0.85	0.84	0.67	1.00

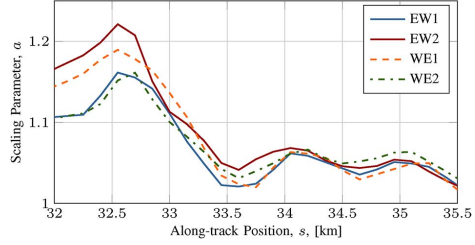


Fig. 14. Zoom of the parameter signal for all four passes.

Since the flat surface model is inappropriate at the peninsula, the fitted scaling parameter is unreliable for this region. The corresponding data are therefore masked out in all plots and disregarded in the further analysis.

When the scaling parameter is considered as a function of along-track position, it is referred to as the *parameter signal*. The resampled parameter signal for WE1 is shown in Fig. 13.

The signal is seen to vary along the track in terms of a slow negative linear trend overlaid by some faster smaller variations, including a number of distinctive spikes. To test the null hypothesis stating that the variations could be an artefact, e.g., introduced by the system or related to the acquisition, the data from the different passes are mutually correlated. The moving average based on 100 datapoints (30 km) is subtracted from each parameter signal before correlating. The correlation coefficients of the mutual correlations are shown in Table I. The coefficients vary from 0.62 to 0.90 between the different combinations, suggesting that the parameter variation is not an artefact and therefore is related to the ice. A zoom of the parameter signal for all four passes is shown in Fig. 14, which illustrates the correlation between the signals.

In addition to the mutual correlations of the different passes, the parameter signal is also correlated with the intensity of the radar reflection for each pass separately. The intensity signal is extracted in the along-track direction at a fixed range. Correlations are in this way performed for a number of range gates. The results are shown in Fig. 15, where the range is expressed as the nominal DOA according to the flat surface model in (18). Before each correlation, the moving average is subtracted from both of the two signals.

To assess any along-track variation of the correlation coefficient, the signals are divided into nonoverlapping segments of 100 datapoints (30 km). Corresponding segments of the scaling parameter and the intensity are correlated, and statistics based on all segments from all passes are calculated and presented in the figure. A large variation is observed for the near-nadir



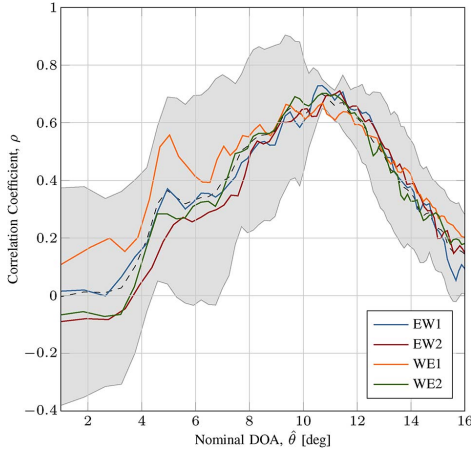


Fig. 15. Along-track correlation coefficient of the scaling parameter and the radar reflection intensity for each pass. The independent variable (nominal DOA) represents the simulated off-nadir angle at which the intensity signal is extracted. The dashed black line is the average of the four passes. The gray shaded area represents the distance of  $\pm 1$  standard deviation from the mean.

TABLE II  
CORRELATION OF SCALING PARAMETER AND INTENSITY FOR EACH PASS

EW1	EW2	WE1	WE2
0.75	0.71	0.72	0.73

returns, whereas a relatively low variation is seen at larger off-nadir angles with a minimum around  $11^\circ$ . In addition to the minimum variation, the correlation coefficients themselves attain a maximum at this same DOA. The correlation coefficients at this extremum are presented in Table II. The relatively high correlation coefficients strengthen the hypothesis of a relation between the ice characteristics and the scaling parameter.

The hypothesis of varying penetration as the underlying mechanism is supported by the three following observations.

First, in Fig. 13, it is shown that the scaling parameter is larger than 1 for all along-track positions, which is consistent with the occurrence of a lowered effective scattering center.

Second, the intensity waveforms at locations A, B, and C (see Fig. 8) indicate different dominating scattering mechanisms, which can explain the variation in depth of the effective scattering center. The A-scopes for the three locations are shown in Fig. 16. At location A, the shape of the two-way antenna pattern is clearly seen in the intensity. This indicates that the signal is dominated by scattering related to the air-ice interface, and therefore also is in agreement with the model ( $a \approx 1$ ). When looking at locations B and C, the scaling increases, and the shape of the antenna pattern becomes less distinct. This indicates that the scattering is less dominated by an interface but rather volume scattering, which means larger penetration. The antenna pattern is smeared out in the case of volume scattering since the wave is reflected from a large DOA range, which makes the effective backscattering coefficient insensitive to a

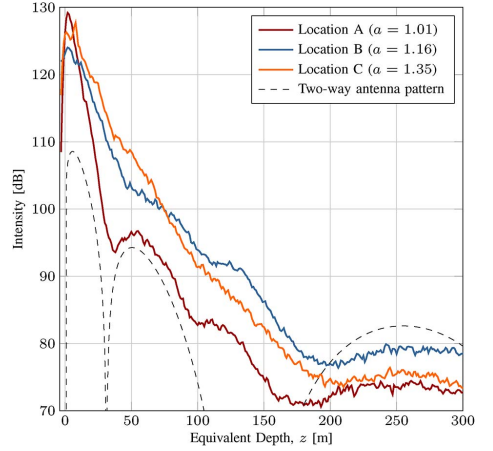


Fig. 16. A-scopes at locations A, B, and C in pass WE1. The receive pattern is nadir looking, synthesized using beamsteering. Simulated normalized two-way antenna power pattern is included for comparison.

narrow null. Furthermore, the stronger peak with faster rise and fall times at location A is also characteristic for surface scattering. A larger specular component due to the smooth ice surface increases the received power at very small incidence angles, whereas increased forward scattering decreases the backscatter power at larger angles.

Third, the extremum at  $11^\circ$  in Fig. 15 coincides with the first null in the nadir-looking receive pattern, which corresponds to the dashed curve (desired transmit pattern) in Fig. 7. This means that the extremum occurs where the gain toward the surface is low, which could indicate that the correlation is related to volume scattering. Since the correlation coefficients are positive, high radar intensity corresponds to a large DOA deviation and thereby a large penetration depth. This is consistent in the way that stronger volume scattering would be expected for a lowered effective scattering center.

The analysis suggests a relation between penetration depth and intensity. The interpretation of this is a glaciological aspect that will not be treated further in this paper.

## V. CONCLUSION

The problem of spatial aliasing is relevant in relation to possible future space-based ice sounding systems. A large spacing of the effective array phase centers and thereby possible spatial undersampling might be the compromise in order to reduce system complexity while at the same time maintaining a large antenna length. In relation to this, we have formulated the problem of DOA ambiguities for a ULA as spatial aliasing and provided the mathematical foundation that is analog to what is known from the classical sampling theory. We have estimated the DOA of spatially undersampled ice sounding data and used the spatial sampling theory to successfully unwrap aliased surface returns.

Furthermore, we have analyzed the estimated surface DOA for multiple passes of the same scene and observed a deviation in the DOA estimate compared with a flat surface model. The deviation varies as a function of geographic location, and the analysis suggests a varying depth of the effective phase center as the underlying mechanism. This finding is highly relevant in relation to the development of DOA-based surface clutter suppression algorithms, where simulations show that the reported DOA deviations can significantly degrade the suppression performance. This applies to algorithms based on simple surface models and even when high-accuracy digital elevation models are used. Such models represent the physical air-ice interface and not the surface defined by the effective phase center as seen by a low-frequency sounding radar. By using a correlation-based method, the DOA deviation as a function of along-track position is compared with the radar intensity of the surface return for a range of off-nadir angles. It is found that the correlation coefficient attains a positive maximum at an off-nadir angle corresponding to minimum antenna gain toward the surface. This suggests that the variation in depth of the effective phase center is related to the intensity of the volume scattering.

In addition to the finding itself and its relevance in relation to clutter suppression, the presented method is a novel application of DOA estimation, which can be used to characterize the ice surface and in this way directly provide glaciological information.

#### ACKNOWLEDGMENT

The POLARIS data acquisition campaign was part of the ICEGRAV project—a DTU airborne geophysics project in cooperation with the University of Texas, the Norwegian Polar Institute, the University of Bergen, Instituto Antartico (Argentina), and the British Antarctic Survey.

The authors would like to thank S. S. Kristensen (DTU), who operated the POLARIS system during the Antarctic campaign, and A. Kusk (DTU) for SAR processing of the data. Finally, they would also like to thank the two anonymous reviewers for their helpful comments and suggestions.

#### REFERENCES

- [1] B. Batrick, Ed., "The changing earth," Eur. Space Agency Publications Division, Noordwijk, The Netherlands, SP-1304, Jul. 2006.
- [2] S. Gogineni, T. Chuah, C. Allen, K. Jezek, and R. Moore, "An improved coherent radar depth sounder," *J. Glaciol.*, vol. 44, no. 148, pp. 659–669, 1998.
- [3] J. Dall *et al.*, "ESA's POLarimetric Airborne Radar Ice Sounder (POLARIS): Design and first results," *IET Radar, Sonar Navigat.*, vol. 4, no. 3, pp. 488–496, Jun. 2010.
- [4] K. C. Jezek *et al.*, "Two-frequency radar experiments for sounding glacier ice and mapping the topography of the glacier bed," *IEEE Trans. Geosci. Remote Sens.*, vol. 49, no. 3, pp. 920–929, Mar. 2011.
- [5] R. Scheiber, P. Prats, and F. Hélière, "Surface clutter suppression techniques for ice sounding radars: Analysis of airborne data," in *Proc. EUSAR*, Friedrichshafen, Germany, Jun. 2008.
- [6] D. Bekaert *et al.*, "Multichannel surface clutter suppression: East Antarctica P-band SAR ice sounding in the," *Ann. Glaciol.*, vol. 55, no. 67, pp. 9–21, Jul. 2014.
- [7] U. Nielsen, J. Dall, A. Kusk, and S. S. Kristensen, "Coherent surface clutter suppression techniques with topography estimation for multi-phase-center radar ice sounding," in *Proc. EUSAR*, Nuremberg, Germany, Apr. 2012, pp. 247–250.
- [8] J. Li *et al.*, "High-altitude radar measurements of ice thickness over the Antarctic and Greenland Ice sheets as a part of operation IceBridge," *IEEE Trans. Geosci. Remote Sens.*, vol. 51, no. 2, pp. 742–754, Feb. 2013.
- [9] R. Scheiber *et al.*, "Comparison of digital beamforming techniques for enhanced ice sounding radar data processing," in *Proc. EUSAR*, Berlin, Germany, Jun. 2014, pp. 32–35.
- [10] S. Kogon, "Robust adaptive beamforming for passive sonar using eigenvector/beam association and excision," in *Proc. SAM*, Washington, DC, USA, Aug. 2002, pp. 33–37.
- [11] X. Wu *et al.*, "Ice sheet bed mapping with airborne SAR tomography," *IEEE Trans. Geosci. Remote Sens.*, vol. 49, no. 10, pp. 3791–3802, Oct. 2011.
- [12] P. Stoica and R. L. Moses, *Introduction to Spectral Analysis*. Englewood Cliffs, NJ, USA: Prentice-Hall, 1997.
- [13] M. J. Hinich, "Processing spatially aliased arrays," *J. Acoust. Soc. Amer.*, vol. 64, no. 3, pp. 792–794, Sep. 1978.
- [14] R. O. Schmidt, "Multiple emitter location and signal parameter estimation," *IEEE Trans. Antennas Propag.*, vol. 34, no. 3, pp. 276–280, Mar. 1986.
- [15] I. Ziskind and M. Wax, "Maximum likelihood localization of multiple sources by alternating projection," *IEEE Trans. Acoust., Speech, Signal Process.*, vol. 36, no. 10, pp. 1553–1560, Oct. 1988.
- [16] P. Stoica and A. Nehorai, "MUSIC, maximum likelihood, and Cramér-Rao bound," *IEEE Trans. Acoust., Speech, Signal Process.*, vol. 37, no. 5, pp. 720–741, May 1989.
- [17] P. Stoica and A. Nehorai, "MUSIC, maximum likelihood, and Cramér-Rao bound: Further results and comparisons," *IEEE Trans. Acoust., Speech, Signal Process.*, vol. 38, no. 12, pp. 2140–2150, Dec. 1990.
- [18] J. Luis Vazquez-Roy, V. Krozer, and J. Dall, "Wideband dual-polarization microstrip patch antenna array for airborne ice sounder," *IEEE Antennas Propag. Mag.*, vol. 54, no. 4, pp. 98–107, Aug. 2012.
- [19] S. López-Peña, J. F. Zürcher, R. Torres, A. G. Polimeridis, and J. R. Mosig, "Modeling and manufacturing of a series of identical antennas for a P-band ice sounder," in *Proc. EuCAP*, Barcelona, Spain, Apr. 2010, pp. 1–5.
- [20] R. Bindshadler *et al.*, "The Landsat image mosaic of Antarctica," *Remote Sensing Environ.*, vol. 112, no. 12, pp. 4214–4226, 2008.
- [21] R. Bindshadler *et al.*, "Getting around Antarctica: New high-resolution mappings of the grounded and freely-floating boundaries of the Antarctic ice sheet created for the International Polar Year," *Cryosphere*, vol. 5, no. 3, pp. 569–588, 2011.
- [22] A. Kusk and J. Dall, "SAR focusing of P-band ice sounding data using back-projection," in *Proc. IEEE IGARSS*, Honolulu, HI, USA, Jul. 2010, pp. 4071–4074.
- [23] S. N. Madsen and H. A. Zebker, *Manual of Remote Sensing. Principles and Applications of Imaging Radar*, 3rd ed. Hoboken, NJ, USA: Wiley, 1998, vol. 2, ch. 6.



**Ulrik Nielsen** (S'10) received the B.Sc. and M.Sc. degrees in electrical engineering from the Technical University of Denmark, Kongens Lyngby, Denmark, in 2008 and 2011, respectively. He is currently working toward the Ph.D. degree in signal processing at the Technical University of Denmark.

His current research is focused on development of advanced signal and array processing algorithms for radio echo sounding of ice sheets.



**Jørgen Dall** (M'07) received the M.Sc. degree in electrical engineering and the Ph.D. degree from the Technical University of Denmark, Kongens Lyngby, Denmark, in 1984 and 1989, respectively.

Since 1993, he has been an Associate Professor with the Technical University of Denmark. He has been working with the Danish airborne SAR, i.e., EMISAR, e.g., he led the development of onboard and offline SAR processors, was responsible for the data processing, and organized the EMISAR data acquisition campaigns in a five-year period. Later, he led the development of the POLarimetric Airborne Radar Ice Sounder and SAR. His research interests include various aspects of ice sheet penetration, e.g., interferometric SAR (InSAR) elevation bias, polarimetric InSAR extinction coefficients, tomographic ice structure mapping, and ice sounding.

## **Direction-of-Arrival Analysis of Airborne Ice Depth Sounder Data**

Ulrik Nielsen, Jie-Bang Yan, Sivaprasad Gogineni, and  
Jørgen Dall

Submitted to IEEE Transactions on Geoscience and Remote Sensing,  
Jan. 2015.





# Direction-of-Arrival Analysis of Airborne Ice Depth Sounder Data

Ulrik Nielsen, *Member, IEEE*, Jie-Bang Yan, *Member, IEEE*,  
Sivaprasad Gogineni, *Fellow, IEEE*, and Jørgen Dall, *Member, IEEE*

**Abstract**—In this paper, we analyze the direction of arrival (DOA) of the ice sheet data collected over Jakobshavn Glacier with the airborne Multi-channel Coherent Radar Depth Sounder/Imager (MCoRDS/I) during the 2006 field season. We extracted weak ice-bed echoes buried in signals scattered by the rough surface of fast-flowing glaciers like Jakobshavn by analyzing the direction of arrival of signals received with a 5-element receive-antenna array. This allowed us to obtain much needed ice thickness information for generating bed topography of Jakobshavn Glacier. We also estimated ice-bed roughness and bed slope from the combined analysis of the DOA and radar waveforms. The bed slope is about 12 degrees and height standard deviation is about 50 cm.

**Index Terms**—Airborne radar, direction-of-arrival (DOA) estimation, glacier, ice sounding, radar remote sensing, surface scattering.

## I. INTRODUCTION

SATELLITE observations show that both the Greenland and Antarctic ice sheets are losing mass [1], [2]. Most of the ice loss is occurring around ice-sheet margins and through fast-flowing glaciers [3]. Although satellites provide much-needed information on ice-surface elevation, surface velocity, and total mass, there is currently no satellite-based sensor that is able to measure ice thickness. Bed topography and basal conditions for areas losing ice are needed to improve ice-sheet models. These models are essential to predicting the response of the ice sheets to a warming climate. One of the key parameters needed is ice sheet thickness, which can be extracted using radar depth sounding techniques [4], [5]. In addition, we are interested in the basal conditions of the ice sheets as it determines the boundary conditions of the ice sheet models.

### A. Multi-phase-center-based Radar Ice Sounding

The weak nadirradar signals from the ice-bed interface are often masked by off-nadir surface clutter, signals scattered from extremely rough crevassed surfaces in ice sheet margins. Synthetic Aperture Radar (SAR) processing can be used to suppress surface clutter in the along-track direction, but it is

ineffective in reducing the across-track clutter. Large across-track antenna arrays can be used to obtain a narrow across-track antenna beam to suppress surface clutter in this direction. At the same time, to avoid excessive attenuation of the signals reflected within the ice, radars are normally operated in the VHF part of the electromagnetic spectrum. The long wavelengths in this band require large-antenna dimensions to obtain an antenna beam that is sufficiently narrow to reduce across-track surface clutter. Such large antenna dimensions cannot be accommodated on airborne platforms, and additional clutter suppression is, therefore, needed to compensate for these limitations. The current research in this field is based on multi-channel systems combined with advanced coherent post-processing of data. By using multi-channel-receivers to sample array elements individually, beamforming techniques can be utilized to synthesize adaptive-antenna patterns that suppress the surface clutter from specific off-nadir angles while a high gain is maintained in the nadir direction [6].

### B. DOA Estimation in Radar Ice Sounding

In addition to beamforming, the multi-phase-center systems also provide the opportunity to perform direction-of-arrival (DOA) estimation of the different signal components within the received returns. Previously, DOA estimation has been applied to data acquired with the 4-channel POLarimetric Airborne Radar Ice Sounder (POLARIS) [7] developed by the Technical University of Denmark (DTU), to improve the performance of surface clutter suppression techniques [8]. The DOA angles of the surface clutter can be estimated and used to optimize the synthesis of the antenna patterns for improving clutter suppression. In [9] DOA data are used as the primary data product to produce swath measurements of the ice surface and bedrock-topography. The results reported in [9] are based on data acquired by the Multi-channel Coherent Radar Depth Sounder/Imager (MCoRDS/I) [10] developed by the Center for Remote Sensing of Ice Sheets (CReSIS) at the University of Kansas (KU). The radar system is in this experiment operated in ping-pong mode to provide 12 effective receive phase centers. Estimation of the DOA angles of the surface clutter and bed return are used to compute relative elevations in slant-range geometry, followed by a mapping to ground range to obtain the topographic map in Cartesian coordinates. Recently, DOA estimation based on POLARIS data is used to show an along-track variation of the effective scattering

This work was supported in part by the National Science Foundation (NSF) under Grant No. ANT0424589.

U. Nielsen and J. Dall are with the Department of Microwaves and Remote Sensing, National Space Institute, Technical University of Denmark, e-mail: ulrik@space.dtu.dk.

J.-B. Yan and S. Gogineni are with the Center for Remote Sensing of Ice Sheets (CReSIS) at the University of Kansas, Lawrence, KS 66047 USA, e-mail: syan@ku.edu.

center of the surface return caused by a varying penetration depth [11], which directly provides glaciological information.

In this paper we present further applications of the DOA estimation technique for radar ice sounding. We used MCoRDS/I multi-phase-center data collected over Jakobshavn Glacier during the 2006 Greenland field season to convert radar echograms into a DOA representation. With this representation of the radar data we were able to close some of the critical gaps with respect to bed detection along the channel of the fastest flowing glacier on the earth. A model-based approach was then used to interpret the DOA estimation of the bed return. Further analysis showed that the backscattering characteristics of the ice-bed could be estimated by combining the DOA data and the radar waveform data. Based on the data, the across-track slope of the bed was estimated as a fitted model parameter. Finally, information on the bed roughness was obtained by forward modelling using the Incoherent Kirchhoff Model (IKM).

### C. Paper Outline

The paper is organized as follows. Section II provides details on the MCoRDS/I system and the associated dataset. A signal model is presented in Section III along with algorithms for DOA estimation. In Section IV the algorithms are applied to data and used to provide an alternative representation based on DOA. This representation is used for detection of the bed in Section V and for retrieval of its backscattering characteristics in Section VI. Finally, in Section VII, we summarize and conclude the paper.

## II. SYSTEM AND DATA DESCRIPTION

MCoRDS/I is a high-sensitivity radar system developed for the collection of ice-sheet data. During the 2006 Greenland field mission, MCoRDS/I was installed on the DHC-6 Twin-Otter aircraft from de Havilland Canada Ltd. At this time, the system was referred to as the Multi-Channel Radar Depth Sounder (MCRDS) [12] and was operated at 150 MHz with a bandwidth of 20 MHz. The system was effectively configured with a 10-element antenna array of folded dipoles mounted in the across-track direction. The array was divided into two 5-element sub-arrays installed under each wing, as shown in Fig. 1. The left wing sub-array was used for transmission and the right for reception. All elements in the transmit array were excited with uniform weights during transmission. The pulse length was  $10\mu\text{s}$  with a total transmit power of 800 W. A multi-channel receiver was used to sample signals from each receive-antenna element individually. The spacing of the effective phase centers was approximate  $0.3\lambda$ , where  $\lambda$  is the wavelength in free space of the center frequency.

Data acquired with the MCoRDS/I system in 2006 at the Jakobshavn Glacier were used for the DOA analysis. The data were acquired according to the flight tracks shown in Fig. 2. Results for a segment perpendicular to the ice flow are presented in this paper. The segment was flown northward and is highlighted in red in the figure. The altitude is approximate 750 m above the ice surface.



Fig. 1. A photograph showing the 5-element sub-array of folded dipole elements mounted under the right wing of the Twin-Otter aircraft.

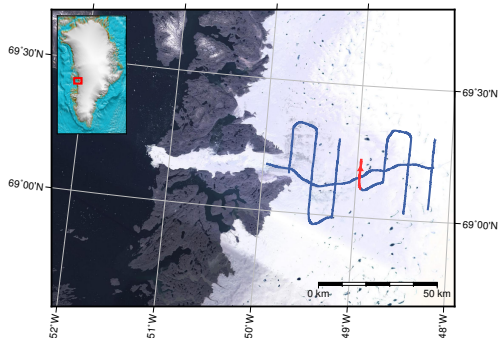


Fig. 2. Flight tracks over the Jakobshavn Glacier at the west coast of Greenland in the 2006 field season.

### A. Signal Processing

A linear frequency-modulated chirp was used for transmitted pulses to employ pulse compression. The received data were compressed using a matched filter with a frequency-domain Hanning window to suppress range sidelobes.

SAR processing was used to improve the along-track resolution by synthesizing a long aperture. The frequency-wavenumber (F-K) focusing algorithm that exploits the Fast Fourier Transform (FFT) for computational efficiency was used for processing.

By using pulse compression and SAR processing, a nominal resolution in range and azimuth of 25 ns (7.5 m in air) and 5 m, respectively, was obtained.

## III. DIRECTION-OF-ARRIVAL ESTIMATION

Several algorithms for DOA estimation exist. They include the well-established Multiple Signal Classification (MUSIC) [13] and Maximum Likelihood (ML) [14] algorithms. Both of these algorithms have super-resolution capabilities. Due to this and further desirable properties, as well as their applications in a number of fields, MUSIC and ML are the algorithms chosen for the study in this paper. Within the field of radar ice sounding, the algorithms have previously been applied a

few times for different purposes. In [15], MUSIC has been applied to data acquired with MCoRDS/I in a ground-based configuration, while ML has been applied to data from the airborne experiments in [9], [8], and [11].

We will now briefly describe the array signal model that is the basis for both algorithms.

#### A. Signal Model

The signal received at time  $t$  by the  $N$  array sensors can be expressed in vectorial form as

$$\mathbf{x}(t) = \mathbf{a}(\theta)s(t) + \mathbf{e}(t) \quad (1)$$

where  $\mathbf{x}(t)$  is an  $N \times 1$  vector,  $s(t)$  is the complex echo signal at a reference sensor,  $\mathbf{e}(t)$  is an additive Gaussian noise component, and  $\mathbf{a}(\theta)$  is the so-called array transfer vector (or steering vector). This vector describes the phase shift at each of the sensors corresponding to the inter-element time delays determined by the array geometry and the given DOA,  $\theta$ :

$$\mathbf{a}(\theta) = [H_1(\theta)e^{-j\omega_c\tau_1} \quad \dots \quad H_N(\theta)e^{-j\omega_c\tau_N}]^T \quad (2)$$

where  $(\cdot)^T$  is the transpose operator,  $\omega_c$  is center angular frequency, and  $\tau_n$  is the time delay at the  $n$ th sensor relative to an arbitrary reference sensor. Equation (2) also takes into account the sensor transfer functions,  $H_n(\theta)$ .

By applying the superposition principle to (1),  $Q$  simultaneously received echo signals with different DOA can be described in the following way

$$\mathbf{x}(t) = \mathbf{A}(\Theta)\mathbf{s}(t) + \mathbf{e}(t) \quad (3)$$

where  $\mathbf{A}$  is the  $N \times Q$  steering matrix formed by column-wise concatenation of the steering vectors corresponding to each of the  $Q$  signals, and  $\mathbf{s}(t)$  is a vector collecting the  $Q$  signal components at time  $t$ , i.e.,

$$\mathbf{s}(t) = [s_1(t) \quad \dots \quad s_Q(t)]^T. \quad (4)$$

The steering matrix  $\mathbf{A}$  is a function of the DOA vector  $\Theta$ , which contains the  $Q$  DOA angles.

A vector in a set of  $M$  array samples acquired at time instances  $t_1, \dots, t_m$ , where the scene can be assumed stationary, is denoted a *snapshot*. A collection of  $M$  snapshots can be modelled as

$$\mathbf{X} = \mathbf{A}(\Theta)\mathbf{S} + \mathbf{E} \quad (5)$$

where  $\mathbf{X}$  and  $\mathbf{E}$  are  $N \times M$  matrices,  $\mathbf{A}$  is  $N \times Q$ , and  $\mathbf{S}$  is  $Q \times M$ . Each column in  $\mathbf{X}$ ,  $\mathbf{S}$ , and  $\mathbf{E}$  corresponds to a specific snapshot. For further details regarding the signal model see [9], [16].

Before we move on to a review of the two algorithms, we first define the sample covariance matrix as

$$\mathbf{R} = \frac{1}{M} \sum_{m=1}^M \tilde{\mathbf{x}}(t_m)\tilde{\mathbf{x}}^H(t_m). \quad (6)$$

where  $(\cdot)^H$  is the Hermitian transpose and  $\tilde{\mathbf{x}}$  is a measured array sample corresponding to the signal model from (3). In this way, the covariance matrix is estimated as an average over a given set of snapshots. In this paper, the snapshots are extracted as a number of consecutive samples in azimuth—all at the same given range gate.

#### B. Multiple Signals Classification (MUSIC)

MUSIC exploits the eigen-decomposition of  $\mathbf{R}$ , i.e.,

$$\mathbf{R} = \mathbf{U}\mathbf{\Lambda}\mathbf{U}^H \quad (7)$$

where  $\mathbf{\Lambda}$  is a diagonal matrix containing the  $N$  eigenvalues of  $\mathbf{R}$ , and  $\mathbf{U}$  is an orthonormal basis consisting of the corresponding eigenvectors.

The DOA estimates are determined as the  $Q$  highest peaks of the so-called MUSIC-spectrum [13] given by

$$P_{\text{MU}}(\theta) = \frac{1}{\mathbf{a}^H(\theta)\mathbf{U}_n\mathbf{U}_n^H\mathbf{a}(\theta)} \quad (8)$$

where  $\mathbf{U}_n$  is the subset of eigenvectors in  $\mathbf{U}$  that corresponds to the  $N - Q$  smallest eigenvalues. The subspace spanned by  $\mathbf{U}_n$  is known as the noise subspace.

#### C. Maximum Likelihood (ML)

The ML solution [14] of the DOA vector can be expressed as

$$\Theta_{\text{ML}} = \min_{\Theta} \text{tr} \left[ \mathbf{A}(\Theta) (\mathbf{A}^H(\Theta)\mathbf{A}(\Theta))^{-1} \mathbf{A}^H(\Theta)\mathbf{R} \right] \quad (9)$$

where  $\text{tr}[\cdot]$  is the trace of the bracketed matrix. The ML estimator with the assumption of  $Q$  signal components involve a computationally-intensive  $Q$ -dimensional search. The computation time can be reduced by applying the alternating projection algorithm [14] based on alternating maximization, which transforms the optimization problem into a sequence of much faster one-dimensional searches.

### IV. DOA REPRESENTATION OF RADAR ECHOGRAMS

Now we will utilize the DOA algorithms to obtain an alternative representation of the radar data. Consider the intensity echogram in Fig. 3, which generated by coherently averaging data from all receive channels. The DOA is estimated for each pixel in the echogram. The number of signal components to be estimated can be difficult to determine for the individual pixels. For this reason, and to simplify the processing and interpretation, the number of signal components are assumed to be one for all pixels, i.e.  $Q = 1$ , even though this is incorrect for some regions of the image. When this assumption does not hold, the DOA of the dominating signal component tends to be the one estimated, and in this way the estimate is still meaningful.

By presenting the DOA estimates as an image with the pixel color representing the DOA angle, the procedure can be considered as a DOA representation of the echogram. The DOA representation of the echogram from Fig. 3 can be seen in Fig. 4 and Fig. 5 using MUSIC and ML respectively. The covariance matrix is estimated based on 5 snapshots, and the DOA images are filtered using a  $5 \times 5$  median filter to reduce noise and outliers. The array manifold, i.e. the set of steering vectors for the DOA interval of interest, is simulated [17] using the electromagnetic FEM simulation software package HFSS by ANSYS Inc., based on a combined model of the antenna elements and the aircraft.

The outputs of the two algorithms are similar with respect to the large-scale content. The DOA of the near-range pixels

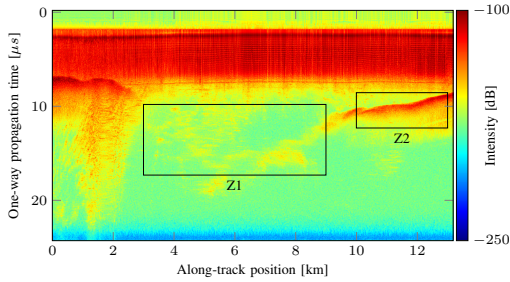


Fig. 3. Echogram based on coherently averaging of the receive channels. The black rectangles show regions of interest: glacier channel (Z1) and bedrock (Z2).

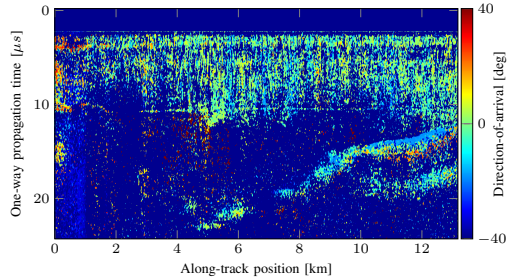


Fig. 4. MUSIC-based DOA image.

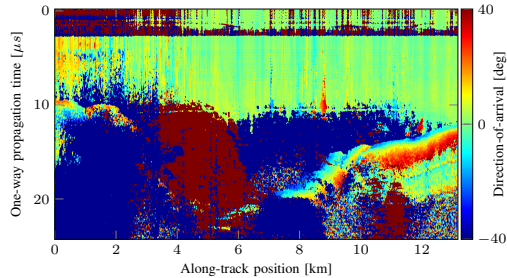


Fig. 5. ML-based DOA image.

are estimated with small (numerical) values, while the DOA of the far-range pixels is large. Dark blue and dark red represent far off-nadir signals while green represents near-nadir returns. Parts of the ice-bed interface can be detected as an abrupt transition from large to small estimated DOA angles, where the dominating signal component changes from off-nadir surface clutter or noise, to the first (near-nadir) return from the bedrock. With respect to the small scale content, the MUSIC images are much noisier compared to the ML image. Furthermore, the ML image reveals large areas of off-nadir surface clutter that appears due to a change of sign in DOA angle compared to the background. The transition from

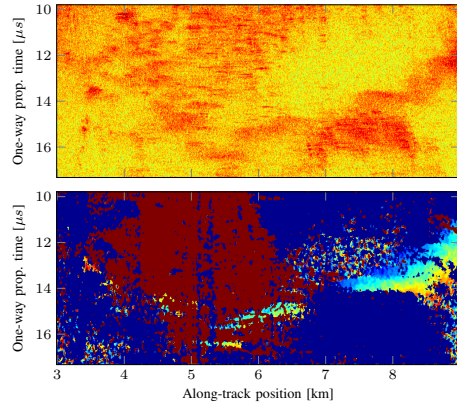


Fig. 6. Enlargement (Z1) of glacier channel, echogram (upper) and ML DOA image (lower).

ice to bedrock is much more significant in the ML image. In both images, a distinctive color sweep-pattern in the estimated DOA angle is seen right after the first bed return. Again, the phenomenon is more pronounced in the ML image. Based on this visual comparison of the MUSIC image and the ML image, we conclude that the ML algorithm for this specific scene and clutter scenario is preferable for the further analysis.

The next two sections address observations in the DOA representation in terms of the detectability of the ice-bed interface, and the sweep-pattern in the estimated DOA angle at the bed.

## V. RECOVERY OF ICE BED DETECTION GAP

By examining the echogram in Fig. 3, we can see that the subsurface returns are highly contaminated by surface clutter. The bedrock is detectable at the beginning and end of the frame (left/right of the glacier channel), but at the middle section (glacier channel), the weak bed return cannot be discriminated from the clutter. Therefore, detection of the bed is not possible, which nevertheless constitutes an important data product in glaciological modelling.

Instead we consider the ML DOA representation for bed detection. In Fig. 6, enlargements of the glacier channel in the echogram and DOA image are stacked for easy comparison. The colormap of the enlarged echogram is scaled to enhance the local features. It is seen that the bed signal can be discriminated from the clutter in the DOA image, which is not possible in the radar-intensity echogram. Even though the bed signal is flickering in the strong clutter region, the coverage is sufficient to perform a reasonable trace of the interface as illustrated in Fig. 7. The tracing is done by scanning each line through range until a significant discontinuity from off-nadir to near-nadir is detected. In the strong clutter region, the detection might be based only on a few pixels in range. The trace is interpolated at lines where no bed signal is present at all.

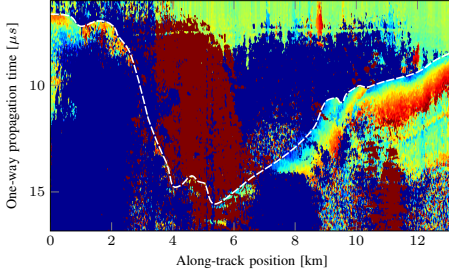


Fig. 7. Bed detection (white, dashed) based on the ML DOA image.

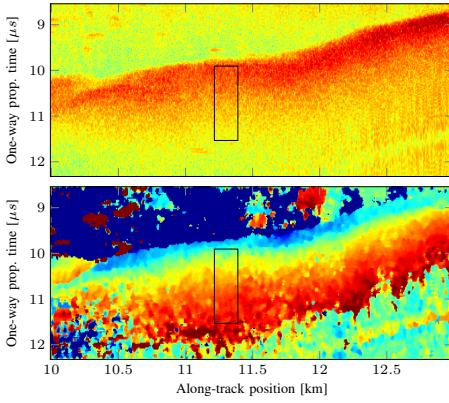


Fig. 8. Enlargement (Z2) of the bed, echogram (top) and ML DOA image (bottom).

In this way the DOA image can be a powerful representation for discrimination and visualization of different types of targets, which can be used to interpret the echogram or for direct applications such as bed detection.

## VI. ICE BED BACKSCATTERING CHARACTERISTICS ESTIMATION

We will now analyse the DOA sweep-pattern observed near the bed. An enlargement containing a part of the bed is shown in Fig. 8. A sub-image for further analysis is marked in the figure. The following analysis suggests that the DOA pattern represents an off-nadir return from a rough sloped bed.

The sounding geometry with notation associated with a sloped (across-track) bed is illustrated in Fig. 9. Since the data are Doppler processed in the along-track direction, the along-track extent of the resolution cell is small. In this way, the extent of the resolution cell is (pulse) limited to the across-track direction at zero Doppler. At  $t_0$  the first bed return is reflected corresponding to the shortest electrical distance from the radar to the bed. By taking the refraction at the air–ice interface into account, the DOA of this return corresponds to the across-track slope of the bed. Later time, i.e. at  $t_1, t_2, \dots$ , two signals are reflected corresponding to the left-hand side (LHS)

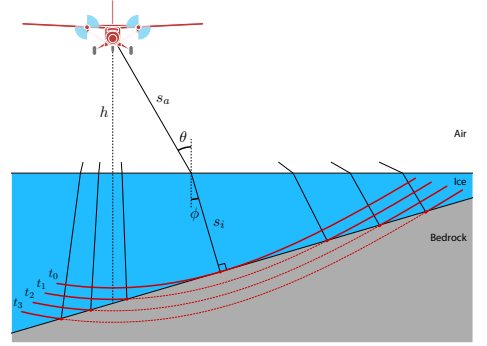


Fig. 9. Geometry and notation associated with illumination of sloped (across-track) bed at different range gates.

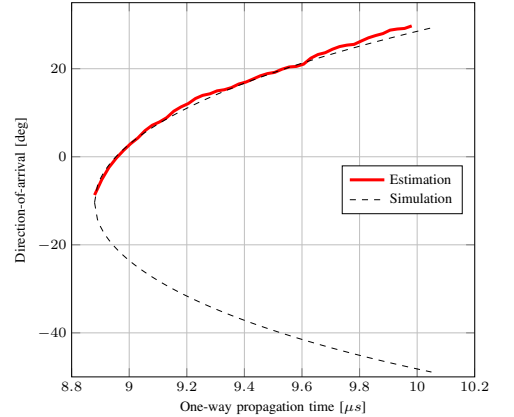


Fig. 10. DOA estimation of the bed return along with a simulation based on the geometric model from Fig. 9.

and right-hand side (RHS) intersections of the wavefront with the ice–bed interface, as illustrated in the figure. It should be noted that when referring to one of these two components, a specific point on the bed can be described by either range, DOA, or (propagation) time. Therefore, the representations should be read as being ambiguous or interchangeable if either the LHS or RHS intersection is considered. A rough ice–bed interface is assumed such that energy is scattered back towards the radar.

The across-track slope,  $\phi(t_0)$ , and depth,  $s_i(t_0)$ , of the bed is estimated using radar and DOA data for the boxed region in Fig. 8. Based on these parameters, a DOA simulation for a flat sloped bed is conducted. Furthermore, the DOA estimate of the boxed region is averaged in the along-track direction to a single line and plotted with the simulation as a function of time in Fig. 10.

The simulation consists of an approximately symmetric two-legged curve, where each leg corresponds to the LHS and

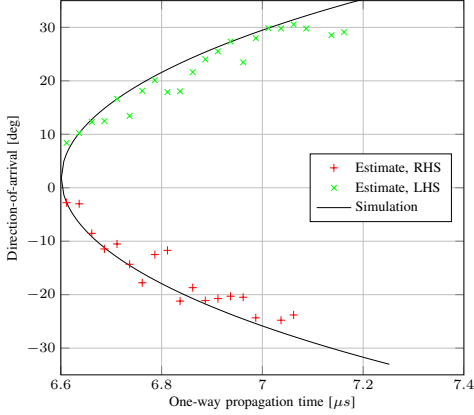


Fig. 11. Two-signal ML DOA estimation and simulation of bed return.

RHS bed signal, respectively. It is seen that the estimate and simulation fits very well, but clearly only one of the two components is estimated by the DOA algorithm. The reason for this is that a one-signal ( $Q = 1$ ) ML estimation was performed. In this case, the most positive DOA component is estimated because of the transmit antenna pattern. Since the pattern is directed towards nadir, the given signal component is the one dominating the combined signal, hence the one estimated by the DOA algorithm. At a less sloped part of the bed, it was possible with a two-signal estimation to recover both of the signal components from the bed, as seen in Fig. 11. In the case of a small slope, the geometry is symmetric which results in bed signals of equal amplitude. The retrieval of both bed signals in the low slope scenario strengthens the hypothesis of the bed reflections being the mechanism behind the sweep-pattern.

The case of a single dominating bed signal combined with the DOA information makes it possible to estimate the backscattering characteristics of the bed for a range of incidence angles. This is done by combining the intensity waveform with the corresponding DOA estimate. However, the backscattering information contained in the waveform is affected by several factors such as a varying propagation distance, antenna patterns, refraction at the air-ice interface etc. These factors need to be taken into account to get an accurate estimate of the bed characteristics. In the following section, we will describe a procedure for estimating the backscattering pattern of the bed, which includes corrections of the intensity waveform.

#### A. Detrending

We are still considering the data region marked in Fig. 8. To get an accurate estimate of the DOA trace and the waveform of the bed return, both the DOA data and the intensity radar data are averaged in the along-track direction. However, the bed has an along-track slope, which distorts the shape of the DOA trace and the waveform when the data are averaged. Therefore,

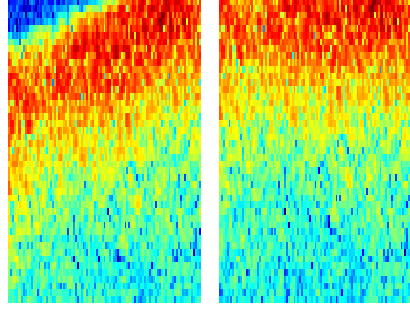


Fig. 12. Illustration of the detrending procedure. Original echogram (left) and the corresponding detrended output (right).

the data are detrended with respect to the along-track slope before averaging. This is done by tracing the leading edge of the waveform and shifting each line in range accordingly. The procedure is equivalent to averaging in the surface parallel direction and is illustrated in Fig. 12. The resulting DOA trace and waveform after averaging are plotted as a function of time in Fig. 13.

#### B. Fitting of Bed Model

To correct for attenuation and refraction at the air-ice interface etc., the geometric model in Fig. 9 is adopted. The model is fitted to the data shown in Fig. 13. As illustrated in the figure with the vertical dashed lines, the data are clipped in the range direction to capture the trailing edge of the waveform and the valid part of the DOA trace. The bed model is now fitted to the data by adjusting the slope parameter and the propagation time corresponding to the closest approach. The error, which is minimized, is evaluated in the DOA representation corresponding to the difference between the data and the model in Fig. 10. The across-track slope of the bed is estimated by the fitted parameter to  $\phi = 9^\circ$ , which for the specific flight segment corresponds to the slope of the glacier channel.

#### C. Waveform Correction

The data are now corrected for four mechanisms:

- 1) Receive gain
- 2) Transmit gain
- 3) Attenuation loss
- 4) Geometric spreading

1) *Receive Gain*: To improve the signal-to-clutter ratio, suppress clutter and the secondary bed return, beamforming is used to steer the receive-beam towards the direction of the dominating bed return.

The output  $y$  of beamforming formulated as a spatial filtering process is given by

$$y = h^H x, \quad (10)$$



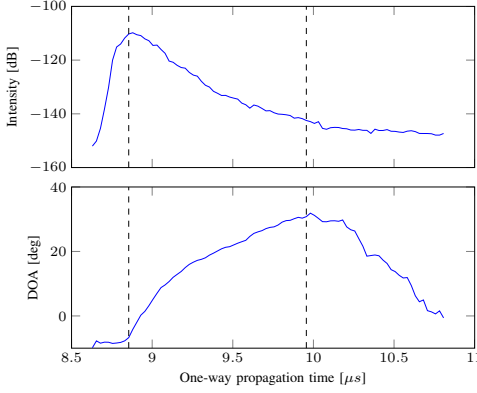


Fig. 13. Along-track averaged waveform of the bed return (top) and the correspondingly averaged DOA estimate (bottom).

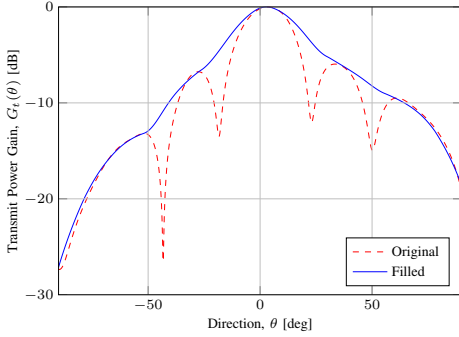


Fig. 14. Transmit pattern in the across-track direction, based on a HFSS-simulation of the array manifold.

where  $\mathbf{h}$  is the  $N \times 1$  filter weight vector. In the case of beamsteering, the filter weights are given by [16]

$$\mathbf{h} = \frac{\mathbf{a}(\theta)}{\mathbf{a}^H(\theta)\mathbf{a}(\theta)}, \quad (11)$$

where  $\theta$  represents the steering angle. The normalization ensures unity gain in the  $\theta$ -direction, and the correction for the receive gain is in this way incorporated into the filtering process.

DOA data are simulated based on the fitted model and are used as the steering angle in (11). A range varying beam is in this way synthesized for, and applied to, each azimuth line. The filtered data are then detected, detrended, and averaged according to the procedure described earlier.

2) *Transmit Gain*: All transmit elements are used for transmission without any tapering. The resulting transmit pattern is shown in Fig. 14. By using the estimated DOA data in combination with the pattern, the waveform can be corrected for the antenna transmit gain. The antenna pattern is based on simulations [17] and does not take dynamic

factors such as wing flexure and vibration into account. This affects the true pattern particularly regarding the depth of the nulls. Furthermore, energy from the secondary bed return and from surface and volume clutter contributes to the received signal, which smoothens the waveform when the transmit gain towards the bed is low. Therefore, if the waveform is corrected with the unmodified simulated pattern with deep nulls, high amplification of the clutter will occur at angles corresponding to the nulls. To avoid this clutter amplification, the nulls of the pattern are filled before the correction is applied. The modified transmit pattern is shown in blue in Fig. 14.

3) *Attenuation Loss*: The electromagnetic propagation within the ice involves attenuation losses due to absorption and internal scattering. It is seen from the geometry in Fig. 9 that the propagation distance in ice ( $s_i$ ) for the bed return varies with DOA. When the attenuation coefficient is assumed constant, the attenuation loss is exponentially proportional to the propagated distance in ice, i.e.

$$L_A \propto 10^{s_i}. \quad (12)$$

The attenuation loss varies with DOA and it can be taken into account. Using the model, the distance is calculated as a function of range and the waveform is corrected accordingly.

4) *Geometric Spreading*: The inverse-square law and the two-way propagation of the pulse result in the geometric spreading loss factor that is related to range in the following way

$$L_{GS} \propto R^4. \quad (13)$$

When  $s_a$  is the propagated distance in air, the range is defined as  $R = s_a + s_i$  which takes the refraction at the air-ice interface into account. As for the attenuation loss, the geometric model is used to calculate the range for each sample, and the data are corrected accordingly.

#### D. Backscattering Pattern

The corrected waveform that represents backscatter from the bed surface can be expressed as

$$\sigma(\theta) = K \frac{P_{BS}(\theta) 10^{s_i} R^4}{G_t(\theta)} \quad (14)$$

where  $P_{BS}(\theta)$  is the received power using beamsteering, and  $K$  is a product of factors independent of DOA such as the system gain and the attenuation coefficient of the ice. The normalized backscatter is computed by dividing with the backscatter at zero incidence, i.e.

$$\hat{\sigma}(\theta) = \frac{\sigma(\theta)}{\sigma(\theta_0)} \quad (15)$$

where  $\theta_0$  is the DOA angle corresponding to zero incidence at the bed, i.e.  $t = t_0$  in Fig. 9. Based on the model, the angle of incidence at the bed is calculated from the refracted angle  $\phi$  and the estimated bed slope. The normalized backscatter as a function of incidence angle is plotted in Fig. 15.



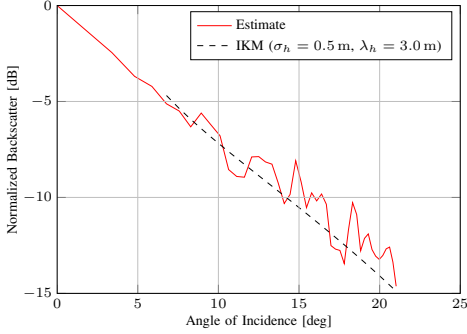


Fig. 15. Estimated and simulated backscattering pattern of the bed surface.

With the assumption of a random surface with a Gaussian height distribution, the IKM [18][19] is used to model the backscattering coefficient:

$$\sigma_{\text{IKM}}^0(\alpha) = \frac{\Gamma}{2m_s^2 \cos^4 \alpha} \exp\left(-\frac{\tan^2 \alpha}{2m_s^2}\right) \quad (16)$$

where  $\alpha$  is the angle of incidence,  $\Gamma$  is the Fresnel reflectivity [20] evaluated at normal incidence, and  $m_s$  is the root mean square (RMS) slope of the surface given by [19]

$$m_s = \frac{\sqrt{2}\sigma_h}{\lambda_h}. \quad (17)$$

The parameters  $\lambda_h$  and  $\sigma_h$  are the surface correlation length and RMS height, respectively. The IKM only depends on the RMS slope and is therefore invariant with respect to a common scaling of  $\lambda_h$  and  $\sigma_h$  as long as the validity conditions [18] are fulfilled.

The backscatter is obtained by multiplying the coefficient with the time-varying illuminated area, which is calculated based on the fitted geometric model. Since the illuminated area is rapidly changing for small incidence angles, backscatter is only modeled for larger angles, where the estimate of the area is more accurate and robust. The IKM is fitted to the estimated data and is included in Fig. 15. A relative permittivity for ice and bedrock equal to 3.2 and 6, respectively, is assumed. Based on the fit of the IKM, the RMS slope is estimated to 0.22 or 12°, which represents a measure of the bed roughness. For comparison, a recent study [21] estimates bed RMS slopes of Thwaites Glacier in West Antarctica based on radar ice sounding, but with a different surface model. The slopes are estimated to be between 6° and 8°, which are comparable with our findings for Jakobshavn Glacier.

## VII. CONCLUSION

Novel applications of DOA estimation in relation to airborne radar ice sounding are presented in this paper. We use the MUSIC and ML estimators to convert the radar data into a DOA representation, where the latter is seen to provide superior performance. The DOA representation offers a better visualization of the desired signals and clutter. Based on this

we are able to discriminate the desired bed return from strong surface clutter in the channel of the challenging Jakobshavn Glacier. We show how this can be used to close some of the critical gaps in bed detection along the channel.

Furthermore, a geometric model is used to show how the across-track slope of the bed is related to the DOA pattern of the bed return. In a low slope scenario where the associated geometry gives rise to comparable amplitudes of the LHS and RHS bed signals, the DOA for both components is retrieved and validated with the model. For larger slopes, it is shown that the bed component received closest to nadir is dominant due to amplification caused by the combination of the transmit pattern and asymmetric geometry. This is exploited to retrieve bed characteristics by combining DOA data and waveforms of the radar data. By fitting the geometric model to the data, the across-track slope is estimated. Based on the model, a number of corrections are applied to the waveform to retrieve the received backscatter of the bed surface as a function of the local incidence angle. The backscattering pattern holds information on the bed roughness. To further quantify the roughness, the IKM is fitted to the data and used to estimate a 12° RMS slope of the surface.

## REFERENCES

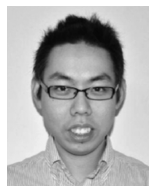
- [1] E. Rignot, I. Velicogna, M. R. van den Broeke, A. Monaghan, and J. T. M. Lenaerts, "Acceleration of the contribution of the Greenland and Antarctic ice sheets to sea level rise," *Geophys. Res. Lett.*, vol. 38, no. 5, p. L05503, Mar. 2011.
- [2] A. Shepherd *et al.*, "A Reconciled Estimate of Ice-Sheet Mass Balance," *Science*, vol. 338, no. 6111, pp. 1183–1189, Nov. 2012.
- [3] E. Rignot, J. Mouginot, M. Morlighem, H. Seroussi, and B. Scheuchl, "Widespread, rapid grounding line retreat of pine island, thwaites, smith, and kohler glaciers, west antarctica, from 1992 to 2011," *Geophys. Res. Lett.*, vol. 41, no. 10, pp. 3502–3509, May 2014.
- [4] S. Gogineni *et al.*, "Coherent radar ice thickness measurements over the Greenland ice sheet," *Journal of Geophysical Research: Atmospheres*, vol. 106, no. D24, pp. 33 761–33 772, Dec. 2001.
- [5] J. Dall *et al.*, "P-band radar ice sounding in Antarctica," in *Proc. IGARSS'12*, Munich, Germany, Jul. 2012, pp. 1561–1564.
- [6] J. Li *et al.*, "High-Altitude Radar Measurements of Ice Thickness Over the Antarctic and Greenland Ice Sheets as a Part of Operation IceBridge," *IEEE Trans. Geosci. Remote Sens.*, vol. 51, no. 2, pp. 742–754, Feb. 2013.
- [7] J. Dall *et al.*, "ESA's POLarimetric Airborne Radar Ice Sounder (POLARIS): design and first results," *IET Radar, Sonar & Navigation*, vol. 4, no. 3, pp. 488–496, 2010.
- [8] U. Nielsen, J. Dall, A. Kusk, and S. S. Kristensen, "Coherent Surface Clutter Suppression Techniques with Topography Estimation for Multi-Phase-Center Radar Ice Sounding," in *Proc. EUSAR'12*, Nuremberg, Germany, Apr. 2012, pp. 247–250.

- [9] X. Wu, K. C. Jezek, E. Rodriguez, S. Gogineni, F. Rodríguez-Morales, and A. Freeman, "Ice Sheet Bed Mapping with Airborne SAR Tomography," *IEEE Trans. Geosci. Remote Sens.*, vol. 49, no. 10, pp. 3791–3802, Oct. 2011.
- [10] F. Rodríguez-Morales *et al.*, "Advanced Multifrequency Radar Instrumentation for Polar Research," *IEEE Trans. Geosci. Remote Sens.*, vol. 52, no. 5, pp. 2824–2842, May 2014.
- [11] U. Nielsen and J. Dall, "Direction-of-Arrival Estimation for Radar Ice Sounding Surface Clutter Suppression," *IEEE Trans. Geosci. Remote Sens.*, to be published.
- [12] A. Lohofener, "Design and Development of a Multi-Channel Radar Depth Sounder," Master's thesis, University of Kansas, Lawrence, KS, USA, Nov. 2006.
- [13] R. O. Schmidt, "Multiple Emitter Location and Signal Parameter Estimation," *IEEE Trans. Antennas Propag.*, vol. 34, no. 3, pp. 276–280, Mar. 1986.
- [14] I. Ziskind and M. Wax, "Maximum Likelihood Localization of Multiple Sources by Alternating Projection," *IEEE Trans. Acoust., Speech, Signal Process.*, vol. 36, no. 10, pp. 1553–1560, Oct. 1988.
- [15] J. Paden, T. Akins, D. Dunson, C. Allen, and P. Gogineni, "Ice-sheet bed 3-D tomography," *Journal of Glaciology*, vol. 56, no. 195, pp. 3–11, 2010.
- [16] P. Stoica and R. L. Moses, *Introduction to Spectral Analysis*. Prentice Hall, 1997.
- [17] J.-B. Yan *et al.*, "Measurements of In-Flight Cross-Track Antenna Patterns of Radar Depth Sounder/Imager," *IEEE Trans. Antennas Propag.*, vol. 60, no. 12, pp. 5669–5678, Dec. 2012.
- [18] F. T. Ulaby, R. K. Moore, and A. K. Fung, *Microwave Remote Sensing: Active and Passive*. Addison-Wesley, 1982, vol. II.
- [19] G. Picardi *et al.*, "Performance and surface scattering models for the Mars Advanced Radar for Subsurface and Ionosphere Sounding (MARSIS)," *Planetary and Space Science*, vol. 52, no. 1–3, pp. 149–156, 2004.
- [20] F. T. Ulaby, R. K. Moore, and A. K. Fung, *Microwave Remote Sensing: Active and Passive*. Addison-Wesley, 1981, vol. I.
- [21] D. M. Schroeder, D. D. Blankenship, D. A. Young, A. E. Witus, and J. B. Anderson, "Airborne radar sounding evidence for deformable sediments and outcropping bedrock beneath Thwaites Glacier, West Antarctica," *Geophys. Res. Lett.*, vol. 41, no. 20, pp. 7200–7208, Oct. 2014.



**Ulrik Nielsen** (S'10) received the B.Sc. and M.Sc. degrees in electrical engineering from the Technical University of Denmark, Copenhagen, Denmark, in 2008 and 2011, respectively, where he is currently working toward the Ph.D. degree in signal processing.

His current research is focused on developing of advanced signal and array processing algorithms for radio echo sounding of ice sheets.



**Jie-Bang Yan** (S'09-M'11) received the B.Eng. degree (first class honors) in electronic and communications engineering from the University of Hong Kong in 2006, the M.Phil. degree in electronic and computer engineering from the Hong Kong University of Science and Technology in 2008, and the Ph.D. degree in electrical and computer engineering from the University of Illinois at Urbana-Champaign in 2011.

He was a Croucher Scholar from 2009 to 2011 during his Ph.D. study at Illinois. Upon graduation, he joined the Center for Remote Sensing of Ice Sheets (CRISIS) at the University of Kansas as an Assistant Research Professor. His research interests include design and analysis of MIMO and reconfigurable antennas, antennas and phased arrays for radar systems, RF propagation, and fabrication of on-chip antennas. He holds two U.S. patents and a U.S. patent application related to novel antenna technologies.

Dr. Yan was the recipient of the Best Paper Award at the 2007 IEEE (HK) AP/MTT Postgraduate Conference and the 2011 Raj Mittra Outstanding Research Award at Illinois. He serves as a technical reviewer for several journals and conferences on antennas, electromagnetics and remote sensing. He is also a technical program committee member of various antenna-related symposia since 2013.



**Sivaprasad Gogineni** (M'84-SM'92-F'99) received the Ph.D. degree in electrical engineering from The University of Kansas (KU), Lawrence, KS, USA, in 1984.

He is currently the Deane E. Ackers Distinguished Professor with the Department of Electrical Engineering and Computer Science, KU, and the Director of the NSF Science and Technology Center for Remote Sensing of Ice Sheets. He has authored or coauthored over 90 archival journal publications and more than 200 technical reports and conference presentations. He developed several radar systems currently being used at KU for sounding and imaging of polar ice sheets, and he has also participated in field experiments in the Arctic and Antarctica. His research interests include the application of radars to the remote sensing of the polar ice sheets, sea ice, ocean, atmosphere, and land.

Dr. Gogineni is a member of URSI, the American Geophysical Union, the International Glaciological Society, and the Remote Sensing and Photogrammetry Society. From 1994 to 1997, he served as the Editor of the IEEE GEOSCIENCE AND REMOTE SENSING SOCIETY NEWSLETTER.



**Jørgen Dall** (M'07) received the M.Sc. degree in electrical engineering and the Ph.D. degree from the Technical University of Denmark, Copenhagen, Denmark, in 1984 and 1989, respectively. He has been an Associate Professor since 1993. He has been working with the Danish airborne SAR, EMISAR, e.g. he led the development of onboard and offline SAR processors, was responsible for the data processing and organized the EMISAR data acquisition campaigns in a five year period. Later he led the development of the POLARIS sounder and SAR. His

research interests include various aspects of ice sheet penetration, e.g. InSAR elevation bias, PolInSAR extinction coefficients, tomographic ice structure mapping, and ice sounding.



This page intentionally left blank



# Nomenclature

The following notation is used globally in the dissertation. However, some symbols may have different meanings locally.

## Functions and Operators

$\star$	Convolution operator
$\odot$	Hadamard product (elementwise multiplication)
$(\cdot)^*$	Complex conjugate
$(\cdot)^T$	Transpose of a vector or matrix
$(\cdot)^H$	Hermitian (conjugate) transpose of a vector or matrix
$\langle \cdot, \cdot \rangle$	The inner product
$ x $	The modulus of the complex scalar $x$
$\ \mathbf{x}\ $	The Euclidean norm of the vector $\mathbf{x}$
$\arg(x)$	The argument of the complex scalar $x$
$\arg \max_x f(x)$	The maximising argument of $f(x)$
$\mathbf{A}^+$	The Moore-Penrose pseudoinverse of the matrix $\mathbf{A}$
$E\{\cdot\}$	Expectation value of a random variable
$\text{diag}(\mathbf{x})$	Diagonal matrix having the elements of $\mathbf{x}$ as diagonal
$\ln x$	The natural logarithm of $x$ (base $e$ )
$\log x$	The common logarithm of $x$ (base 10)
$\mathcal{P}_{\mathbf{A}}$	Projection onto the range space of the matrix $\mathbf{A}$
$\text{tr}[\mathbf{A}]$	The trace of the matrix $\mathbf{A}$
$\text{var}\{\cdot\}$	Variance of a random variable
$\det[\mathbf{A}]$	The determinant of the square matrix $\mathbf{A}$
$\nabla f$	The gradient of the scalar field $f$
$\nabla^2 f$	The Laplacian of the function $f$

*continued on next page*

$\nabla \cdot \mathbf{V}$	The divergence of the vector field $\mathbf{V}$
$\nabla \times \mathbf{V}$	The curl of the vector field $\mathbf{V}$

### Symbols

$\mathbf{a}$	Steering vector ( $N \times 1$ )
$A$	Illuminated area
$\mathbf{A}$	Steering matrix ( $N \times Q$ )
$B$	Bandwidth
$c$	Speed of light in free space
$d$	Array sensor (element) spacing
$\mathbf{e}$	Noise vector ( $N \times 1$ )
$\mathbf{E}$	Noise matrix ( $N \times M$ )
$f$	Temporal frequency
$h$	Height over ground or altitude
$\mathbf{h}$	Spatial filter weight vector ( $N \times 1$ )
$\mathbf{I}$	Identity matrix
$k$	Wavenumber
$k_e$	Effective wavenumber
$L$	Surface height correlation length
$L_s$	Length of synthetic aperture
$m_s$	Surface RMS slope
$M$	Number of snapshots
$n$	Refractive index
$N$	Number of array sensors (elements)
$P$	Power
$\mathbf{P}$	Signal covariance matrix ( $Q \times Q$ )
$Q$	Number of signals impinging on the array
$R$	Range
$\mathbf{R}$	Covariance matrix ( $N \times N$ )
$\hat{\mathbf{R}}$	Sample covariance matrix ( $N \times N$ )
$R_p$	Fresnel reflection coefficient, $p$ -polarization
$s(t)$	Complex baseband signal
$\mathbf{s}$	Signal vector ( $Q \times 1$ )
$\mathbf{S}$	Signal matrix ( $Q \times M$ )
$t$	Time
$t_d$	Time delay, two-way propagation time

*continued on next page*

---

$T_p$	Fresnel transmission coefficient, $p$ -polarization
$u$	Propagation velocity
$\mathbf{U}$	Eigenvector
$\mathbf{x}$	Array signal vector ( $N \times 1$ )
$\mathbf{X}$	Data matrix ( $N \times M$ )
$z$	Depth
$\beta$	Phase excitation
$\Gamma$	Reflectivity or reflectance
$\epsilon$	Permittivity
$\epsilon_0$	Permittivity of free space
$\eta$	Intrinsic impedance
$\theta$	DOA angle
$\theta_i$	Angle of incidence
$\theta_r$	Angle of reflection
$\theta_t$	Angle of refraction (transmission)
$\Theta$	DOA vector ( $Q \times 1$ )
$\kappa$	Noise scaling factor
$\lambda$	Wavelength
$\lambda_e$	Effective wavelength
$\mathbf{\Lambda}$	Eigenvector matrix
$\mu$	Magnetic permeability
$\mu_0$	Magnetic permeability of free space
$\rho$	Range resolution
$\rho_a$	Azimuth resolution, real aperture
$\rho_s$	Azimuth resolution, synthetic aperture
$\sigma$	Radar cross section
$\sigma^\circ$	Scattering coefficient
$\sigma_h$	Surface height standard variation
$\sigma_n^2$	Gaussian noise variance
$\tau$	Pulse width
$\Upsilon$	Transmissivity or transmittance
$\omega$	Temporal angular frequency
$\omega_s$	Spatial angular frequency
$\parallel$	Parallel polarization
$\perp$	Perpendicular polarization



**Abbreviations and Acronyms**

AF	Array Factor
AM	Alternating Maximisation
BF	Beamforming
BS	Beam-Steering
CM	Capon's Method
CNR	Clutter-to-Noise Ratio
CRB	Cramér-Rao Bound
CRISIS	Center for Remote Sensing of Ice Sheets
CS	Compressive Sensing or Sampling
DEM	Digital Elevation Model
DML	Deterministic Maximum Likelihood
DOA	Direction of Arrival
DTU	Technical University of Denmark
EGI	Embedded GPS/Inertial Navigation
ESA	European Space Agency
ESTEC	European Space Research and Technology Center
FFT	Fast Fourier Transform
FSIR	Flat Surface Impulse Response
GISMO	Global Ice Sheet Mapping Orbiter
H	Horizontal (polarization)
IEM	Integral Equation Model
IKM	Incoherent Kirchhoff Model
IPCC	Intergovernmental Panel on Climate Change
KU	University of Kansas
LHS	Left-Hand Side
LIMA	Landsat Image Mosaic of Antarctica
LS	Least Squares
LTI	Linear Time-Invariant
MARSIS	Mars Advanced Radar for Subsurface and Ionosphere Sounding
MCoRDS/I	Multi-channel Coherent Radar Depth Sounder/Imager
MCRDS	Multi-Channel Radar Depth Sounder
ML	Maximum Likelihood
MLE	Maximum Likelihood Estimate
MSE	Mean Square Error

*continued on next page*

---

MU	Spectral MUSIC
MUSIC	MUltiple SIgnal Classification
MVDR	Minimum Variance Distortionless Response
NS	Null-Steering
OB	Optimum Beamformer
PDF	Probability density function
POLARIS	POLarimetric Airborne Radar Ice Sounder
PSD	Power Spectral Density
PTR	Point Target Response
RHS	Right-Hand Side
RIP	Restricted isometry property
RM	Root MUSIC
RMS	Root Mean Square
RMSE	Root-Mean-Square Error
SAR	Synthetic Aperture Radar
SCR	Signal-to-Clutter Ratio
SCS	Surface Clutter Suppression
SDS	Shallow/Deep Sounding
SML	Stochastic Maximum Likelihood
SNR	Signal-to-Noise Ratio
SPM	Small Perturbation Model
SVD	Singular Value Decomposition
UAS	Unmanned Aircraft System
ULA	Uniform Linear Array
V	Vertical (polarization)



---

## Bibliography

- [1] ESA, *The Changing Earth*, B. Battick, Ed. ESA Publications Division, Jul. 2006, European Space Agency, SP-1304.
- [2] P. H. Gleick, “Water resources,” in *Encyclopedia of Climate and Weather*, S. H. Schneider, Ed. New York: Oxford University Press, 1996, vol. 2, pp. 817–823.
- [3] I. Allison, R. B. Alley, H. A. Fricker, R. H. Thomas, and R. C. Warner, “Ice sheet mass balance and sea level,” *Antarctic Science*, vol. 21, no. 5, pp. 413–426, 2009.
- [4] E. Rignot, I. Velicogna, M. R. van den Broeke, A. Monaghan, and J. T. M. Lenaerts, “Acceleration of the contribution of the Greenland and Antarctic ice sheets to sea level rise,” *Geophys. Res. Lett.*, vol. 38, no. 5, p. L05503, Mar. 2011.
- [5] A. Shepherd, E. R. Ivins, A. Geruo, V. R. Barletta, M. J. Bentley, S. Bettadpur, K. H. Briggs, D. H. Bromwich, R. Forsberg, N. Galin, M. Horwath, S. Jacobs, I. Joughin, M. A. King, J. T. M. Lenaerts, J. Li, S. R. M. Ligtenberg, A. Luckman, S. B. Luthcke, M. McMillan, R. Meister, G. Milne, J. Mouginot, A. Muir, J. P. Nicolas, J. Paden, A. J. Payne, H. Pritchard, E. Rignot, H. Rott, L. S. Sorensen, T. A. Scambos, B. Scheuchl, E. J. O. Schrama, B. Smith, A. V. Sundal, J. H. van Angelen, W. J. van de Berg, M. R. van den Broeke, D. G. Vaughan, I. Velicogna, J. Wahr, P. L. Whitehouse, D. J. Wingham, D. Yi, D. Young, and H. J. Zwally, “A Reconciled Estimate of Ice-Sheet Mass Balance,” *Science*, vol. 338, no. 6111, pp. 1183–1189, Nov. 2012.

- [6] IPCC, "Summary for Policymakers," in *Climate Change 2013: The Physical Science Basis. Contribution of Working Group I to the Fifth Assessment Report of the Intergovernmental Panel on Climate Change*, T. F. Stocker, D. Qin, G.-K. Plattner, M. Tignor, S. K. Allen, J. Boschung, A. Nauels, Y. Xia, V. Bex, and P. Midgley, Eds. Cambridge, United Kingdom and New York, NY, USA: Cambridge University Press, 2013.
- [7] S. Gogineni, T. Chuah, C. Allen, K. Jezek, and R. Moore, "An improved coherent radar depth sounder," *Journal of Glaciology*, vol. 44, no. 148, pp. 659–669, 1998.
- [8] J. Dall, S. S. Kristensen, V. Krozer, C. C. Hernández, J. Vidkjær, A. Kusk, J. Balling, N. Skou, S. S. Søbjerg, and E. L. Christensen, "ESA's POLarimetric Airborne Radar Ice Sounder (POLARIS): design and first results," *IET Radar, Sonar & Navigation*, vol. 4, no. 3, pp. 488–496, 2010.
- [9] J. J. Legarsky, S. Gogineni, and T. L. Akins, "Focused Synthetic Aperture Radar Processing of Ice-Sounder Data Collected Over the Greenland Ice Sheet," *IEEE Trans. Geosci. Remote Sens.*, vol. 39, no. 10, pp. 2109–2117, Oct. 2001.
- [10] F. Hélière, C.-C. Lin, H. Corr, and D. Vaughan, "Radio Echo Sounding of Pine Island Glacier, West Antarctica: Aperture Synthesis Processing and Analysis of Feasibility from Space," *IEEE Trans. Geosci. Remote Sens.*, vol. 45, no. 8, pp. 2573–2582, Aug. 2007.
- [11] D. J. Daniels, Ed., *Ground Penetrating Radar*, 2nd ed. IEE, 2004.
- [12] K. C. Jezek, S. Gogineni, X. Wu, E. Rodríguez, F. Rodríguez-Morales, A. Hoch, A. Freeman, and J. G. Sonntag, "Two-Frequency Radar Experiments for Sounding Glacier Ice and Mapping the Topography of the Glacier Bed," *IEEE Trans. Geosci. Remote Sens.*, vol. 49, no. 3, pp. 920–929, Mar. 2011.
- [13] G. Picardi, S. Sorge, R. Seu, J. Plaut, W. Johnson, R. L. Jordan, D. Gurnett, R. Orosei, L. Borgarelli, G. Braconi, C. Zelli, and E. Zampolini, "The Mars Advanced Radar for Subsurface and Ionosphere Sounding (MARSIS): concept and performance," in *Proc. IGARSS'99*, vol. 5, Hamburg, Germany, Jun. 1999, pp. 2674–2677.

- [14] G. Picardi, S. Sorge, R. Seu, G. Fedele, and R. L. Jordan, "Coherent Cancellation of Surface Clutter for Radar Sounding," in *Proc. IGARSS'99*, vol. 5, Hamburg, Germany, Jun. 1999, pp. 2678–2680.
- [15] R. Henderson *et al.*, "P-Band sounder instrument design for Antarctica," ESTEC Concurrent Design Facility, Noordwijk, The Netherlands, Tech. Rep., Mar. 2003.
- [16] B. R. Velado, "Radio Echo Sounding of Antarctica Using a Spaceborne P-band radar," ESTEC, Noordwijk, The Netherlands, ESA Working Paper No. 2243, Jul. 2004.
- [17] J. Bruniquel, A. Houpeit, J. Richard, L. Phalippou, M. Dechambre, and J. Guijarro, "Spaceborne P-band radar for ice-sheet sounding: design and performances," in *Proc. IGARSS'04*, vol. 5, Anchorage, USA, Sep. 2004, pp. 2834–2837.
- [18] J. Dall, N. Skou, A. Kusk, S. S. Kristensen, and V. Krozer, "P-sounder: an airborne P-band ice sounding radar," in *Proc. IGARSS'07*, Barcelona, Spain, Jul. 2007, pp. 4225–4228.
- [19] R. Seu, D. Biccari, R. Orosei, L. V. Lorenzoni, R. J. Phillips, L. Marinangeli, G. Picardi, A. Masdea, and E. Zampolini, "SHARAD: The MRO 2005 shallow radar," *Planetary and Space Science*, vol. 52, no. 1–3, pp. 157–166, 2004.
- [20] N. Walker, "Advanced Concepts for Radar Sounders; Final Report," EADS Astrium, Portsmouth, England, ESA Contract No. 4997/05/NL/HE, Aug. 2009.
- [21] R. Scheiber and P. Prats, "Surface Clutter Suppression for Ice Sounding Radars by Coherent Combination of Repeat-Pass Data," in *Proc. IGARSS'07*, Barcelona, Spain, Jul. 2007, pp. 3559–3562.
- [22] R. Scheiber, P. Prats, and F. Hélière, "Surface Clutter Suppression Techniques for Ice Sounding Radars: Analysis of Airborne Data," in *Proc. EUSAR'08*, Friedrichshafen, Germany, Jun. 2008.
- [23] R. K. Raney, "Radar Sounder: Cross-Track Polarimetric Selectivity," in *Proc. EUSAR'08*, Friedrichshafen, Germany, Jun. 2008, pp. 1–4.

- [24] A. Lohofener, "Design and Development of a Multi-Channel Radar Depth Sounder," Master's thesis, University of Kansas, Lawrence, KS, USA, Nov. 2006.
- [25] K. Jezek, P. Gogineni, X. Wu, E. Rodríguez, F. Rodríguez, J. Sonntag, A. Freeman, A. Hoch, and R. Forster, "Global Ice Sheet Mapping Orbiter Concept: Airborne Experiments," in *Proc. EUSAR'12*, Friedrichshafen, Germany, Jun. 2008, pp. 1–4.
- [26] K. Jezek, E. Rodríguez, P. Gogineni, A. Freeman, J. Curlander, X. Wu, J. Paden, and C. Allen, "Glaciers and Ice Sheets Mapping Orbiter concept," *J. Geophys. Res.*, vol. 111, no. E6, Jun. 2006.
- [27] S. Gogineni, J.-B. Yan, J. Paden, C. Leuschen, J. Li, F. Rodriguez-Morales, D. Braaten, K. Purdon, Z. Wang, W. Liu, and J. Gauch, "Bed topography of Jakobshavn Isbræ, Greenland, and Byrd Glacier, Antarctica," *Journal of Glaciology*, vol. 60, no. 223, pp. 813–833, 2014.
- [28] C. Leuschen, R. Hale, S. Keshmiri, J. Yan, F. Rodriguez-Morales, A. Mahmood, and S. Gogineni, "UAS-Based Radar Sounding of the Polar Ice Sheets," *IEEE Geosci. Remote Sens. Mag.*, vol. 2, no. 1, pp. 8–17, 2014.
- [29] J. Li, J. Paden, C. Leuschen, F. Rodríguez-Morales, R. D. Hale, E. J. Arnold, R. Crowe, D. Gomez-Garcia, and P. Gogineni, "High-Altitude Radar Measurements of Ice Thickness Over the Antarctic and Greenland Ice Sheets as a Part of Operation Ice-Bridge," *IEEE Trans. Geosci. Remote Sens.*, vol. 51, no. 2, pp. 742–754, Feb. 2013.
- [30] P. S. Tan, J. Paden, J. Li, J.-B. Yan, and P. Gogineni, "Robust Adaptive MVDR Beamforming for Processing Radar Depth Sounder Data," in *Proc. ARRAY'13*, 2013, pp. 622–629.
- [31] D. Bekaert, N. Gebert, C.-C. Lin, F. Hélière, J. Dall, A. Kusk, and S. S. Kristensen, "Surface Clutter Suppression Techniques for P-band Multi-channel Synthetic Aperture Radar Ice Sounding," in *Proc. EUSAR'12*, Nuremberg, Germany, Apr. 2012.
- [32] C.-C. Lin, D. Bekaert, N. Gebert, F. Hélière, C. Buck, T. Casal, M. Davidson, J. Dall, A. Kusk, S. S. Kristensen, J. Mosig, and

- J.-F. Zürcher, "Surface Clutter Suppression Techniques Applied to P-band Multi-Channel SAR Ice Sounder Data from East Antarctica," presented at the 32nd EARSeL Symposium, 2012.
- [33] D. Bekaert, N. Gebert, C.-C. Lin, F. Hélière, J. Dall, A. Kusk, and S. S. Kristensen, "Multichannel surface clutter suppression: East Antarctica P-band SAR ice sounding in the presence of grating lobes," *Annals of Glaciology*, vol. 55, no. 67, pp. 9–21, 2014.
- [34] R. Scheiber, M. Nannini, P. Prats, M. Villano, K. Morrison, J. Bennett, and H. Corr, "Multi Phase Center Processing of Ice Sounding Radar Signals for Across Track Surface Clutter Cancellation," DLR, ESA Contract No. 4000104671/11/NL/CT, 2014.
- [35] R. Scheiber, P. Prats, M. Nannini, M. Villano, K. Morrison, and N. Gebert, "Comparison of Digital Beamforming Techniques for Enhanced Ice Sounding Radar Data Processing," in *Proc. EU-SAR'14*, Berlin, Germany, Jun. 2014, pp. 32–35.
- [36] A. Reigber and A. Moreira, "First Demonstration of Airborne SAR Tomography Using Multibaseline L-Band Data," *IEEE Trans. Geosci. Remote Sens.*, vol. 38, no. 5, pp. 2142–2152, 2000.
- [37] A. Budillon, A. Evangelista, and G. Schirinzi, "Three-Dimensional SAR Focusing From Multipass Signals Using Compressive Sampling," *IEEE Trans. Geosci. Remote Sens.*, vol. 49, no. 1, pp. 488–499, 2011.
- [38] J. Paden, T. Akins, D. Dunson, C. Allen, and P. Gogineni, "Ice-sheet bed 3-D tomography," *Journal of Glaciology*, vol. 56, no. 195, pp. 3–11, 2010.
- [39] X. Wu, K. C. Jezek, E. Rodríguez, S. Gogineni, F. Rodríguez-Morales, and A. Freeman, "Ice Sheet Bed Mapping with Airborne SAR Tomography," *IEEE Trans. Geosci. Remote Sens.*, vol. 49, no. 10, pp. 3791–3802, Oct. 2011.
- [40] K. Jezek, X. Wu, P. Gogineni, E. Rodríguez, A. Freeman, F. Rodríguez-Morales, and C. D. Clark, "Radar images of the bed of the Greenland Ice Sheet," *Geophys. Res. Lett.*, vol. 38, no. 1, p. L01501, 2011.



- [41] U. Nielsen, J. Dall, A. Kusk, and S. S. Kristensen, "Coherent Surface Clutter Suppression Techniques with Topography Estimation for Multi-Phase-Center Radar Ice Sounding," in *Proc. EUSAR'12*, Nuremberg, Germany, Apr. 2012, pp. 247–250.
- [42] U. Nielsen and J. Dall, "Direction-of-Arrival Estimation for Radar Ice Sounding Surface Clutter Suppression," *IEEE Trans. Geosci. Remote Sens.*, vol. 53, no. 9, pp. 5170–5179, Sep. 2015.
- [43] U. Nielsen, J.-B. Yan, S. Gogineni, and J. Dall, "Direction-of-Arrival Analysis of Airborne Ice Depth Sounder Data," *IEEE Trans. Geosci. Remote Sens.*, submitted for publication.
- [44] D. K. Cheng, *Field and Wave Electromagnetics*, 2nd ed. Addison-Wesley, 1989.
- [45] *IEEE Standard Letter Designations for Radar-Frequency Bands*, Institute of Electrical and Electronics Engineers, Inc. IEEE Std 521™-2002(R2009), 2003.
- [46] J.-S. Lee and E. Pottier, *Polarimetric radar imaging : from basics to applications*. CRC Press, 2009.
- [47] F. T. Ulaby and C. Elachi, Eds., *Radar Polarimetry for Geoscience Applications*. Artech House, 1990.
- [48] J. Dall, "Polarimetric ice sounding at P-band: First results," in *Proc. IGARSS'09*, vol. 2, Cape Town, South Africa, Jul. 2009, pp. 1024–1027.
- [49] J. Dall, S. S. Kristensen, A. Kusk, and N. Reeh, "P-Band Ice Sounding Radar Demonstrator Development; System Analysis and Requirements," Technical University of Denmark, Kongens Lyngby, Denmark, ESA Contract No. 19307/05/NL/JA, Apr. 2007.
- [50] G. Picardi, D. Biccari, R. Seu, L. Marinangeli, W. Johnson, R. Jordan, J. Plaut, A. Safaenili, D. Gurnett, G. Ori, R. Orosei, D. Calabrese, and E. Zampolini, "Performance and surface scattering models for the Mars Advanced Radar for Subsurface and Ionosphere Sounding (MARSIS)," *Planetary and Space Science*, vol. 52, no. 1–3, pp. 149–156, 2004.

- [51] K. Matsuoka, J. A. MacGregor, and F. Pattyn, "Predicting radar attenuation within the antarctic ice sheet," *Earth and Planetary Science Letters*, vol. 359–360, pp. 173–183, Dec. 2012.
- [52] S. Fujita, T. Matsuoka, T. Ishida, K. Matsuoka, and S. Mae, "A summary of the complex dielectric permittivity of ice in the megahertz range and its applications for radar sounding of polar ice sheets," in *Physics of Ice Core Records*, Hokkaido, Japan, 2000, pp. 185–212.
- [53] H. Corr, "Feasibility Study of Imaging the Antarctic Ice using a Spaceborne P-Band Radar," British Antarctic Survey, ESA Contract No. 18195/04/NL/CB, Aug. 2005.
- [54] F. T. Ulaby, R. K. Moore, and A. K. Fung, *Microwave Remote Sensing: Active and Passive*. Addison-Wesley, 1981, vol. I.
- [55] C. A. Balanis, *Advanced Engineering Electromagnetics*, 2nd ed. John Wiley, 2012.
- [56] F. T. Ulaby, R. K. Moore, and A. K. Fung, *Microwave Remote Sensing: Active and Passive*. Addison-Wesley, 1982, vol. II.
- [57] M. I. Skolnik, *Introduction to Radar Systems*, 3rd ed. McGraw-Hill, 2002.
- [58] M. I. Skolnik, *Radar Handbook*, 3rd ed. McGraw-Hill, 2008.
- [59] N. J. Willis and H. D. Griffiths, Eds., *Advances in Bistatic Radar*. SciTech Publishing, 2007.
- [60] A. Khenchaf, F. Daout, and J. Saillard, "The two-scale model for random rough surface scattering," in *Proc. OCEANS'96*, Fort Lauderdale, USA, Sep. 1996, pp. 887–891.
- [61] A. Fung and K. Chen, *Microwave Scattering and Emission Models for Users*. Artech House, 2010.
- [62] C. Elachi and J. van Zyl, *Introduction to the Physics and Techniques of Remote Sensing*, 2nd ed. John Wiley, 2006.
- [63] A. Moreira, P. Prats-Iraola, M. Younis, G. Krieger, I. Hajnsek, and K. P. Papathanassiou, "A Tutorial on Synthetic Aperture Radar," *IEEE Geosci. Remote Sens. Mag.*, vol. 1, no. 1, pp. 6–43, Mar. 2013.

- [64] A. F. Harvey, *Microwave engineering*. Academic Press, 1963.
- [65] M. Kowatsch and H. R. Stocker, "Effect of Fresnel ripples on sidelobe suppression in low time-bandwidth product linear FM pulse compression," *IEE Proceedings*, vol. 129, no. 1, pp. 41–44, Feb. 1982.
- [66] C. A. Balanis, *Modern Antenna Handbook*. John Wiley, 2008.
- [67] P. Stoica and R. L. Moses, *Introduction to Spectral Analysis*. Prentice Hall, 1997.
- [68] S. Andersson, "On dimension reduction in sensor array signal processing," Ph.D. dissertation, Linköping University, Linköping, Sweden, 1992, Linköping Studies in Science and Technology, Dissertations No. 290.
- [69] U. Nielsen, "Coherent Surface Clutter Suppression Techniques for Airborne and Space-based Radar Ice Sounding," Master's thesis, Technical University of Denmark, Kongens Lyngby, Denmark, Feb. 2011.
- [70] M. J. Hinich, "Processing spatially aliased arrays," *J. Acoust. Soc. Am.*, vol. 64, no. 3, pp. 792–794, Sep. 1978.
- [71] B. D. Van Veen and K. M. Buckley, "Beamforming: A Versatile Approach to Spatial Filtering," *IEEE ASSP Mag.*, vol. 5, no. 2, pp. 4–24, Apr. 1988.
- [72] D. Johnson and D. Dudgeon, *Array Signal Processing*. Prentice Hall, Feb. 1993.
- [73] H. Van Trees, *Optimum array processing*. John Wiley & Sons, 2002.
- [74] Capon, "High-resolution frequency-wavenumber spectrum analysis," *Proceedings of the IEEE*, vol. 57, no. 8, pp. 1408–1418, 1969.
- [75] P. Stoica and R. Moses, *Spectral Analysis of Signals*. Prentice Hall, 2005.
- [76] S. Kogon, "Robust adaptive beamforming for passive sonar using eigenvector/beam association and excision," in *Proc. SAM'02*, Washington D.C., USA, Aug. 2002, pp. 33–37.

- [77] J. R. Guerci, *Space-time adaptive processing for radar*. Artech House, 2003.
- [78] L. C. Godara, *Smart antennas*. CRC Press, 2004.
- [79] J. Li, P. Stoica, and Z. Wang, "On robust capon beamforming and diagonal loading," *IEEE Trans. Signal Process.*, vol. 51, no. 7, pp. 1702–1715, Jul. 2003.
- [80] I. J. Gupta and A. A. Ksienski, "Effect of Mutual Coupling on the Performance of Adaptive Arrays," *IEEE Trans. Antennas Propag.*, vol. AP-31, no. 5, pp. 785–791, Sep. 1983.
- [81] H. Steyskal and J. Herd, "Mutual Coupling Compensation in Small Array Antennas," *IEEE Trans. Antennas Propag.*, vol. 38, no. 12, pp. 1971–1975, Dec. 1990.
- [82] J. G. Proakis and D. G. Manolakis, *Digital Signal Processing; Principles, Algorithms, and Applications*, 4th ed. Pearson, 2007.
- [83] H. Krim and M. Viberg, "Two decades of array signal processing research," *IEEE Signal Process. Mag.*, vol. 13, no. 4, pp. 67–94, 1996.
- [84] S. L. Marple, *Digital spectral analysis*. Prentice-Hall, 1987.
- [85] R. O. Schmidt, "Multiple Emitter Location and Signal Parameter Estimation," *IEEE Trans. Antennas Propag.*, vol. 34, no. 3, pp. 276–280, Mar. 1986.
- [86] I. Ziskind and M. Wax, "Maximum Likelihood Localization of Multiple Sources by Alternating Projection," *IEEE Trans. Acoust., Speech, Signal Process.*, vol. 36, no. 10, pp. 1553–1560, Oct. 1988.
- [87] C. M. Bishop, *Pattern Recognition and Machine Learning*, 2nd ed. Springer, 2006.
- [88] P. Lancaster and M. Tismeneysky, *The Theory of Matrices*, 2nd ed. Academic Press, 1985.
- [89] P. Stoica and A. Nehorai, "MUSIC, maximum likelihood, and Cramér-Rao bound," *IEEE Trans. Acoust., Speech, Signal Process.*, vol. 37, no. 5, pp. 720–741, May 1989.

- [90] P. Stoica and A. Nehorai, "MUSIC, maximum likelihood, and Cramér-Rao bound: further results and comparisons," *IEEE Trans. Acoust., Speech, Signal Process.*, vol. 38, no. 12, pp. 2140–2150, Dec. 1990.
- [91] E. Candes and M. Wakin, "An Introduction To Compressive Sampling," *IEEE Signal Process. Mag.*, vol. 25, no. 2, pp. 21–30, 2008.
- [92] X. X. Zhu and R. Bamler, "Tomographic SAR Inversion by  $L_1$ -Norm Regularization—The Compressive Sensing Approach," *IEEE Trans. Geosci. Remote Sens.*, vol. 48, no. 10, pp. 3839–3846, 2010.
- [93] J. Luis Vazquez-Roy, V. Krozer, and J. Dall, "Wideband Dual-Polarization Microstrip Patch Antenna Array for Airborne Ice Sounder," *IEEE Antennas Propag. Mag.*, vol. 54, no. 4, pp. 98–107, Aug. 2012.
- [94] J. Dall, C. Hernandez, S. Kristensen, V. Krozer, A. Kusk, J. Vidkjoer, J. Balling, N. Skou, S. Sobjerg, and E. Christensen, "P-band Polarimetric Ice Sounder: Concept and First Results," in *Proc. IGARSS'08*, vol. 4, Boston, USA, Jul. 2008, pp. 494–497.
- [95] S. López-Peña, J. F. Zürcher, R. Torres, A. G. Polimeridis, and J. R. Mosig, "Modeling and Manufacturing of a Series of Identical Antennas for a P-Band Ice Sounder," in *Proc. EuCAP'10*, Barcelona, Spain, Apr. 2010, pp. 1–5.
- [96] A. Kusk and J. Dall, "SAR focusing of P-band ice sounding data using back-projection," in *Proc. IGARSS'10*, Honolulu, Hawaii, Jul. 2010, pp. 4071–4074.
- [97] A. Kusk, J. Dall, and S. S. Kristensen, "POLARIS User Data Products, v13.02," Technical University of Denmark, Kongens Lyngby, Denmark, Tech. Rep., Feb. 2013.
- [98] S. N. Madsen and H. A. Zebker, *Manual of Remote Sensing. Principles and Applications of Imaging Radar*, 3rd ed. John Wiley and Sons, 1998, vol. 2, ch. 6.
- [99] J. Dall, A. Kusk, S. S. Kristensen, U. Nielsen, R. Forsberg, C.-C. Lin, N. Gebert, T. Casal, M. Davidson, D. Bekaert, and

- C. Buck, "P-band radar ice sounding in Antarctica," in *Proc. IGARSS'12*, Munich, Germany, Jul. 2012, pp. 1561–1564.
- [100] R. Bindshadler, P. Vornberger, A. Fleming, A. Fox, J. Mullins, D. Binnie, S. J. Paulsen, B. Granneman, and D. Gorodetzky, "The Landsat Image Mosaic of Antarctica," *Remote Sensing of Environment*, vol. 112, no. 12, pp. 4214–4226, 2008.
- [101] R. Bindshadler, H. Choi, A. Wichlacz, R. Bingham, J. Bohlander, K. Brunt, H. Corr, R. Drews, H. Fricker, M. Hall, R. Hindmarsh, J. Kohler, L. Padman, W. Rack, G. Rotschky, S. Urbini, P. Vornberger, and N. Young, "Getting around Antarctica: new high-resolution mappings of the grounded and freely-floating boundaries of the Antarctic ice sheet created for the International Polar Year," *The Cryosphere*, vol. 5, no. 3, pp. 569–588, 2011.
- [102] S. Pivnenko and O. Breinbjerg, "Study of Very Large Aperture P-Band Antenna Performance Verification Methodology and Facilities; TR8: POLARIS Antenna Test Report," Technical University of Denmark, Kongens Lyngby, Denmark, ESA Contract No. 4000102325/10/NL/JA, Dec. 2011.
- [103] F. Rodríguez-Morales, S. Gogineni, C. J. Leuschen, J. D. Paden, J. Li, C. C. Lewis, B. Panzer, D. G.-G. Alvestegui, A. Patel, K. Byers, R. Crowe, K. Player, R. D. Hale, E. J. Arnold, L. Smith, C. M. Gifford, D. Braaten, and C. Panton, "Advanced Multifrequency Radar Instrumentation for Polar Research," *IEEE Trans. Geosci. Remote Sens.*, vol. 52, no. 5, pp. 2824–2842, May 2014.
- [104] J.-B. Yan, J. Li, F. Rodríguez-Morales, R. Crowe, D. Gomez-Garcia, E. J. Arnold, J. Paden, C. J. Leuschen, and S. Gogineni, "Measurements of In-Flight Cross-Track Antenna Patterns of Radar Depth Sounder/Imager," *IEEE Trans. Antennas Propag.*, vol. 60, no. 12, pp. 5669–5678, Dec. 2012.
- [105] D. M. Schroeder, D. D. Blankenship, D. A. Young, A. E. Witus, and J. B. Anderson, "Airborne radar sounding evidence for deformable sediments and outcropping bedrock beneath Thwaites Glacier, West Antarctica," *Geophysical Research Letters*, vol. 41, no. 20, pp. 7200–7208, Oct. 2014.

- 
- [106] N. Niamsuwan, “Electromagnetic Scattering Models for the Global Ice Sheet Mapping Orbiter Demonstrator,” Ph.D. dissertation, Ohio State University, 2009.
  - [107] G. S. Brown, “The average impulse response of a rough surface and its applications,” *IEEE Trans. Antennas Propag.*, vol. AP-25, no. 1, pp. 67–74, Jan. 1977.

---

## Index

### A

Alternating maximisation, 63  
Alternating projection, 63  
Array factor, 35  
Attenuation, 18, 122

### B

Beam-steering, 46

### C

Capon beamforming, 48  
Compressive sensing, 68  
Convolution model, 124  
Cramér-Rao bound, 67

### E

Electromagnetic spectrum, 15  
Equivalent nadir depth, 6

### F

Far field, 40  
Frequency, 15  
    radar, 15  
    spatial Nyquist, 44  
Fresnel Equations, 18  
Fresnel zone, 31

### G

Geometric spreading, 122

### I

Integral Equation Model, 25

### K

Kirchhoff Model, 23

### M

Maximum Likelihood, 61  
Maxwell's equations, 13  
MCoRDS/I, 89  
MUSIC, 58  
    Root MUSIC, 60  
Mutual coupling, 55

### N

Noise scaling, 52  
Null-steering, 47  
Nyquist–Shannon theorem, 44

### O

Optimum beamforming, 50

### P

Permittivity, 14  
    of free space, 14  
    of ice, 18  
    of rock, 18  
    relative, 14  
Plane wave approximation, 40  
POLARIS, 3, 79



Polarization, 15

Pulse compression, 28

## **R**

Radar cross section, 21

Radar equation, 21, 127

Reflectivity, 19

## **S**

Scattering coefficient, 21

    backscatter, 22

    flat surface, 22

    rough surface, 22

Self-nulling, 49, 54

Small Perturbation Model, 25

Snapshot, 43

Snell's law, 20

Spatial aliasing, 44

Spatial angular frequency, 44

Synthetic aperture radar, 27

    processing, 29

    unfocused, 31

## **T**

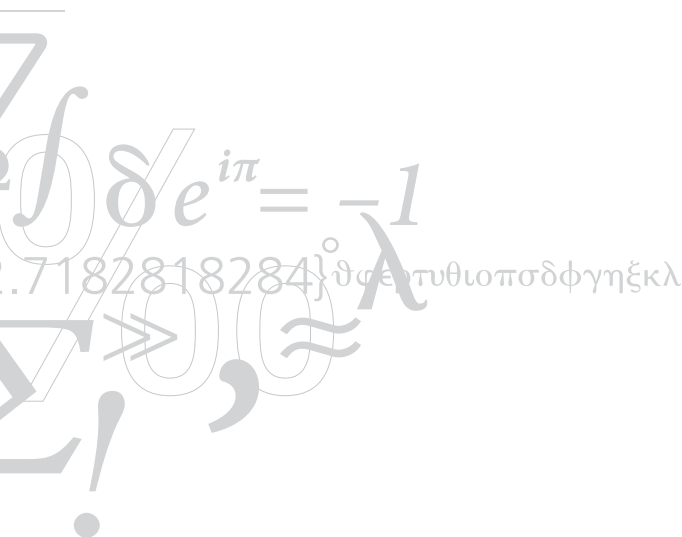
Transmissivity, 19

## **U**

Uniform linear array, 36

## **W**

Wave equation, 14



**DTU Space**  
**National Space Institute**  
**Technical University of Denmark**

Ørstedes Plads  
Building 348  
DK-2800 Kgs. Lyngby  
Tel. (+45) 4525 9500

[www.space.dtu.dk](http://www.space.dtu.dk)

